

Dissertation

submitted to the
Combined Faculty of Mathematics, Engineering and Natural Sciences
of Heidelberg University, Germany
for the degree of
Doctor of Natural Sciences

Put forward by

Lilo Höcker

born in: Baden, Switzerland

Oral examination: 16th of October 2024

Progress and Challenges in Setting up an Ultracold ^{23}Na - ^{39}K Quantum Gas Experiment

Referees: Prof. Dr. Markus Oberthaler
Prof. Dr. Thomas Pfeifer

ABSTRACT

Progress and Challenges in Setting up an Ultracold ^{23}Na - ^{39}K Quantum Gas Experiment

This thesis describes the ongoing construction of an ultra-cold atomic mixture experiment using sodium (^{23}Na) and potassium (^{39}K). The planned experimental setup consists of a two-dimensional trap geometry with a high-resolution imaging system for observing the atoms. This new setup aims to provide a robust and stable mixture experiment, ensuring as much flexibility and independence of the two species as possible.

In this experiment, sodium atoms have been cooled to degeneracy, and Feshbach resonance measurements of thermal potassium in the optical dipole trap have been conducted [1]. The achievement of a dual-species degeneracy has been impeded by considerable three-body losses between sodium and potassium to date.

This thesis describes the experimental setup, focusing on the vacuum system and the two-dimensional magneto-optical trap, and provides a critical discussion of these components. These components influence the efficient loading of atoms into the subsequent stages of the experiment. In addition, this thesis describes the design and optical characterisation of the two-dimensional optical dipole trap and the vertical high numerical aperture imaging system. Both are important steps towards the two-dimensional geometry of the system and the first experiments after achieving the dual species condensate.

ZUSAMMENFASSUNG

Fortschritte und Herausforderungen beim Aufbau eines ultrakalten ^{23}Na - ^{39}K -Quantengasexperiments

Diese Arbeit beschreibt den laufenden Aufbau eines Experiments mit ultrakalten atomaren Mischungen aus Natrium (^{23}Na) und Kalium (^{39}K). Die geplante Versuchsanordnung besteht aus einer zweidimensionalen Fallengeometrie mit einem hochauflösenden Bildgebungssystem zur Beobachtung der Atome. Dieser neue Aufbau soll ein robustes und stabiles Mischungs-Experiment ermöglichen, das so viel Flexibilität und Unabhängigkeit wie möglich für die beiden Spezies ermöglicht.

In diesem Experiment wurden Natriumatome bis zur Entartung gekühlt und Feshbach-Resonanzmessungen von thermischem Kalium in der optischen Dipolfalle durchgeführt [1]. Die Erreichung einer Entartung zweier Spezies wurde bisher durch erhebliche Dreikörperverluste zwischen Natrium und Kalium behindert.

Diese Arbeit beschreibt den Versuchsaufbau mit Schwerpunkt auf dem Vakuumsystem und der zweidimensionalen magnetooptischen Falle und bietet eine kritische Diskussion dieser Komponenten. Diese Komponenten beeinflussen das effiziente Laden der Atome in den nachfolgenden Phasen des Experiments.

Darüber hinaus beschreibt diese Arbeit das Design und die optische Charakterisierung der zweidimensionalen optischen Dipolfalle und des vertikalen Bildgebungssystems mit hoher numerischer Apertur. Beide sind wichtige Schritte in Richtung der zweidimensionalen Geometrie des Systems und der ersten Experimente nach der Erzeugung des zweiatomigen Kondensats aus zwei Komponenten.

CONTENTS

1	INTRODUCTION	1
2	KEY CONCEPTS	5
2.1	Optical Dipole Trap	6
2.2	Bose-Einstein Condensate	9
2.3	Two Component Condensate	12
3	SOPA EXPERIMENT IN A NUTSHELL	17
3.1	Brief Overview of the SoPa Experiment	17
3.2	History of the SoPa Experiment	20
3.3	Current Status of the SoPa Experiment	23
4	VACUUM	29
4.1	Overview of the SoPa Vacuum System	30
4.2	Designing Considerations for a Vacuum System	34
4.3	Navigating Vacuum Challenges	36
4.3.1	Cleaning of Vacuum Parts	36
4.3.2	Vacuum Component Assembly and Handling	37
4.3.3	Bake-out	41
4.3.4	Oven Filling and Cleaning	45
4.3.5	Flooding the Vacuum Chamber	47
4.3.6	Sudden Leak in a Viewport	48
4.3.7	Opaque Coating of the Viewport on the Vacuum Side	49
4.3.8	Sudden Rise of Ion Pump Current	50
4.3.9	Curiosities in the Vacuum System	52
5	TWO-DIMENSIONAL MAGNETO-OPTICAL TRAP	55
5.1	2D Magneto-Optical Trap Setup	55
5.1.1	Brief Overview	55
5.1.2	2D MOT Beams	56
5.1.3	Quadrupole Magnetic Field	60
5.2	2D MOT Optimization	62
6	CRITICAL DISCUSSION OF THE EXPERIMENTAL SETUP	71
6.1	Separation of the Atomic Species	71
6.2	Vacuum System on a Translation Stage	72
6.3	2D MOT Chamber	73
6.4	2D MOT Optics	77
6.5	Summary	77
7	TWO-DIMENSIONAL DIPOLE TRAP	79
7.1	Two-Dimensional Optical Dipole Trap Setup	79
7.2	Design Considerations	80
7.2.1	Trap Geometry	80
7.2.2	Choice of Optical Components	83
7.2.3	Mechanical Setup	85
7.3	Characterization	87

7.4	Signal Hunting and Optimization	88
8	HIGH RESOLUTION IMAGING	93
8.1	Absorption Imaging	94
8.2	Objective	95
8.3	Vertical Imaging Setup	96
8.4	Objective Characterization	99
8.5	Objective Holder	109
8.6	MOT Compensation Optics	112
8.6.1	Brief Overview	112
8.6.2	Optics	114
8.6.3	Lens and Mirror Holder	115
8.6.4	Pneumatic Translation Stage	118
8.7	Summary and Discussion	120
9	SUMMARY AND OUTLOOK	123
	Appendix	129
A	TECHNICAL DRAWINGS AND SPECIFICATION SHEETS	130
A.1	Objective	131
A.2	Objective Holder	132
A.3	Brass Mirror Mount	136
A.4	Compensation Optics Mounts	137
A.5	Vacuum	139
A.5.1	Main and Science Chamber	139
A.5.2	2D MOT Chamber	144
A.5.3	Science Chamber Mount	147
A.6	2D Optical Dipole Trap Block	148
A.7	Magnet Mount	150
B	VACUUM SYSTEM ESTIMATION CALCULATIONS	153
B.1	Estimating Pressure Discrepancies between 2D MOT Cham- ber and Ion Pump	153
B.2	Estimating Getter Saturation Time	155
	BIBLIOGRAPHY	163

LIST OF FIGURES

Figure 1.1	The Quantum Problem Landscape	2
Figure 2.1	Polarizability of Sodium and Potassium	8
Figure 2.2	Differential Gravitational Sag	10
Figure 2.3	Species Overlap in Optical Dipole Trap	13
Figure 2.4	Excitation Branches Two Component BEC	14
Figure 3.1	Overview of Experimental Setup and Cooling Sequence	17
Figure 3.2	Time-Lapse Disruptive Transformation	22
Figure 3.3	Sodium Dipole Trap Evaporation to BEC	24
Figure 3.4	Stern-Gerlach Imaging	25
Figure 3.5	Sodium Push Beam Fluorescence	27
Figure 3.6	Fluorescence in Sodium Spectroscopy Cell	27
Figure 4.1	Gas Sources and Outgassing in a Vacuum Cham- ber	30
Figure 4.2	SoPa Vacuum Setup	31
Figure 4.3	2D MOT Chamber	32
Figure 4.4	Science Chamber	33
Figure 4.5	Vacuum Gallery	40
Figure 4.6	Ion Pump Current 2D MOT K	50
Figure 4.7	Leakage Current Measurements	51
Figure 5.1	2D MOT Overview	56
Figure 5.2	2D MOT Optics Overview	57
Figure 5.3	2D MOT Optics	58
Figure 5.4	Position and Mounting of Permanent Magnets	60
Figure 5.5	Visualization of Simulated Magnet Displacements	61
Figure 5.6	Sensitivity of Slower Magnetic Field Depending on Magnet Position	63
Figure 5.7	Sensitivity of Magnetic Field along MOT Beam Depending on Magnet Position	64
Figure 5.8	MOT Loading Curve	65
Figure 5.9	MOT Loading Rate vs. Beam Power and Cooler Detuning	66
Figure 5.10	MOT Loading Rate vs. Oven Temperature	67
Figure 5.11	MOT Loading Rate vs. Slower Detuning and Power	69
Figure 6.1	New Permanent Magnets Characterization	76
Figure 7.1	Optics for 2d Optical Dipole Trap	81
Figure 7.2	Usage of Optical Access Science Chamber	82
Figure 7.3	Knife Edge Measurement	88
Figure 7.4	Two-Dimensional Optical Dipole Trap Signal	90
Figure 8.1	Absorption Imaging	95
Figure 8.2	Sketch High NA Objective	96

Figure 8.3	Vertical Imaging Setup	97
Figure 8.4	Mount for Bottom Dichroic Imaging Mirror . . .	99
Figure 8.5	Image of the Gold Foil	100
Figure 8.6	Test Setups for Objective Characterization Mea- surements	101
Figure 8.7	Camera Image of Gold Foil	101
Figure 8.8	High NA Objective Focus Characterization Mea- surements	103
Figure 8.9	Field of View for Potassium Light	106
Figure 8.10	Field of View for Sodium Light Reflecting on a Dichroic Mirror.	107
Figure 8.11	Field of View for Potassium Light Transmitting through a Dichroic Mirror.	108
Figure 8.12	Objective Holder Assembly	110
Figure 8.13	Overview of MOT Compensation Optics	113
Figure 8.14	General Schematic of a Three-Lens System.	114
Figure 8.15	MOT Beam Compensation Optics for Vertical Imaging Setup	116
Figure 8.16	Mirror and Lens Mount Assembly	117
Figure 8.17	Removing Magnets from Pneumatic Translation Stage	119
Figure 8.18	Pneumatic Translation Stage Circuits	120
Figure B.1	2D MOT Conductance Estimation	154

INTRODUCTION

In recent years, the study of quantum many-body systems has revealed the limitations of classical computational methods. As the complexity of these systems increases, classical simulations become insufficient due to the exponential growth of the problem size, a challenge that current computational power cannot overcome [2]. While Moore's Law has historically predicted the exponential growth of computing power [3], this trend is reaching its physical limits as transistor sizes approach the nanoscale, where quantum effects begin to interfere with further miniaturisation [4].

Although the concept of a quantum computer, first proposed in the 1980s [5], promises to revolutionise our approach to complex quantum systems, the technology is still in its early stages. Current quantum computers are limited by challenges such as managing decoherence, controlling large numbers of qubits and performing reliable error correction [6–9]. These limitations mean that fully functional quantum computers capable of simulating large quantum systems are still a distant goal [10, 11].

Nevertheless, it is not strictly necessary to study quantum systems with a universal quantum computer. Figure 1.1 illustrates the landscape of quantum problems. The smallest subset of problems (depicted in purple) comprises those that are analytically solvable, including for example the hydrogen atom and the quantum harmonic oscillator. The application of numerical techniques allows for the expansion of the subset of problems that can be addressed. In consequence of the ongoing development of the field, these boundaries are not always clearly defined. The subset of problems that can be addressed using quantum simulators is represented by the red subset, and it also has indistinct borders due to ongoing advancements in this field. The remainder of the landscape represents problems that remain intractable, depicted as mountains. Hidden valleys may reveal problems we might not have anticipated.

In recent years, several analogue quantum simulation technologies have been developed, including trapped ions, superconducting qubits, and ultra-cold atoms, to name a few [2, 12]. This work focuses on ultra-cold atoms as an analogue quantum simulation platform [13–15].

Following the initial experimental observation of a Bose-Einstein condensate in 1995 [16, 17], the field of ultra-cold atoms experienced a period of rapid growth. Further atomic species were condensed [18],

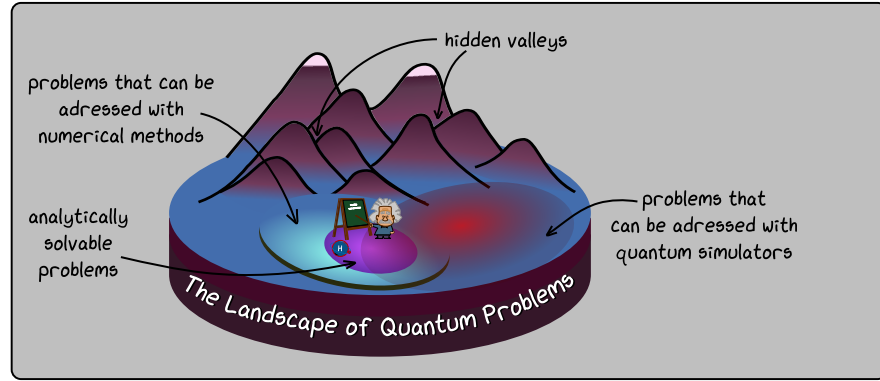


Figure 1.1: Illustration of the landscape of quantum problems. While only a very small subset of problems is analytically solvable, other methods are helping to explore more problems. With numerical methods it is possible to widen the amount of problems that can be tackled. Although, it is not exactly clear where the edges are, the subset remains rather small. Quantum simulators give access to a larger set of problems. The overlap with the analytical and numerical tackling problems can be used to benchmark the quantum simulator. Being outside of that results have to be confirmed with other quantum simulators. Mountains with hidden valleys represent all the problems we cannot address up to date.

and new trapping, cooling, and manipulation methods were developed [19, 20]. Consequently, ultra-cold atom experiments today represent a versatile platform with a robust toolbox of highly controllable experimental parameters [13]. The potential applications for these analogue quantum simulators are numerous and diverse, spanning a range of areas including the study of universal dynamics far from equilibrium [21, 22] and the simulation of curved space-time [23, 24].

Extending ultracold atom experiments further, researchers have mixed atoms in different spin states to form homonuclear spin mixtures, first achieved with rubidium [25]. They have also combined different species or atomic isotopes to create heteronuclear mixtures, first realised with potassium-41 and rubidium-87 [26] [27]. For the sake of simplicity, we will refer to heteronuclear mixtures as "mixture experiments" in this thesis.

Mixture experiments imply additional complexities however allow to control more experimental parameters, such as inter- and intraspecies interactions, species-specific optical potentials or phase imprints, enhancing the flexibility and precision of experiments [27]. Mixture experiments have the potential to contribute to a number of different fields of study, including those concerned with dynamical gauge fields [28], polaron studies [29–31], vortices in superfluids [32, 33]. Consequently, new apparatuses are constantly being built and developed [34–36]. This

thesis describes the setup of a new ultra-cold mixture experiment.

The design choices made for the experiment are of fundamental importance for the subsequent degree of versatility and controllability of the experimental parameters.

The most restrictive choice is that of the atomic species, which determines the statistical behaviour (bosonic or fermionic) and the possible range of interaction strengths due to atomic Feshbach resonances [37]. Moreover, the design choices made for the trap setup have an impact on the trapping geometry, which in turn affects the dimensionality of the system [38].

The configuration of the magnetic field coils establishes the maximum attainable magnetic fields and ramps, thereby defining the accessible interaction strengths. Although these parameters are fixed within the experimental apparatus, the ongoing nature of these experiments allows for continuous development, thereby making the apparatus both versatile and engaging to work with.

The experimental parameters, including the number of atoms, density, spin state, and interaction strength within the constraints set by the atomic species employed, can be specified within the experimental sequence.

In the case of the experiment described in this thesis, the atomic species chosen are sodium and potassium-39. The combination of these two offers a favourable set of Feshbach resonances at moderate magnetic fields (below 300 G), as demonstrated by Schulze et al. [39]. This enables the working regime to be in both the strong attractive and repulsive limits. Sodium was among the first elements to be condensed [18], while potassium-39 condensation was achieved more recently [40]. However, combining these bosonic species remains a challenge and is pursued by only a few groups [35, 39, 41, 42]. Furthermore, potassium has several stable isotopes, which makes it in principle possible to further develop the experiment to use one of the other isotopes, namely ^{40}K [36, 43] or ^{41}K [44]. Potassium-40 is fermionic and therefore allows the study of Bose-Fermi mixtures; however, it is less abundant. Potassium-41 is bosonic and the recently measured background scattering rates [44] make it an interesting choice for ultra-cold atom experiments allowing to work at low magnetic bias fields.

The experimental platform in the lab is going to have a two-dimensional geometry, which allows for direct observation of the atoms using a high numerical aperture (NA) imaging system without averaging atomic densities. Furthermore, if the atoms are strongly confined, a quasi-two-dimensional system can be created, enabling the study of interesting dynamics [24, 33, 45].

The structure of the thesis is as follows

In **Chapter 2** key theoretical concepts of optical dipole traps and Bose-Einstein condensate theory are discussed.

Chapter 3 provides a brief overview of the experiment by introducing the various building blocks of the experimental sequence. It also outlines the history of the SoPa experiment and its current status, including experimental milestones and challenges.

Chapter 4 first describes the vacuum system of the SoPa experiment, the following sections provide more practical guidance on dealing with the vacuum, based on numerous observations and experiences made during the course of this thesis.

Chapter 5 focuses on the 2D MOT after a brief description of the setup. Details of the optical layout and the magnetic field configuration are given. Finally, the optimisation routine of the 2D MOT is presented.

Chapter 6 provides a critical discussion of the experimental setup, evaluating design choices and discussing solutions to identified problems.

In **Chapter 7**, the configuration of the two-dimensional optical dipole trap is first described. The design considerations are then described, followed by the characterisation of the beam waist in a test setup. Finally, the signal hunting and optimisation procedures are described.

Chapter 8 describes the planned high-resolution vertical imaging setup. The absorption imaging technique used at SoPa is briefly described. Before that, the planned imaging setup is presented and its characteristics are evaluated in a test setup. In the following section, the planned physical implementation of the imaging system is described in detail, as well as the required compensating optics for the vertical MOT beam. Finally, the results are summarised and discussed.

The last **Chapter 9** gives an outlook on future directions of the experiment.

In **Appendix A** technical drawings of various components are provided and in **Appendix B** a calculation to estimate the conductance in the 2D MOT chamber is done.

KEY CONCEPTS

In this chapter we will first give a brief overview of the different traps commonly used for neutral atoms, where we will go into more detail for optical dipole traps. We then briefly summarise the most important properties of a Bose-Einstein condensate.

A number of traps have been developed for neutral atoms, which can be grouped into three principal categories based on the nature of the underlying interaction [38]:

RADIATION PRESSURE TRAPS such as the magneto-optical trap (MOT), exhibit strong dissipative forces. Therefore, are used at the early stage of the experiment to cool atoms from a thermal gas. The strong optical excitations limit the traps performance in temperature and density. The temperature is limited by the photon recoil $T_{\text{recoil}} = \frac{\hbar^2 k^2}{mk_{\text{B}}}$ ¹ while the density is limited by radiation trapping and light-assisted inelastic collisions. Comprehensive details about the magneto optical MOT can be read in [46].

MAGNETIC TRAPS utilize a state-dependent conservative force on the magnetic dipole moment, necessitating an inhomogeneous magnetic field. Typical trap depths are in the order of 100 mK. However, the state dependence of these traps restricts the choice of experiments and possible trapping geometries. A comprehensive introduction to magnetic traps is given in [47].

OPTICAL DIPOLE TRAPS use far-detuned light, which results in weaker electric dipole interactions compared to the previous two trap categories. The far detuning suppresses light-induced losses and heating mechanisms, allowing typical trap depths around 1 mK. An additional advantage of optical dipole traps is their independence from the atomic state, enabling a wide variety of trapping geometries [48–52] through beam shaping [53, 54] and interference methods [55, 56]. This flexibility makes optical dipole traps a standard tool for the final trapping stages of neutral atoms. A comprehensive review of dipole traps can be found in [38].

In the following sections, we will delve into the specifics of optical dipole traps (Section 2.1) and explore basic properties of Bose-Einstein condensates (Section 2.2) produced within these traps.

¹ $T_{\text{recoil}, {}^{23}\text{Na}} = 2.4\mu\text{K}$, $T_{\text{recoil}, {}^{39}\text{K}} = 0.84\mu\text{K}$

2.1 OPTICAL DIPOLE TRAP

In this section, optical dipole traps are described in more detail, following the review article by Grimm et al. [38].

When an atom is treated as a simple oscillator in the electric field \mathbf{E} of laser light, it acquires an induced atomic dipole moment \mathbf{p} that oscillates at the driving frequency ω . The relationship between the amplitude of the electric field and the induced dipole moment is given by $p = \alpha(\omega)E$, where α represents the complex polarizability of the atom. The interaction potential is determined by the in phase oscillation, which corresponds to the real part of the polarizability

$$U_{\text{dipole}}(\mathbf{r}) = -\frac{1}{2\epsilon_0 c} \text{Re}(\alpha)I(\mathbf{r}), \quad (2.1)$$

where the intensity of the light is $I(r) = 2\epsilon_0 c|E|^2$, ϵ_0 the vacuum permittivity and c the speed of light. The out-of-phase term, described by the imaginary part, represents the photon scattering rate

$$\Gamma_{\text{sc}}(\mathbf{r}) = \frac{1}{\hbar\epsilon_0 c} \text{Im}(\alpha)I(\mathbf{r}), \quad (2.2)$$

where \hbar is the reduced Planck constant.

The polarizability α is given by

$$\alpha = 6\pi\epsilon_0 c^3 \frac{\Gamma/\omega_0^2}{\omega_0^2 - \omega^2 - i(\omega^3/\omega_0^2)\Gamma} \quad (2.3)$$

where ω_0 is the resonance frequency and Γ the on-resonance damping rate. The classical model for the damping rate provides good approximation, however, a semi-classical model in which the atom is considered as two-level system offers a more precise representation. In this model, the damping rate is depends on the dipole matrix element between the ground and excited states $\langle e|\mu|g\rangle$ and is given by

$$\Gamma = \frac{\omega_0^3}{3\pi\epsilon_0 \hbar c^3} |\langle e|\mu|g\rangle|^2. \quad (2.4)$$

For large detunings and negligible saturation, the dipole potential is given by the expression

$$U_{\text{dip}}(\mathbf{r}) = -\frac{3\pi c^2}{2\omega_0^3} \left(\frac{\Gamma}{\omega_0 - \omega} + \frac{\Gamma}{\omega_0 + \omega} \right) I(\mathbf{r}) \quad (2.5)$$

and the corresponding scattering rate by

$$\Gamma_{\text{sc}}(\mathbf{r}) = \frac{3\pi c^2}{2\hbar\omega_0^3} \left(\frac{\omega}{\omega_0} \right)^3 \left(\frac{\Gamma}{\omega_0 - \omega} + \frac{\Gamma}{\omega_0 + \omega} \right)^2 I(\mathbf{r}). \quad (2.6)$$

In the case of small detuning $\Delta = \omega - \omega_0 \ll \omega_0$, the rotating wave approximation is valid. Consequently, the counter-rotating term resonant for $\omega = -\omega_0$ can be neglected and the approximation $\omega/\omega_0 \approx 1$ and the resulting simplified expressions can be used:

$$U_{\text{dip}}(\mathbf{r}) = \frac{3\pi c^2 \Gamma}{2\omega_0^3 \Delta} I(\mathbf{r}) \quad (2.7)$$

$$\Gamma_{\text{sc}}(\mathbf{r}) = \frac{3\pi c^2}{2\hbar\omega_0^3} \left(\frac{\Gamma}{\Delta}\right)^2 I(\mathbf{r}). \quad (2.8)$$

In this simplified form it is clear that atoms are attracted to high intensities for red-detuned beams ($\Delta < 0$) and repelled for blue-detuned beams ($\Delta > 0$). This also explains the rationale behind the choice of typical large detuning and high intensities: The dipole potential scales with I/Δ and the scattering rate scales with I/Δ^2 .

A similar result can be obtained by using a fully quantum mechanical model, where the electromagnetic field is also quantised. In the presence of the light field, the atomic state undergoes an energy shift $\Delta E = \pm \frac{3\pi c^2 \Gamma}{2\omega_0^3 \Delta} I$, known as the *AC Stark shift*. The dipole potential given in Equation 2.7 represents the shift experienced by the ground state. In the case of a multi-level atom it is necessary to consider the dipole matrix elements of all states. In the case of a significant detuning in comparison to the hyperfine splitting, it is sufficient to consider only the spin-orbit coupling in the excited state. In the case of alkali metals this leads to the formation of the D1 and D2 lines. Taking into account the two D-lines the dipole potential is given by

$$U_{\text{dip}}(\mathbf{r}) = \frac{\pi c^2 \Gamma}{2\omega_0^3} \left(\frac{2 + \mathcal{P} g_F m_F}{\Delta_2} + \frac{1 - \mathcal{P} g_F m_F}{\Delta_1} \right) I(\mathbf{r}), \quad (2.9)$$

with the magnetic quantum number m_F , g_F the Landé factor, \mathcal{P} a factor characterising the polarisation of the laser. For linear polarised light $\mathcal{P} = 0$, for circular σ^\pm polarised light $\mathcal{P} = \pm 1$.

Using the equations given in Equation 2.1 and 2.9, it is possible to calculate the real part of the polarizability for sodium and potassium [57, 58]. Figure 2.1 shows the polarizability as a function of the trapping wavelength. For far red-detuned dipole traps with a typical wavelength of 1064 nm the polarizability of potassium-39 is observed to be higher than that of sodium.

For a Gaussian beam propagating in the x-direction the intensity $I(r)$ is given by

$$I(\mathbf{r}) = I_0(x) \exp\left[-2\frac{r^2}{w^2(x)}\right] = \frac{2P}{\pi w_y w_z} \exp\left[-2\frac{r^2}{w^2(x)}\right], \quad (2.10)$$

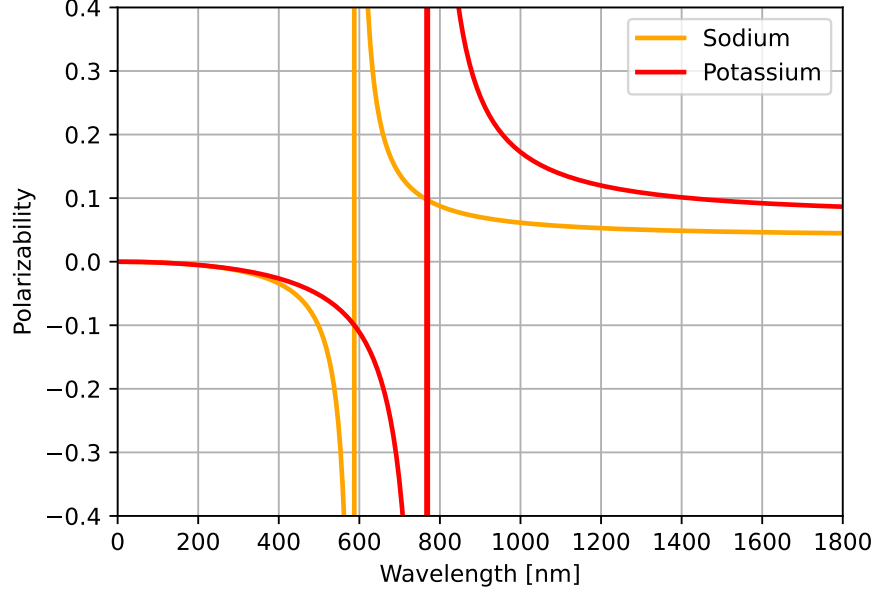


Figure 2.1: Polarizability of sodium and potassium as a function of the wavelength of the light field. The polarizability diverges at the D1 and D2 lines for sodium at 589.756 nm and 770.108 nm and for potassium-39 at 589.158 nm and 766.701 nm.

where $I_0(x) = \frac{2P}{\pi w^2(x)}$, r the radial coordinate, and the waist of the beam is given by

$$w(x) = w_0 \sqrt{1 + \left(\frac{z}{z_R}\right)^2}, \quad (2.11)$$

where w_0 is the minimum beam waist at the focus and the Rayleigh range is $z_R = \pi w_0^2 / \lambda$.

The thermal energy of the atoms is typically small compared to the potential depth, and the extent of the atomic sample is also small compared to the beam waist and Rayleigh length. Consequently, the dipole potential can be approximated by a harmonic oscillator. Comparing the coefficients of a harmonic oscillator $U_{\text{harmonic}} = \frac{m\omega^2 x^2}{2}$ with the second order Taylor expansion of the dipole potential around its minimum

$$U_{\text{dipole}}(r, z) \approx -U_0 \left[1 - 2 \left(\frac{r}{\omega_0}\right)^2 - \left(\frac{z}{z_R}\right)^2 \right] \quad (2.12)$$

where $U_0 = U_{\text{dipole}}(r = 0, z = 0)$, the axial and radial trapping frequencies can be defined by

$$\omega_z = \sqrt{\frac{2U_0}{mz_R^2}}, \quad \omega_r = \sqrt{\frac{4U_0}{mw_0^2}}. \quad (2.13)$$

In the experiment the atomic potential is also affected by gravity

$$U_z = U_{\text{dipole}}(z) + mgz, \quad (2.14)$$

with the gravitational acceleration g . This results in a displacement from the trapping centre, called gravitational sag. The gravitational sag is given by

$$z_0 = -\frac{g}{\omega_z^2}. \quad (2.15)$$

The ratio of the trapping frequencies of sodium and potassium for a given dipole beam depends only on the polarizability and mass of the atoms

$$\frac{\omega_{i,K}}{\omega_{i,Na}} = \sqrt{\frac{\alpha_K m_{Na}}{\alpha_{Na} m_K}}. \quad (2.16)$$

The overlap between the two atomic species can be expressed by the differential gravitational sag

$$\begin{aligned} \delta z &= |z_{0,Na} - z_{0,K}| \\ &= \left| g \left(-\frac{1}{\omega_{z,Na}^2} + \frac{1}{\omega_{z,K}^2} \right) \right| \\ &= \left| \frac{g}{\omega_{z,Na}^2} \left(\frac{\alpha_{Na} m_K}{\alpha_K m_{Na}} - 1 \right) \right|. \end{aligned} \quad (2.17)$$

Figure 2.2 shows the differential gravitational sag of Equation 2.17 as a function of trapping frequency for sodium. The higher the trapping frequency, the smaller is the gravitational sag. In the next Section 2.2 the size of the Bose-Einstein condensate is approximated and compared with the differential gravitational sag.

2.2 BOSE-EINSTEIN CONDENSATE

In this section, the most important properties of a Bose-Einstein condensate (BEC) are briefly summarised, mainly following the book by Pitaevski and Stringari [59].

A Bose-Einstein condensate is a state of matter that occurs when the phase space density ρ of bosonic particles exceeds a critical value:

$$\rho = n\lambda_{dB}^3 \geq 2.61, \quad (2.18)$$

depending on the atomic density n and the thermal De Broglie wavelength of the atoms $\lambda_{dB} = \sqrt{\frac{2\pi\hbar^2}{mk_B T}}$, with the Boltzmann constant k_B , the Planck constant \hbar and depending on the mass m and temperature T of the atoms. In practice, this is usually the case for temperatures close to absolute zero. At this point, a large fraction of the atoms occupy the ground state, leading to a situation where quantum effects become apparent on a macroscopic scale. Therefore, instead of describing the

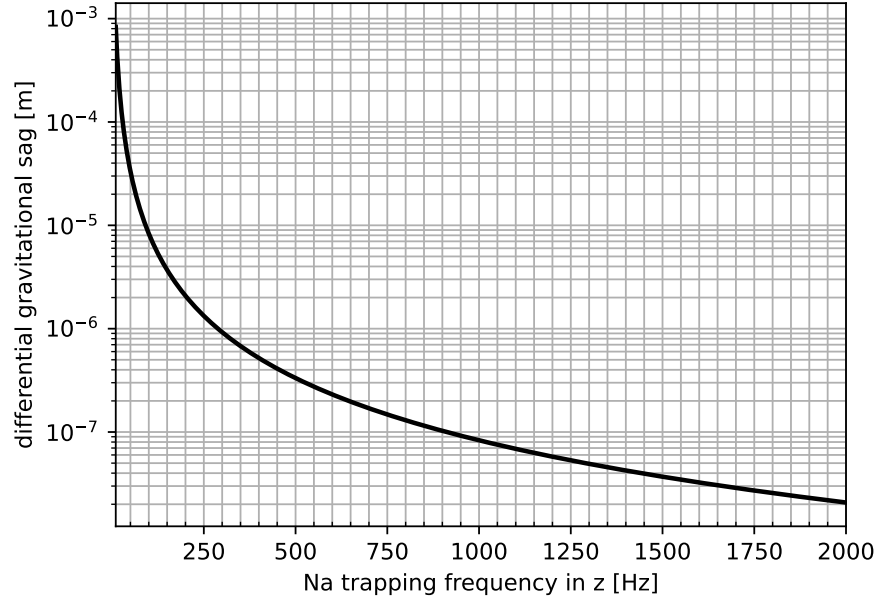


Figure 2.2: The differential gravitational sag defined in the Equation 2.17 as a function of the trapping frequency $f_z = \frac{\omega_z}{2\pi}$ for sodium. The higher the trapping frequency, the smaller the differential gravitational sag.

N atoms in the BEC microscopically by N single particle equations, the BEC can be described macroscopically by a field operator $\hat{\Psi}(\mathbf{r})$

$$\begin{aligned}\hat{\Psi}(\mathbf{r}) &= \sum_i \varphi_i \hat{a}_i \\ &= \varphi_0(\mathbf{r}) \hat{a}_0 + \sum_{i \neq 0} \varphi_i(\mathbf{r}) \hat{a}_i,\end{aligned}\quad (2.19)$$

where \hat{a}_i (\hat{a}_i^\dagger) are the annihilation (creator) operators of a particle in the state φ_i . Simplifications can be applied due to the large occupation in the ground state φ_0 . Therefore, in the Bogoliubov approximation, only the atoms in the ground state are considered and treated as a classical field $\psi(\mathbf{r})$, while the atoms in the excited states are neglected in the first order or treated as a small perturbation $\delta\hat{\psi}(\mathbf{r})$

$$\hat{\Psi}(\mathbf{r}) = \psi(\mathbf{r}) + \delta\hat{\psi}(\mathbf{r}). \quad (2.20)$$

$\psi(\mathbf{r})$ is called the wave function of the condensate and characterises the BEC as an order parameter.

For an ideal weakly interacting gas further simplifications can be applied by treating the condensate as a reservoir of particles, where the creation and annihilation of a particle in the ground state does not affect the large population in the ground state, and therefore the operators can simply be replaced by $\sqrt{N_0}$ where N_0 the number of atoms in the ground state.

In the case of a non-uniform trapped interacting quantum gas the condensate wavefunction can be described as a classical field as in Equation 2.20. The Gross-Pitaevski equation is an analogue to the non-linear Schrödinger equation for the macroscopic wavefunction $\psi = \psi + \delta\hat{\psi}$ of the condensate with an additional term taking interaction into account

$$i\hbar \frac{\partial \psi}{\partial t} = \left(-\frac{\hbar^2}{2m} \nabla^2 + V_{\text{ext}} + g|\psi|^2 \right) \psi \quad (2.21)$$

with the external potential V_{ext} , the interaction strength $g = \frac{4\pi\hbar^2 a}{m}$ and the s-wave scattering length a .

In the case $T = 0$ the fluctuations can be neglected and the wave function is simply described by the macroscopic order parameter $\psi(r, t)$. Since kinetic energy terms are mainly relevant at the boundaries, they can be neglected in the Thomas-Fermi approximation, where Equation 2.21 simplifies to

$$\left(V_{\text{ext}} + g|\psi|^2 \right) \psi = \mu \psi \quad (2.22)$$

with μ the eigenvalue and chemical potential, which can be easily rearranged to

$$|\psi|^2 = \frac{\mu - V_{\text{ext}}}{g} \quad (2.23)$$

with $|\psi|^2 = n(r, t)$ the density. Therefore, the density profile has the shape of the negative trapping potential up to a certain level, depending on the chemical potential μ . An estimate of the size of the atoms in the harmonic trap with $V_{\text{ext}} = \frac{1}{2}m\omega^2 r^2$ is therefore the radius where the density vanishes $n(R_F) = 0$

$$R_F = \sqrt{\frac{2\mu}{m\omega^2}}. \quad (2.24)$$

Normalizing the density the chemical potential can be written as

$$\mu_{TF} = \frac{\hbar\omega_{ho}}{2} \left(\frac{15Na}{a_{ho}} \right)^{2/5} \quad (2.25)$$

with the oscillator length $a_{ho} = \sqrt{\hbar/(m\omega_{ho})}$ and the geometrical average $\omega_{ho} = (\omega_x\omega_y\omega_z)^{1/3}$ so that the Thomas Fermi radius in direction k is given by

$$R_k = a_{ho} \left(\frac{15Na}{a_{ho}} \right)^{1/5} \frac{\omega_{ho}}{\omega_k}. \quad (2.26)$$

For some phenomena it is interesting to reduce the dimensions of the condensate. The dimensions can be reduced by adding anisotropy to the system creating trapping frequencies, that effectively freeze out the dimensionality since to high energies are needed to excite the system.

This is the case if $k_B T \ll \frac{1}{2} \hbar \omega_z$, which also leads to the rule of thumb that the trap depth needs to be approximately 20 Hz/nK. Considering a temperature of 50 nK of the atoms a trapping frequency higher than $\omega_z = 1$ kHz to ensure a quasi 2D system.

A good overlap between the two species can be considered, if the size of the atomic cloud in z -direction is larger or comparable to the differential gravitational sag. In the SoPa experiment two optical dipole traps are implemented:

The **crossed optical dipole trap** in which the atoms will be cooled to degeneracy by evaporative cooling. This trap has the measured trapping frequencies of $f_x = 506$ Hz, $f_y = 604$ Hz and $f_z = 828$ Hz [1] for a power of 5 W per beam.

The **two-dimensional optical dipole trap** that confines the atoms strongly in z direction. This trap has the calculated trapping frequencies of $f_x = 33$ Hz, $f_y = 15$ Hz and $f_z = 1$ kHz for a power of 10 W (see Chapter 7).

Figure 2.3 compares the gravitational sag at a given trapping frequency, with the Thomas Fermi radius in z direction. The Thomas Fermi radius depends on the oscillator length and the geometrical average. Therefore, the trapping frequencies are scaled with \sqrt{P} in the case of the crossed optical dipole trap (cODT) the single beam power is varied from 0.1 W to 40 W and for the 2D optical dipole trap the beam power is varied from 0.1 to 10 W. The Thomas Fermi radius is for powers above approximately 1 W at least an order of magnitude larger than the differential gravitational sag. For small powers around 0.1 the Thomas Fermi radius is approaching the same order of magnitude than the differential gravitational sag.

Taking first order fluctuations into account for a homogeneously trapped gas and performing the Bogoliubov transformation to diagonalize the Hamiltonian elementary excitations can be described by the Bogoliubov dispersion law

$$\epsilon(p) = \sqrt{\frac{gn}{m} p^2 + \left(\frac{p^2}{2m}\right)^2}. \quad (2.27)$$

In the limit of small momenta p the dispersion relation is linear and featuring collective phononic excitations with a sound velocity $c = \sqrt{gn/m}$. In the case of large momenta the dispersion relation is behaving similar to a free particle dispersion relation giving rise to single particle excitations.

2.3 TWO COMPONENT CONDENSATE

So far only a single component has been considered. In this section mainly follows Jan Kilinc PhD thesis [1, 59–61]. In the case of two

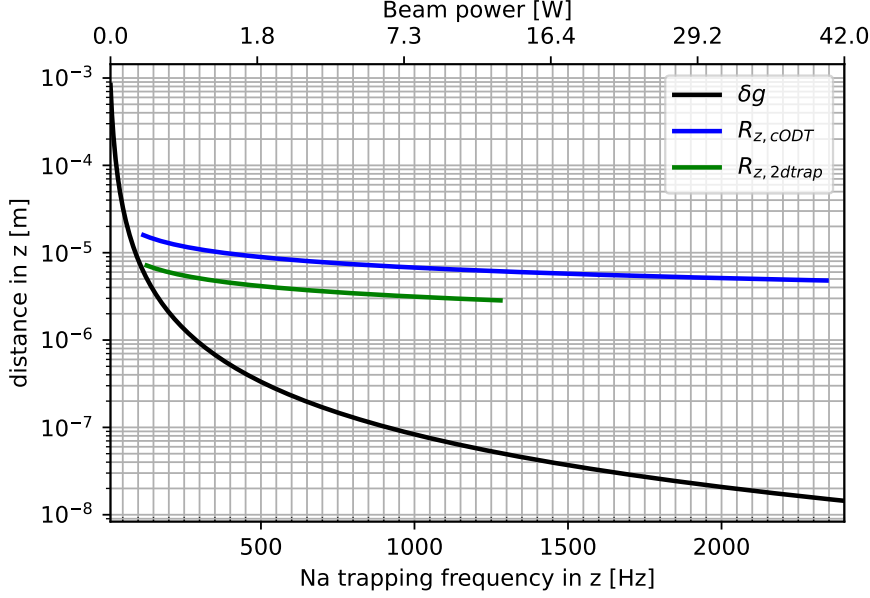


Figure 2.3: Comparing the differential gravitational sag defined in Equation 2.17 with the Thomas Fermi radius in z direction for the crossed optical dipole trap (cODT) and the 2D optical dipole trap. The available power range is converted into the according trapping frequency in z . In the crossed optical dipole trap the power per beam is varied between 0.1 W and 40 W. For the 2D optical dipole trap the beam power is varied between 0.1 W and 10 W.

components two coupled Gross-Pitaevski equations are used to describe the system

$$i\hbar \frac{\partial}{\partial t} \Psi_1 = \left(-\frac{\hbar^2 \nabla^2}{2m_1} + V_{1,ext}(r) + g_{11} |\Psi_1|^2 + g_{12} |\Psi_2|^2 \right) \Psi_1 \quad (2.28)$$

$$i\hbar \frac{\partial}{\partial t} \Psi_2 = \left(-\frac{\hbar^2 \nabla^2}{2m_2} + V_{2,ext}(r) + g_{22} |\Psi_2|^2 + g_{12} |\Psi_1|^2 \right) \Psi_2. \quad (2.29)$$

for simplicity we from now on consider atoms trapped in a box potential $V_{ext} = 0$. In the ground state the system can either be a uniform mixture, where both species are distributed over the same volume V or the two species are fully separated where each species occupies their own volume V_i , the index i denoting the species. In the fully separated case the energy is given by

$$E_{sep} = \frac{g_{11}}{2} \frac{N_1^2}{V_1} + \frac{g_{22}}{2} \frac{N_2^2}{V_2}. \quad (2.30)$$

In the uniform case the energy is given by

$$\begin{aligned} E_{uni} &= \frac{g_{11}}{2} \frac{N_1^2}{V} + \frac{g_{22}}{2} \frac{N_2^2}{V} + g_{12} \frac{N_1 N_2}{V} \\ &= \frac{g_{11}}{2} \frac{N_1^2}{V} + \frac{g_{22}}{2} \frac{N_2^2}{V} + \sqrt{g_{11} g_{22}} \frac{N_1 N_2}{V}. \end{aligned} \quad (2.31)$$

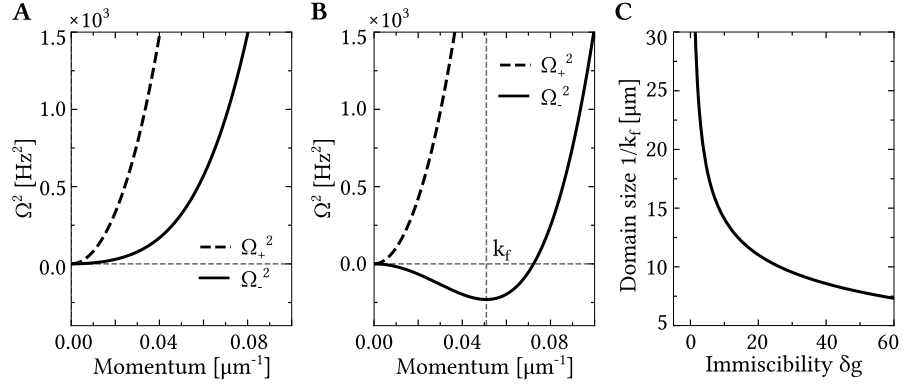


Figure 2.4: **A:** Two Excitation branches in the miscibility regime ($\delta g = 0.9$). **B:** Two branches in the immiscible regime, minimum in the Ω_- branch below zero. **C:** Domain size depending on the immiscibility parameter δg . Figure taken from [1]

In order to phase separate the energy of the phase separation case has to be lower than the uniform case $E_{uni} > E_{sep}$ and consequently $g_{12} > \sqrt{g_{11}g_{22}}$ from which the miscibility parameter δg can be defined with

$$\delta g := \frac{g_{12}^2}{g_{11}g_{22}} - 1 > 0 \quad (2.32)$$

The mixture is miscible if $\delta g > 0$ and immiscible for $\delta g < 0$. Note that all interactions have to be repulsive $g_i > 0$, otherwise the gases collapse. With one exception known as quantum droplets where the inter-component attraction is small and balanced with the intra-component repulsion [61].

Taking again fluctuations into account the dispersion of the excitations are given by [60]

$$\Omega_{\pm, k}^2 = \frac{\omega_{1, k}^2 + \omega_{2, k}^2}{2} \pm \frac{\sqrt{(\omega_{1, k}^2 - \omega_{2, k}^2)^2 + 4 \frac{g_{12}^2}{g_{11}g_{22}} c_1^2 c_2^2 k^4}}{2} \quad (2.33)$$

where $c_{1,2} = \sqrt{\frac{n_{1,2}\lambda_{1,2}}{m_{1,2}}}$ are the sound velocities of the condensate of species 1 and 2 respectively and $\omega_{1,k}, \omega_{2,k}$ the Bogoliubov dispersion relations $\hbar\omega_{i,k} = \sqrt{\frac{\hbar^2 k^2 n_i g_{ii}}{m_i} + \left(\frac{\hbar^2 k^2}{2m_i}\right)^2}$ (see Equation 2.27). For the case of vanishing intra-component interaction the dispersion relation is given by the Bogoliubov dispersion given by Equation 2.27. For the interacting system in the miscible region the excitations are uncoupled and two branches exists. If the system approaches the transition to the immiscible region domains are forming and the Ω_- branch develops a minimum which can get negative. Length and timescale of the domains forming are characterized by the minimum in the dispersion relation [1, 62]. This phenomena is shown in Figure 2.4.

In the experiment a trapping potential is used and most likely the

atom numbers are unbalanced. Both effect the miscibility immiscibility transition. In the case of population imbalance the minimum is shifted to smaller momenta. Therefore, larger domains are expected [1, 62]. In inhomogeneous traps the species with a smaller interaction strength tend to accumulate in the trap centre, an effect called buoyancy [60, 63, 64]. It was observed, that the phase transition for a sodium potassium mixture in an inhomogeneous trap is shifted towards higher magnetic fields [65]. A good discussion is provided in [1].

SOPA EXPERIMENT IN A NUTSHELL

This chapter provides a brief overview of the newly built sodium-potassium experiment called SoPa (*So* from sodium and *P* from potassium, combined to form the Spanish word *sopa*, soup). The chapter is divided into three sections: The first section aims to guide the reader through this thesis and other references by giving an overview of the SoPa experiment. The second section describes the history of the experiment and addresses some general issues. The third section describes the current status and challenges of the experiment.

3.1 BRIEF OVERVIEW OF THE SOPA EXPERIMENT

The SoPa experiment is an ultracold atomic mixture experiment with sodium 23 and potassium 39. Figure 3.1 illustrates the building blocks of the cooling sequence:

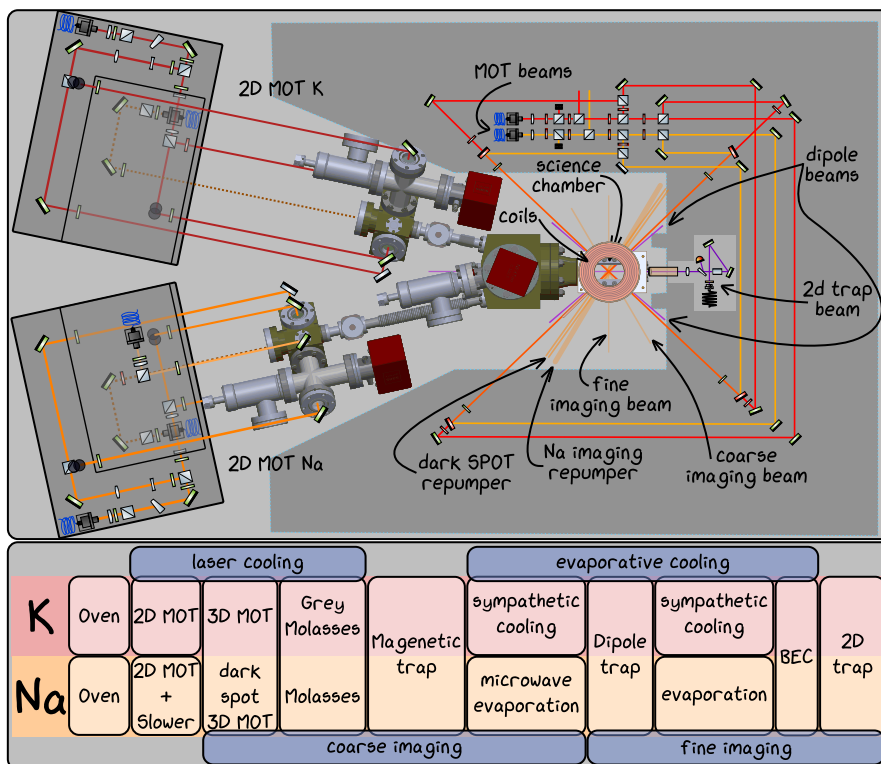


Figure 3.1: The experimental setup (top) consists of two atomic species that are separated in their pre-cooling stage (2D MOT). The atoms are then combined and further cooled, requiring the use of multiple beams. The science chamber is surrounded by a breadboard (shown in dark grey) for mounting the optics. The cooling sequence consists of several building blocks (bottom).

Vacuum: To ensure long enough lifetimes in the traps, a good vacuum is essential for a cold atom experiment. If the vacuum is not good enough, atoms will be lost from the trap through collisions with the background gas. The SoPa vacuum system is designed to separate the two atomic species before the science chamber, where the atoms are first brought together in the 3D magneto-optical trap (MOT). To do this, the atoms are evaporated from an oven cup and pre-cooled in a 2D MOT before being pushed towards the science chamber. The 2D MOT chamber and the science chamber are separated by a differential pumping stage. This ensures that pressures below 10^{-11} mbar can be achieved in the science chamber, while higher background pressures ($\approx 10^{-8}$ mbar) of atoms can be used in the 2D MOT for atom loading. Details can be found in the Chapter 4 of this thesis.

Laser Table: Laser light is generated and stabilised to an atomic transition by saturation absorption spectroscopy. The light is then split into different paths and frequency shifted by a few MHz using acousto-optic modulators (AOMs) in double-pass paths. Finally, the light is transmitted to the experimental table via polarisation-maintaining optical fibres. In order to have enough space for the optics for each species, two separate optical tables are used - one for sodium and one for potassium. Further information can be found in Jan Kilinc's PhD thesis [1].

Magnetic Field Coils: Coils are used to generate the magnetic field gradient for the 3D MOT and the magnetic trap, as well as the bias magnetic field for tuning the interaction strength using Feshbach resonances. The same set of coils is used for both. Consequently, the magnetic field coils have to be switched from Helmholtz to an anti-Helmholtz configuration using an H-bridge circuit. A passband controls the current in the coils. To compensate for stray magnetic fields in the laboratory, three pairs of offset coils are used to zero the magnetic field at the atomic position. For more details see [1].

2D MOT: The 2D magneto-optical trap (MOT) captures the atoms from the oven, which are then transferred into the science chamber using a push beam. The 2D MOT uses four independent laser beams and stacks of permanent magnets to generate the quadrupole field. For sodium an additional slower beam is used to improve performance. Details can be found in this thesis in Chapter 5.

3D MOT: The 3D magneto-optical trap (MOT) is the first stage in trapping atoms and the first point where sodium and potassium atoms meet. In the 3D MOT, magnetic field coils generate

the quadrupole field and six red-detuned, circularly polarised independent laser beams are used. The light for sodium and potassium is overlapped at the last mirror to ensure the best possible decoupling. For sodium we use a dark spontaneous-force optical trap (dark SPOT) [66]: Unlike a MOT, where the cooler and re-pumping laser light are provided by the MOT beams, in the dark-SPOT the six MOT beams contain only cooler light. The re-pump light comes in an additional beam with a dark spot in the middle. In this way, the re-pumper light is only available in the outer part of the MOT, resulting in atoms in the "dark" state ($F = 1$ in the case of sodium), where the repulsive forces between atoms are reduced due to re-scattered radiation. Details of the 3D MOT can be found in [1].

Molasses: A molasses is used to further cool the atoms below the Doppler limit before they are loaded into a magnetic trap. In a molasses, the magnetic gradient is switched off while the MOT beams remain on, causing the atomic cloud to expand. Sweeping the frequency, but keeping the light red-detuned, improves the addressing of different velocity classes. This technique is not efficient for potassium due to the low separation of the ground state splitting of the D2 line.

D1 Grey Molasses: Grey Molasses is a sub-Doppler cooling scheme that combines two effects: Sisyphus cooling and velocity selective coherent population trapping (VSCPT). It uses a Λ system with ground states $4^2S_{1/2} F = 1, 2$ and an excited state $4^2P_{1/2} F = 2$. Combined with the laser light, which is realised as three blue-detuned counter-propagating circularly polarised laser beams (cooler + repumper), the system has two bright states and one dark state (in reality it is a grey state due to the multi-level structure of the atom) which is not coupled to the excited state. Due to the polarisation gradient of the counter-propagating beams, the bright state has a sinusoidal potential landscape. The exit rate from the dark state to the lower bright state is velocity dependent, allowing moving atoms to transition from the dark state to the bright ground state. In the bright state the atoms climb the sinusoidal potential and are pumped back to the dark state, losing kinetic energy. Lower temperatures can be achieved with the D1 line than with the D2 line. The D1 line has been implemented for potassium [67–69] and sodium [70]. In the SoPa experiment, the D1 light is coupled into the MOT fibres. For more details on the D1 grey matter with potassium see [1] and with sodium see [71].

Magnetic trap: The magnetic trap is used to transfer more atoms into the dipole trap. The magnetic gradient field is generated by water-cooled coils which can achieve a gradient of up

to 300 G/cm. Atoms are trapped in the ($F = 1, m_F = -1$) state. After ramping up the field and holding it for 100 ms, the dipole beams are switched on, resulting in a hybrid trap. The sodium atoms in the hybrid trap are cooled by microwave evaporation. Details about the magnetic trap and the coils can be found in [1].

Optical Dipole Trap: The atoms are transferred from the hybrid trap to the optical dipole trap by reducing the magnetic field gradient. The crossed optical dipole trap (cODT) is formed by two far-red detuned laser beams that intersect in the centre of the science chamber. The atoms are attracted to the intensity maximum at the intersection by the AC Stark effect. The trapping frequency is $f_x = 506$ Hz, $f_y = 604$ Hz and $f_z = 828$ Hz [1]. Sodium atoms are further cooled evaporatively by reducing the intensities of the dipole beams. Whereas potassium, which is not cooled as efficiently by evaporation itself, is cooled sympathetically by the sodium atoms. The difference in evaporation efficiency is caused by the polarisability of the atomic species. Details of the dipole trap can be found in [1].

BEC: Once the phase space density of the atoms is high enough, they condense to form a Bose-Einstein condensate (BEC). While condensation of sodium atoms has been achieved in the SoPa experiment, condensation of potassium atoms is still a challenge. A detailed description of the dipole trap and the attempts made so far to include potassium atoms can be found in [1]. An update is given in Section 3.3 of this chapter.

Imaging: To capture images of the atoms at different stages of the sequence, three imaging systems are planned for each species. Horizontally, a coarse imaging system that demagnifies by a factor of 0.44 and a fine imaging system that magnifies by a factor of 20.3 will be implemented. The coarse imaging system is used for the early stages of the sequence up to the magnetic trap. It is still possible to observe the sodium BEC (on a few pixels), but it is impossible to identify that it is a BEC. The horizontal fine imaging system will be used for the later stages of the sequence, from the dipole trap onwards. The details of the horizontal imaging system are described in [1]. The final imaging system is in the vertical plane using a high numerical aperture objective (NA= 0.5) with a magnification of $M = 33$. Details of this imaging can be found in this thesis in the Chapter 8.

3.2 HISTORY OF THE SOPA EXPERIMENT

The SoPa experiment was designed as a second generation mixture experiment to overcome the problems of the old sodium-lithium (NaLi) mixture experiment [72–74]. The NaLi experiment had a number of

disadvantages in its experimental design, which have been addressed in the new setup. A major drawback was that the two species were closely coupled during all experimental steps:

Optics: Single-pass Acoustic Optical Modulator (AOM) paths on the laser tables require re-alignment after small frequency changes. Optical fibres are used to transport the light from the laser table to the experimental table. In the NaLi experiment, both sodium light 589 nm and potassium light 767 nm were coupled into the same fibre, so it was already necessary to adjust between the two. Individual optimisation was not possible on the test bench. The beam alignment and polarisation of the MOT beams had to be compromised for both atomic species.

Vacuum Apparatus: The atomic species were mixed directly after the oven cup, so the oven temperature had to be compromised. In addition, any problem in the oven area of one species, e.g. empty oven or clogged nozzle, affects the other species.

Atomic Properties: The mixture of Na and Li does not exhibit broad interspecies Feshbach resonances, which limits the experimental tunability of the interaction strength between the two species. [75]

This required a lot of compromise in the settings, but also made the system very buggy, and it was impossible to work on one species setup while continuing with the other. In addition to this disadvantage, the experiment was in a state where vacuum problems interrupted the experimental workflow quite often [72].

Therefore, a second generation experiment was started [76–78]. As the atomic properties were not ideal, another pair of species was chosen: Sodium and Potassium. The advantages of sodium and potassium are a broad Feshbach resonance at moderately low magnetic fields [39, 79]. An additional advantage was that our group already had experience with both species [80–83]. In addition, knowledge about the mixture exists in several other groups, mainly to study molecules [39, 79, 84–86]. The SoPa experiment was set up in the same laboratory as the NaLi experiment, so it had to be very compact. This led to some awkward configurations, such as stacking the Na and K laser tables on top of each other, or having only a small space between the wall and the laser table. During the construction phase of the SoPa experiment, the NaLi experiment had major vacuum problems, so unfortunately the SoPa experiment was the only one to be continued. At that time it became apparent that the current coil design of the SoPa experiment was not capable of driving high enough gradients for a high atomic number magnetic trap [78]. The opportunity to design new coils was taken to change the orientation of the coils from vertical to horizontal. The change in coil orientation necessitated the redesign of a large part

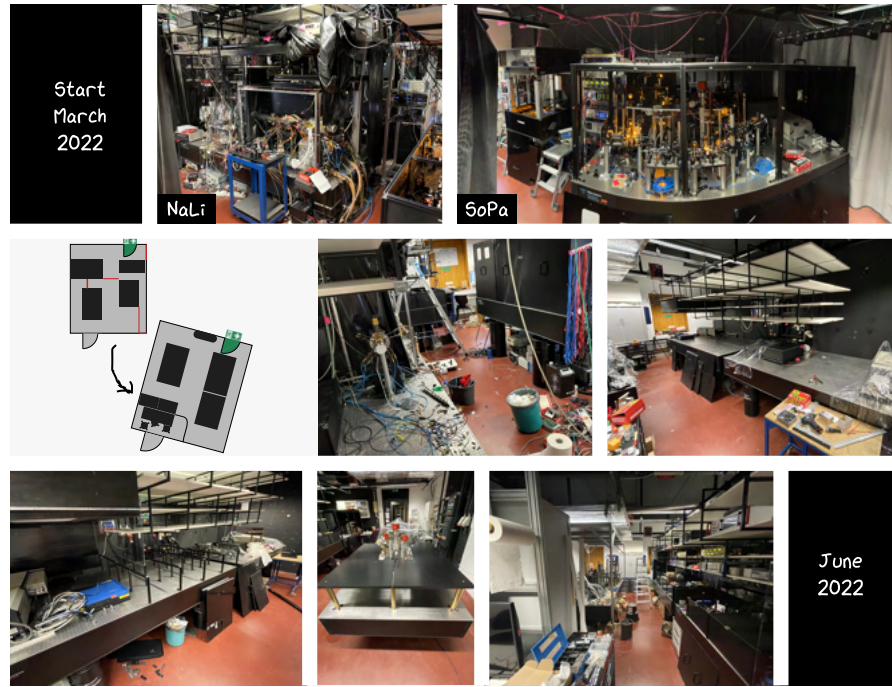


Figure 3.2: The transformation of the laboratory in pictures. First row: NaLi laboratory and SoPa laboratory before the transformation. Second row: New plan for organising the lab. The transformation includes dirty and clean phases. Third row: Clean start of reconstruction.

of the optics. Since more space in the lab was available for the SoPa experiment, we ended up building a new experiment using only the vacuum system from the old SoPa setup, while dismantling the NaLi setup. By reorganising the lab space, many improvements could be made:

- More space in the lab, including larger optical tables for all our AOM paths, more options for storing lab equipment and materials in the lab, and ensuring access around the experimental setup with a minimum passage width of 75 cm.
- Change of MOT optics to larger beam diameters and independent beams instead of retro-reflection.
- The reuse of NaLi equipment leads to a dedicated optical table for the laser setups of each atomic species, as well as the luxury of an additional 1 W of laser power for sodium, which can be tuned independently.
- Tidiness of the lab, all drawers and cupboards, shelves have been cleaned, re-organised and labelled.
- Workspace for up to three people behind a laser curtain.

The process is summarised in pictures (see Figure 3.2), as nothing can describe the changes better. We started the transformation in March 2022, one year and two months later we got our first BEC of sodium.

3.3 CURRENT STATUS⁰ OF THE SOPA EXPERIMENT

This section summarises the milestones achieved and the current challenges of the SoPa experiment. The next tools to be implemented in the experiment, the quasi two-dimensional trap and the vertical high-resolution imaging, are reported in the Chapters 7 and 8 of this thesis.

BOSE EINSTEIN CONDENSATION OF SODIUM

In the SoPa experiment, a Bose-Einstein condensate (BEC) of sodium atoms was achieved (see Figure 3.3). The experimental sequence for the sodium BEC starts with the loading of the sodium dark SPOT MOT. The loading time is between 4 and 6s, depending on the system performance, resulting in about $2 \cdot 10^8$ atoms with a temperature of about $200 \mu\text{K}$. After loading, the atoms are pumped into the $F=1$ hyperfine ground state for $200 \mu\text{s}$ by turning off the repumper light. The MOT light is then switched off completely to load the atoms into the magnetic trap. The magnetic trap is first set to an initial magnetic field gradient of 100 G/cm and then ramped up to 300 G/cm in 100 ms . This ramping sequence is empirically determined and is necessary because the atoms will heat up if the magnetic field gradient is changed too quickly and therefore not adiabatically. The control of the coil current also provides a limiting factor. A hybrid trap configuration is used, i.e. the crossed optical dipole trap (cODT) (70 W) is switched on after the final magnetic field gradient of 300 G/cm has been reached. Microwave evaporation is performed in the hybrid trap. During the 3 s microwave evaporation, a microwave signal transfers atoms from the trapped $|F = 1, m_F = -1\rangle$ state to the untrapped $|F = 2, m_F = 2\rangle$ state. The microwave is directed onto the atoms using a single loop antenna with a radius of 4 cm . The microwave signal is amplified by a 15 W amplifier and the frequency is swept from 1.70 GHz to 1.76 GHz during evaporation. The atoms are loaded into the optical trap by turning off the magnetic field gradient at 100 ms and the dipole beam intensity to 80 W . This leaves about $5 \cdot 10^5$ atoms with a temperature of about $10 \mu\text{K}$. In the crossed dipole trap, two linear evaporation ramps are used to produce the sodium BEC with about $7 \cdot 10^4$ atoms. The first ramp lasts 2 s and reduces the power from 80 W to 10 W . The second ramp takes 4 s and reduces the power further down to 0.15 W . Figure 3.3 shows absorption images taken at different steps of the last evaporation ramps. In the integrated column density one can clearly see the evolution of the bimodal density distribution of the BEC. At higher temperatures the atoms are thermal and therefore have a Gaussian density distribution. When the atoms start to condense, one still observes the Gaussian density distribution of the thermal atoms, but a sharper parabolic shape

⁰ Although progress in the experiment often feels slow, it is certainly faster than writing a PhD thesis. Therefore, a more accurate title would be "Collection of snapshots of the SoPa experiment, highlighting milestones and setbacks".

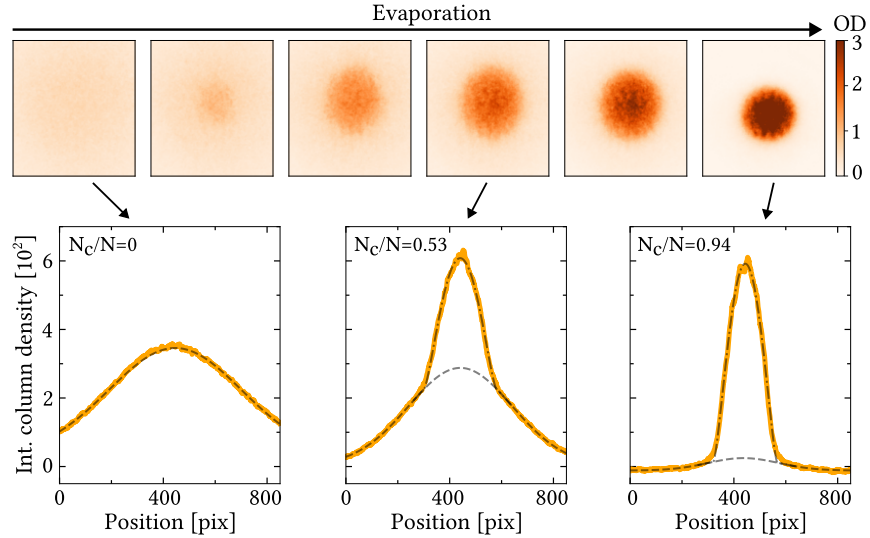


Figure 3.3: Formation of a Bose-Einstein condensation of sodium during evaporation in the cODT. Top row: Absorption images of the sodium atomic cloud as evaporation proceeds on the right. Bottom row: Integrated column density of some of the above absorption images. One can clearly see the bimodal density distribution as evaporation proceeds. The part of the thermal atoms, the Gaussian distribution, is fitted with the dashed line, while the part of the condensed atoms, the sharper parabolic part, is fitted with the dashed-dotted line. Figure taken from [1]

appears in the centre, which is due to the atoms being trapped in the ground state (see Chapter 2.26).

DUAL SPECIES OPTICAL DIPOLE TRAP LOADING

After the achievement of sodium BEC, efforts were directed towards two species condensation with sodium and potassium, which has not yet been successful. In order to be able to cool both atomic species to degeneracy, the experimental sequence has to be adapted. A molasses phase was added after the MOT phase. While a standard molasses was used for sodium, a D1 grey molasses was implemented for potassium, so that the potassium atoms were cooled first. Problems arise when both species are loaded simultaneously into the dipole trap, where one atomic species is lost. We attribute these problems to inter-species three-body losses in the hybrid trap due to high densities and poor overlap between the magnetic and dipole traps, thus heating the atoms.

FESHBACH RESONANCES

In the case of potassium being successfully loaded into the dipole trap, the *Feshbach* resonances of potassium were measured. We located the low-field s-wave *Feshbach* resonances for the $|F = 1, m_F = -1\rangle$ spin state of potassium using atom-loss spectroscopy (as reported in detail in [1]) at 33.9(1) G and 162.4(2) G. Our measurements were in good

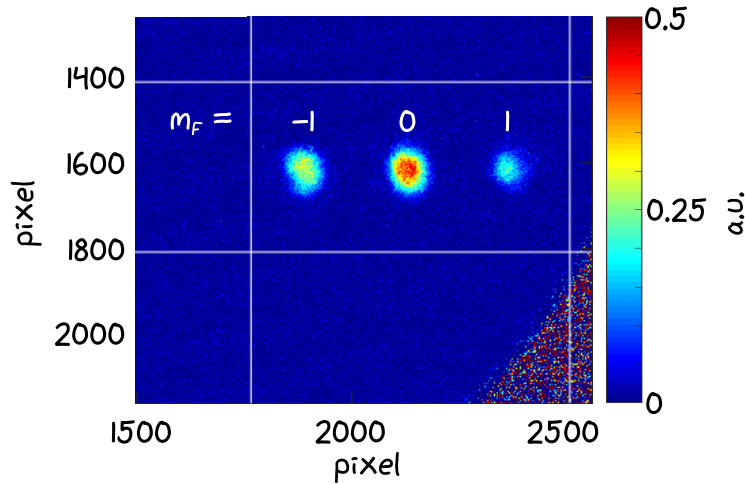


Figure 3.4: *Stern-Gerlach* Imaging of sodium after applying a 110 ms RF pulse at 20 Hz. The atoms separate into three clouds corresponding to the three magnetic states $m_F = -1, 0, 1$. The plot is constructed from a screenshot.

agreement with previously reported experimental data [87, 88]. In addition, we observed another loss feature in the magnetic field region 75 – 110 G caused by stray light and a narrow resonance at 131.6(2) G, which we attribute to a higher partial wave Feshbach resonance.

STERN GERLACH IMAGING

In the search for the cause of the loss feature in atom loss spectroscopy, it was of interest to know the spin state of the atoms. A good tool for determining atomic spin states is *Stern-Gerlach* imaging, where a magnetic gradient field is turned on during the time of flight of the atoms. Due to the magnetic gradient, atoms have different trajectories depending on their spin state. With a suitable choice of time of flight and gradient field, the atoms with different spin states can be well separated on the image (see Figure 3.4). Since all our atoms are prepared in the $|F = 1, m_F = -1\rangle$ spin states, to test *Stern-Gerlach* imaging it is necessary to populate the atoms in other spin states. We therefore installed a five-loop antenna with an inner diameter of 1". An RF pulse is used to transfer atoms in their spin state. We use the *Breit-Rabi* formula to calculate the resonance transition frequency at a given magnetic field between two states in the ground state manifold [57]. For the RF pulse we use a 20 Hz signal which is resonant in the magnetic field of 28.2 G. By scanning the expected coil control voltage around this value with RF pulse durations of a few tens of ms we could populate the other m_F spin states. For the *Stern-Gerlach* image, the gradient field is turned on for 5 ms, with 4 ms still in the dipole trap and only 1 ms at the time of flight (TOF). With this and a gradient of 64.3 G/cm we were able to separate atoms with different spin states nicely on our image as shown in the Figure 3.4. In a dual species config-



Typical laboratory items such as one-inch posts are not only useful as posts, but are also excellent for winding antennas. The appropriate number of loops can be easily estimated as derived on page 117 in Helmut Strobel's PhD thesis [89].

uration, however, the choice of RF pulse frequency and corresponding bias field is not so arbitrary, as care must be taken not to get too close to a *Feshbach* resonance.

We have not further optimised either the *Stern-Gerlach* imaging pulse or the RF pulse, although we have focused on the dual-species BEC.

SLOSHING IN THE MAGNETIC TRAP

A time series of images at different holding times revealed sloshing behaviour of the atoms in the magnetic trap. The sloshing is attributed to a poor overlap between the magnetic trap and the MOT/molasses stage. In addition, the loading from the magnetic trap to the dipole trap is also not very efficient, which is also attributed to the poor overlap between the magnetic trap and the dipole trap. This mode mismatch leads to heating of the atoms during the transfer. This topic is discussed in more detail in [90]. Furthermore, high loss rates of potassium atoms in the magnetic trap have been observed, which we attribute to collisions due to the high densities in the steep magnetic trap. Efforts have been made to achieve better mode matching between the traps, but the challenge of the two species being strongly confined in the magnetic trap remains an issue.

Consequently, we plan to reduce the time in the magnetic trap as much as possible and try to work with a shallower magnetic trap or an all-optical approach. Therefore, we have got the atoms cooler in the previous step, which led us to try double D1 grey molasses.

ATOMIC SOURCE

Our sodium atom source degraded to the point where the number of atoms was so low that we could no longer load an MOT. Fortunately, sodium atom deposits were visible in the lower viewports, and a ring of Na atom deposits could be seen at the top of the oven tube through the slower viewport. Heating the lower viewports to about 100°C helped to get enough atoms again (the 2D MOT setup is described in detail in the Chapter 5). This allowed stable operation, but the source seems to be coming to the end of its life. Droplets of sodium can be seen in the chamber.

SPECTROSCOPY SIGNAL DEGRADATION

We have suddenly lost our sodium spectroscopy signal. At the sodium laser table, we lock the laser to the crossover transition of the D2 line using saturated absorption spectroscopy. To generate the error signal for locking, the spectroscopy signal is modulated by a magnetic field introduced by a coil wrapped around the vapour cell. This was accompanied by saturation of the photodiode used to monitor the spectroscopy signal. Changing the gain of the photodiode and increasing the temperature helped to recover the signal, but it was much worse than before and continued to degrade over the course of a day.

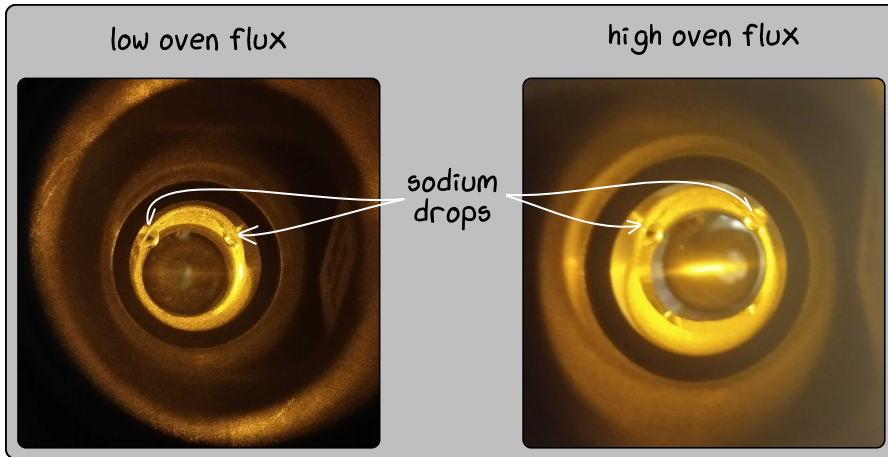


Figure 3.5: Sodium push beam fluorescence observed through the top view-port of the 2D MOT, which is normally used for the slower beam. Left: A case of low oven flux from the oven where the fluorescence is weak, here very few atoms have been in the MOT. Right: high fluorescence and a higher oven flux, so that enough atoms have been in the MOT to get a BEC. In both images you can see drops of sodium that have accumulated on the wall.

We have learned that alkali metals can react with the glass body of the vapour cell, degrading the atomic vapour in the cell. This reaction takes place above 110°C .



Figure 3.6: Strong beam fluorescence is visible in the new sodium spectroscopy cell. The central part of the cell is not wrapped in aluminium foil, which creates a cold spot and prevents atoms from condensing on the surfaces through which the beam passes.

D1 GREY MOLASSES FOR SODIUM

With the successful implementation of D1 grey molasses for potassium and another sodium laser system available, it was possible to follow the approach for sodium [70] and implement a D1 grey molasses also for sodium, hopefully eliminating the long evaporation process in the

magnetic trap. The updated laser system and the implementation of the D1 grey molasses scheme for sodium are described in detail in [71].

Vacuum is classified in several regions based on pressure: rough vacuum (from atmospheric pressures to 1 mbar), medium vacuum (from 1 mbar to 10–3 mbar), high vacuum (HV) (from 10^{-3} and 10^{-8} mbar), ultra-high vacuum (UHV) (from 10^{-8} and 10^{-12} mbar) and extreme-high vacuum (below 10^{-12} mbar) [91]. Achieving these different vacuum levels varies in complexity.

In ultra-cold atom experiments atoms are heated by collisions with background particles and are thus removed from the trap, these processes lead to limited trap lifetimes of the atoms. To reduce the scattering with background particles the system is set up under ultra-high vacuum (UHV).

Outgassing mainly limits the achievement of an ultra-high vacuum. Outgassing describes all kinds of processes, that lead to creation of gases while one is pumping against it. Figure 4.1 illustrates sources of outgassing. Key processes include desorption from surfaces and diffusion from bulk materials [92]. In UHV systems, it is necessary to minimize all outgassing sources, ideally leaving only hydrogen gas, which is outgassing from the chamber walls [93].

Most of the time, students who are not involved in the initial pump-down process do not have to deal with the vacuum system of their experiment. However, occasionally, the experiment requires vacuum maintenance, which is often the nightmare of every student working on the experiment.

During my time working on the SoPa experiment, I did not only deal with the vacuum setup of the SoPa experiment but got also involved in the order process of a new vacuum system for another sodium-potassium experiment, the NaKa, troubleshooting the NaLi (sodium-lithium) experiment, seeing crashed turbopumps and vacuum failures due to sudden leaks at the ATTA (argon trace trap analysis) and the BECK (potassium BEC) experiment.

The aim of this chapter is to provide a description of the SoPa vacuum setup and to report on the practical insights, solutions and observations that have been gathered over the past five years. It places greater emphasis on the practical experiences gained with vacuum systems in ultracold atom experiments, rather than focusing exclusively on the technical details of vacuum technology. For a comprehensive overview of vacuum technologies, one may refer to books such as those



At a DPG spring meeting, someone asked the speaker in the prize talk session what was the most challenging part of his PhD. The speaker's answer was quick and easy: vacuum.

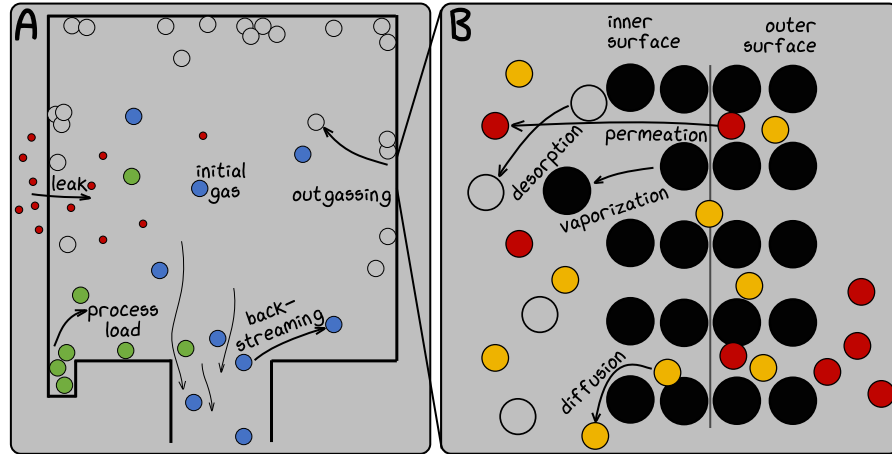


Figure 4.1: Gas sources and outgassing in a chamber. **A:** Sources of gas load in a pumped chamber, including initial chamber gas (blue), outgassing from the chamber bulk material (grey), leaks (red), and a gas from oven evaporation (green). **B:** Detailed view of outgassing processes from the chamber wall: Vaporization (black) of molecules from the surface material, desorption (grey) of gases from the chamber wall due to thermal or stimulated/induced processes (e.g. light), diffusion (yellow) of gas released from the bulk material, and permeation (red) of gases through the bulk material. Figure adopted from [92]

by Jousten, and Pramod [94, 95], as well as the websites of vacuum companies like *Pfeiffer* and their books [91], or the conference report of the *CERN Accelerator School* [96, 97]. A brief overview of vacuum considerations from the ultracold atom perspective can be found in [98].

The chapter is structured as follows:

First, Section 4.1 provides a brief overview of the SoPa vacuum system, without going into detail. Following this, Section 4.2 discusses design considerations for building an ultracold atom experiment. Section 4.3 focuses on practical experiences and challenges encountered in vacuum maintenance and operation.

4.1 OVERVIEW OF THE SOPA VACUUM SYSTEM

This section briefly describes the SoPa vacuum system. Detailed technical drawings of the components and supports can be found in Appendix A.5. To effectively load atoms into our traps, we need to evaporate them from the oven at vapour pressures of the order of 10^{-8} mbar. However, this pressure affects the atoms in the traps and reduces their lifetime. To overcome this, the system operates in a two-chamber configuration. In the first chamber, atoms can be evaporated at relatively high vapour pressures, while in the second chamber an ultra-high vacuum (UHV) is maintained, ensuring low background scattering rates in the final

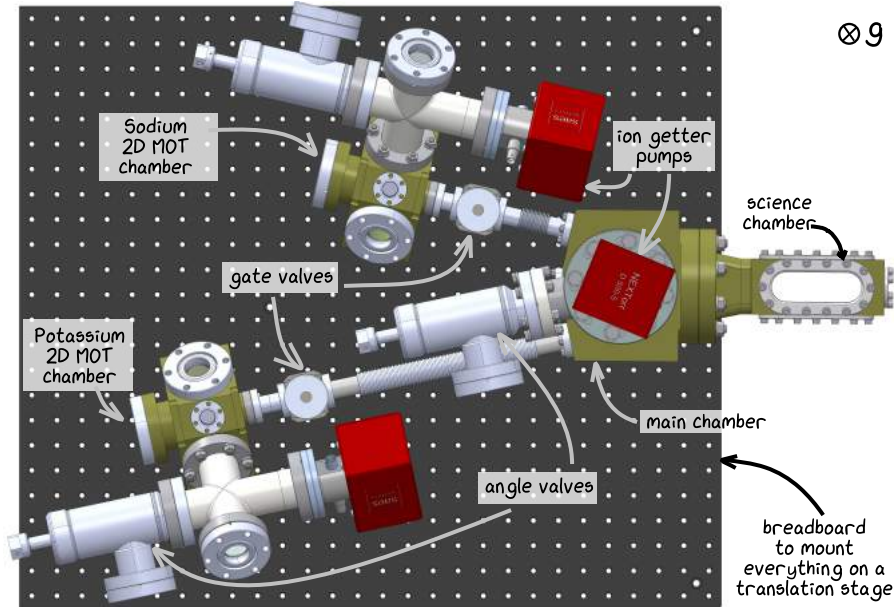


Figure 4.2: SoPa vacuum setup. This top view illustrates the separation of sodium and potassium oven regions into two distinct 2D MOT chambers. The ovens are not visible in this view as they are positioned beneath the 2D MOT vacuum chamber opposing the small viewport at the top. The main chamber connects the 2D MOT chambers with the science chamber. Three ion-getter pumps are distributed over the vacuum system (red). Each 2D MOT chamber can be isolated from the main chamber by a gate valve, and an angle valve separates the chambers from the pumping station. The entire assembly is mounted on a breadboard, which is used to mount everything on a translation stage. This figure is adapted from [77].

optical dipole traps. A differential pumping stage separates the two chambers, allowing for the pressure differences.

OVERVIEW SOPA VACUUM SYSTEM

A top view of the SoPa vacuum system is shown in Figure 4.2. The oven and 2D MOT chamber of the two atomic species are spatially separated to decouple the operation settings. The atoms are evaporated and initially pre-cooled in a two-dimensional magneto-optical trap. The main chamber connects the 2D MOT chambers with the science chamber. The bellows for sodium and potassium, which connect the 2D-MOT chambers to the main chamber, have different lengths to ensure enough space for opto-mechanics. The whole setup is mounted on a translation stage, with a travel range of 42 cm. This translation stage gives the possibility to move the whole vacuum setup out of the optics and coil configurations for vacuum maintenance. The translation stage consists of a rail system with lubricant-free friction bearings¹ on which

¹ T25 series from *igus*

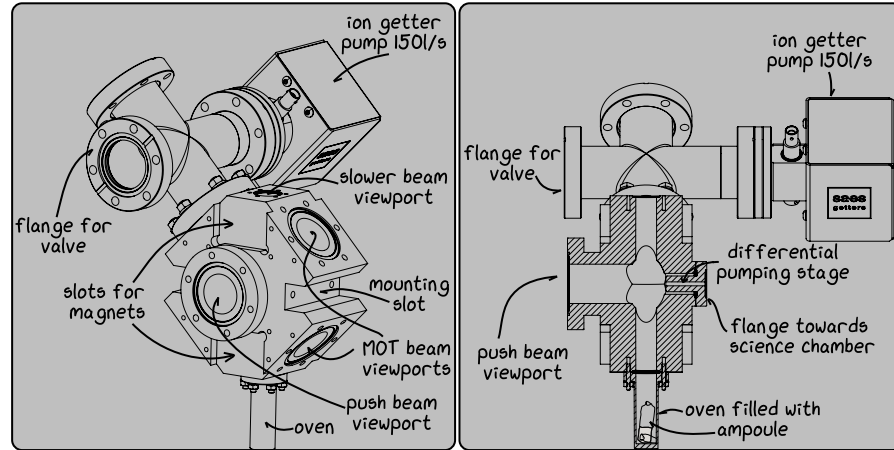


Figure 4.3: 2D MOT chamber (titanium), with pumping cross (316 stainless steel), ion getter pump and oven cup (316 stainless steel). The left image shows the outer view, while in the right image, a cut view through the 2D MOT chamber is shown. Slots give space for mounting permanent magnets and the chamber to the desired height. The oven cup is a blind pipe, which is filled with an ampoule. Figure adapted from [77].



The end position is fixed with clamps since the clamp on the sledge will loosen with time.

a 600×700 mm breadboard is mounted, which supports the vacuum system.

In total, three ion getter pumps are used to pump the vacuum system. One in each 2D MOT region² and one for the main and science chamber³. To initially pump down the system, all-metal angle valves⁴ are used for the connection to the pumping stage. Gate valves⁵ give the possibility to separate the 2D MOT region from the main chamber. Each 2D MOT chamber is connected via a differential pumping stage, a small pipe of dimensions diameter of $d = 3$ mm, and length of $l = 30$ mm, to the science chamber configuration. The differential pumping stage allows for a pressure difference in the order of 10^{-4} mbar between the chambers.

2D MOT CHAMBER

In the 2D MOT chamber, the atoms are evaporated from an oven, resulting in a vapour pressure in the order of 10^{-8} mbar. A cut view of a 2D MOT chamber is illustrated in Figure 4.3. The chamber is manufactured from titanium, the design is inspired by [42]. The oven consists of a blind tube which is mounted below the 2D MOT chamber and filled with 1 g sodium (potassium) ampoules⁶. Optical access is ensured with

² Nexttor Z100 from SAES getters

³ Nexttor D500 from SAES getters

⁴ all-metal angle valve from MDC 314003

⁵ gate valve from MDC 302011 with Kalrez sealing

⁶ purchased from Sigma Aldrich.

Sodium 1g: <https://www.sigmaldrich.com/DE/de/product/aldrich/262714>

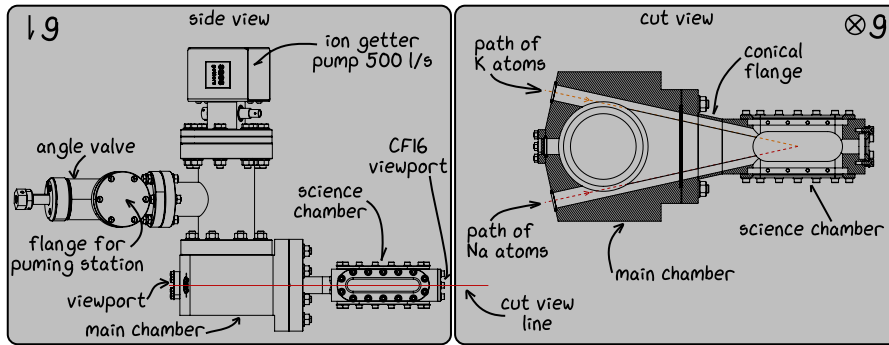


Figure 4.4: Science chamber with main chamber (titanium) and pumping tee (316 stainless steel), ion getter pump. The left image shows the outer side view, while in the right image, a cut view through the Science and main chamber is shown.

four CF40 viewports⁷ for the MOT beams, an additional CF40 viewport for the push beam, as well as a CF16 viewport opposite the oven. The chamber is fixed with both mounting slots to an aluminium beam. The two beams are screwed to a *Thorlabs* 1.5-inch post. The 2D MOT has therefore a height of 433 mm to the optical table. Technical drawings of the 2D MOT chamber parts are provided in Appendix A.6.

MAIN & SCIENCE CHAMBER

The main chamber and science chamber⁸ are also made from titanium. Figure 4.4 displays sketches of the main and science chamber. For the science chamber, a glass cell was not possible since the two atomic beams are coming in from one side under a 25° angle. To ensure good optical access the science chamber has custom elongated viewports⁹, which are sealed with indium wire¹⁰. The oval viewport dimensions are 90×30 mm for the top(bottom), and 90×15 mm for the sides. Details on the sealing procedure are described in [77]. The science chamber is fixed through the main chamber, which is mounted on a custom breadboard. The breadboard gives the possibility to use the main chamber viewport as another optical access point to the science chamber. To level the science chamber tilt, the main chamber is not mounted to fixed 1.5-inch posts as it was done for the 2D MOT chamber, but instead, the posts are mounted on a levelling knuckle foot¹¹, which itself is clamped to the breadboard. Technical drawings of the vacuum chambers, as well as the main chamber mounting breadboard are attached in Appendix A.5.1 and A.5.3.

⁷ fused silica broadband coated, purchased from *MDC VPZ38QBBAR*

⁸ The flanges that hold the glass in place are made of aluminium. In principle, if the indium had been baked well enough, the flanges could be removed.

⁹ 6mm BK7 glass plates with AR coating 500 – 1100 nm purchased from *LENS-Optics GmbH*

¹⁰ purchased from *GoodFellow 323-645-36*

¹¹ *ITEM 0.0.478.22*

4.2 DESIGNING CONSIDERATIONS FOR A VACUUM SYSTEM

In this section, the focus is placed on the design considerations of the vacuum system. The design process involves taking into account outer constraints and requirements such as optical access as well as bare vacuum design criteria.

Planning a cold atom experiment, one has to define first the experimental constraints. What kind of atom preparation technique is required prior to the MOT e.g. 2D MOT or Zeeman Slower? What is the vapour pressure of the atomic species, i.e. at what temperature do we have to operate the oven? Is more than one species needed? On the other side, the basic vacuum criteria are quite clear. A system is best pumped with as little corners and large pipes as possible [94]. The vapour of alkali metals might also not be the healthiest environment for the pump. For cold atom experiments, we have the following requirements:

- A **two-chamber configuration** is used. One chamber serves to create an atom beam, where atoms are evaporated and the other one for the final trap with better vacuum to increase the lifetime of the atoms in the trap. The chambers are separated by a differential pumping stage and a valve. The differential pumping stage ensures a pressure gradient between higher pressures in the oven region and the very low pressures in the science chamber. The valve ensures that one can maintain the UHV in the science chamber, while one is performing vacuum maintenance in the oven region e.g. refilling the oven.
- An **atom source** from where atoms are evaporated into the system. Typical approaches are the standard oven cup, which is nothing else than a blind pipe, or commercially available dispensers [99–102], where atoms are evaporated by reduction of an alkali metal salt, which is done by an electric current. The other gases created by the chemical reaction are directly trapped with a getter. [103]
- **Optical access** to the chambers is required for the various cooling stages and traps, as well as for monitoring and imaging purposes. Most optical access is required at the science chamber where many traps are employed, e.g. MOT, dipole trap, 2D dipole trap. However, optical access is also required for the 2D MOT chamber or the Zeeman slower. Typical solutions for the science chamber are rectangular glass chambers made by anodic bonding of glass plates¹². Chambers with standard CF viewports, such as those from *Kimball physics*, are also often used. An alternative approach is to use small octagonal glass chambers such as those

¹² At the BECK experiment the material is *Spectrosil 2000*

offered by *Precision glassblowing* [104]. Custom sealed solutions are rarely used.

- The choice of **material** for vacuum components is critical. The ideal material should have low outgassing rates, resistance to corrosion from vaporised atoms and coatings on the chamber walls, non-magnetic properties, non-conductivity to prevent eddy currents during rapid magnetic field ramps, and be easily machinable. Standard vacuum components are typically made from 304 stainless steel, with 316 stainless steel available in some cases, which offers better magnetic and outgassing properties than 304 [92]. In certain custom applications, titanium is also used [105]. However, comparing outgassing rates across materials can be challenging due to the significant influence of the manufacturing process. A recent study compared geometrically similar chambers made from different materials, some of which had been subjected to vacuum firing, including 304L, 316L and 316LN stainless steels, titanium and aluminium [106]. The study measured water and hydrogen outgassing rates. The best water outgassing rates were observed for the 316 stainless steels, both vacuum fired and untreated, followed by titanium. In contrast, 304L stainless steel and aluminium had the highest water outgassing rates. Notably, the initial difference between 304L and 316 stainless steels was only a factor of 10, and this advantage was maintained over time only by the 316LN chambers.

For hydrogen outgassing, titanium showed the lowest rates, approximately 300 times lower than 304L stainless steel, followed by aluminium and vacuum fired 316L and 316LN stainless steels. In contrast, all untreated stainless steels had significantly higher hydrogen outgassing rates.

- The **vacuum conditions** in an ultracold atom experiment are considered dirty and corrosive from a vacuum engineering point of view [94]. Depending on the melting point of the atomic species, surfaces can easily become coated with atoms. The corrosive nature of alkali atoms requires that functional parts of the vacuum system, such as pumps, gauges or valves, are not placed directly in the path of an atom beam. Viewports are particularly susceptible to being obscured by atomic deposits, which are sometimes unavoidable in direct view of the viewport. Heating the viewport often helps to keep it free of atoms, but alkali atoms can react with glass (e.g. fused silica) and corrode the metal-to-glass transitions, typically made of Kovar. It is therefore advisable to minimise direct contact.

4.3 NAVIGATING VACUUM CHALLENGES

The aim of this chapter is to address some practical questions concerning vacuum, which include:

Subsection 4.3.1: Cleaning of Vacuum Parts

Subsection 4.3.3: Vacuum Bakeout

Subsection 4.3.2: Vacuum Component Assembly and Handling

Subsection 4.3.4: Oven Filling & Cleaning Procedures

Subsection 4.3.5: Flooding the Vacuum Chamber

Subsection 4.3.6: Sudden Leaks in Viewports

Subsection 4.3.7: Opaque Coatings of Viewports

Subsection 4.3.8: Sudden Rise of Ion Pump Current

Subsection 4.3.9: Curiosities in the Vacuum

4.3.1 *Cleaning of Vacuum Parts*

The surface of the chamber wall typically consists of layers of grease, oxides and hydroxides above the actual surface of the bulk material. These layers may have irregularities resulting from the manufacturing processes used. Achieving ultra-high vacuum (UHV) conditions is dependent on the cleanliness of the components, as residues left on the parts can prevent the desired vacuum quality from being achieved. The outgassing of oily substances, for example, can limit the pump-down process as they have high vapour pressures and outgassing rates [107]. It is therefore essential to ensure that all parts are kept clean.

It can be assumed that parts cleaned in-house by the vacuum company and shipped in a properly sealed package are sufficiently clean for ultracold atom experiments [108]. In addition to the standard cleaning procedures, vacuum companies may offer air baking or vacuum firing, which reduces the rate of hydrogen outgassing from the bulk material [109]. Air baking typically involves heating the component to temperatures between 150 and 500 °C in an air atmosphere. Vacuum baking involves exposing the component to temperatures of up to 960 °C in a vacuum. Air baking appears to be a more advantageous process than vacuum firing [93].

It is therefore recommended that parts which have been stored unsealed for an extended period of time be cleaned prior to installation. At the SoPa experiment, only new parts that had been cleaned and sealed by the company were installed, and thus no additional cleaning

was performed.

For detailed instructions on cleaning processes, overviews are available in [92, 107]. Additionally, the notes from CERN meetings provide very detailed instructions on cleaning vacuum parts [96] especially the contribution by Taborelli. In general, the cleaning procedure follows several steps, progressing from coarse cleaning to finer cleaning methods.

4.3.2 Vacuum Component Assembly and Handling

Proper assembly of vacuum components is critical to achieving ultra-high vacuum (UHV) conditions, as improper assembly often results in major leaks and compromised system performance. This section provides information on various vacuum components and their assembly, including practical tips. It emphasises standard practices that are essential for successful assembly and draws attention to common mistakes made in the SoPa experiment due to lack of knowledge. As discussed in the previous Section 4.3.1, it is crucial to avoid contamination of parts during assembly. The human hand is a significant source of grease, which can have a serious impact on the cleanliness of the vacuum. Therefore, clean, powder-free and oil-free gloves, preferably PVC or nitrile cleanroom gloves [98], should be used.

FLANGES & GASKETS

ConFlat (CF) flanges are commonly used in UHV applications. These flanges have a cutting edge that seals by pressing into a softer material that adapts to the smallest structures and provides a good seal. Typically the gasket material is oxygen-free copper. Annealed copper gaskets are used for viewports to reduce stress. Silver plated copper gaskets are often used in systems with high temperature bake-outs above 200 °C to prevent component welding. In highly corrosive applications, nickel gaskets can be used ¹³.

When connecting vacuum components, care should be taken to tighten them evenly. Otherwise, the cutting edge may press unevenly into the copper, resulting in a poor seal. In the worst case, overtightening screws initially can create a leak, as the opposite side cannot be pressed together anymore. It is best to tighten screws in a criss-cross pattern, increasing the torque gradually until the final torque is reached. There are two common philosophies: tightening flanges until they touch, as recommended by *Kurt J. Lesker* or *Pfeiffer Vacuum*, or tightening less

¹³ *Kurt J Lesker* offers them. No specific definition for corrosive environments could be found, but in general it should hold that nickel seals are used, where the standard seals turned out to be not sufficient. In the NaLi experiment, nickel seals were used, which resulted in the knife edge becoming worn due to the frequent oven switching cycles and the harder nickel seals. This resulted in the knife edge having to be renewed on a regular basis. [110]

Table 4.1: Maximum torques for a lubricant-free assembly of A2-70 and A4-80 screws. Values taken from [91].

Screw Type	Material	max. Torque [Nm]
M4	A2-70	3.3
	A4-80	4.4
M6	A2-70	11.3
	A4-80	15
M8	A2-70	27.6
	A4-80	36.8

and leak testing each flange, tightening further if a leak is found [98]. This latter approach reduces stress and prevents knife edge wear.

Most vacuum companies recommend tightening to flange contact without specifying a torque. However, the maximum torque is limited by the strength of the screw material and the friction during assembly. Guideline values for maximum torque are available from some vacuum companies, the vacuum technology books by *Pfeifer*[91] provide detailed estimates of the maximum torque values to be applied to the screws. Typically, screws for vacuum assembly are made of A2-70 material. As these screws are magnetisable, A4-80 screws were preferred for the SoPa experiment. Table 4.1 summarises the maximum torques for a high friction case (no lubricant) for these two materials. Silver coated screws are available to reduce friction and prevent cold welding at high temperature bake-outs above 200°C.

In the SoPa experiment, we used lower torques and did not tighten the gaskets until they touched, leaving room for further tightening if necessary. For heavy parts, it was helpful to compensate for gravity by using a higher initial torque for the upper bolts. Most of the vacuum connections were tightened without a torque wrench, especially the small CF16 flanges, which were difficult to access. However, a torque wrench can ensure uniform torque and prevent screw break-off.

ALL-METAL ANGLE VALVES

All-metal angle valves are sealed with a poppet copper gasket, similar to a gasket. To allow multiple closing cycles, the valve is uniformly tightened with the same torque, ensuring a defined compression of the poppet copper gasket. This position changes gradually until the poppet copper gasket needs to be replaced, which is usually marked on the valve knob. At the SoPa experiment, we have found that the maximum torques for angle valves vary considerably from manufacturer to manufacturer. It is advisable to consult the manufacturer for torque values to avoid tearing the valve knob.

HANDLING VACUUM COMPONENTS

This paragraph outlines a few practical techniques, though they may be unconventional, with the hope that they might be useful for someone. The theoretical process of dealing with vacuum systems is straightforward: evenly tightening screws in a criss-cross pattern. However, this becomes challenging when heavier parts need to be connected in tight spaces, and even more so when one or both flanges are rotatable.

Support: For larger vacuum parts, we started to use tension straps for support. The straps are wrapped around the part to prevent slippage and tightened to hold the part roughly in position. This allows easy adjustment to the correct angle without having to support the entire weight.

Keeping rotatable flange in position: Rotating flanges offer more degrees of freedom, but can be problematic if they push back or tilt during assembly. For short lengths of pipe, the use of flange caps as pushers works well. Fold the caps in half and place them behind the flange (see Figure 4.5 A). They can be easily removed once the bolts are in place. Because they are so easy to remove, they can also fall off easily. Unfortunately, if only one is left, the flange can easily tilt and get stuck. In this case, care must be taken to ensure that the flange does not get stuck accidentally.

Holding gasket in position: With vertical flanges, it can be a challenge to keep the gasket in place. Small parts such as viewports can be prepared with a seal and then folded onto the flange without losing the seal. However, for larger or heavier parts where the flanges rotate or the angle is difficult to maintain, it becomes more difficult to position everything without losing the gasket. In such cases, we use small pieces of *Kapton* tape to secure the gasket, as shown in Figure 4.5 A. When placing the tape, care must be taken to position it outside the cutting edge. Up to three pieces of tape are usually sufficient, but more can be used if necessary. The *Kapton* tape can either be left in place or removed if higher bake-out temperatures are required beyond the tolerance of the tape. To remove the tape, tighten the flanges slightly to hold the gasket in place, but leave enough slack to allow the tape to be removed. A commercial solution is to use gasket clips to hold the gasket in place at the leak check slots (the two radial grooves on each flange). These clips can be effective in assemblies where the alignment of the grooves can be ensured and there is sufficient space for the clips.



The angle valve has one rotating flange, providing a degree of freedom during assembly. We initially didn't consider the valve's orientation, but it became tough when connecting long parts e.g. the turbopump. It would be helpful if the flange is oriented horizontally or vertically making it easier to hold the part in the correct angle.

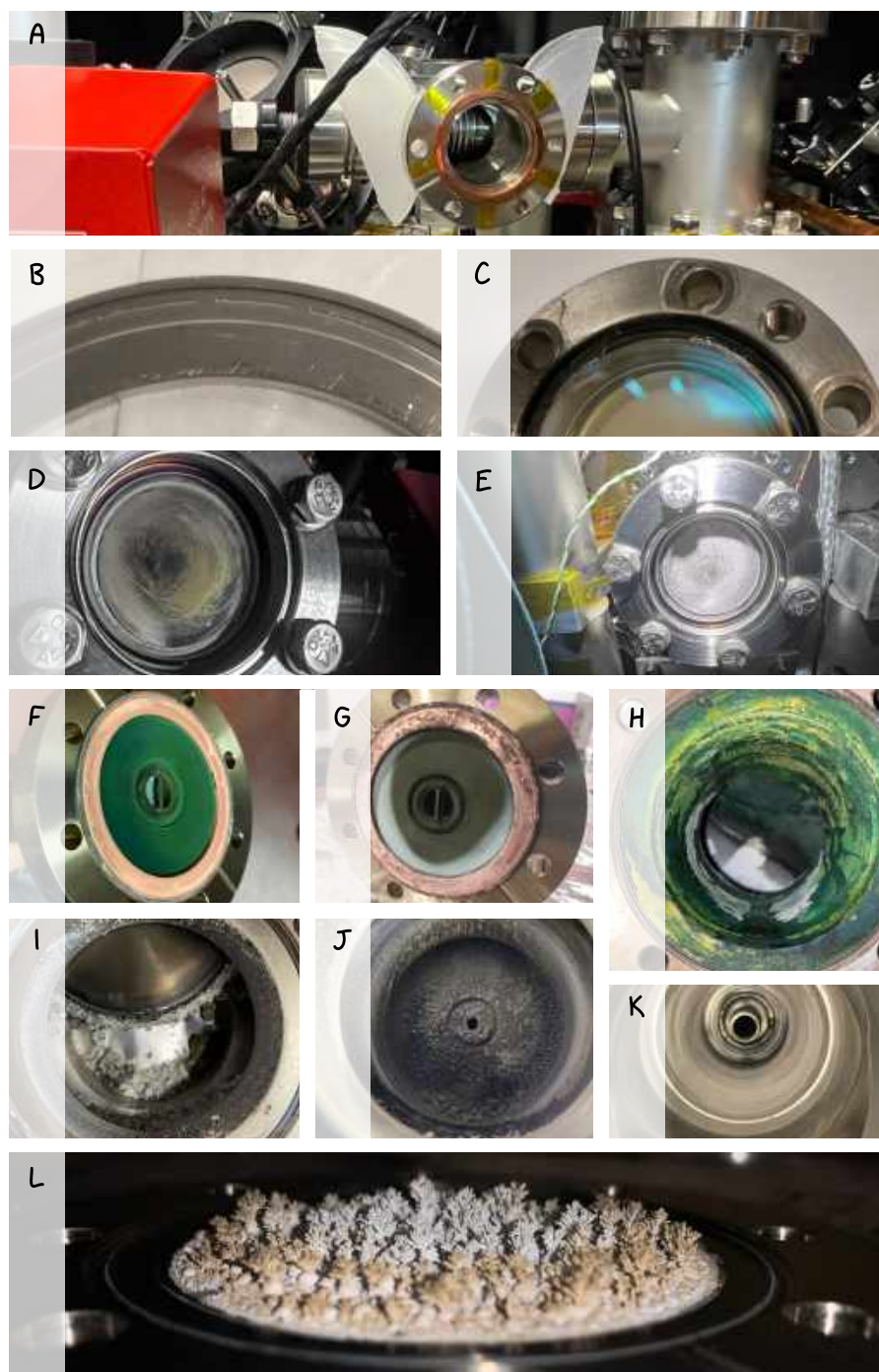


Figure 4.5: Vacuum gallery with images of the SoPa (A,D,E), NaLi (B,F-L) and BECK (C) experiments. **A:** Technique where a rotating flange is pushed into position and the gasket is taped in place with Kapton. **B:** Large leakage due to damage to the cutting edge of the flange. **C:** Corrosion of the glass-to-metal seal on a viewport. **D:** Unknown milky film on the inner surface of a viewport. **E:** Milky viewport due to sodium deposits. **F-H:** Green coating in vacuum chamber. While **F** and **H** show the colour immediately after opening the system, the green coating started to change its colour quickly to a darker shade (**G**). **I-L:** White cauliflower coating in a vacuum chamber. **I:** Gate valve seal covered with white coating. **K:** The other side of the differential pumping stage in **J**. **L:** Blank flange next to an atomic beam shutter positioned before **J**.

4.3.3 Bake-out

As mentioned previously, achieving UHV requires the reduction of outgassing rates. A significant source of outgassing is the desorption of gases, mainly water, adsorbed on the chamber walls during assembly or exposure to air. The rate of water desorption is temperature dependent and can be increased by heating (baking) the vacuum system to 100 – 250 °C [92, 106]. At higher temperatures other gases such as CH_4 , CO and CO_2 also desorb and temperatures of 300 °C are sufficient to desorb all gases that contribute to the gas load due to desorption at room temperature [92]. This higher temperature could additionally reduce the outgassing rate of hydrogen [98], although air baking or vacuum firing appears to be more effective than bake-out at moderate temperatures [93, 109, 111]. In this thesis, bake-out always refers to heating the vacuum system during pumping.

During a bake-out, the system is uniformly heated to 100 – 450 °C while being pumped, in our case by a pumping station consisting of a turbo pump¹⁴ and its oil-free roughing pump¹⁵, a residual gas analyser¹⁶ (RGA) and a vent valve¹⁷. The temperature greatly accelerates the desorption of water, so the pressure rises and soon begins to fall slowly. The temperature is usually maintained until the rate of pressure drop becomes small. In the SoPa experiment, this "equilibrium" pressure was slightly above the initial pressure and is reached within a few weeks, depending on the temperature. During cooling, the pressure continues to fall well below the initial pressure.

In practice, the bake-out temperature is limited by the vacuum components used. Common temperature limiting elements include sealing parts such as viewports and valves, and temperature sensitive components such as viewport coatings and ion pump magnets. Table 4.2 lists the maximum temperatures for components used in the SoPa vacuum system. It is worth noting that the custom indium seal used on the science chamber drastically limits the maximum temperature.

The species of atoms in the vacuum chamber can also limit the bake-out, as their vapour pressure may be high enough to be completely evaporated after bake-out. For potassium, the oven is not heated to prevent the atoms from baking, resulting in higher outgassing rates from the oven cup. However, this is manageable as the oven volume is small and the chamber is designed for a higher vapour pressure.

A practical approach may be two bake-outs [98, 112]: one at high tem-

¹⁴ *HiPace 80* from *Pfeiffer Vacuum* with air cooling kit *PM Z01 300 AT*

¹⁵ *HiScroll 6* from *Pfeiffer Vacuum*

¹⁶ *RGA 100* from companySRS

¹⁷ *F0275XVALVE* from *Kurt J. Lesker*

Table 4.2: Maximum temperature ratings for components of the SoPa vacuum system.

Component	max. Temperatur [°C]
Viewport	200
Ion Getter Pump	
with magnets	150
wo magnets	250
cable	200
Gate Valve	
open	250
closed	200
Indium Sealing at Science Chamber	110
Angle Valve	450
Turbo Pump at UHV Flange	120
RGA	
wo electronics	300

perature (300 – 450 °C) when temperature sensitive components such as viewports are replaced with blind flanges, and a second bake-out at moderate temperature (100 – 250 °C) after viewport assembly to remove water vapour adsorbed during assembly. If the system is flooded with a clean argon or nitrogen gas during assembly, adsorption of slowly desorbing gases can be minimised.

For the SoPa experiment, only a low temperature bake-out was performed at around 150 °C for the 2D MOT chambers and 90 – 100 °C for the science chamber, as the parts were pre-treated by the vacuum company to reduce hydrogen outgassing.



Fibreglass heaters are inconvenient because the glass fibres spread. We tried silicone insulated heaters for bake-out temperatures below 200 °C, but they were thinner, harder to fix and became brittle.

Heating the entire vacuum chamber evenly can be a challenge. To ensure proper heat transfer, the vacuum system is wrapped in aluminium foil after several thermocouples¹⁸ have been placed to monitor the temperature. After wrapping the apparatus in aluminium foil, the vacuum chamber is evenly wrapped in heating tapes, avoiding crossings. For the SoPa experiment, glass-fibre insulated heating tapes¹⁹ were used, which can withstand temperatures up to 450 °C. The heating tapes were manually controlled by an autotransformer, making the baking process tedious.

¹⁸ We use type K thermocouples at SoPa

¹⁹ purchased from *SAF Wärmetechnik* KM-HT-BS30

The viewports are carefully covered with aluminium foil to ensure even temperature distribution without directly touching the glass. As the viewports are sensitive to rapid temperature changes, these should not exceed $2 - 3^\circ\text{C}$ per minute²⁰. In the SoPa experiment, the temperature of a viewport is monitored by bending a thermocouple so that it is close to the centre of the viewport without touching it, and taping it to the flange of the viewport. In general, rapid temperature changes lead to stress in all parts and could also lead to leaks at the flanges.

Baking is therefore a standard procedure in UHV systems and is essential for efficient pump-down. Despite its necessity, baking is time consuming and often tedious, leading to attempts to shorten the process. These experiences in the SoPa experiment are discussed below.

AVOID THE BAKING PROCESS?

Bake-outs take time and are tedious to perform. The question therefore arises as to whether UHV vacuum can be achieved in a reasonable time without bake-out by increasing the pumping speed. Indeed, it has been studied and proposed that the non-evaporable getter (NEG) can help to reduce bake-out times [114, 115]. In the early stages of the SoPa vacuum setup, we tried pumping down without bake-out. Skipping the bake-out seemed to work well, as pressures of 10^{-10} mbar could be achieved [77], which dropped further down to 10^{-11} mbar (minimum value of the ion pump). Although the pressure reading from the ion pump was good, when we had problems in the potassium 2D MOT, e.g. several arcing events and the resulting shutdown of the ion pump, the poor baking was questioned as a possible cause. In the end, especially with more knowledge and further insight, the problems were most likely caused by leakage current from the ion pump (as discussed in Section 4.3.8) and had nothing to do with the no bake approach. We had no problems with the sodium 2D MOT. It is still questionable whether this approach is recommendable for the cold atom community, since it is unclear whether the pressure reading is valid for the whole system or only for the ion pump located behind the NEG element. It depends on the geometry of the chamber as the gases are in the molecular flow regime and therefore move ballistically through the chamber. In Appendix B.1 the partial pressure difference between the ion pump and the centre of the 2D MOT chamber was estimated to be three to four orders of magnitude. As we were setting up the experiment, progress was slow in getting all the parameters right to find the first signal from the MOT, so there was time for the system to outgas. It will be interesting to see if there is any effect on the MOT performance after refilling the oven of a running system. In addition, water is mainly adsorbed at



In the BECK experiment, the thermocouple was taped to the viewport with Kapton, after the bake-out the residue of the Kapton tape was difficult to remove, in the end Xylol worked.[113]



In Appendix B.2 times are estimated how long it takes until the getter material of the ion getter pump is saturated.

²⁰ for Kodial viewports. Fused Silica and Sapphire viewports can sustain temperature ramps up to 20°C per minute. Values taken from *Pfeiffer vacuum* products

the wall surface and the alkali metals used react with water to form their hydroxide, so the system could be covered with a layer of sodium hydroxide which is corrosive and reacts, for example, with the fused silica viewports built in [116].

PUMP OUT THE ATOMS?

We had some troubles with our 2D MOT chamber for potassium as described in the Section 4.3.8. In order to solve the "vacuum problem" we did a week long bake-out heating the hole system to 150°C also the oven was at 80°C. After this bake-out we had a clean vacuum chamber, without any atoms. Loosing all the atoms means of course that the system has to be flooded again and the oven refilled.

The atoms do not magically disappear, they were pumped by the turbo pump out. In case of potassium with a low vapour pressure, it is not so likely, that the atoms will cover the turbo pump blades. However, the turbo pump used at the NaLi experiment was after a normal system bake-out (not baking all atoms out of the oven) clearly coated with sodium. Therefore, the turbo pump is getting corroded with time.

PROBLEMATIC ATOMIC DEPOSITIONS ON THE CHAMBER WALL?

The NaLi vacuum system had accumulated thick atomic deposits, sometimes several centimetres thick, on the chamber walls over several years (see Figure 4.5 I, J, L). These deposits did not initially limit the ultimate pressure achievable in the system. For years they caused no vacuum problems, but this changed after an oven refill. When the roughing pump was switched on, the pressure did not drop as expected. Normally, the roughing pump reaches its final pressure almost immediately, while the turbopump takes about half an hour. This time, however, the pressure drop was so slow that the RGA could not operate (maximum 10^{-4} mbar).

Initially we suspected a leak in the oven connection, but on inspection the seal appeared intact, ruling out such a significant leak. During the second pump-down attempt, we did not believe there was a leak and waited longer to activate the RGA (about half a day). The RGA readings showed that the system was primarily filled with water vapour. It is likely that the thick deposits had increased the surface area inside the vacuum chamber and, due to their hygroscopic nature, were adsorbing additional water. This created a pseudo-leakage effect during pump-down, causing the water to be released slowly. Although it was possible to achieve UHV conditions with an extended bake-out, the process took significantly longer than usual to remove all the water.

The deposits were probably sodium and lithium carbonate formed during a previous flooding of the vacuum chamber. During extended oven runs, the entire cauliflower-like structure of the deposits was coated with fresh sodium and lithium, which would react with the water when the system was flooded and act as a getter. However, when the pump-

down problems occurred, the system had not been run for such a long time, so the surface was probably not coated with fresh sodium/lithium, leaving a large hygroscopic surface exposed.

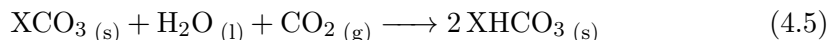
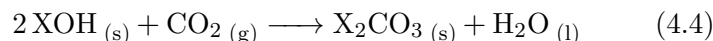
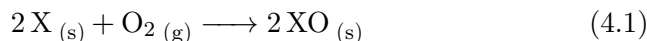
While these wall deposits mainly affected the pump-down process, deposits inside the ion pump also caused significant problems. They frequently caused short circuits, necessitating the replacement and refurbishment of the ion pump [72].

4.3.4 Oven Filling and Cleaning

The time when the oven is filled is one of the times when cold atom experimentalists actually have to deal with chemistry. It is therefore important to know what one is dealing with.

The best way to fill the oven depends on the atomic species. In the following the focus is on the alkali atoms, sodium and potassium.

Alkaline metals react exothermically with oxygen and water in air²¹. Sodium and potassium X react with oxygen O_2 to form their oxide X_2O_2 . With water H_2O they react to their hydroxide XOH , which is formed when the peroxide reacts with water. The hydroxide then reacts with carbon dioxide CO_2 to form its carbonate:



[117, 118]. This is why alkali metals are stored in a protective way. The most common way in a chemistry laboratory is to store them in kerosene, paraffin or mineral oil, which are not suitable for cold atom experiments. As oils have a high outgassing rate [107] and can therefore spread easily within the vacuum system, forming a layer on functional components such as pressure gauges and leading to their malfunction [98], they should be avoided in UHV systems. Other options are bars in glass ampoules (typically available in 1g and 5g) which need to be cleaned and crushed or, if larger quantities are required, packaged under an inert gas atmosphere, typically argon or nitrogen²². For the inert gas atmosphere package, a glove box under inert gas atmosphere is required to store the leftover for the next oven filling. Under normal circumstances, the short contact with air during the oven filling pro-

²¹ Lithium also reacts with nitrogen

²² bought from *Sigma Aldrich*.

Sodium 1g: <https://www.sigmaaldrich.com/DE/de/product/aldrich/262714>

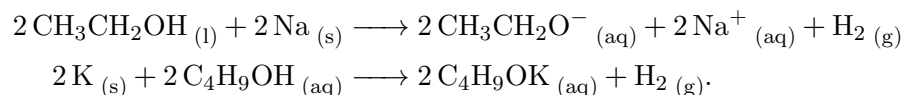
Sodium 50g: <https://www.sigmaaldrich.com/DE/de/product/sial/282065>

Table 4.3: Alcohol used for the destruction of alkali metal residues in the oven. [119]

leftover alkali metal	alcohol to be used for cleaning
sodium	ethanol
lithium	ethanol
potassium	tert-butyl alcohol

cess cannot be avoided²³, but for this short time the oxidation should only be on the surface. Flooding the vacuum system with non-reactive gas has several advantages. Less gas, e.g. water, is adsorbed on the chamber walls during the oven filling process, which also preserves the performance of the ion getter pumps and reduces the time the freshly filled sodium/potassium is oxidised during contact with the air. Typical flooding gases are argon or nitrogen, which is less expensive. When choosing the correct gas, the reactivity of the atoms used should be considered. Sodium does not react with nitrogen and potassium does react with nitrogen. However, it decomposes at room temperature and is therefore not relevant [117]. For the SoPa experiment, nitrogen is a good flooding gas. The flooding process is described in more detail in the next Section 4.3.5.

If the oven needs to be refilled, it may need to be cleaned before reuse or storage. As the cleaning process takes some time, it may be helpful to use a second set of oven cups. A chemical laboratory with appropriate equipment should be used for the cleaning process. If the oven needs to be cleaned of small amounts of alkali metal residues, they can be cleaned by slowly adding alcohol. The type of alcohol to be used depends on the alkali metal (see Table 4.3). Process details can be found in the books *Prudent Practices in the Laboratory: Handling and Disposal of Chemicals* and *Wasserstoff und Alkalimetalle: Elemente der ersten Hauptgruppe* by Hermann Sicius [118, 120]. As a general rule, the more reactive the alkali metal, the less reactive the alcohol should be. For sodium and lithium ethanol can be used, for potassium tert-butyl alcohol must be used [118, 119]. This process can take some time and should be handled with care as hydrogen is produced during the chemical reaction [118, 121]



Details of oven cleaning for the sodium and lithium NaLi experiment are reported in [72].

For sodium and potassium, another method has been published [116],

²³ It is possible to improvise a glove box around the oven area.

in which the alkali metal residue is buried in dry quartz sand in a ceramic flower pot, which is placed in a porcelain beaker to be filled with water. The water is then drawn up into the sand by capillary action, causing the sodium to react with the release of hydrogen to form sodium hydroxide. The sodium hydroxide reacts with the sand SiO_2 to form sodium silicate $NaSi$ and water. The sand can be easily washed and reused after drying. This technique may in principle be a good solution for cleaning the oven of alkali metal residues, but the process has only been tested on a small amount of 0.5 g sodium. The problem is that in most cases it is difficult to determine how much is left in the oven and how reactive the residue is. In addition, the entire oven has to be buried in sand and then cleaned. Therefore, a controlled test should be carried out with sodium/potassium in a stainless steel container and larger amounts of sodium/potassium.

4.3.5 Flooding the Vacuum Chamber

To break the vacuum, it is usually slowly flooded with gas. Air is usually avoided because water is adsorbed by the inner walls of the vacuum chamber, making it more difficult to achieve UHV. In addition, UHV pumps (e.g. the *Nextorr D500/ Z100* used in the SoPa experiment) age when kept in air, and deposits of the atomic species used in the system oxide in air. Argon or nitrogen are common gases recommended by pump suppliers, with nitrogen being the cheaper option. The system must be slowly flooded with the gas, and during a oven change the gas must flow out of the system to prevent air from entering, but care must be taken not to over pressurise the system, especially if glass parts are fitted as viewing ports. A metering valve is used for this application.

For the SoPa and NaLi experiments, the system was flooded without a dosing valve. The nitrogen cylinders were connected to the vent valve via a glove acting as a balloon. In this method, the glove is connected between a vent valve and the outlet of a gas cylinder. The size of the glove allows the pressure and therefore the flow of gas to be monitored. Throughout the process, the valve of the gas cylinder is manipulated so that the size of the glove remains constant. More details on this technique are described in [77]. However, if it is particularly important to avoid water in the system to maintain a good vacuum, this may not be the best option.

[113] This was the case at the BECK experiment, where a viewport suddenly cracked (more details in the next Section 4.3.6). Additionally to the viewport crack the valve connecting to the science chamber had a small leak. To avoid disassembling all optics around the science chamber for a bake-out, efforts were made to reduce the amount of water getting into the system by flooding.



Note

that there are different grades of gas available, which can vary quite drastically in the amount of other gases. Consider a nitrogen gas containing 5 ppm of H_2O , which is used to flood a vacuum system. If the system is flooded with this gas at atmospheric pressure of 1 bar, the resulting partial pressure of H_2O in the chamber will be $5 \cdot 10^{-3}$ mbar.

Bottled nitrogen can contain a significant amount of water and other impurities, depending on the grade²⁴. Therefore, the nitrogen for flooding was filtered using a nitrogen purifier²⁵ before it was injected into the chamber. The filter claims to reduce gas contaminants from the ppm (10^{-6}) level to the low ppb (10^{-9}) level²⁶. The filter was tested in the ATTA experiment with qualitative results: The filter did indeed reduce the amount of water detected, and the standard pipes used to connect the gas to the vacuum chamber let in quite a lot of water and should be reduced as much as possible. In the BECK experiment, the replacement of the viewing window was successful and the vacuum in the science chamber was maintained without bake-out.

This was because the leakage rate of the valve was low enough to keep the system at a vacuum of 10^{-4} mbar during the 2D MOT maintenance process. The use of the nitrogen purifier is promising to ensure that the vacuum chamber is flooded with dry nitrogen. In any case, metal pipes should be avoided in the flooding setup. In this respect, the glove technique described above to control the gas flow into the chamber is not a good choice in terms of the amount of impurity gases during flooding.

4.3.6 Sudden Leak in a Viewport

Viewports are the most sensitive parts in a vacuum chamber. Most commonly, a sudden crack occurs during a bake-out or other heating process, where too rapid or uneven heating or cooling causes the glass to crack. The cracked glass can be identified by a sudden increase in the partial pressures of nitrogen and oxygen, where nitrogen should be four times higher than oxygen. In this case you can try to seal the leak with *Vacseal* (a substance that looks like transparent nail polish).

In the NaLi experiment, a *Kodial* glass viewing window cracked after the system was successfully baked and the turbo pump removed. The exact cause of the crack is unclear. It is most likely that the viewport was under stress from the assembly and bake-out process, and the vibrations from removing the turbo pump were sufficient to cause it to crack.

Another source of sudden leakage is the corrosion of seals. This problem was observed in the BECK experiment on a viewport seal. Standard viewports are typically sealed with *Kovar*. Although other sealing materials are available, no data could be found to indicate better corrosion stability. The challenge for a viewport gasket is that the gasket material

²⁴ e.g. Nitrogen 5.0 from *Linde* has $O_2 \leq 3$ ppm, $H_2O \leq 5$ ppm, hydrocarbons ≤ 0.2 ppm.

²⁵ MS-P300-2 from *vici*

²⁶ an inlet of 50 ppm nominal concentration is filtered to an outlet of: $CO, CO_2, O_2, H_2O \leq 1$ ppb, non-methane hydrocarbons ≤ 3 ppb

must be flexible enough to accommodate the different thermal expansion rates of the metal and glass used. *Kovar*, the standard sealing material for CF viewports, was developed specifically for this application [122].

During the writing of this thesis, corrosion of the viewport seal also occurred in the SoPa experiment (late June 2024). In the sodium 2D MOT, one viewport started to leak. It is the upper CF40 viewport which is directly connected to the 2D MOT chamber body. As broadband coated fused silica viewports are used, the glass-to-metal seal is also made of *Kovar*. Although the *Vacseal* seems to be considered as permanent solution, the corrosion will not stop. It took two weeks to be leaking again - although the process could have been enhanced due to heating of all coated viewport to remove the sodium deposits.

An alternative option for our viewports could be the use of a so-called *Housekeeper* viewport. This type of viewport is sealed by a direct metal-glass transition, where the metal is gradually thinned to become flexible enough to follow the thermal expansion of the glass, which is fused directly onto the thin metal.

Although this sealing method results in a relatively long viewport, it could be advantageous for the SoPa 2D MOT. The increased length means that the glass is less likely to become coated with sodium due to the increased distance from the oven. However, potential disadvantages of this viewport include its extended length and a less flat glass surface.

4.3.7 Opaque Coating of the Viewport on the Vacuum Side

At the SoPa we have several problems with viewports becoming opaque and blind.

A major problem is that sodium deposits on the viewports due to the short distance from the oven, causing them to become blind (see Figure 4.5 E). Details of how we are currently dealing with this problem and our future plans to overcome it are discussed in the Section 6.

Another problem is that all the viewports have developed a slight opacity from the inside, as if someone had wiped them clean (see Figure 4.5 D). This phenomenon was not noticed during assembly and it is unclear when it started. The viewports were delivered in sealed bags and mounted directly without any treatment or contact by us.

Discussions with Brian Bostwick and Florian Schreck revealed that there are two possible causes for this problem. One is prolonged bake-outs at high temperatures, which can destroy the anti-reflective coating [123]. The other is the use of inappropriate cleaning procedures



Corrosion continued as the writing progressed. After exactly 2 weeks, the ion pump current jumped back up to the same order of magnitude. Although starting from a higher base current as the viewports are heated to remove sodium. Using Vacseal again on the same viewport helped to reduce the current again.

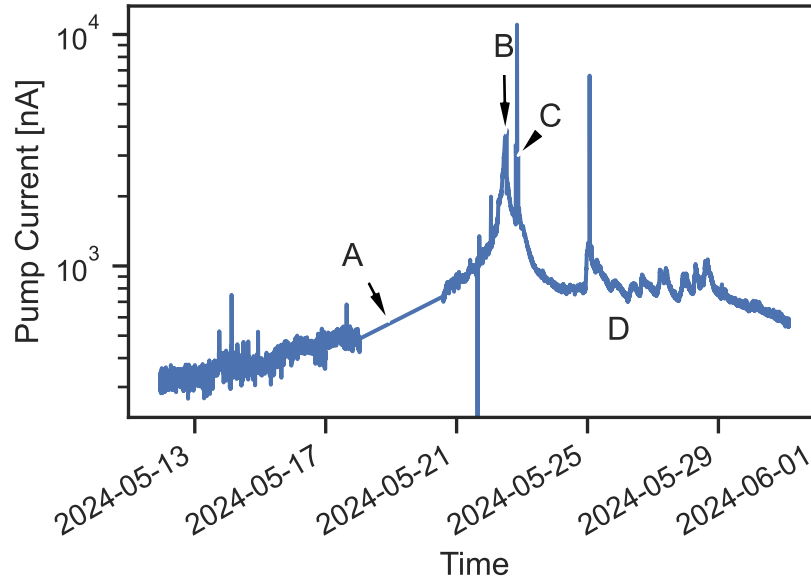


Figure 4.6: Ion pump current in the potassium 2D MOT in May 2024. The pressure increased slowly for some time and then began to show exponential behaviour. **A**: Ion pump read script failed, no data during this period. **B**: Peak ion pump current and the point at which the ion pump operating voltage was reduced to 3 kV. **C**: Arcing when the operating voltage was briefly restored to the original value of 5 kV. **D**: Arcing and jerking as the ion pump current drops again.

that leave cleaning residues on the viewport that react with the anti-reflective coating during bake-out [123, 124].

4.3.8 Sudden Rise of Ion Pump Current

In the SoPa vacuum system, there is no dedicated pressure gauge; instead, the pressure is inferred from the ion pump current readings. While this approach provides a rough estimate of the pressure, it may not be sufficient for accurate monitoring. In the potassium 2D MOT chamber, we occasionally have problems with the pressure in the chamber. In May 2024, we observed a gradual increase in pressure over time, which eventually accelerated exponentially. Figure 4.6 illustrates the ion pump current readings during this period. We suspected that the increase in ion pump current was due to conductive deposits within the ion pump. To address this, we reduced the ion pump operating voltage from 5 kV to 3 kV after turning off the oven. This adjustment stopped the upward pressure trend.

However, subsequent measurements of the leakage current showed an increase in the leakage current compared to the previous levels (see Figure 4.7). After the current readings had stabilised, the oven was switched

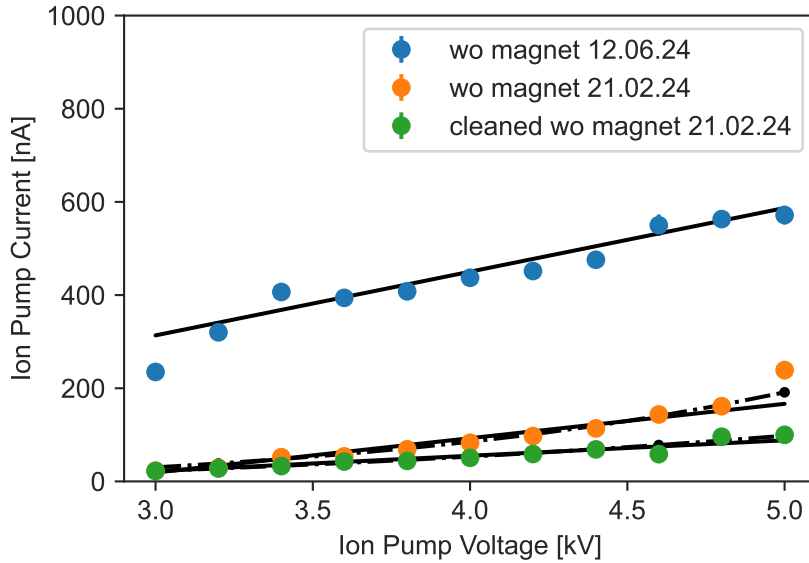


Figure 4.7: Leakage current measurements for the potassium 2D MOT ion pump. Leakage currents were measured before exponential current growth in February (orange and green) and after in June (blue). In February, the ion pump was cleaned by increasing the operating voltage several times to 6 kV for a maximum of five minutes (green). Note that the leakage current is measured without (wo) magnets installed.

back on and a new upward trend in pressure was observed a few days later. Further leakage current tests confirmed a continuing increase in leakage current. There are two types of leakage current, which differ in their dependence on the operating voltage: Linear dependence, caused by conductive deposits on the surface of the ion pumps. Exponential dependence, caused by sharp edges or protrusions on the electrodes. Although leakage current does not directly affect the pumping efficiency of the ion pump, it does affect the accuracy of the pressure readings, effectively leaving the system without reliable pressure monitoring.

Whilst the MOT continues to work well, indicating that pressures are likely to be within acceptable ranges, the loss of pressure indication means that vacuum problems cannot be ruled out if the MOT signal is lost. In addition, the ion pumps in the NaLi experiment have had to be refurbished on a regular basis, most likely due to the build-up of sodium and lithium [72]. Therefore, it is useful to keep the leakage current low, especially when the effort is low. It is possible to reduce the leakage current in the ion pump. Sharp edges on the electrodes can be softened by operating the ion pump at higher voltages for a short time, as specified by the pump supplier. This process can help to smooth the electrodes. While the conductive coating on the surface cannot be removed directly, oxidising the coating by flooding the system may help.

In the case of our potassium 2D MOT ion pump, the leakage current has a linear dependence on voltage, indicating that it is due to conductive deposits on the pump surface. Since similar problems are not observed with sodium, and potassium has a higher vapour pressure, it is likely that the coating is caused by potassium deposits. A possible solution is to create a cold spot near the pump arm to slow down the deposition of potassium on the ion pump surface.

4.3.9 *Curiosities in the Vacuum System*

The previous sections have focused on maintaining the cleanliness of the vacuum system. Most ultracold atom vacuum systems are rarely opened. However, during operation, atoms are evaporated into the vacuum chamber and spread along the walls.

In the SoPa experiment, we observed a thin layer of sodium almost everywhere in the 2D MOT chamber. This layer becomes thinner with increasing distance from the oven and increasing temperature. Directly above the oven there are three droplet formations (see Figure 3.5). As the vacuum was never broken, the deposits are all sodium, giving them a metallic, shiny appearance. In contrast, the potassium 2D MOT chambers showed no visible deposits, probably due to potassium's higher vapour pressure at room temperature, which makes it less prone to sticking to surfaces.

In the NaLi experiment, the vacuum system had to be opened relatively frequently and the oven had to be refilled on a regular basis. This resulted in significant evaporation of sodium and lithium atoms into the system. The vacuum system of the NaLi experiment revealed some unexpected discoveries. In addition to a thick layer of sodium carbonate, we discovered cauliflower-like deposits and a surprising green coating.

CAULIFLOWER-LIKE DEPOSITS

In the NaLi experiment, the oven had to be filled with a considerable amount of sodium on a regular basis, which means that a large number of atoms are distributed throughout the vacuum system. The system has to be flooded (nitrogen was used) to refill the oven. Water vapour, oxygen and carbon dioxide entering the chamber during the flooding process react with sodium and its products (see Equations 4.1, the chemical reactions are described in Section 4.3.4) to form thick white coatings. These coatings are most likely a mixture of all sodium products (oxides, hydroxides and carbonates) with the highest amount of sodium carbonate being the final product. Figure 4.5 I-L provide images of such coatings and formations, particularly fascinating is the

cauliflower-like deposition on a blind flange.

The coating of sodium carbonate, oxides and hydroxides does not in principle damage the vacuum system. However, the coating is hygroscopic and, due to its fractal structure, significantly increases the surface area, so in large quantities it can adsorb a significant amount of water, resulting in pseudo-leakage during pump-down as described in Section 4.3.3. The formation of cauliflower structures is an interesting fractal growth behaviour [125–127], unfortunately the cauliflower deposits grew in a part of the vacuum system that could not be observed during growth.

GREEN COATINGS

While thick white cauliflower-like deposits could be considered normal in the NaLi experiment, the experiment surprised with a dark green deposit after a new oven design was tested [72]. In the Figures 4.5 F-H images of the green oven are shown. Not only the large surface of the oven flange turned green, but also the sodium pipe towards the oven cup and the whole chamber after the oven (see Figure 4.5 G).

Lithium was also filled into the oven, but was not used during the experiments. The new oven design had a different geometry and was made of AISI 316L stainless steel instead of the AISI 304 stainless steel of the previous oven. During the relatively short test period, the system underwent a bake-out at 275 °C, followed by an operating temperature of 340 °C at the cup and 280 °C for the rest of the oven. After approximately two weeks of operation, the oven was removed due to poor performance [72], revealing the unusual green surface.

Green deposits have been reported before in the NaLi experiment, but only in the oven cup [110], another sodium experiment has also seen green deposits [128]. Both suggest that sodium salts may be responsible for the green colour. We tried to analyse the green coating further.

Lennart Singer was kind enough to analyse a sample of the green coating using energy dispersive X-ray spectroscopy (EDS). It is advantageous to dry the sample to reduce the background of the signal. However, the sample was so hygroscopic that it could not be dried prior to analysis. Analysis of the sample showed that oxygen, sodium, chromium, iron and aluminium are chemical constituents. We attribute the aluminium to the fact that we wrapped the green stove in aluminium foil before taking a sample of the coating.

In fact, AISI 316L stainless steel has a higher chromium content but is considered to be more corrosion resistant. Corrosion of AISI 316L stainless steel with liquid sodium has been studied [129–133] where small

amounts of oxygen lead to selective corrosion where sodium chromite $NaCrO_2$ is formed - sodium ferrite $NaFeO_2$ is unlikely. The corrosion studies are still of interest as the Gibbs free energy of sodium chromite has recently been measured [134]. The corrosion of liquid sodium has been studied at atmospheric pressure for different temperatures 500 K, 1000 K [131], 773 K, 873 K [132] and 923 K [130]. The experimental conditions are compared below.

In cold atom experiments three cases of green deposit near the oven cup have been observed. The green deposit occurs in 304 stainless steel containing 40 – 50 g of sodium and heated to 326 – 365 °C [110, 128], as well as in 316L stainless steel containing 20 g of sodium, where the green deposit occurred near the part heated to 450 °C, but also on parts that were at room temperature.

Although the pressures and temperatures are much higher than in the 600 – 723 K cold atom experiments, the selective corrosion forming sodium chromite is consistent with optical observations: Sodium chromite appears dark green [133, 134], sodium ferrite is green-brownish [133], while sodium oxide itself is white.

In the reported corrosion studies, oxygen dissolved in liquid sodium plays an important role. However, in the case of the cold atom experiments, corrosion occurred where sodium was vaporised and where the system was under UHV conditions, while temperatures were high enough for the sodium deposits to be liquid. It is also unknown whether the corrosion occurred during bake-out or normal operation. Possible sources of oxygen are micro-leakages at the flange, old sodium deposits, sodium oxide, hydroxide and carbonates which react with sodium. It could also be that sodium hydroxide, rather than liquid sodium, is responsible for the corrosion, although it is questionable how large quantities of sodium hydroxide could have gotten to the oven flange.

TWO-DIMENSIONAL MAGNETO-OPTICAL TRAP

This section describes the two-dimensional magneto-optical trap (2D MOT). The 2D MOT is the first cooling stage for the atoms and provides a flux of pre-cooled atoms for the 3D MOT. Its performance is therefore essential for the later stages. Recent work has shown that a 2D MOT is advantageous over a traditional Zeeman slower, since a comparable flux can be generated with a better collimated atomic beam and a more compact and easier to design experimental setup [42, 135, 136]. To optimise the 2D MOT for both species independently, they are separated in two different vacuum chambers. The setup for both species is largely identical, with the addition of a slower beam for the sodium 2D MOT.

The first section describes the 2D MOT setup (inspired by [42]), including the additional slower beam for sodium. A brief overview is given, followed by details of the laser beams and the magnetic field. The second section focuses on the optimisation procedure of the 2D MOT. In the next Chapter 6 the setup is critically evaluated.

5.1 2D MAGNETO-OPTICAL TRAP SETUP

5.1.1 *Brief Overview*

The 2D MOTs are set up in two separate chambers adjacent to the science chamber - see the Chapter 4 for more details. In each chamber, atoms from the oven are vaporised by heating the oven to 180 °C for sodium (70 °C for potassium) using a heating clamp¹. The oven consists of a blind vacuum cup filled with a freshly cracked glass ampoule of sodium (potassium). The 2D MOT is loaded transversely by an effusive oven beam. A 2D MOT slows down the atomic velocities in two directions, forming an atomic jet. In order to slow down and trap the atoms in both directions, a quadrupole magnetic field shifts the atomic transition, resulting in a spatially dependent force. The quadrupole field is generated by four stacks of neodymium magnets². Two counter-propagating laser beams for each cooling direction are needed to slow down the atoms. Figure 5.1 shows a section through the 2D MOT, with the laser beams indicated. The resulting atom jet out of the laser beam plane is sufficient for atom transfer into the science chamber, but the performance can be improved by using a near-resonant laser beam, the

¹ sealed mica band heaters from *Acim Jouanin* L34420C9A5

² *Eclipse* N750-RB

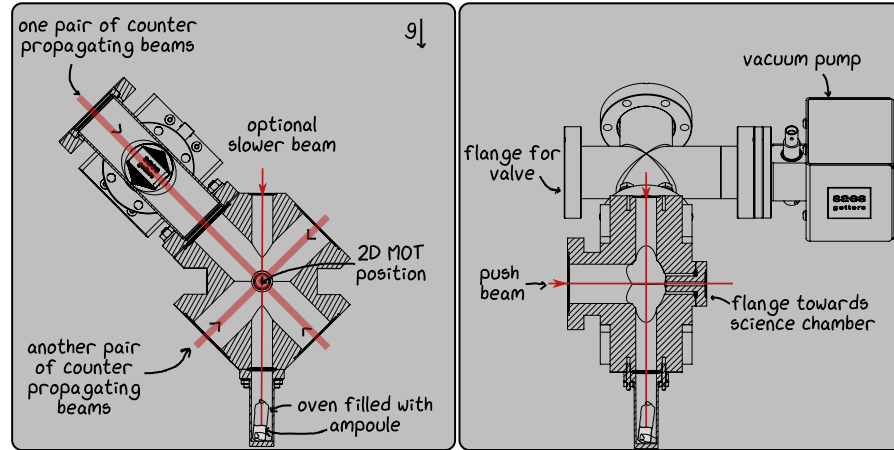


Figure 5.1: 2D MOT overview. **Left:** Cross-section of the 2D MOT plane. The oven is at the bottom of the 2D MOT, the MOT beams enter at an angle of 45° . **Right:** Cross-section through the push beam. The structure is extended on one side to provide space for a vacuum pump.

push beam, to push the atom into the science chamber [135]. The next subsections discuss the MOT beams in more detail, as well as the slower beam for sodium and the magnetic field.

5.1.2 2D MOT Beams

A 2D MOT requires two pairs of counter-propagating laser beams. While a common approach is to use two beams and retro-reflect them after passing through the chamber once [77], recent work has taken this laser power saving approach even further by using only a single laser beam in a bow-tie configuration [104, 137, 138]. In contrast, the SoPa experiment implements a 2D MOT with four independent cooling beams, which allows for sensitive adjustment of beam balancing and alignment at the cost of requiring more laser power.

The 2D MOT optics are mounted on a breadboard³, which allows the optics to be removed and the vacuum system to be retracted. Figure 5.2 gives an overview of the optics setup, while Figure 5.3 shows the detailed 2D MOT setup for sodium.

The 2D MOT light, containing both cooler and repumper light, is transferred from the laser table via a single mode polarisation maintaining fibre, coupled out⁴, polarisation cleaned, followed by a beam sampler which removes a small fraction of the light from the beam path. The small fraction of light is then directed to a photodiode for power monitoring and a *Fabry-Pérot interferometer* to monitor the repumper

³ Thorlabs MB3045/M

⁴ We used mounted achromatic doublets from Thorlabs AC254-30-A-ML

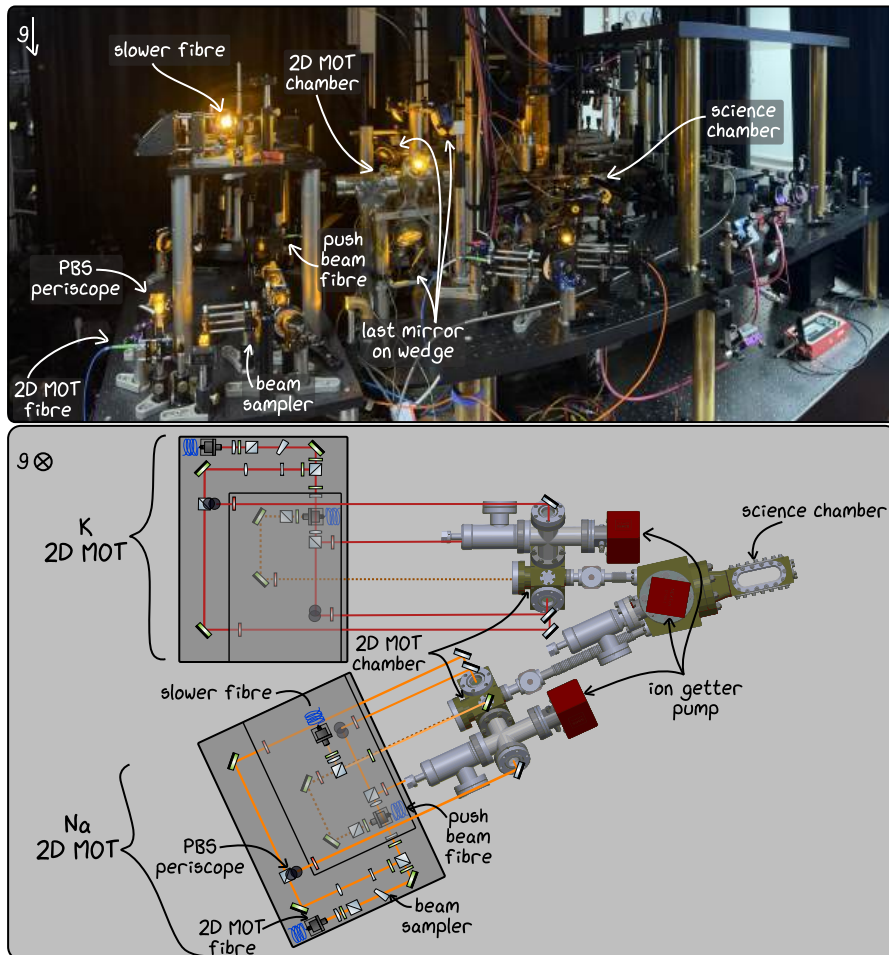


Figure 5.2: **Upper part** Image of the experimental table in the laboratory. **Lower part** shows an overview schematic of the 2D MOT optics and the vacuum system. The 2D MOT optics are mounted on two stacked breadboards in front of the 2D MOT chambers. The optical setups are the same for both species, except for an additional slower beam used for sodium.

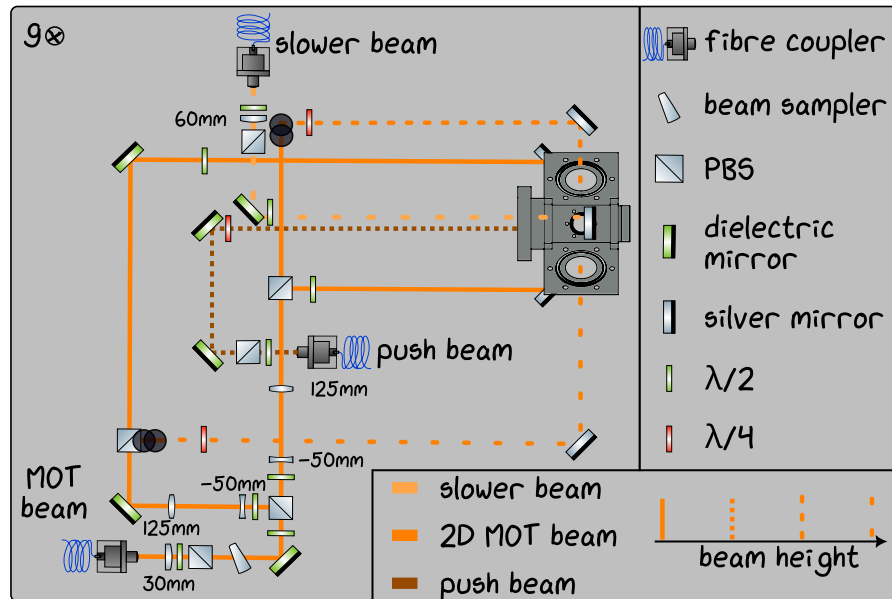


Figure 5.3: 2D MOT optics for sodium - potassium is the same without the slower beam. The MOT light is polarisation cleaned and a beam sampler is used to obtain a small fraction of the light for monitoring purposes. The light is split into the two beams which are magnified by a telescope and split into counter-propagating beam pairs. The circular polarisation is adjusted with a quarter wave plate in front of the last mirror. The final mirrors are mounted near the chamber on freestanding posts or chamber posts. The different line styles indicate different beam heights, the higher the beam the more space between the lines. For better visibility, the upper parts of the push and slow beams are slightly offset. The push beam and slower beam are both polarisation cleaned and directed into the 2D MOT chamber.

Table 5.1: 2D MOT beam parameters. Detuning of the transition and powers for sodium (potassium). The cooling detuning refers to the $F_g = 2$ to $F_e = 3$ transition and the repumper detuning refers to the $F_g = 1$ to $F_e = 2$ transition. Values taken from [1].

	Detuning [MHz]	Power [mW]	beam diameter [mm]
2D MOT cooling	-42 (-37)	130 (300)	17 (13.8)
2D MOT repumper	-23 (-22)	65 (150)	17 (13.8)
push beam (cooling)	-12 (-37)	5 (3.5)	2.5 (2)
Slower cooling	-108	330	13.6
Slower repumper	-104	83	13.6

power. The main beam is split into two beams, then both beams are expanded to a beam diameter of 17 mm for sodium (13.8 mm for potassium). The beams are then split again into the opposing beams. In this way, the splitting waveplates adjust the beam balance between the two beam pairs and the two counter-propagating beams. For precise adjustment in the counter-propagating beam pairs, the waveplates are mounted in precision rotary mounts⁵. The axis of the MOT beams is rotated 45° from the z-axis so that the two counter-propagating beams must be at different heights. Periscopes are therefore used to change the height of the beams. On an upper breadboard⁶, the beam is folded back to the horizontal plane and directed into the 2D MOT chamber. The polarisation is adjusted with a quarter wave plate in front of the last mirror. This waveplate placement was chosen due to space limitations and to avoid heating the waveplate. To reduce the polarisation change of the mirrors, the last mirror is a silver mirror.

All the optics, except for the last mirrors, are mounted as units on a breadboard so that they can be removed together if the vacuum chamber needs to be translated. Two stacked breadboards are used to mount the optics. The bottom one splits the light and directs it to the lower viewports. On the upper breadboard, the optics are mounted from above and below. The optics for directing the light to the higher viewports (pumping tee 2D MOT and slower viewport) are mounted at the top, and the lower ones (2D MOT viewport and push beam) are mounted at the bottom. The Table 5.1 summarises the laser beam characteristics and frequencies for the 2D MOT. For the sodium repumper, light is generated using an electro-optic modulator (EOM), which generates two sidebands of the carrier frequency. The EOM is chosen so that the frequency shift of the sideband is exactly the ground state splitting (≈ 1.7 GHz). The ratio between the cooler and the repumper is adjusted by the power, but cannot be measured directly because the



The EOM controllers have a lock that locks the resonator to minimal losses, which means that it is effectively locking the power rather than the frequency. This is not ideal.

⁵ Thorlabs CRM1PT/M

⁶ Thorlabs MBH4560/M

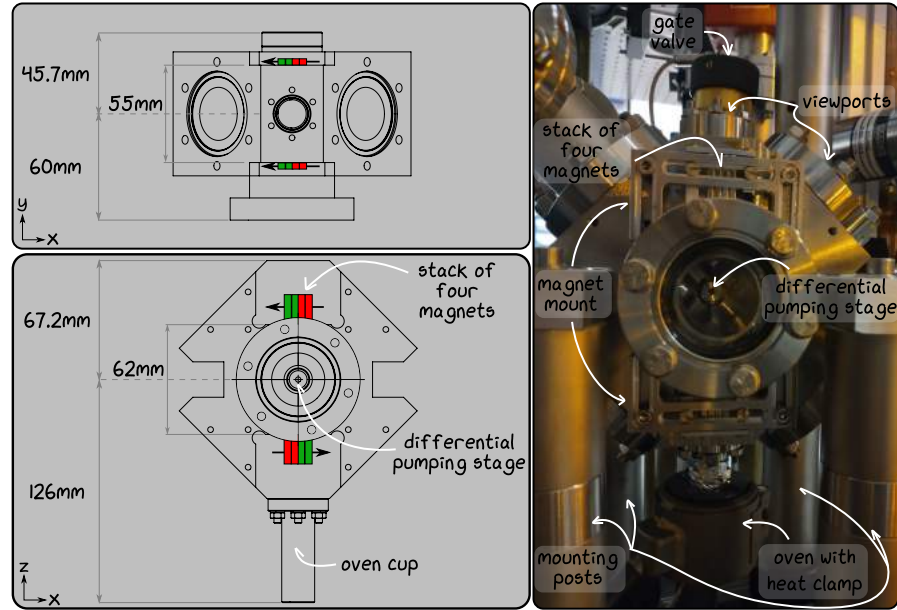


Figure 5.4: The position of the magnet stacks in the xz - and xy -planes is shown on the **left**. On the **right** is an image of the potassium 2D MOT setup showing the mounting bracket of the magnet stack.

light overlaps. Therefore a *Fabry-Pérot interferometer* is needed.

For sodium, an additional laser beam through the top viewport, the slower beam, improves the 2D MOT performance. The additional beam is far detuned and the permanent magnets are positioned so that a changing magnetic gradient along the vertical axis acts like a tiny Zeeman Slower [42, 76, 77].

5.1.3 Quadrupole Magnetic Field

To ensure the spatial dependence of the cooling force around the centre line of the magnetic trap, a quadrupole magnetic field is required. To generate the quadrupole magnetic field, we follow the approach of Lamporesi et al. [42] and use four stacks of neodymium bar magnets with 9 (4) magnets per stack generating a gradient of 60 G/cm (30 G/cm) for sodium (potassium). The magnets have a maximum working temperature of 80°C⁷, which appeared to be a problem for the sodium 2D MOT (see Chapter 6).

The titanium 2D MOT chamber has a cut-out for mounting the magnets. The first iteration had a simple clamping solution. To mount the magnets, we used a magnetic screwdriver to hold the magnets in place, then fixed them to the chamber and simply pulled out the screwdriver. For the second iteration, the magnets are placed in a sleeve mounted

⁷ Eclipse N750-RB

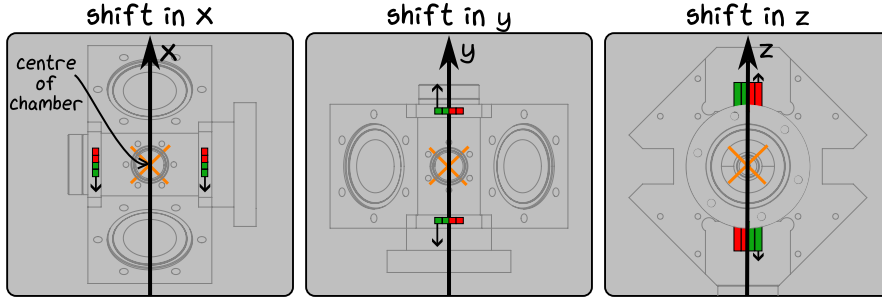


Figure 5.5: Visualisation of how the magnets are displaced in the simulation. The position of the magnets is varied relative to the centre of the chamber, indicated by the orange cross.

on elongated slots. These allow the stack of magnets to move independently in the vertical and horizontal directions. So far, the second iteration has only been implemented for potassium. Figure 5.4 shows the positions of the magnets and an image of the mounted magnets in their mount on the potassium 2D MOT chamber. Technical drawings of the second iteration magnet mount are provided in Appendix A.7.

To estimate the needed number of magnets, we calculate the magnetic field at position \mathbf{r} , where the magnetic field for a magnet with dipole moment \mathbf{m} at position \mathbf{r}_0 is given by [139]

$$B(\mathbf{r}) = \frac{\mu_0}{4\pi} \left(\frac{3(\mathbf{r} - \mathbf{r}_0) [\mathbf{m} \cdot (\mathbf{r} - \mathbf{r}_0)]}{|\mathbf{r} - \mathbf{r}_0|^5} - \frac{\mathbf{m}}{|\mathbf{r} - \mathbf{r}_0|^3} \right). \quad (5.1)$$

In our simplified model we calculate the magnetic field for each magnet. As reported in [139], the absolute value has to be scaled to fit the experiment due to magnetisation effects. Therefore, we focus on changes in the magnetic field due to the number of magnets or different placement of the magnets. Figures 5.6 and 5.7 show how the magnetic field responds to different positions of the magnets. In Figure 5.6 the magnetic field is plotted along the slower axis and in Figure 5.7 the magnetic field is plotted along a MOT beam axis. The different figures show the change in magnetic field for moving the magnets along the y-axis/beam axis (subfigure B), the z-axis/slower axis (subfigure C) and the x-axis/horizontal axis between the magnets (subfigure A) (see Figures 5.5 and 5.4). In subfigure A, all magnet stacks are moved in the same direction with respect to the chamber centre, while the distance between the stacks is kept constant. In subfigures B and C, all magnets are moved towards or away from the chamber centre by the same amount, so the distance between the magnets changes along this direction.

Both the magnetic field along the slower beam and along the MOT beam show similar behaviour. Moving the magnets along the x-axis has little effect on the magnetic field. However, along the y- and z-axes,

where the distance between the magnet stacks is changed, is the effect significant. Interestingly, the distance between the magnets along the thrust beam (y -) axis is the most sensitive and shows huge differences in magnetic field amplitudes. The position of the magnets along the push beam direction is limited and fixed by the mounting of the magnets.

5.2 2D MOT OPTIMIZATION

The 2D MOT is used to generate an atomic beam for the 3D MOT. The loading of the atoms $\frac{dN(t)}{dt}$ in the 3D MOT can be described by [140]

$$\frac{dN(t)}{dt} = L - \alpha N(t) - \beta N^2(t), \quad (5.2)$$

where L describes the loading rate, the linear loss term corresponds to collisions with the background gas and the quadratic loss term to intra-MOT collisions. The latter term depends on the atomic density and the trapping volume and becomes significant at high atomic densities. In the following, the quadratic term is neglected as we are in a regime of low atomic densities. Neglecting the intra-MOT collisions Equation 5.2 simplifies to

$$\frac{dN(t)}{dt} = L - \alpha N(t), \quad (5.3)$$

with the solution

$$N(t) = \frac{L}{\alpha} (1 - \exp(-\alpha t)). \quad (5.4)$$

A typical loading of a sodium dark SPOT with the fitted Equation 5.4 is shown in Figure 5.8. An absorption image is taken after a certain loading time. The atomic number is estimated from the signal as described in 8.1. Note that at the time the data were taken the atomic number in the MOT was not stable, at that time good values obtained in the SoPa experiment were in the order of $2 - 5 \cdot 10^8$ atoms. The instabilities were caused by drifts of various components, most likely caused by environmental changes, e.g. the temperature of the laboratory. Since the 2D MOT affects the loading rate L but not the atom losses, the 2D MOT can be optimised to the loading rate of the 3D MOT loading.



In the BECK experiment, the 2D MOT, optimised for efficient loading into the 3D MOT, is barely visible. While a visible signal is helpful in the beginning, performance is what really counts later on.

Since it is not very practical to optimise all the parameters by taking data from an entire load curve and fitting the model to it, the linear regime of the load curve is a good estimate of an efficient load. Therefore, the shutter for the 3D MOT light is connected to a function generator. The frequency is set so that only the linear loading regime is visible to us. The fluorescence of the MOT is collected as a signal on a photodiode. The 2D MOT is optimised to increase the linear slope. Initially, the beam powers are set so that all beams have

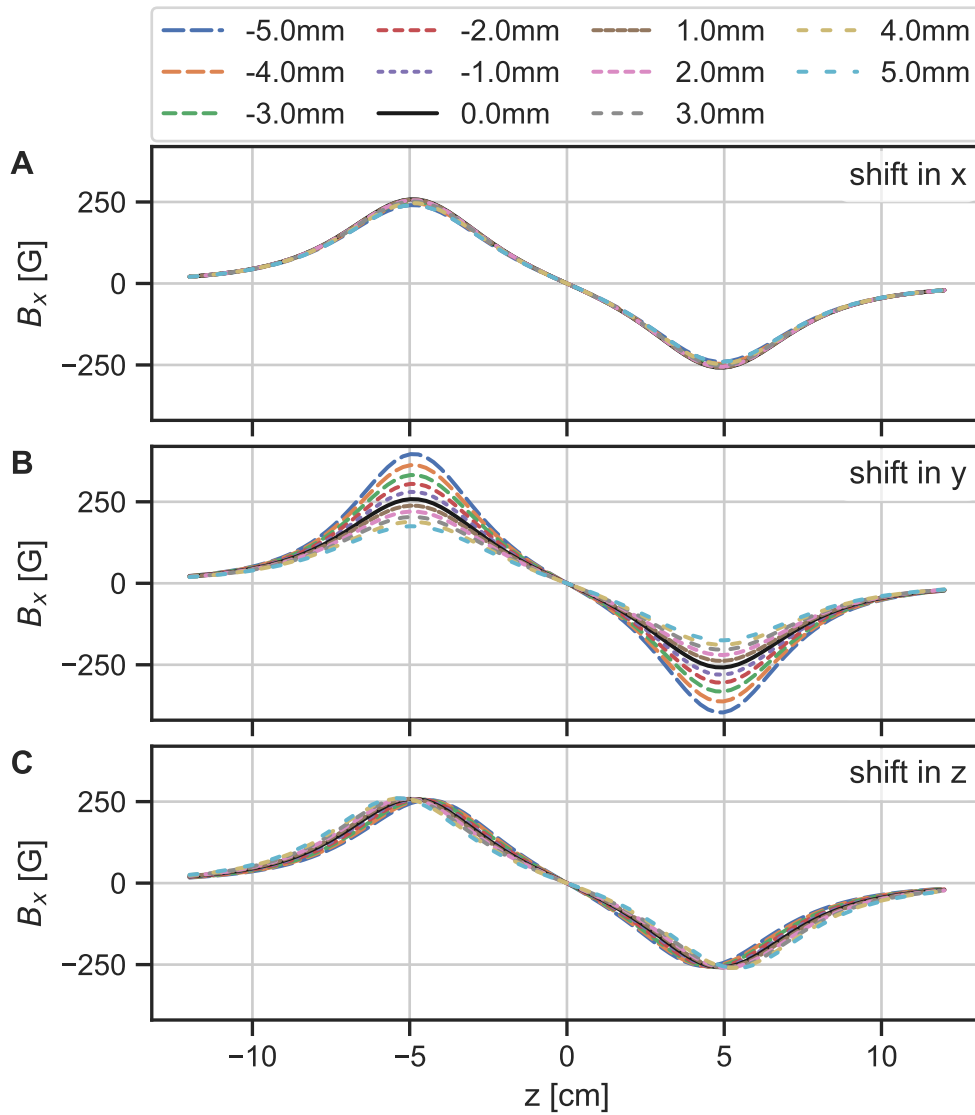


Figure 5.6: Sensitivity of the magnetic field along the slower axis. For each axis, all the magnets are moved in the same direction with respect to the centre of the chamber, e.g. all the stacks are moved towards or away from the centre. A set of distances results in a set of curves. **A:** Moving along the x-axis moves all four magnets, the distance between the magnets remains constant. **B:** Move along y-axis. The distance between the magnet stacks along the beam changes. **C:** Move along the z-axis. Changes the distance between the magnet stacks along the slower beam.

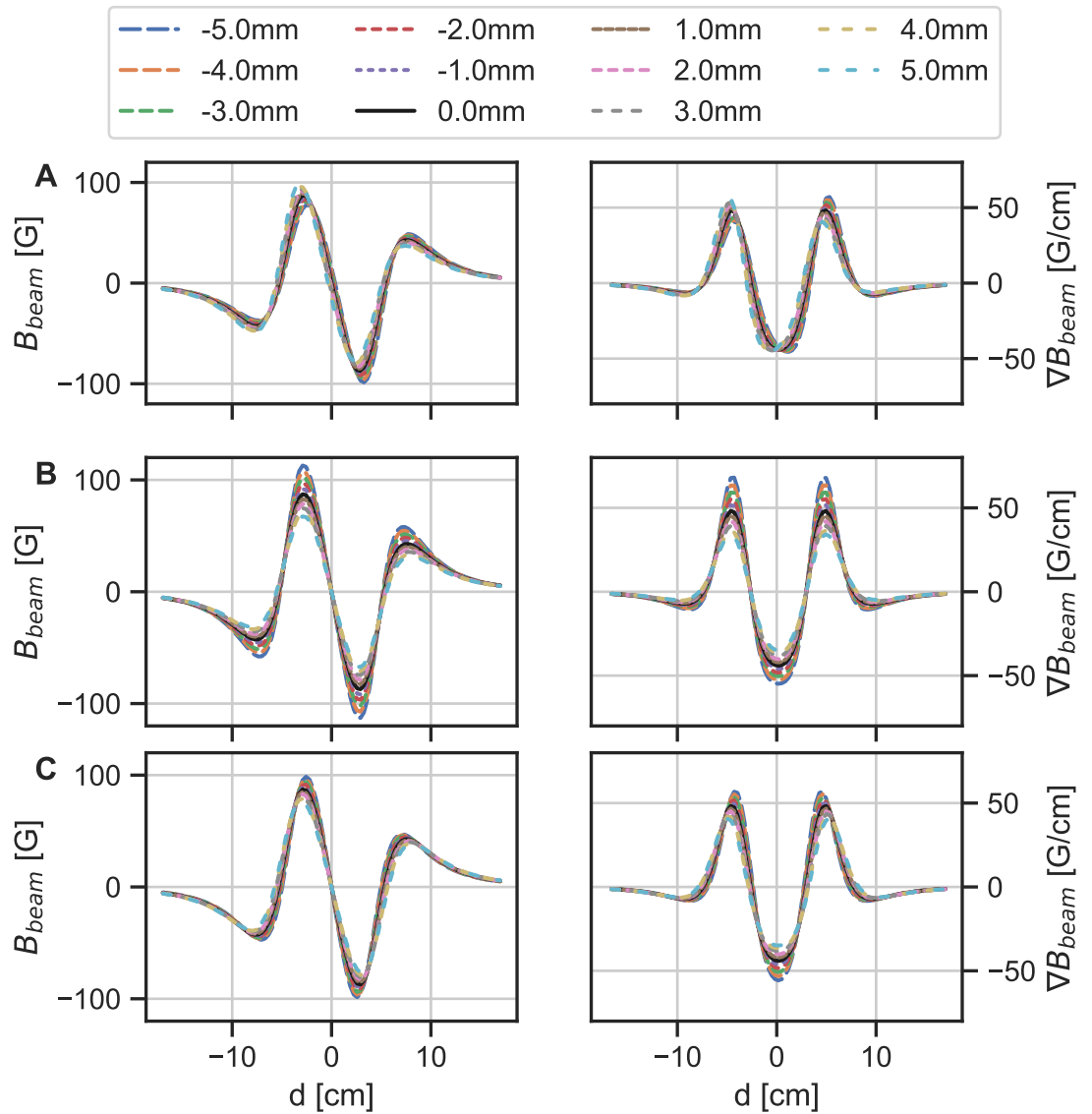


Figure 5.7: Sensitivity of the magnetic field along the MOT beam axis. For each axis, all the magnets are moved in the same direction with respect to the centre of the chamber, e.g. all the stacks are moved towards or away from the centre. A set of distances results in a set of curves. **A:** Moving along the x-axis moves all four magnets, the distance between the magnets remains constant. **B:** Move along y-axis. The distance between the magnet stacks along the push bar changes. **C:** Move along the z-axis. Changes the distance between the magnet stacks along the slower beam.

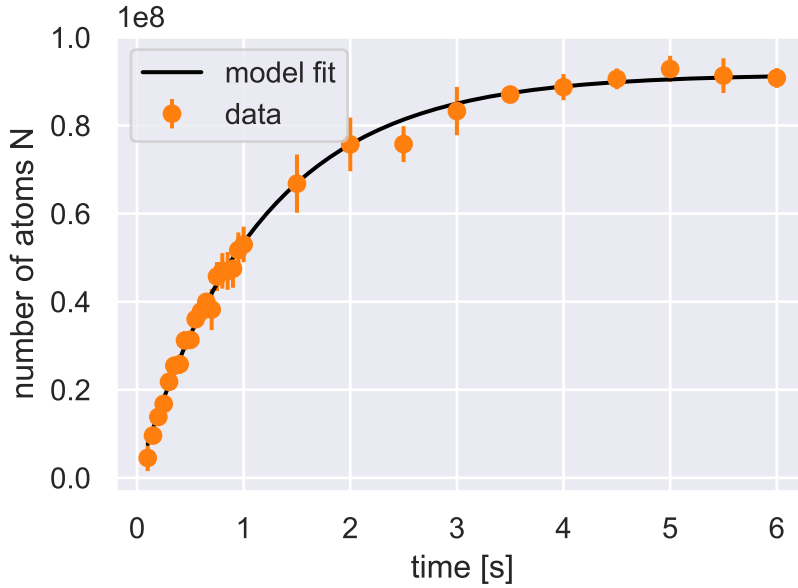


Figure 5.8: MOT loading curve. Atom number is extracted by summing over the ROI of the image. Data points (orange) are the averaged results of three runs. Initially, the loading is linear, while for longer times the loading rate slows down until a steady atomic number is reached. The resulting atomic number depends on loss collisions with the background gas and intra-MOT collisions. A model fit (black) of the Equation 5.4 to the data is performed.

the same power and all beams are in the centre of the 2D MOT viewports. The following settings are optimised in iterations: last mirror, push beam alignment, power balance, cooler to repumper ratio, detuning and powers (for sodium also the slower beam parameters). Of all these parameters, the push beam pointing proved to be very sensitive to the 3D MOT performance.

In the following, the 3D MOT loading rate is determined for some parameters of the sodium 2D MOT.

POWER AND COOLER DETUNING IN 2D MOT BEAMS The influence of the total power of the 2D MOT beams on the 3D MOT loading rate is shown in Figure 5.9 A. The loading rate clearly increases with increasing beam power. Close to the maximum achievable power, the loading rate seems to settle or to decrease. We cannot exclude that this is due to fluctuations of the measured loading rate. At the moment we are still working with the maximum power we can achieve. Figure 5.9 B shows the effect of the cooler detuning of the 2D MOT beams, for which a clear maximum can be found.

OVEN TEMPERATURE Figure 5.10 shows the effect of oven temperature on the 3D MOT loading rate. Since the vapour pressure of sodium

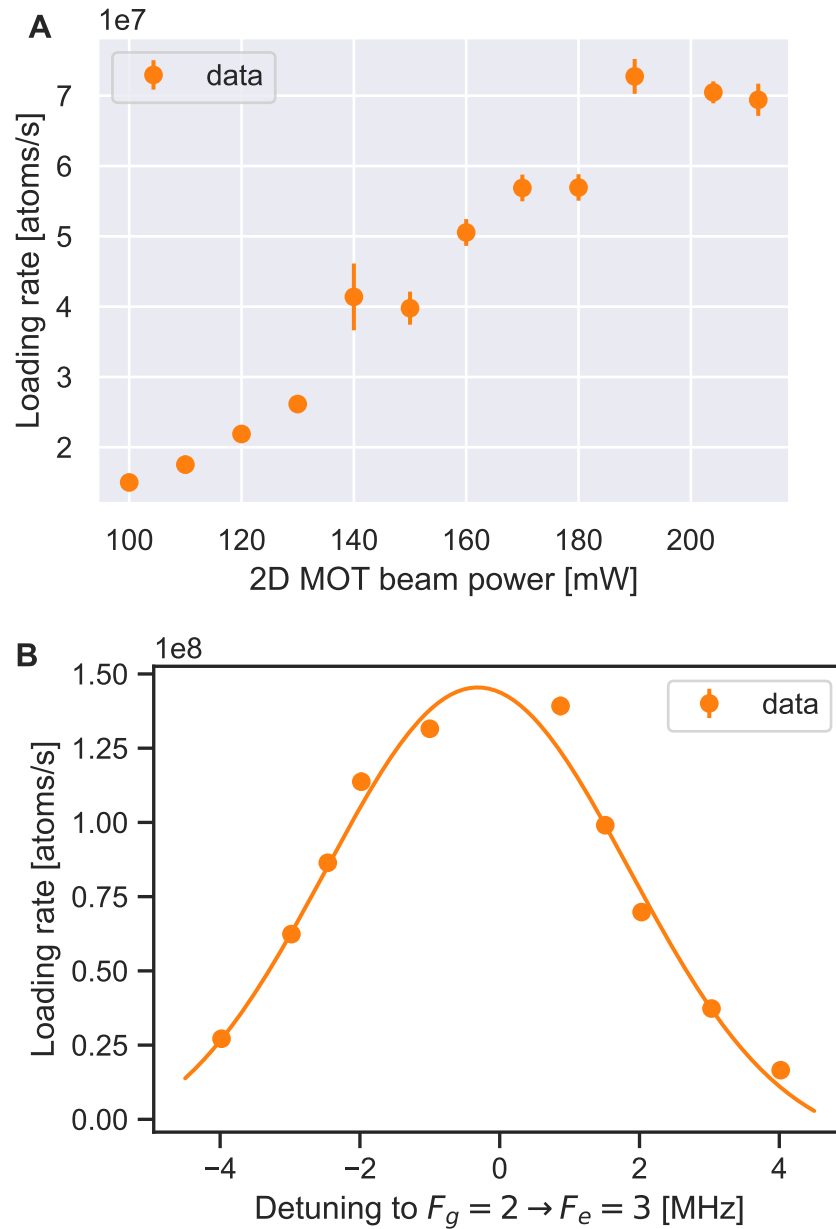


Figure 5.9: MOT loading rate as a function of total 2D MOT beam power **A** and cooler detuning **B**. The cooler to repumper ratio is assumed to be constant. For each data point the loading rate is extracted by a model fit (eq. 5.4) to the average of three MOT loading curves as explained for Figure 5.8. **A**: At higher powers the loading rate seems to settle as reported in [135, 136]. Unfortunately, higher powers could not be achieved. At least in the range of powers measured, the loading rate is better at higher powers. **B**: A clear maximum can be found for the cooler detuning. To help the eye, a Gaussian is fitted to the data.

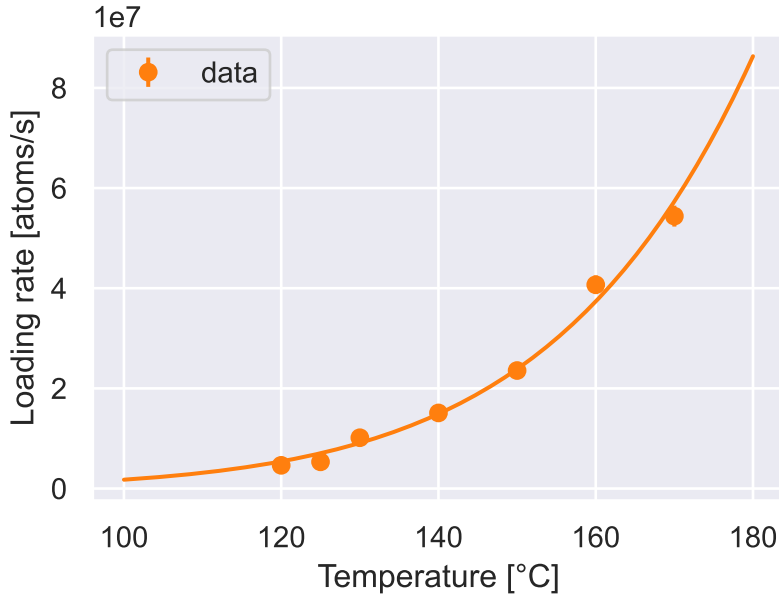


Figure 5.10: MOT loading rate as a function of oven temperature. For each data point, the loading rate is extracted by a model fit (Equation 5.4) to the average of three MOT loading curves, as explained for Figure 5.8. An exponential function is fitted to the data for eye guidance. At higher temperatures collision processes will reduce the loading rate [42, 135, 136].

depends exponentially on temperature, [57] an exponential function is fitted to the loading rate. The dependence fits well with the exponential fit. In [42, 135, 136] it was shown that at higher temperatures the loading rate is damped due to collisions with the hot atoms from the oven and the background gas. We run the oven at rather low temperatures because we have problems with sodium deposits on the viewports, from previous measurements we know that the loading rate settles at an oven temperature of 210 °C.

SODIUM SLOWER BEAM For sodium, an additional slower beam is used which significantly enhances the performance of the 2D MOT.

As the slower beam has to be far detuned and two lasers are available for sodium light, the slower beam was first optimised with a free-running laser. In contrast to the experiment [42], where the slower beam has a detuning of -304 MHz, the best performance was found at frequencies closer to the atomic transition with a detuning of -104 MHz (see Table 5.1).

At the time of the measurement, the laser configuration was set up with two lasers. One is stabilised to an atomic transition using saturation absorption spectroscopy, and the other is frequency stabilised

to an offset with respect to this first laser. The one stabilised to the atomic transition provides the light for all the paths except the slower path, which is provided by the second laser. Details of the laser table can be found in [1]. Meanwhile, the laser system is being updated so that the slower light is generated by an AOM pass. Details of the new setup can be read in [71].

Figure 5.11 shows the dependence of the 3D MOT loading rate on slower beam parameters (beam power and detuning). In A the detuning is scanned for different power settings. A Gaussian is fitted to each data set for eye guidance. The best loading rate performance can be achieved at higher, slower beam powers where the system is more sensitive to detuning than at lower, slower beam powers. In B, a contour plot is shown using the Gaussians fitted from A. It is clear that the best local settings lie on a branch that achieves the global maximum for higher beam powers. Unfortunately, we could not reach higher beam powers where saturation of the loading rate is expected [42]. We are still working at the maximum power we can achieve. We attribute the decrease in the loading rate for 390 mW compared to 380 mW to system fluctuations, we could not confirm 390 mW as the optimum power.

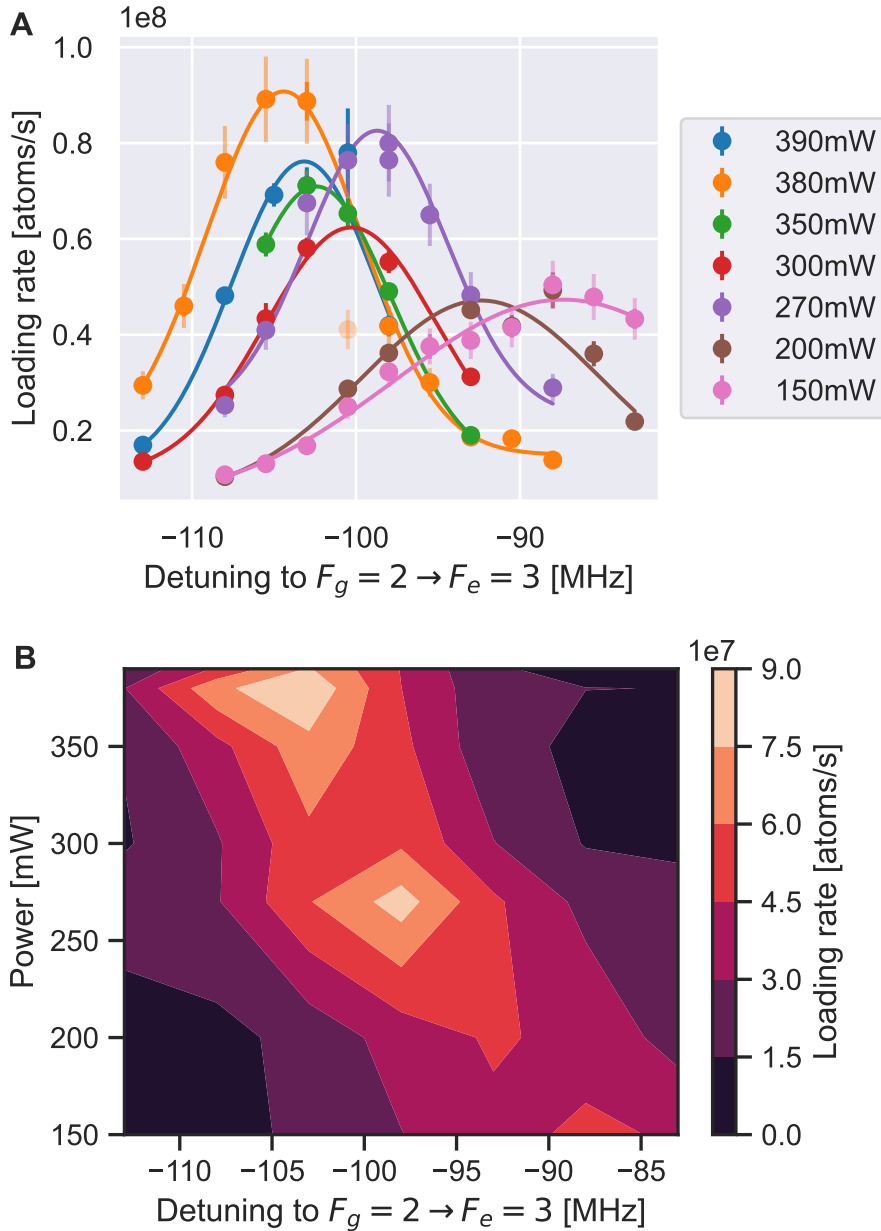


Figure 5.11: MOT loading rate as a function of slower beam detuning and slower beam power. The cooler to repumper ratio is assumed to be constant. **A:** For each data point the loading rate is extracted by a model fit (eq. 5.4) to the average of three MOT loading curves as explained for Figure 5.8. The detuning is sampled over several powers. A Gaussian fit is performed on each data set. Depending on the power, the best performing detuning shifts. For low powers the performance becomes less sensitive to detuning, while the overall performance also drops. **B:** For better visualisation of the two scanned parameters, a contour plot is made using the eye-guiding Gaussian fitted to the data in **A**. There appears to be a linear relationship between detuning and beam power for the local maximum, while the global maxima are reached at high powers. Unfortunately, higher powers could not be obtained.

CRITICAL DISCUSSION OF THE EXPERIMENTAL SETUP

This chapter critically discusses the experimental setup. The SoPa experiment was designed to overcome the problems encountered in the NaLi experiment. A major challenge for NaLi was the coupling of the two atomic species at different stages of the experiment. In addition, the NaLi experiment faced vacuum-related problems that were time-consuming to solve. [72, 83, 110]

In response, the SoPa vacuum system was designed to separate the two atomic species. The system was designed to be mounted on a translation stage so that it could be easily retracted to address vacuum issues in the science chamber without having to dismount the optics around it.

In recent years, a 2D MOT has proven to be a compact, simple and effective alternative to Zeeman slower setups and has been realised for more and more atomic species [42, 135, 136, 138, 141]. Our 2D MOT setup was strongly inspired by Lamporesi et al. [42] and slightly modified. To structure the discussion, this chapter is divided into three main sections: separation of atomic species, vacuum system on a translation stage, and modifications to the 2D MOT chambers and optics.

6.1 SEPARATION OF THE ATOMIC SPECIES

The challenge of coupling two species is a major concern in mixture experiments. For example, in the NaLi experiment, the coupling of two atomic species occurred at different stages: in the oven region and on the optical side of the laser table.

The use of a combined oven for both species requires a compromise in oven temperature, especially when dealing with significantly different vapour pressures. In the NaLi experiment, the two species were mixed together from two oven cups separated by a differential pump stage, which allowed independent adjustment of temperature and flux for the two atomic species. To avoid clogging of the differential pumping stage and back diffusion from the other species, the nozzle (450 °C) and the oven cups (Na: 365 °C, Li: 380 °C) were heated to high temperatures [83, 110, 142] and cooled down at night to save atoms. Unfortunately, this approach resulted in an inefficient use of the reservoir, as the oven had to be filled with 50 g of sodium and 25 g of lithium [72, 83, 110]. The oven in the NaLi experiment had to be replaced frequently due

to several problems: clogging due to sodium and lithium deposition, degradation of high vacuum conditions due to reactive alkali metals, and mechanical stress from repeated heating and cooling cycles to save atoms. In addition, vacuum components such as ion pumps were degrading and the nickel-sealed flanges required specific maintenance to repair the worn knife edge.

On the optical side, the use of the same optical fibre to transmit the light from both species to the experiment meant that it was not possible to optimise either species independently on the experimental side.

In the SoPa experiment, great care was taken to ensure the separation of atomic species to the greatest extent possible. This process began with the use of two separate 2D MOT chambers at the source, which could be individually optimised and maintained, as implemented in other experiments [143]. The separation was meticulously maintained throughout the 3D MOT optics up to the final mirror [1]. This thorough separation of atomic species has proven to be extremely beneficial, allowing the sequential addition and maintenance of species without disrupting the alignment of those already in place.

6.2 VACUUM SYSTEM ON A TRANSLATION STAGE

When a vacuum problem requires bake-out, the affected section of the vacuum system must be evenly wrapped with aluminium foil and heating bands. In many experiments, heat sensitive optics are mounted close to the science chamber, leaving insufficient space to properly wrap the system. As a result, these optics must be removed and then reassembled and realigned after bake-out. Ideally, the oven change should not affect the UHV vacuum region; however, faulty valves can necessitate bake-outs in areas not originally intended for such procedures.

To facilitate potential bake-outs, the SoPa vacuum system is mounted on a translation stage, allowing the science chamber to be pulled out of the optics. To maintain atomic separation, the 2D MOTs are angled towards the science chamber, creating spatial challenges for the 2D MOT optics. To overcome these challenges, bellows of different lengths were chosen to connect the 2D MOT chambers to the science chamber.

The ability to move the translation stage imposes several constraints on further constructions. Although all constraints have been solved so far, the need to retain this capability is often questioned. For the 2D MOT optics, a compromise has been made where the translation stage is blocked by the posts supporting the 2D MOT optics breadboard. Therefore, in order to move the translation stage, the 2D MOT optics breadboard and one of the posts must be removed. Initially, another

justification for the translation stage was to allow the science chamber to be pulled out for direct measurements at the atomic position. However, this feature has not been used due to the considerable effort required to remove the 2D MOT optics.

Overall, the translation stage is an advantageous option for solving large vacuum problems. However, it causes some limitations and the travel range cannot be kept completely free. This limitation reduces the potential benefits of the translation stage. However, if a bake-out of the science chamber is required, removing the blocking 2D MOT optics is far less disruptive than disassembling the entire MOT and dipole optics. To date, no vibrational instabilities have been noticed as a result of the vacuum system being mounted on a translation stage.

6.3 2D MOT CHAMBER

The design of the 2D MOT chamber for the SoPa experiment was initially inspired by Lamporesi et al. [42], but underwent several modifications. While Lamporesi et al. used a CF40 cross, the SoPa vacuum chamber was made more compact by using a bulk material with a cut-out for direct magnet mounting. This setup was intended to save space, but the actual benefits of these changes are debatable.

In line with the trend towards more compact ultracold atom experiments, we aimed to reduce the size of our setup. Using the 2D MOT design from [42] as inspiration, we were able to reduce the overall length of the experiment from 2.5 m in the NaLi experiment to 0.8 m. This reduction frees up more space on the experimental table for optics, which is useful, especially when sharing space with another experiment. However, this reduction also presented significant challenges and may not have been the most practical decision.

One challenge is accessing certain parts of the system. For example, the assembly of a gate valve on a super-short nipple is a one-time, time-consuming task, but the installation of the oven is a recurring event. The design, which maximises the inside diameter of the oven, resulted in a slightly larger outside diameter for the CF16 tube. This means that the nut is extremely close to the oven wall, making it difficult to tighten (normal size washers are too large). In addition, the 2D MOT chamber is mounted on four 1.5-inch posts which restrict the working angle of a standard wrench, making assembly cumbersome.

In addition to the challenging and time-consuming oven assembly process, the small diameter of the oven only allows 1 g ampoules to be filled, resulting in a shorter operating cycle before the oven needs to be refilled.



The linear translation stage is also used in a new lithium experiment in Selim Jochim's group [104]. They may also report on the stability of the stage in the future. Another stage is used in Manuel Endres' group in a strontium tweezer experiment [144].

The small oven diameter, allowing only for the use of 1g ampoules, means shorter operating cycles and more frequent refills. Theoretically, 5g should just fit in, however our 5g ampoules had a slightly larger diameter and consequently did not fit in. This adds to the operational burden and may outweigh the intended benefits of the compact design. However, there is enough space to replace the current oven with a CF40 oven cup, which could be connected using a CF40 to CF16 adapter nipple.

In addition, the sodium and potassium chambers have species-specific problems that pose additional challenges. The issues discussed in the following sections suggest that the design changes may not be as beneficial as originally thought.

ISSUES AROUND THE SODIUM CHAMBER

Particularly with sodium, which has a fairly high melting point, the viewports can easily become coated with sodium and eventually become blocked (see Figure 4.5 D). We have tried three approaches to solve this problem:

LIGHT-INDUCED ATOM DESORPTION (LIAD) Our first approach was to use light-induced atomic desorption with a diffuse 1 W UV light. Unfortunately, this method was ineffective in cleaning the viewports and did not help to keep them clean for long periods of time. However, we observed that leaving the 2D MOT lights on reduced the coating effect at the beam positions.

INCREASING DISTANCE TO VIEWPORTS Another possible solution is to modify the setup of the 2D MOT chamber by increasing the distance between the chamber and the viewports. This can be achieved either by adding a nipple between the vacuum chamber and the viewport, or by replacing the viewports with *Housekeeper* viewports, which we have considered mainly because of their different sealing technique, which may be less vulnerable to corrosion (more details in Section 4.3.6), but the optical quality needs to be tested. As it is not feasible to break the vacuum just to replace the viewports, we are keeping this option in mind for when the oven needs to be refilled. Additionally, replacing the CF16 oven cup with a CF40 oven cup and a CF16 to CF40 adapter nipple would also increase the distance.

HEATING THE VIEWPORTS We are currently using this third approach to heating the viewports. The two viewports that experience the most significant coating are the upper CF40 viewport, which is mounted directly on the chamber, and the CF16 viewport, which is

directly in line of sight of the oven. However, heating only these two viewports will result in the coating of the lower viewports within approximately one year.

Heating all the viewports is not currently an option because the permanent magnets would get too hot, and cooling them is not feasible due to space constraints. In addition, mounting the magnets out of direct contact with the chamber changes their spacing, which is critical in the most sensitive direction of displacement (see Figures 5.6 and 5.7).

The neodymium magnets¹ currently in use have an operating temperature limit of 80 °C. Higher intrinsic coercivity (Hci) values have been considered to allow higher operating temperatures.

In the future we plan to replace our magnets with Samarium Cobalt (SmCo32) magnets², which can operate at temperatures up to 350 °C and should provide similar magnetisation. Although not available as stock items, these magnets can be custom manufactured. To ensure compatibility with the existing mounts and to match the magnetic moment, magnets with dimensions of 10 × 25 × 3 mm³ have been purchased.

To characterise the magnetic moment of the new magnets, a magnet was mounted on a linear translation stage and a magnetic field sensor³ was moved along the stage. The magnetic field sensor provides a linearly scaled output voltage with a conversion factor of 1 V/G and an error of 0.5%. The magnetic field was measured at different distances along the magnetisation axis, as shown in Figure 6.1. A stack of three magnets is measured to average out the fluctuations of the magnets. The magnetic field at position \mathbf{r} of a magnet with a dipole moment m at position \mathbf{r}_0 is given by [139]

$$B(r) = \frac{\mu_0}{4\pi} \left(\frac{3(\mathbf{r} - \mathbf{r}_0) [\mathbf{m} \cdot (\mathbf{r} - \mathbf{r}_0)]}{|\mathbf{r} - \mathbf{r}_0|^5} - \frac{\mathbf{m}}{|\mathbf{r} - \mathbf{r}_0|^3} \right). \quad (6.1)$$

A fit to the measured data resulted in an average magnetic moment of $m = 0.49(1) \text{ A m}^2$ and with a volume of 10 × 25 × 3 mm³ a magnetization of $M = 6.5(1) \cdot 10^5 \text{ A m}^{-1}$. This result is smaller than the company's rough estimate, but increasing the number of magnets from nine to twelve should compensate for the smaller magnetic moment.

ISSUES AROUND THE POTASSIUM CHAMBER

With potassium, the viewports close to the oven are not a problem,

¹ *Eclipse Magnetics* N750-RB

² custom 10 × 25 × 3 mm SmCo32 magnets, purchased from *Eclipse Magnetics*

³ *Bartington* Mag031E1000

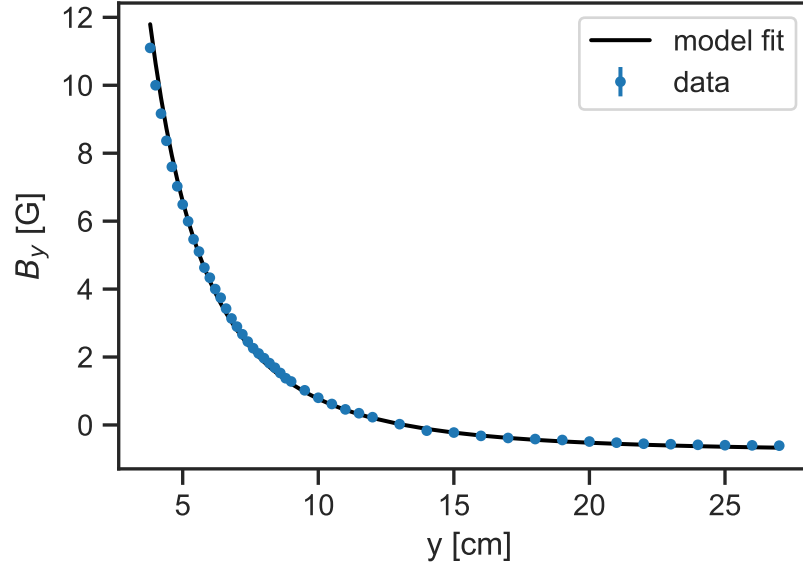


Figure 6.1: Measured magnetic field B_y strength of three permanent magnets at position y . The model fit of the Equation 5.1 is fitted to the data to extract the magnetic moment.

but we did have problems with the vacuum. Initially we experienced occasional arcing events which became more frequent, accompanied by a slow increase in ion pump current. This escalation continued until the ion pump shut down due to too many arcing events in a short period of time. In response, we baked and reactivated the system. Unfortunately, during this process, a power failure caused the turbopump to fail, which also damaged the ion pump controller. The system was flooded with air, baked, reactivated with a new NEG element and the ion pump controller replaced. In the end, the explanatory hypothesis was that potassium had accumulated near the ion pump, causing desorption and subsequent arcing events.

After these interventions, the vacuum remained stable for about a year. Although we observed several arcing events, which are common in the UHV range, they became difficult to track. The new controller included an arc bypass, which prevented the ion pump from shutting down and therefore the events from being recorded.

Recently, the ion pump reading has begun to increase exponentially, as described in Section 4.3.8. This increase is probably due to the build-up of conductive deposits on the surface of the ion pump, leading to a leakage current. We attribute these deposits to potassium. Although this leakage current does not affect the performance of the pump, it makes the pressure indication unreliable. These deposits could be removed by oxidation by flooding the chamber, but this is not feasible for us. Instead, we plan to manage the deposits by slightly heating the

ion pump and introducing a cold spot in front of the ion pump to accumulate potassium atoms.

Recent evidence suggests that the earlier problems may not have been vacuum related, but rather due to the build-up of leakage current sources. While it remains unclear whether the earlier problems were also caused by leakage currents, the actions taken to resolve them are consistent with this hypothesis.

6.4 2D MOT OPTICS

The 2D MOT optics are arranged to minimise disassembly when the vacuum system is moved. All of the optics, except the final mirror, are mounted on a breadboard that can be easily removed when the vacuum system needs to be moved. It was not possible to position the optics far enough from the 2D MOT chamber to allow the vacuum system to be moved out, as the angle between the two atomic beam axes would cause the system to exceed the width of our 1.5 m optical table.

6.5 SUMMARY

In summary, the separation of atomic species works well. The translation stage remains a valuable addition, although it requires careful planning to avoid blockages, which complicates subsequent design choices. A compromise was reached for the 2D MOT optics: the vacuum system can only be moved by removing the 2D MOT optics, which are mounted on a breadboard. This design preserves the ability to address vacuum issues more easily, but limits flexibility for other uses, such as short-term magnetic field measurements at the atoms' location.

The more compact design of the 2D MOT chamber has its drawbacks, particularly for sodium, as the viewports become coated over time. Several approaches are being investigated to mitigate this problem in the future. For potassium, the exact problem with the pump remains unresolved. The current hypothesis is that potassium accumulates near the ion pump and that a cold finger could solve this problem.

TWO-DIMENSIONAL DIPOLE TRAP

After successfully cooling the atoms to degeneracy in a crossed optical dipole trap, the next step is to transfer the atoms into a two-dimensional optical dipole trap. The two-dimensional trapping geometry allows direct observation of the atoms with a high numerical aperture imaging system. Furthermore, with sufficiently high confinement in the z -direction, the dimensionality of the atoms can be reduced to effectively two dimensions, allowing physics to be studied in two dimensions. Due to the strong confinement in z , a sufficiently cold quantum gas can only populate trap levels in the xy -plane, where thermally excited particles cannot move along the strongly confined axis z , leading to a quasi two-dimensional BEC.

This chapter describes the two-dimensional dipole trap. It starts with a description of the optical layout and is followed by sections on further details, including design considerations, signal hunting techniques and characterisation measurements of the beam waist.

7.1 TWO-DIMENSIONAL OPTICAL DIPOLE TRAP SETUP

The setup of the 2D trap (see Figure 7.1) is quite simple: A single red-detuned elliptical beam traps the atoms in its focus. We use 1064 nm single-frequency light generated by a combined 1064 /532 nm *Azurlight* laser¹ (20 W/10 W).

The light is polarisation cleaned and directed through a single AOM² pass, which is used for switching and power stabilisation. The AOM is mounted on a 4-axis translation stage³ for more precise and stable alignment. The light is then coupled into a high-power fibre⁴, which leads to the 2D trap setup.

In the 2D trap setup, the light is collimated to a beam of 3.2 mm diameter using an achromatic doublet⁵ with a focal length of $f = 30$ mm. The beam is first passed through two mirrors and then polarised by a Glan-Taylor prism. A beam sampler is then placed in the beam path.

The polarisation cleaned light is shaped into a surfboard geometry by

¹ ALS GR 532 10 I CP SF

² G&H 3080-199 AOM

³ Newport 9071

⁴ from NKT photonics aeroGUIDE POWER-15-PM

⁵ from Thorlabs ACA254-030-1064



In the near field of the Azurlight laser (in front of the waist at about 150 mm) there are high divergence cladding modes which do not interfere with the Gaussian output mode and make the output mode look bad. The laser output is not perfectly collimated at a diameter of 1 mm at 180 mm from the laser head. The beam caustic curve is given and can be used to plan matching optics.

two lenses: a cylindrical achromat with $f = 200$ mm and a spherical high power doublet with $f = 100$ mm⁶. The cylindrical and spherical lenses form a telescope that reduces the beam diameter in the horizontal direction to 1.6 mm, while in the vertical direction the light is focused down by the spherical lens to a beam waist of 20 μ m.

The entire 2D setup is mounted on an aluminium block that can be tilted and translated in height using three micrometer screws. A finely adjustable rotation mount⁷ for the cylindrical lens allows the surfboard to be aligned with gravity. A fine translation stage⁸ in the beam direction allows the trapping frequency to be adjusted in the less restricted direction.

The spherical focusing lens is glued into a *PEEK* lens tube. This allows it to be placed close to the science chamber without being too bulky. *PEEK* was chosen because it is a stiff plastic that is not magnetisable and does not risk inducing eddy currents.

7.2 DESIGN CONSIDERATIONS

This section provides an insight into the design choices made. The requirements were that the achievable trapping frequency should be sufficient for a quasi-2D BEC. After rebuilding the experiment and successfully condensing the sodium, the aim was to be able to implement the trap within a few months in order to start first experiments on the demixing dynamics. Therefore, a laser that was already available was to be used. This laser can provide about 20 W at 1064 nm and 10 W at 532 nm light. Figure 7.2 gives an overview of the different beams passing through the science chamber and where the 2D trap beam should be implemented.

7.2.1 Trap Geometry

We considered three options for generating a two-dimensional trap: A single red-detuned elliptical beam [20, 49, 54, 145–147], two interfering blue-detuned beams (pancakes) [55, 148, 149], or a single blue-detuned beam shaped with a phase plate resulting in a TEM01 mode [52, 150–154]. The accordion lattice [56, 155] was not considered closer, as the design was considered to be time consuming and the tunability of not necessarily needed for the first possible experiments on demixing dynamics [1].

6 *Thorlabs* ACY254-200-B and ACA254-100-1064

7 *Thorlabs* CRM1PT

8 *Thorlabs* SM1ZA

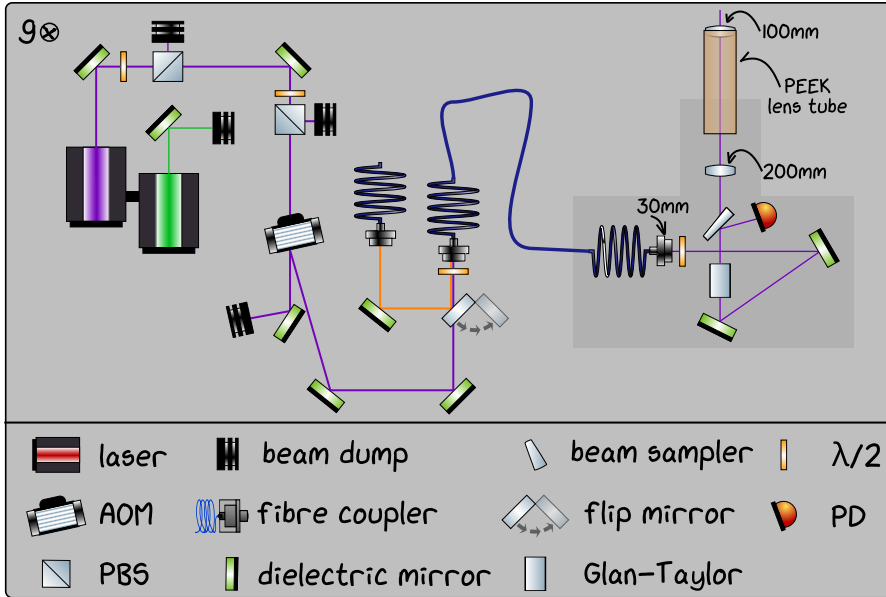


Figure 7.1: Optical setup for the 2D trap. The 1064 nm light (purple) is generated by an IR/532 nm laser. The light is first polarisation cleaned and then passes through another PBS, which allows us to add another AOM path in the future. The light then passes through an AOM where the zeroth order is blocked and the first order of diffraction is coupled into the high power fibre. Sodium light (orange) can be coupled into the fibre using a flip mirror for alignment purposes. The fibre is routed to the aluminium block where the light is coupled out and polarisation cleaned using a *Glan-Taylor* prism. A beam sampler directs a small fraction of the beam to a photodiode to monitor the beam power. The beam is shaped to the surfboard geometry using a cylindrical lens and a spherical lens. The spherical lens is mounted in a PEEK lens tube. The green light 532 nm, which is also produced by the laser, is currently not used.

Pancake:

- Method: Two blue-detuned beams are interfering under an angle, resulting in a stack of horizontal interference fringes in which the atoms can be trapped in the dark volume. [55, 148, 149]
- Considerations: There is already a working interference-based pancake structure in the BECK experiment [55], but space constraints made it impossible to replicate this design. In the BECK experiment, all the optics are mounted on a 25° wedge, a solid block of aluminium for stability. One side of the wedge holds the optics for two pancake beams, which interfere at an angle of 6°, while the other side holds the optics for the red-detuned compressor beam, which compresses the atoms for better loading into the pancakes. Considerable work would have been required to adapt the design to our spatial constraints. Major problems

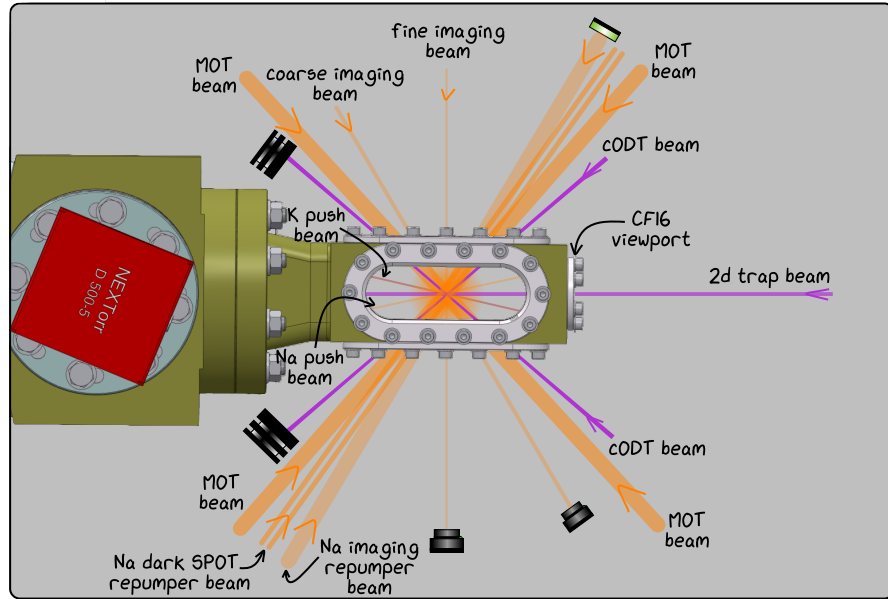


Figure 7.2: Schematic of beams passing through the science chamber. The beams passing through the science chamber are the MOT and push beams for sodium and potassium, with an additional repumper dark SPOT beam for sodium. The coarse and fine imaging beams, with an additional retro-reflected repumper imaging beam for sodium. The two crossed optical dipole trap (cODT) beams and the two-dimensional optical dipole trap beam.

arose from the CF16 viewport. Due to its relatively large distance (about 10 cm) from the atom cloud, it limits the maximum opening angle between the two beams to 6° . This is fine for the two interfering beams, but the compressor cannot be mounted on the other side of the block. The setup is stable in operation at the BECK experiment. A small drawback are the ripples in the interference pattern and therefore in the condensate. These ripples are attributed to dust/dirt on the science chambers or optics. In the SoPa vacuum all standard viewports seem to have some residue on the inside. For the CF16 viewport it is very small, but we expected a greater effect on the interference pattern than for the BECK experiment.

- Advantages: Blue-detuned trapping, and therefore, reduced heating in this confined configuration [38].
- Drawbacks: In the BECK experiments, ripples are observed on the interference pattern and therefore on the condensate, which are attributed to dust/dirt on the optics/glass chamber. The design cannot be easily replicated. To adapt the BECK design for the SoPa experiment, we would need to make significant modifications, essentially requiring a complete redesign. This would result

in a design that is significantly more complex to manufacture than the other options.

Phase-plate:

- **Method:** A blue-detuned beam is shaped with a phase plate to create a TEM01 mode. The beam is phase shifted by $+\frac{\pi}{2}$ on one side and $-\frac{\pi}{2}$ on the other. This creates a dark sheet of destructive interference at the boundary between the two halves. [52, 150–154]
- **Considerations:** This method is fascinatingly simple. However, our group had no prior experience with phase plates and their qualities. In the end, the long delivery times for phase-plates led us to withdraw this idea.
- **Advantages:** Simple design. Blue-detuned trapping, and therefore reduced heating in this confined configuration [38].
- **Drawbacks:** No experience with phase plates and their quality and long delivery times for the phase plate.

Surfboard:

- **Method:** Ideally, this surfboard configuration should confine the atoms quasi two-dimensionally, although an additional top beam may be required to provide confinement in the x- and y-directions. The atoms are confined in its focus. [20, 49, 54, 145–147]
- **Considerations:** In the best case, this surfboard configuration is good enough to confine the atoms quasi two-dimensionally, but an additional top beam may be needed to confine the atoms in the x- and y-directions. Such a configuration can be achieved with a small number of optical components.
- **Advantages:** The surfboard configuration is simple in design and realisation.
- **Drawbacks:** The surfboard trap is not flat in the xy-plane, but can be flattened with an additional blue-detuned beam. Higher heating rates are expected than for a trap using blue-detuned light [38].

We decided to take the approach that was the easiest to design and the fastest to realise: The surfboard geometry.

7.2.2 Choice of Optical Components

The elliptical beam for the surfboard trap can be described as an elliptical Gaussian beam, where each axis can be treated independently as a Gaussian beam [156]. We aimed for trapping frequencies of a few

kHz in the z-direction at a beam power of ≈ 10 W. This is sufficient to provide quasi-2D confinement for atoms with temperatures of 50 nK (see Chapter 2).

The intensity for an elliptical beam propagating in x is given by

$$I_{\text{elliptic}}(\mathbf{r}) = \frac{2P}{\pi w_y(x) w_z(x)} \exp \left[-2 \left(\frac{y^2}{w_y^2(x)} + \frac{z^2}{w_z^2(x)} \right) \right] \quad (7.1)$$

where P is the power of the laser beam and $w_y(x)$ and $w_z(x)$ are the beam waist in the y- and z-directions, respectively.

The dipole potential for a far detuned (non-saturating) elliptical beam at its focus is thus given by (see eq. 2.9 or [38])

$$U_{\text{dip}}(r=0) = -\frac{\pi c^2}{\omega_{0,D_2}^3} \left(\frac{\Gamma_{D_2}}{\omega_{0,D_2} - \omega} + \frac{\Gamma_{D_2}}{\omega_{0,D_2} + \omega} \right) \frac{2P}{\pi w_y w_z} - \frac{\pi c^2}{2\omega_{0,D_1}^3} \left(\frac{\Gamma_{D_1}}{\omega_{0,D_1} - \omega} + \frac{\Gamma_{D_1}}{\omega_{0,D_1} + \omega} \right) \frac{2P}{\pi w_y w_z}, \quad (7.2)$$

where c is the speed of light, Γ_{D_1,D_2} is the line width of the D1 and D2 lines, ω_0 is the transition frequency to the D line, ω_0 and P are the frequency and power of the laser beam, and $w_{y,z}$ is the beam waist along the two axes.

The trapping frequencies in the radial direction ω_r and in the axial direction ω_a are then given by [156]

$$\omega_r = \sqrt{\frac{4U_0}{mw^2}} \quad , \quad \omega_a = \sqrt{\frac{2U_0}{mz_R^2}}, \quad (7.3)$$

where m is the atomic mass and the beam waist w and Rayleigh length z_R are given by

$$w = \frac{2\lambda f}{\pi d} \quad , \quad z_R = \frac{2\pi w}{\lambda}, \quad (7.4)$$

which depend on the wavelength of the laser λ , the focal length of the final focusing lens f and the diameter of the beam before the lens d .

This allows us to calculate the resulting trapping frequencies for a number of scenarios. We are aiming for a few kHz trapping frequency in z. With the planned laser we can achieve about 10 W of power at 1064 nm after the optical fibre. The size and position of the science chamber limits the focal length of the focusing lens to a minimum of 100 mm. The beam diameter before the focusing lens is left as a free parameter to achieve the desired trapping frequency of a few kHz in z-direction.

In the x- and y-directions a small confinement of only a few tenths

Table 7.1: Trapping frequencies of the dipole trap for two different outcoupling lenses.

laser param.	1064 nm , 10 W	
telescope	$f_{sph} = 100$ mm, $f_{cyl} = 200$ mm	
collim. lens	$f = 30$ mm	$f = 50$ mm
beam waist	$w_z = 21.0$ μ m, $w_y = 0.8$ mm	$w_z = 12.6$ μ m, $w_y = 1.3$ mm
trap freq. Na	$f_z = 1.28$ kHz, $f_y = 33$ Hz, $f_x = 15$ Hz	$f_z = 2.13$ kHz, $f_y = 20$ Hz, $f_x = 40$ Hz
trap freq. K	$f_z = 1.57$ kHz, $f_y = 41$ Hz, $f_x = 18$ Hz	$f_z = 2.61$ kHz, $f_y = 25$ Hz, $f_x = 50$ Hz

of a Hz is needed to hold the atoms. Ideally, the x and y confinement should be the same. The above constraints led to the design of a telescope consisting of a cylindrical lens followed by a spherical lens. While the two lenses act as a telescope in the y-direction, reducing the beam diameter by a factor of 2, the z-direction is unaffected by the cylindrical lens and is therefore focused down by the spherical lens at the end (see Figure 7.1).

Originally we wanted to use a 50 mm outcoupler lens. However, due to long delivery times, we started with a 30 mm lens. The comparison between these two outcoupler lenses and a summary of the beam waist and telescope values are given in Table 7.1. To tune the trapping frequencies in the x- and y-directions, the cylindrical lens is mounted on a fine translation stage, allowing us to adjust the trapping in the y direction by misaligning the telescope.

Due to the different detuning and polarisability of sodium and potassium, the trapping frequencies differ slightly. The difference can be compensated for by an additional laser beam that is blue-detuned for potassium and red-detuned for sodium. This additional beam will be implemented at a later stage, when a beam configuration that also flattens the trapping potential in the x- and y-directions is needed. This will be done after measuring the trapping frequencies with the trapped atoms.

7.2.3 Mechanical Setup

We planned to mount all the optics on a large aluminium block to improve stability. This way the optics are mounted in common mode, which means the whole setup vibrates together, improving stability. In order to not delay the implementation of the 2D trap by its manufacturing time, the block design was kept as simple as possible.

For alignment, we used three micrometer screws to tip, tilt, and z-translate the entire setup. To do this, we used micrometer screws⁹

⁹ Mitutoyo 426200 0-25, recycled from another setup the ratchet is of no use in the current setup



We selected springs based on the required working length and estimated strength. We ordered a range of springs to test and fine-tune the strength as required. We found the medium strength to be satisfactory (approx. 40 N). It is important to avoid overstressing the spring during installation. If the top plate tilts slightly when tipped, the screws are too loose.

which are retracted by springs¹⁰ towards the bottom plate. To prevent the micrometer screws from moving sideways, one is held in place by a pinhole and the other is restricted to one axis by two parallel rods. In this way one screw can move freely, one is restricted to one axis and the other is locked in the pinhole. As we use aluminium, which is rather soft, the contact areas are supported by brass elements pressed into the aluminium fitting. The technical drawing for the two aluminium plates are provided in Appendix A.6.

The optical path on the block is folded, due to space constraints and the large bending radius of the high power fibre, to ensure stability, extra stable mirror mounts¹¹ are used.

Our standard polarisation maintaining fibres from *Thorlabs* are used for powers up to about 500 mW - although they are only specified for up to 20 mW (50 mW) for sodium (potassium). For the planned setup, a power of about 10W after the fibre is desired. This means that at least 17 W are required before the fibre (depending on the coupling efficiency). Therefore a high power polarisation maintaining broadband single mode fibre from *NKT Photonics*¹² will be used. A large mode field diameter of 12.5 μm , high power SMA connectors with mode strippers where uncoupled light exits the fibre results in good high power performance. However, this fibre has a large bending radius of about 20 cm, which limits the routing of the fibre and the position of the fibre couplers.

Similar to fibres, standard optics, e.g. achromatic doublets, reach their damage threshold at higher powers because they are mostly cemented. At high powers the cement heats up and starts to loosen, resulting in lens misalignment¹³ or burnt spots in the glue. For the in and out couplers, standard air-spaced lenses from *Thorlabs*¹⁴ will be used, where we will test the high power performance.

Typically our fibre couplers consist of a pre-mounted aspherical lens with an M9 thread which is mounted into an SM1 lens tube using an adapter. The adapter has an O-ring to prevent it from turning unintentionally. For the high power coupler a translation stage¹⁵ is used to adjust the distance of the lens.

¹⁰ *Gutekunst* Z-081AI

¹¹ *Thorlabs* Polaris K1E2

¹² *aeroGuide* POWER-15-PM

¹³ As with the couplers from *Schäfter Kirchhoff*

¹⁴ *Thorlabs* ACA254-030-1064

¹⁵ *Thorlabs* SM1ZA

7.3 CHARACTERIZATION

We characterised the optical layout by performing a knife-edge measurement at the focus of the laser beam. A typical technique for measuring the beam waist involves moving a razor blade and recording the transmitted power on a photodiode. The sharp edge of the razor blade is needed to cut the beam precisely with as little diffraction as possible.

For precise alignment and movement through the beam, the razor blade is mounted on a multi-axis translation stage. For a symmetrical Gaussian beam, the orientation of the blade does not matter. For our elliptical beam, however, the orientation of the razor blade must be aligned with the respective beam axis of the elliptical beam profile.

The focus can be located relatively easily by cutting the beam at different positions and observing the shadow on a screen. If the shadow comes from the same direction as the razor blade, the razor blade is behind the focus. At the focus position, the shadow comes in from all sides, similar to the effect of a closing aperture. However, with an elliptical beam, if the razor blade is not aligned with one of the beam axes, the shadow will appear to come from the right or left.

This was used to align the razor blade with the direction of the beam. To determine the beam waist, we measured the z-position of the razor blade where 90% and 10% of the power is transmitted. The difference in the z-positions is the 90/10 beam waist $w_{90/10}$, which can be converted to the $1/e^2$ beam waist $w_{1/e}$ by multiplying by a factor: $w_{1/e} = 0.78 \cdot w_{90/10}$. [157]

Five repeated measurements were taken for each position along the beam. The results are plotted against the distance from the focusing lens in Figure 7.3.

The beam waist of a focused laser beam propagating along the x-axis has a hyperbolic shape and is given by

$$w(x) = w_0 \sqrt{1 + \left(\frac{x - x_0}{z_R}\right)^2} \quad (7.5)$$

with the Raleigh length $z_R = \frac{\pi w_0^2}{\lambda}$, the beam waist at the focus w_0 and the focus position x_0 .

To accurately determine the focus position and beam waist, the Equation 7.5 is fitted to the data. The fit results are $w_0 = 20.72 \pm 0.65 \mu\text{m}$ and $x_0 = 91.30 \pm 0.15 \text{ mm}$ and we calculate the Rayleigh length to be $z_{Rz} = 1.27 \pm 0.08 \text{ mm}$, which we can compare with the calculated values using the lens specifications in Table 7.2.

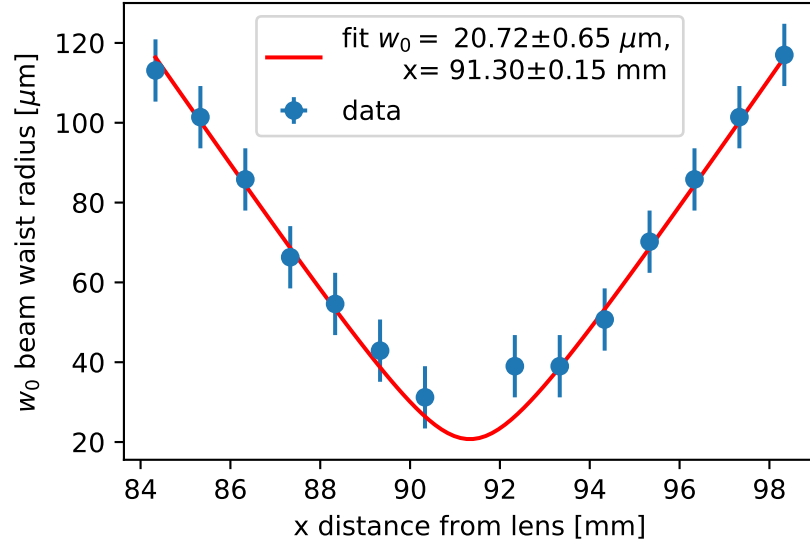


Figure 7.3: Knife edge measurement of the focus in z direction. Data is taken using the 90/10 knife edge method (blue). The data is fitted to the Equation 7.5 (red curve) to determine the beam waist and focus position.

Table 7.2: Comparison of the simulated focus values with the results of the knife edge measurement.

	calculation	knife edge measurement
working distance	91.8 mm	91.3 ± 0.2 mm
beam waist	$21.0 \mu\text{m}$	$20.7 \pm 0.7 \mu\text{m}$
Rayleigh length	1.3 mm	1.3 ± 0.1 mm

7.4 SIGNAL HUNTING AND OPTIMIZATION

The aim of this section is to describe the techniques we used for signal hunting and optimisation of the 2D trap. Since the details differ from experiment to experiment, the focus is on general techniques, leaving out experimental details. The optical layout for the 2D trap was first set up and pre-aligned separately to characterise it in terms of the beam waist obtained, as described in the previous Section 7.3.



The beam height of the optics on the block is kept low, so the mirror mounts are mounted directly on the block, unfortunately the thermal power head is bulky and can't fit anywhere on the block, so the beam has to be folded out with a mirror.

PRE-ALIGNMENT OF THE OPTICS: The optical setup is fairly simple, but care must be taken to ensure that the lenses are properly aligned and the beam is centred on them. Therefore, before mounting the lenses, irises were used to properly align the cylindrical lens mount to the PEEK lens tube. The SM1 threaded iris from *Thorlabs* has the same outer diameter as the PEEK lens tube, so an iris was taped concentrically to the lens tube at each end for alignment. After the collimated beam was aligned to pass through the setup, the lenses were

inserted and fine-tuned. The orientation of the cylindrical lens was aligned to the far field, where a line can be observed that must be aligned horizontally.

INITIAL ALIGNMENT TO THE ATOMS: After characterising the 2D trap outside the experiment by measuring its focus size, the setup was mounted in the experiment. The block can be adjusted in height using the three micrometer screws, but the focus position and beam direction have to be aligned by moving the whole block on the experimental table. It is rather impossible to hit the atoms directly with such a small beam. So two alignment techniques were used. First, the setup was roughly aligned by eye using a laser levelling tool. The in-line viewport on the main chamber was used to check that the beam was entering and exiting straight.

As a second step, the setup was aligned using a resonant laser beam. A resonant laser beam knocks the atoms out of the MOT, making it an ideal tool for aligning a beam to the atoms. To do this, the resonant light (taken from the imaging path) was coupled into the high-power fibre using a flip mirror to switch between the resonant light and the trapped light. To make it easier to see the first effect on the MOT, the MOT gradient was reduced and power from the MOT beams was diverted into the imaging beam to give a strong beam and a weak MOT. After observing the initial distortion of the weak MOT by the beam, the MOT gradient is slowly increased while the 2D trap setup is realigned for maximum destruction. Alignment of the 2D optical dipole trap beam to the high gradient MOT is advantageous because the MOT position shifts slightly with the gradient field and this is the position where the atoms are loaded into the dipole trap.

SIGNAL HUNTING: Once the setup is as good aligned to the high gradient MOT as possible, the signal hunt begins. Typical approaches include shining the light during imaging at various stages of the cooling sequence to observe the influence of the laser beams on the image due to the AC Stark shift.

Another option is to scan the time of flight and observe any influence of the 2D trap beams on the expanding atom cloud or the falling BEC.

The first attempt at signal hunting was not successful. While I began writing this thesis, the dipole beams were realigned [90], and D1 grey molasses for sodium was implemented [71]. Brian Bostwick then took the lead on a second signal hunt. After verifying that the AOM was correctly switched using a 5V TTL signal from our experimental control system, we checked for any effect on the magnetic trap when the 2D optical dipole trap beam was switched on. This time, we quickly

observed a signal: two small faint lines appeared at the top of the magnetic trap in an image taken with coarse imaging. Imaging artefacts in the coarse imaging led to a double feature of these small signals.

SIGNAL OPTIMIZATION: This initial signal was optimized for visibility by tuning the time of flight and testing the molasses stage. From there, the beams were aligned to match the height of the dipole beams. The 2D optical dipole trap was then loaded using a sodium BEC sequence, where sodium atoms are first loaded into the MOT, followed by a D1 grey molasses, then into the magnetic trap, and finally into the cODT, where dipole evaporation is performed to create the BEC. The 2D trap light was turned on during the magnetic trap phase. An image of the signal is shown in Figure 7.4.

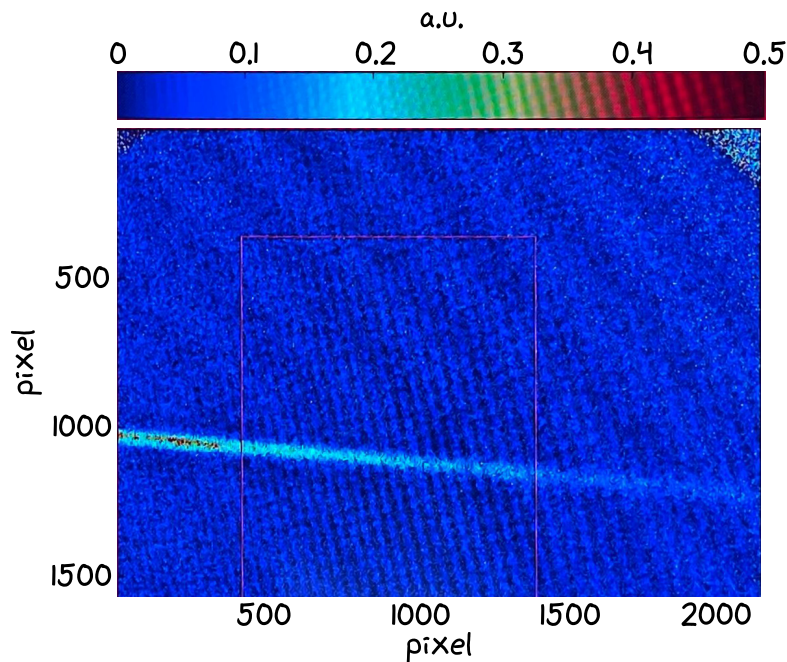


Figure 7.4: Signal of the 2D optical dipole trap. Unfortunately, only a image of the computer screen of the 2D optical dipole trap was saved during the optimization process, before the experiment suddenly degraded and required maintenance. The image was constructed from a phone photo; for better visibility, the original image was distortion-corrected, and the relevant parts were cut out. Artefacts as seen in the colour bar result from the picture being taken of the screen.

The focus of the 2D optical dipole trap is not well aligned with the cODT or the BEC, which is sitting in the centre of the ROI (red box). The misalignment was calculated to be about half a millimetre. Therefore, the focus must be moved by half a millimetre. This can be done either by moving the entire block away from the science chamber or

by adjusting the PEEK lens tube. Attempts to adjust the focus of the 2D optical dipole trap by moving the PEEK lens tube were hindered by sudden instability and degradation of the experiment, resulting in an insufficient number of sodium atoms to proceed with optimizing the 2D optical dipole trap's performance.

At this stage we have an imaging system in the horizontal plane that allows us to image all stages of the sequence up to the Bose-Einstein condensate (BEC). The horizontal imaging system consists of a coarse and a fine imaging. The coarse imaging is demagnifying and is used to image the experimental stages up to the magnetic trap, while the fine imaging is magnifying by a factor of $M = 20$ and is used to image the dipole trap and the BEC. The horizontal imaging is described in detail in [1]. However, the horizontal imaging system is suboptimal for the 2D optical dipole trap, as the atoms are highly confined in the z -direction. To observe the dynamics of the atomic cloud in the two-dimensional trap, an imaging system oriented along the vertical axis is necessary.

The vertical imaging system has to resolve atomic dynamics and density variations in future experiments. These density variations typically occur on the scale of the healing length, which is approximately $1 \mu\text{m}$. The imaging system must provide high-quality images across the entire atomic cloud, which typically spans $50 \mu\text{m}$. As resonant laser light is frequently employed in cold atom experiments to interact with the atoms, it is imperative that the system functions effectively for both sodium and potassium wavelengths, ensuring the focus position remains consistent for both species.

Several parameters characterize an imaging system. The resolution, defining the smallest object that can be resolved, is wavelength-dependent and limited by diffraction. Achieving a resolution close to the diffraction limit requires a high numerical aperture (NA), which describes the maximum light cone that can enter the imaging system, constrained by the objective's working distance and lens diameter.

The field of view (FOV) is the area in the image plane where high-quality imaging is maintained. Ensuring a sufficiently large FOV is essential to capture the entire atomic cloud without significant aberrations. The depth of focus refers to the range along the imaging axis where the best resolution is achieved. A smaller resolution typically results in a smaller depth of focus, necessitating precise alignment of the objective with the atoms.

This chapter first introduces the theoretical description of the imaging technique used, namely absorption imaging, which is outlined in Section 8.1. The objective is then described in Section 8.2, while the vertical imaging setup is outlined in Section 8.3. Section 8.4 presents

the characterisation of the objective in a test setup. Section 8.5 details the mounting of the objective. Section 8.6 describes the planned setup for the compensation optics of the vertical MOT beam.

8.1 ABSORPTION IMAGING



Initially, we faced challenges with a weak absorption imaging signal. To address this, we increased the repumper intensity during imaging, as a higher intensity is necessary since the atoms are trapped in the $|F = 1, m_F = -1\rangle$ state.

Absorption imaging is a standard imaging technique [158] used in ultracold atom experiments and is the main detection tool at the SoPa experiment. For absorption imaging, a resonant laser beam is directed through the atomic cloud and onto a camera. As the beam passes through the cloud, the atoms absorb a portion of the light, creating a contrast in the image that reveals the density distribution of the atoms. The resulting darker areas in the image correspond to regions with a higher concentration of atoms, allowing for precise inference of the atomic density.

The measured transmission $I(x, y)$ of the imaging beam, propagating in z-direction with intensity $I_0(x, y)$, is described by Beer-Lambert's law

$$I(x, y) = I_0(x, y) \exp(-OD(x, y)) = I_0(x, y) \exp-(n(x, y)\sigma), \quad (8.1)$$

with the optical density $OD(x, y)$, the column density $n(x, y)$ and the photon scattering cross section σ . σ depends on the transition wavelength λ_0 , the natural line-width Γ and the detuning Δ :

$$\sigma = \sigma_0 \frac{1}{1 + \delta^2} \text{ with } \sigma_0 = \frac{3\lambda_0^2}{2\pi} \text{ and } \delta = \frac{2\Delta}{\Gamma}. \quad (8.2)$$

Within the experimental sequence three images are taken: The first one is the image with the atoms I_{atom} , while the imaging beam is on, resulting in an image of the beam with a darker area where the atoms have absorbed light. The second one is a reference image I_{ref} , which is taken after the atoms are gone, resulting in an image of the laser beam. The third image is a dark image I_{dark} , where the imaging beam is turned off as well.

In the low intensity limit the optical density is calculated from the three images as

$$OD(x, y) = -\ln \left(\frac{I_{atom}(x, y) - I_{dark}(x, y)}{I_{ref}(x, y) - I_{dark}(x, y)} \right). \quad (8.3)$$

Figure 8.1 shows the three images taken of a sodium BEC and the resulting optical density. The optical density is used to obtain the atom number N taking the pixel size A and the magnification M into account

$$N = \frac{A}{\sigma M} \sum_x \sum_y OD(x, y). \quad (8.4)$$

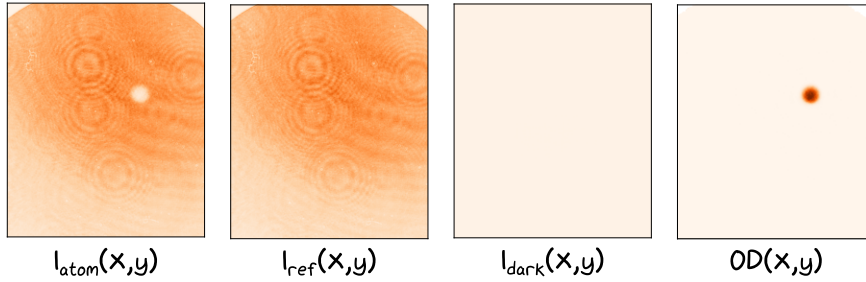


Figure 8.1: Series of three images taken of a sodium BEC to obtain the optical density image (right). Left the image with atoms and imaging beam present. Center left the reference imaging with imaging beam on but no atoms. Center right the dark image. Figure taken from [1].

For higher intensities the above calculations are leading to an underestimation of the atom number due to saturation effects [159, 160].

8.2 OBJECTIVE

The high numerical aperture objective is crucial for achieving the resolution required in our imaging setup. The working distance is limited by the science chamber used in the case of the SoPa experiment the objective was designed for a working distance of 22 mm, it consists of 2 mm of air, 6 mm of glass, and 14 mm of vacuum. So that a 2 mm gap is between the science chamber glass and the objective lens. A sketch of the objective is shown in Figure 8.2, indicating the atomic cloud and the distance to the glass of the science chamber. The width of the top bottom viewport is 30 mm. The objective has an aperture of 33.75 mm and, therefore $NA = 0.5$. A detailed technical drawing and the specsheet of the objective are in Appendix A.1.

In order to image both sodium and potassium the objective features chromatic focal correction for wavelengths ranging from 589 to 767 nm, ensuring accurate imaging across the relevant wavelengths of sodium (589 nm) and potassium (767 nm). The effective focal length for both species is $f_{obj} = 30.0541$ mm.

The objective was manufactured by *Special Optics*. The outer material is made of *Macor*, a machinable glass ceramic, and the objective features a SM2 thread, allowing direct mounting to standard optomechanics.

With the objective specifications established, we will now proceed to plan the imaging setup, as detailed in the next Section 8.3.

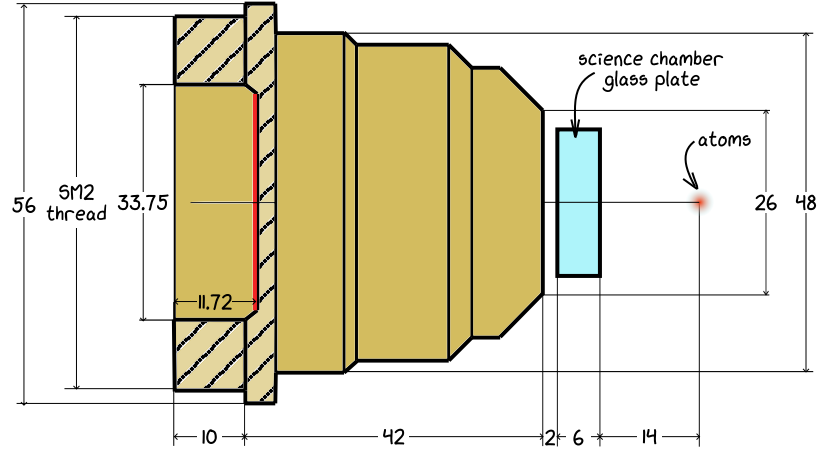


Figure 8.2: Sketch of our high $NA=0.5$ objective. Designed for a working distance of 22 mm, with 2 mm air, 6 mm glass and 14 mm vacuum. The effective focal length is 30.0541 mm, with the principal plane indicated in red. The last 10mm are threaded with a SM2 thread allowing for direct mounting in standard optic holders.

8.3 VERTICAL IMAGING SETUP

In optical absorption imaging, a beam of resonant laser light is absorbed by the atoms, resulting in the transmission of light that is subsequently imaged on a camera. Consequently, the beam must first interact with the atoms and subsequently with the camera. The planned imaging setup is summarised in Figure 8.3.

In order to image both sodium and potassium atoms, it is necessary to overlap the two imaging beams. This is achieved through the use of a dichroic mirror (green). The two beams are reflected together into the vertical plane, where they pass through the science chamber. Subsequently, the imaging beams are reflected back into the horizontal plane. In the horizontal plane, the two imaging beams will be split up again by a dichroic mirror (green) and passed through the $f = 1000$ mm secondary lenses¹ before being guided to the camera. With this setup, a magnification of $M = 33$ should be achieved.

Additional dipole laser beams at 1064 nm or 532 nm can be introduced into the vertical axis by utilising the dichroic top and bottom incoupling mirrors (purple). These provide the possibility for shaping in the trapping potential in the xy-plane or phase imprints. In the first step, a single beam is planned, and later, a digital micromirror device (DMD) setup is planned, similarly to how it was implemented for the BECK experiment [161]. This dichroic mirror (purple) has been custom-made² and is designed to reflect light from sodium and potassium atoms, while

¹ Thorlabs ACT508-1000, A, B coated respectively.

² LENS-Optics GmbH

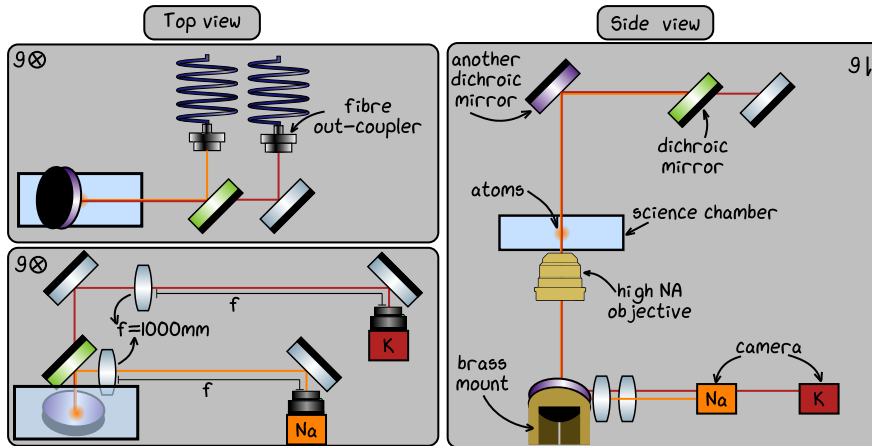


Figure 8.3: Illustration of the planned vertical imaging system. The imaging setup is depicted on the left side from a top view orientation, comprising two layers above and below the science chamber (the top and bottom images, respectively). In the upper layer (top image), light is emitted from both species and overlapped on a dichroic mirror (green), subsequently reflected downwards towards the atoms within the science chamber. At the bottom layer, the light is separated again and two secondary lenses with a focal length of 1000 mm image the beams on a dedicated camera for each species. The position of the cameras is selected to ensure that the distance to the lens is equal to the focal length. The side view of the high-resolution imaging setup is illustrated on the right. The light is overlapped on a dichroic mirror (green) and then reflected downwards through the atoms and the objective. This mirror is also a dichroic mirror (purple), which will be employed in the future to feed in far detuned light for optical dipole traps.

transmitting green (532 nm) and infrared (1064 nm) light.

It should be noted that the dichroic mirrors in this experiment are not from *Thorlabs*, but rather from *LENS-Optics GmbH*, which have a fused silica substrate that is 12 mm thick. The increased thickness of the mirror substrate should mitigate the impact of interfering effects, which have been observed in the BECK experiment.

The group of Lauriane Chomaz has recently conducted a detailed study of dichroic mirrors. A dichroic mirror with a substrate of 12 mm thickness is compared to one with a substrate of 5 mm mm thickness. The curvature bending and stress due to the own weight were simulated, and the wavefront distortion for the transmittance and reflected wavelength was determined. The mirror with a thicker substrate demonstrates superior overall performance, although the transmitted beam is more distorted than that observed for the thin substrate [162]. Furthermore, it was observed that the point spread function is highly dependent on the alignment within the dichroic mirror, with significant distortions occurring in the vicinity of the mounting points [163].

It can be concluded that the selection of a 12 mm thick mirror substrate for the SoPa imaging setup is an appropriate choice, given that the imaging beams are reflected. However, the transmitted path may be somewhat compromised. Nevertheless, for beams of a sufficiently small diameter, this should not have an impact. It is possible that the strong distortions close to the mounting points of the dichroic mirrors may affect the overall field of view, which could be reduced by mounting the dichroic mirror carefully.

Therefore, the bottom dichroic mirror (purple) will be glued only at one point in order to reduce mechanical stress on the mirror. This mirror is mounted on a brass mirror holder (Figure 8.4), which has a hollow construction that ensures optical access from below. The planned beam height is approximately 100 mm. The technical drawing of the brass mirror holder is provided in Appendix A.3.

We have two electron multiplying charge-coupled device (EMCCD) cameras:

- The *HNÜ 512* from *Nüvü Camēras*. This camera has a resolution of 512×512 pixels with a pixel size of $16 \mu\text{m} \times 16 \mu\text{m}$, and a quantum efficiency of approximately 93% at 589 nm and 80% at 767 nm.
- The *ProEM HS:1024BX3* from *Teledyne Princeton Instruments*. This camera features a resolution of 1024×1024 pixels with a pixel size of $13 \mu\text{m} \times 13 \mu\text{m}$, and a quantum efficiency of approximately 94% at 589 nm and 88% at 767 nm at a temperature of 25 °C.

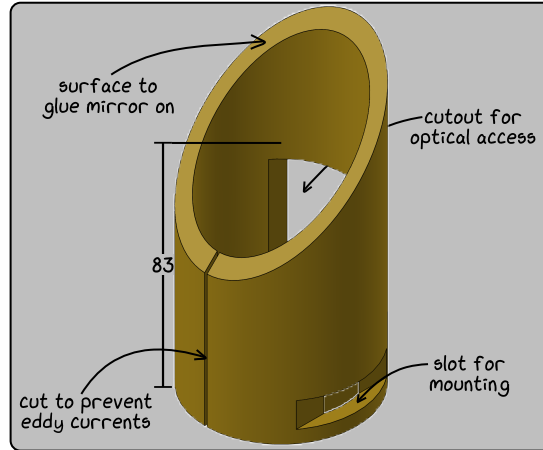


Figure 8.4: Mirror mount for the bottom dichroic mirror (purple) of the fine imaging setup. This mount allows for the coupling of a far-detuned dipole trap from below. The mount is made from brass, with a cut to prevent eddy currents. The height of the brass holder at its centre is 83 mm, resulting in a beam height of 100 mm. The mirror needs to be glued in place. The technical drawing of this mount is provided in Appendix A.3.

The quantum efficiency describes the ratio of incoming photons to created photoelectrons. For small signals, it is advantageous to have a high quantum efficiency, which depends on the temperature and the wavelength. Since the quantum efficiency for sodium is similar for both cameras, but significantly lower for potassium in the Nüvü camera compared to the ProEM camera, the ProEM camera will be used for potassium and the Nüvü camera for sodium.

8.4 OBJECTIVE CHARACTERIZATION

In this section the objective is characterised using a test setup to identify potential imaging artefacts. For simplicity, the test setup is mounted horizontally on an optical table. The point spread function is used to describe the response of the imaging system to a point source. To determine key characteristics such as resolution, depth of field, field of view and relative focus position, a series of images of a point source are taken while varying the position of either the gold foil or the camera.

To generate the point source, a gold foil with a regular pattern of 650 nm diameter holes, spaced $20\ \mu\text{m}$ apart, is employed. An image of the gold foil is shown in Figure 8.5. Each hole functions as an individual point source. The grid of holes is circumscribed by larger square holes, which facilitate alignment. However, single point sources can interfere with each other, resulting in identical images at regular distances between the objective and the gold foil, a phenomenon known as the Talbot effect [164]. The larger holes surrounding the smaller pattern help iden-

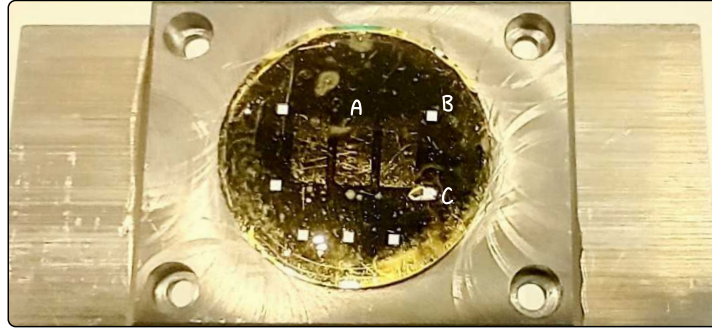


Figure 8.5: Image of the gold foil. **A:** Three rectangular patterns with different light reflections in the centre represent the areas of 650 nm diameter holes spaced $20\ \mu\text{m}$ apart. **B:** One of the larger outer holes to help find the true focus. **C:** The gold foil shows signs of wear and defects due to its age and extensive use.

tify the original image plane.

The test setup is kept as simple as possible ensuring fast change between sodium and potassium light (see *setup 1* in Figure 8.6). Therefore, sodium and potassium light are overlapped using a dichroic mirror before reaching the gold foil. The gold foil is mounted on a kinematic mount attached to a xyz-translation stage. A glass plate, simulating the science chamber viewport, and the objective are mounted with the working distance of 2 mm to each other. The camera is placed in the focus of the secondary lens. The distance between objective and secondary lens is chosen at an arbitrary distance that was convenient for the test setup. The secondary lenses are the same that are planned for the final imaging setup³. The images are captured using a *Mako* camera⁴. The *Mako* camera frame has a resolution of 644×484 pixels and a pixel size of $7.4 \times 7.4\ \mu\text{m}^2$. With a magnification of the imaging system of $M = 33$, the camera is capable of capturing 5×7 holes of the gold foil on the frame. A typical camera image of the gold foil is shown in Figure 8.7. In order to facilitate the switching between sodium and potassium, it is necessary to interchange the secondary lens and the filter on the camera.

The initial step in aligning the setup is to ensure that the sodium and potassium light overlaps. Subsequently, the camera is situated at the focal point of the secondary lens. Following this, the objective is inserted and aligned with respect to the back reflection. Subsequently, the glass plate is positioned at a working distance of 2 mm and also aligned using the back reflection.

Subsequently, the gold foil is inserted and aligned with the back reflection using a mirror. Initially, the image is focused to one of the outer

³ Thorlabs ACT508-1000

⁴ Mako G-030B from *Allied vision technologies*

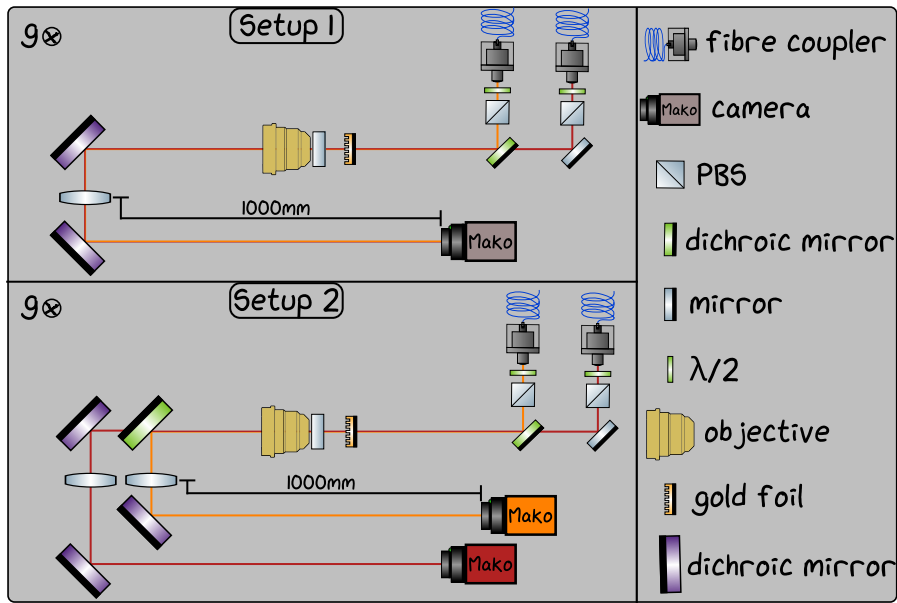


Figure 8.6: Test setups for objective characterization measurements. **Setup 1** can measure only one species at a time, requiring the lens and camera filters to be switched for different species. This setup was used for measuring the resolution, depth of focus, magnetization, and field of view for potassium. **Setup 2** is capable of measuring both species with the same setup and was used for the field of view measurements for both sodium and potassium.

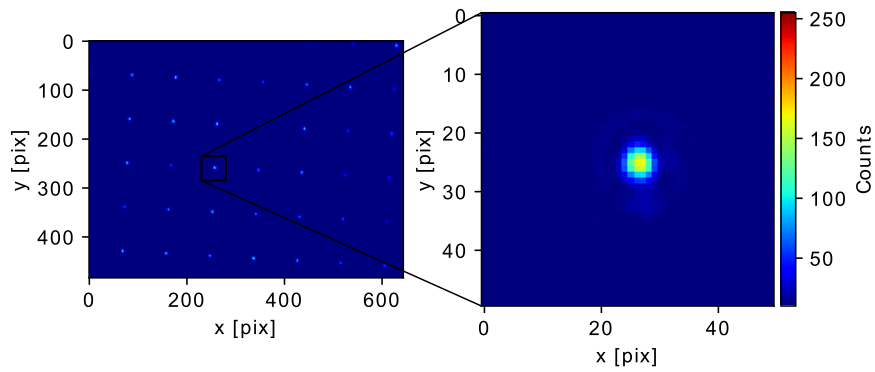


Figure 8.7: Camera image of the gold foil illuminated with potassium light, showing the arrangement of holes. The zoom-in highlights a single hole in greater detail.

larger holes by moving the gold foil. The gold foil is then translated vertically so that the hole pattern is imaged to the camera. The focus is fine-tuned by scanning the gold foil position once more. During alignment it was observed that the alignment of the secondary lens is quite sensitive.

Once the optimal focus position of the gold foil is found, the camera exposure time is adjusted to ensure the image is just below saturation. Subsequently, a series of images is taken for the measurements as described in the next paragraphs.

RESOLUTION, DEPTH OF FOCUS & FOCUS POSITION

The focus is best characterised by taking the point spread function of one hole, situated at the centre of the camera, into account for different positions of the gold foil. The best focus position can be determined based on the dependence of the resolution or intensity on the gold foil position. The position of best focus is where the resolution is minimal and the peak intensity is maximal. where the resolution is minimum and the peak intensity is maximum. Here, the depth of field is typically defined as the range in which the width of the point spread function does not exceed $\sqrt{2}\Delta r$. This corresponds to twice the Rayleigh length.

[164, 165] The intensity profile of light passing through a single hole on the image is described by the squared point spread function, which can be expressed as a function of the first Bessel function (J_1)

$$I(x) = I_0 \left(\frac{2J_1 \left(\frac{1.22\pi(x-x_0)}{\Delta r} \right)}{\frac{1.22\pi(x-x_0)}{\Delta r}} \right)^2 + I_{off}, \quad (8.5)$$

with the peak intensity (I_0), the offset intensity (I_{off}), the peak position (x_0), and the resolution or width (distance to the first minimum) of the central peak (Δr). In accordance with the Rayleigh criterion, the resolution is given by the following equation:

$$\Delta r = \frac{1.22\lambda}{2NA}. \quad (8.6)$$

This results in a diffraction-limited resolution of $0.718 \mu\text{m}$ for sodium and $0.936 \mu\text{m}$ for potassium based on our objective with $NA = 0.5$.

The position of the gold foil is adjusted with a differential micrometer screw, which is rotated in quarter-scale steps of $0.33 \mu\text{m}$. For each increment, an image is taken. To avoid the hysteresis of the micrometer screw, the measurement is only carried out in one direction, starting behind the focus and reducing the distance between objective and gold foil.

The measurement is initially conducted for potassium, and then, following a change in the secondary lens and camera filter, it is repeated

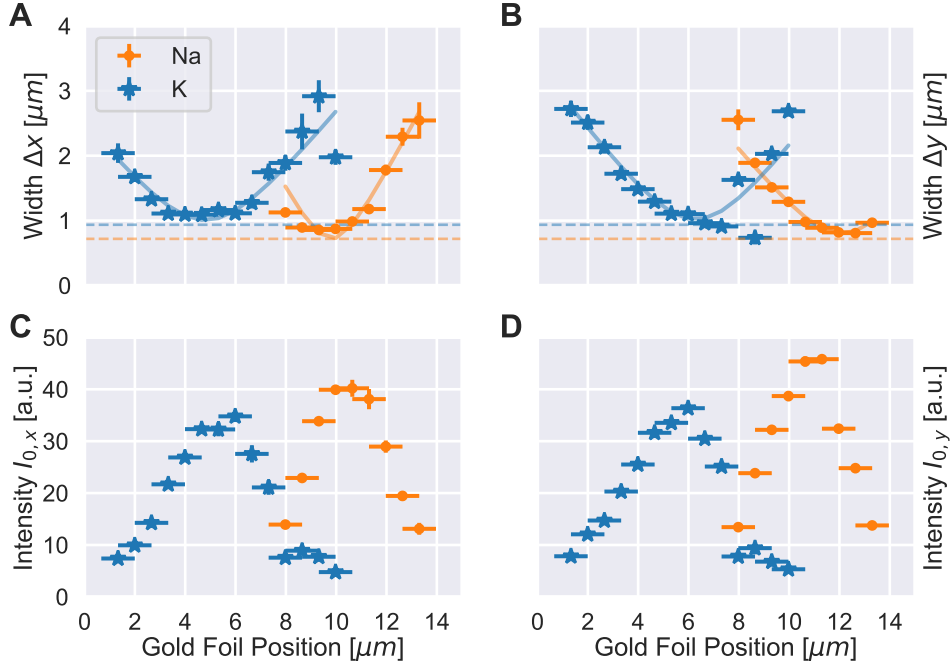


Figure 8.8: Focus characterization measurements. **A & B**: Resolution in x-direction (y-direction) as a function of gold foil position. The dashed lines indicate the diffraction limits for sodium (orange) and potassium (blue) light. A hyperbolic fit is applied to the data to determine the focus position, depth of focus and relative focus position. It should be noted that the fits generally do not fit the data very well, which is likely to contribute to inaccuracies. For example, the value in **B** that falls below the diffraction limit is due to a fit error. **C & D**: Peak intensity in x-direction (y-direction) as a function of gold foil position.

for sodium. This allows the relative focal shift between sodium and potassium to be determined. Figure 8.8 illustrates the resulting data. The resolution achieved for both wavelengths is close to the diffraction limit. A slight discrepancy is observed in the focus position between the x- and y-directions; however, the intensity peak positions are in close agreement with one another. This suggests the presence of a minor astigmatism, which is likely attributable to an imperfect alignment. The mean relative focal shift, determined by fitting the hyperbolic function $w_0\sqrt{1 + ((z - z_0)/z_R)^2}$ to the data, is $5.4\ \mu\text{m}$. In this context, w_0 represents the resolution at the optimal focus position z_0 , while z_R denotes the Rayleigh length. This discrepancy is attributed to the different focal lengths of the two wavelengths of the secondary lens. In accordance with the thin lens equation, a focal shift of $5.4\ \mu\text{m}$ is equivalent to a relative shift of the camera position by 6 mm, which aligns with the anticipated focal shift of the secondary lens of 5.8 mm. Additionally, the resolution at the optimal focus position is derived from the fit, yielding values of $\Delta r_x = 0.72(2)\ \mu\text{m}$ and $\Delta r_y = 0.80(1)\ \mu\text{m}$

for sodium, and $\Delta r_x = 1.01(2) \mu\text{m}$ and $\Delta r_y = 1.02(1) \mu\text{m}$ for potassium. The depth of focus, is determined by $2z_R$ from the fit, is $2z_{R,x} = 1.9(1) \mu\text{m}$ and $2z_{R,y} = 3.3(1) \mu\text{m}$ for sodium, and $2z_{R,x} = 4.2(1) \mu\text{m}$ and $2z_{R,y} = 3.9(1) \mu\text{m}$ for potassium. The reported errors are derived from fitting a hyperbolic function to the data. However, these values are likely to underestimate the total uncertainty as multiple fits were performed during data processing. The observed resolution exceeds the expected diffraction limit, suggesting that alignment errors introduced aberrations that increased the measured resolution. Despite these discrepancies, the objective demonstrates the ability to resolve density variations in the atomic cloud on the order of $1 \mu\text{m}$, which is consistent with experimental requirements.

MAGNIFICATION

Theoretically, the magnification is determined by the focal lengths of the imaging lenses used. For the planned vertical imaging setup, the magnification is calculated as $M_{calc} = \frac{f_{sec}}{f_{obj}} = 33.2733$, where the effective focal length (EFL) of the objective is specified with $f_{obj} = 30.0541 \text{ mm}$ and the secondary lens is chosen to be $f_{sec} = 1000 \text{ mm}$.

To confirm the magnification, an image taken with the target position set to the optimal focus is analysed. The magnification is determined by calculating the single hole distances between the 5×7 holes on the image. The peaks are identified row-wise and column-wise, and the distances to the next peaks are measured. The average distance of all rows and columns is taken, with the theoretical spacing between holes of the gold foil being $20 \mu\text{m}$.

For sodium light, the measured magnification is 33.44 ± 0.18 (rows) and 33.37 ± 0.14 (columns), and for potassium light, it is 33.10 ± 0.27 (rows) and 33.02 ± 0.16 (columns). The reported errors represent the standard error on the mean. The results are in good agreement with the calculated magnification.

FIELD OF VIEW

The field of view (FOV) is defined as the area where the point spread function (PSF) width Δr remains below $\sqrt{2}\Delta r_0$, with Δr_0 being the width on the optical axis. It is reasonable to expect a FOV significantly larger than $50 \times 50 \mu\text{m}^2$, as this is the area where the objective's performance sheet indicates diffraction-limited performance.

In order to obtain the field of view (FOV) of our imaging system, we compared the point spread functions (PSFs) of all point sources located within the gold target. With the planned magnification, only 5×7 holes fit onto the camera sensor, corresponding to a size of $100 \times 140 \mu\text{m}^2$. To observe a larger area along at least one axis, the test setup was modified by mounting the camera on a translation stage, allowing it to move horizontally orthogonal to the beam. Subsequently, the setup

was reconfigured for dual-species imaging to assess the impact of a dichroic mirror, which splits sodium and potassium light and images them on two separate cameras. For both configurations, the system was realigned, and the optimal focus position was determined visually.

During the measurement, the camera was translated in half-frame increments in order to track the holes. The data from the initial image was expanded by three columns of holes for each translation step of the camera frame. For each hole, the width of the point spread function (PSF) was extracted by performing x- and y-cuts and fitting Equation 8.5, as previously done for determining the focus position.

Figure 8.9 presents the results for potassium light in the simple setup (*setup 1* in Figure 8.6). Subfigures A and B display the x- and y-widths, respectively, with each consisting of both upper and lower plots. Vertical lines denote different images captured during the experiment. The upper plots depict the xy-distribution of holes in the gold foil, colour coded by the measured width. The lower plots show the width versus x-position for the central row, with horizontal lines marking the diffraction limit and the maximum acceptable width for the FOV. The results demonstrate good performance for potassium light, achieving an FOV of $400 \times 80 \mu\text{m}^2$. The error in the x-direction is estimated to be about $20 \mu\text{m}$, while the $80 \mu\text{m}$ in the y-direction is only a lower bound.

In order to investigate the influence of the dichroic mirror on the separation of sodium and potassium, the experimental setup was modified to accommodate a dual-species configuration (see *setup 2* in Figure 8.6). In this new configuration, the sodium and potassium light are separated by a dichroic mirror positioned before the secondary lens. The dichroic mirror reflects sodium light and transmits potassium light. Furthermore, an additional camera, mounted on a translation stage, was incorporated to image the sodium light.

The results obtained from the dual-species setup are depicted in Figures 8.10 and 8.11. Figure 8.11 illustrates that the potassium results exhibit enhanced performance in comparison to the single-species setup, achieving a FOV of $440 \times 80 \mu\text{m}^2$. This improvement is likely due to the fact that the alignment has been optimised. With regard to sodium (Figure 8.10), the observed FOV is $160 \times 80 \mu\text{m}^2$, which is in line with expectations overall, despite spatially varying x- and y-widths. It is noteworthy that the y-width decreases following an initial increase, which may be influenced by stress on the dichroic mirror. The error in the x-direction is again estimated to be about $20 \mu\text{m}$, while the result of $80 \mu\text{m}$ in the y-direction is only a lower bound.

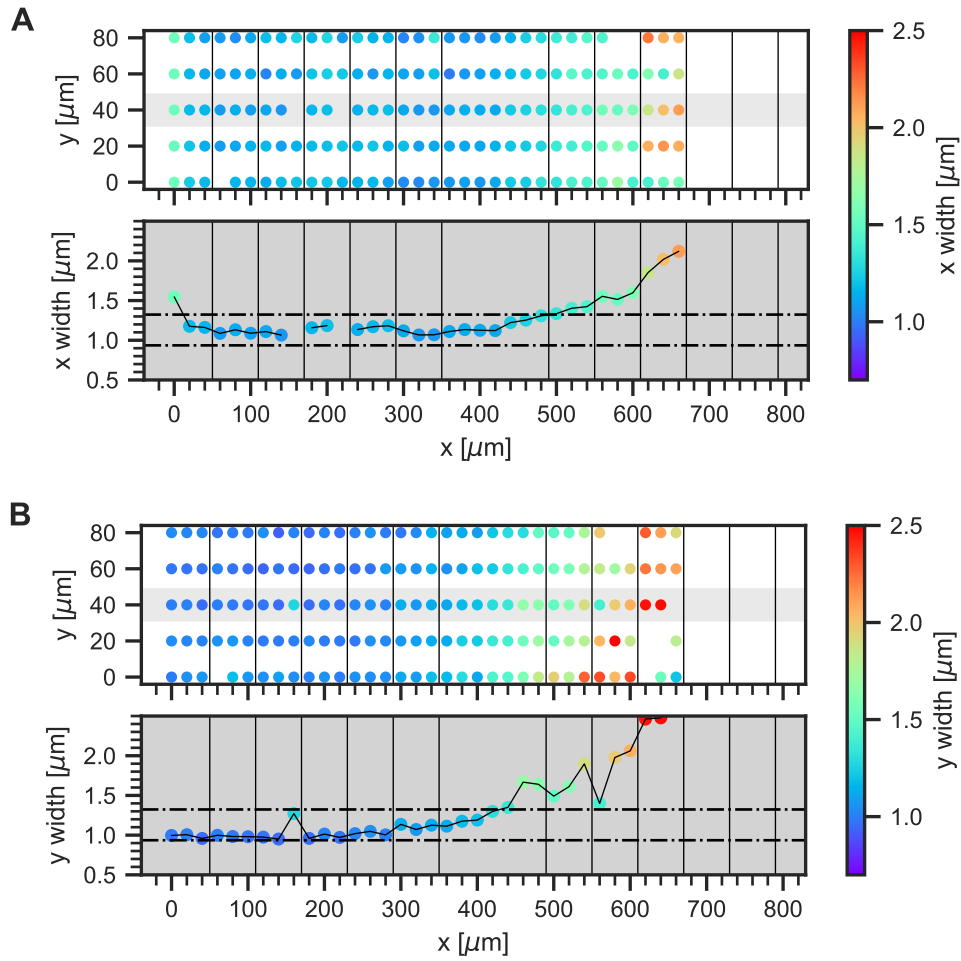


Figure 8.9: Field of view measurement for potassium light. For each hole in the gold foil, fits through the x- and y-cuts determine the x- and y-widths. Subfigure **A** shows the x-widths, and Subfigure **B** shows the y-widths. Each Subfigure consists of an upper and a lower plot. The vertical lines in the plot indicate the single images taken.

In the upper plots, the spatial distribution of widths is presented in the xy-plane. A grey box around a row highlights the row used to present the width versus x-position curve in the bottom plot. Two horizontal lines indicate the diffraction limit Δr and the upper limit for the field of view $\sqrt{2}\Delta r$.

In **A** the field of view in the x direction is $420 \mu\text{m}$ and in **B** it is also $420 \mu\text{m}$. However, the areas of acceptable field of view for the x and y widths do not overlap completely. The field of view in the x-direction, where both widths are acceptable, is $400 \pm 20 \mu\text{m}$. In the y-direction, the field of view is at least $80 \mu\text{m}$ for both widths. The estimated error in the x-direction is about $20 \mu\text{m}$, while the $80 \mu\text{m}$ in the y-direction is a lower limit.

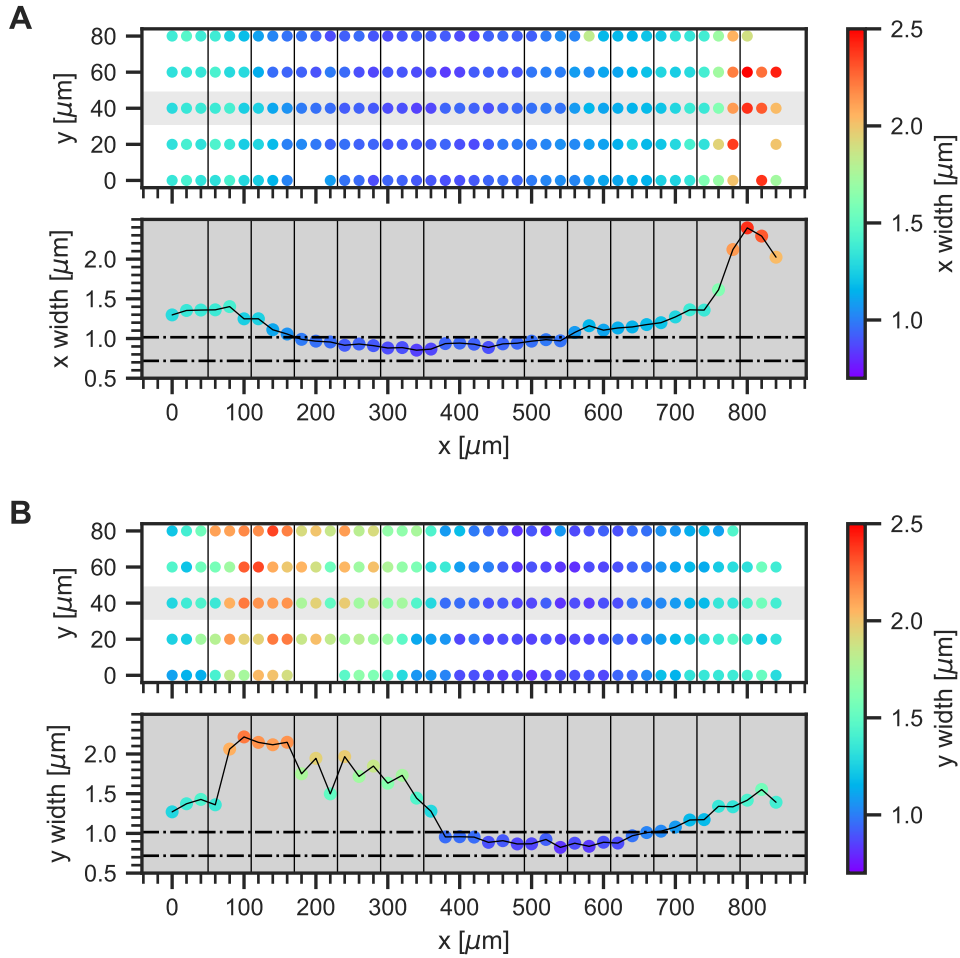


Figure 8.10: Field of view measurement for sodium light in dual-species setup. For each hole in the gold foil, fits through the x- and y-cuts determine the x- and y-widths. Subfigure **A** shows the x-widths, and Subfigure **B** shows the y-widths. Each Subfigure consists of an upper and a lower plot. The vertical lines in the plot indicate the single images taken.

In the upper plots, the spatial distribution of widths is presented in the xy-plane. A grey box around a row highlights the row used to present the width versus x-position curve in the bottom plot. Two horizontal lines indicate the diffraction limit Δr and the upper limit for the field of view $\sqrt{2}\Delta r$.

In **A**, the field of view in the x-direction is $360 \mu\text{m}$, and in **B**, it is also $280 \mu\text{m}$. The areas of acceptable field of view for the x- and y-widths do not fully overlap. The field of view in the x-direction where both widths are acceptable is $160 \pm 20 \mu\text{m}$. In the y-direction, the field of view is at least $80 \mu\text{m}$ for both widths. The error in the x-direction is estimated to be about $20 \mu\text{m}$, while the $80 \mu\text{m}$ in the y-direction is only a lower bound.

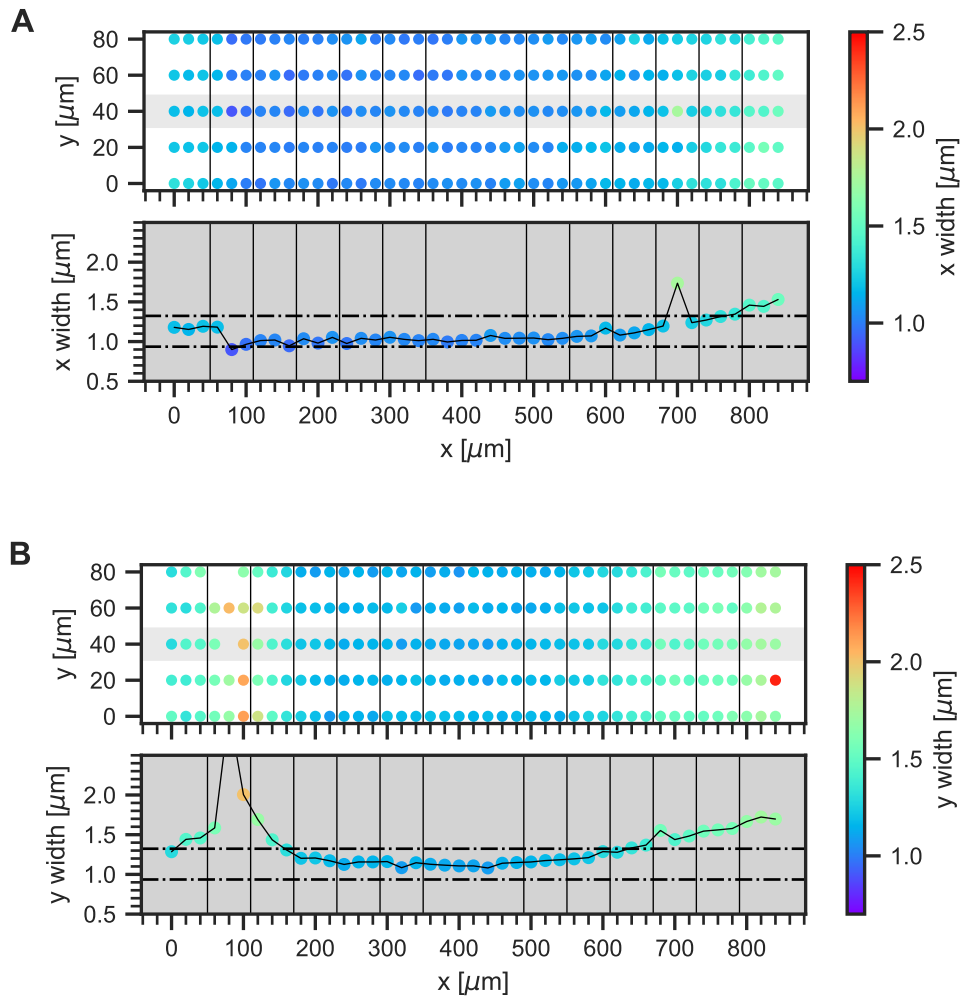


Figure 8.11: Field of view measurement for potassium light in dual-species setup. For each hole in the gold foil, fits through the x- and y-cuts determine the x- and y-widths. Subfigure **A** shows the x-widths, and Subfigure **B** shows the y-widths. Each Subfigure consists of an upper and a lower plot. The vertical lines in the plot indicate the single images taken.

In the upper plots, the spatial distribution of widths is presented in the xy-plane. A grey box around a row highlights the row used to present the width versus x-position curve in the bottom plot. Two horizontal lines indicate the diffraction limit Δr and the upper limit for the field of view $\sqrt{2}\Delta r$.

In **A**, the field of view in the x-direction is $680\ \mu\text{m}$, and in **B**, it is also $440\ \mu\text{m}$. The areas of acceptable field of view for the x- and y-widths do not fully overlap. The field of view in the x-direction where both widths are acceptable is $440 \pm 20\ \mu\text{m}$. In the y-direction, the field of view is at least $80\ \mu\text{m}$ for both widths. The error in the x-direction is estimated to be about $20\ \mu\text{m}$, while the $80\ \mu\text{m}$ in the y-direction is only a lower bound.

Table 8.1: The table lists the effective focal length (EFL), resolution (Δ_r), depth of focus (DOF), magnification (M) and field of view (FOV) for both sodium and potassium. The reported errors correspond to the fit errors, which are likely to underestimate the total uncertainty due to the multiple fits performed during data processing. The expected diffraction limited resolution is outside the reported errors, probably due to imperfect alignment causing aberrations and increasing the measured resolution. For magnification, the error is the standard error of the mean.

	specified	measurement Na	measurement K
EFL	30.0541 mm	-	-
Δr_{Na}	0.718 μm	$0.72 \pm 0.02 \mu\text{m}$ (x) $0.80 \pm 0.01 \mu\text{m}$ (y)	-
Δr_K	0.936 μm	-	$1.01 \pm 0.02 \mu\text{m}$ (x) $1.02 \pm 0.01 \mu\text{m}$ (y)
DOF		$1.9 \pm 0.1 \mu\text{m}$ (x) $3.3 \pm 0.1 \mu\text{m}$ (y)	$4.2 \pm 0.1 \mu\text{m}$ (x) $3.9 \pm 0.1 \mu\text{m}$ (y)
M	33.2733	33.44 ± 0.18 (h) 33.37 ± 0.14 (v)	33.10 ± 0.27 (h) 33.02 ± 0.16 (v)
FOV (x)	$> 50 \mu\text{m}$	$160 \pm 20 \mu\text{m}$	$400 \pm 20 \mu\text{m}$
FOV (y)	$> 50 \mu\text{m}$	$> 80 \mu\text{m}$	$> 80 \mu\text{m}$

SUMMARY

In conclusion, the objective functions as expected, with the results presented in Table 8.1. During the alignment processes, it was observed that the alignment of the secondary lens is sensitive, resulting in focal shifts and aberrations of the point spread function. The utilisation of a multi-axis translation stage for the final imaging setup may prove advantageous over a linear one for achieving optimal alignment and performance.

8.5 OBJECTIVE HOLDER

As demonstrated in the previous section, the objective must be aligned with great care. Due to the limited focal depth, the objective must be capable of precise adjustment along the z-axis. To achieve optimal imaging resolution at the diffraction limit, it is necessary to make adjustments in lateral position and tip-tilt. It is essential to ensure that the z-translation is precisely controlled over a short range; however, the entire travel range must be sufficiently large to accommodate the insertion of the objective along the optical axis through the coils. This is a crucial requirement due to the considerable thickness of the coils, which fully immerse the objective and prevent it from being moved in

from the side.

We adopted a similar mounting configuration to that used in the BECK experiment [166], which permits the future addition of a second objective from above. The objective mount is illustrated in Figure 8.12 and the technical drawings are provided in Appendix A.2.

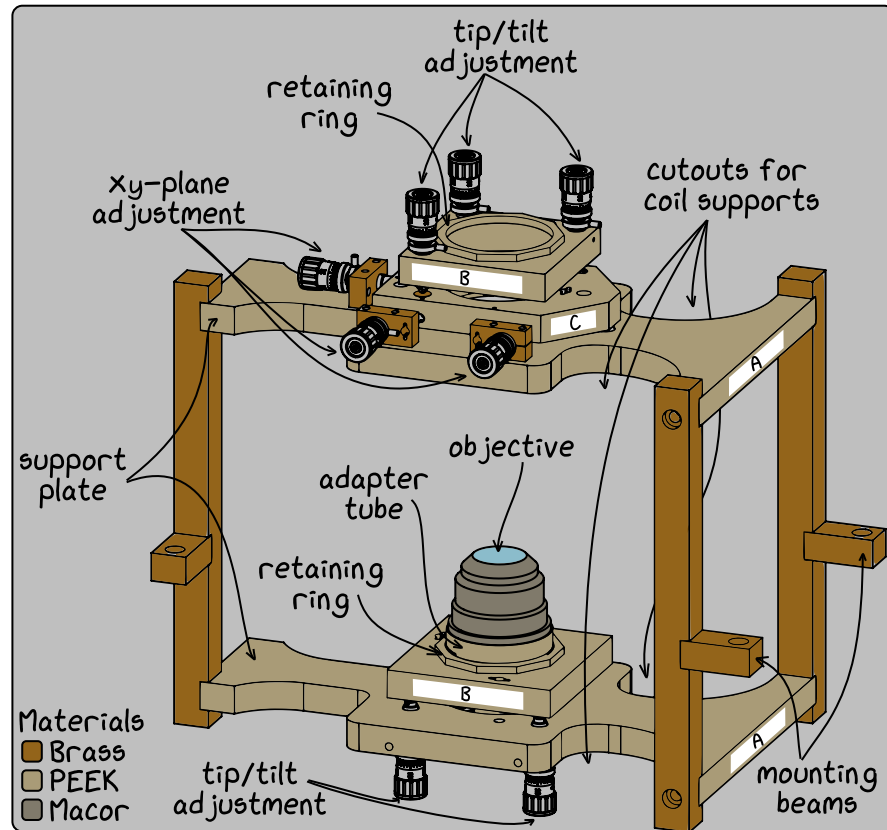


Figure 8.12: Objective holder assembly. The assembly comprises two support plates (labelled A) connected by mounting beams. The lower plate supports the imaging objective, while the upper plate is designed to accommodate a future objective. The entire structure can be moved in the xy-plane for precise positioning. The objective is attached via an adapter tube to a plate that provides tip/tilt adjustment and fine z-direction travel (labelled B). An additional intermediate plate (labelled C) facilitates precise xy-plane alignment for a potential upper objective.

 As the water-cooled coils are likely to vibrate, the posts aren't suitable for mounting optics. By putting all the optical bits on the same breadboard, we make sure they all vibrate the same way.

The mount is comprised of two support plates (labelled A in Figure 8.12): a lower plate for the objective and an upper plate, the latter of which is designed to accommodate a future upper objective. The two layers are connected via brass beams, each of which features a small beam coming out in a 90-degree angle for mounting. These small beams are mounted to conventional half-inch posts in post holders, which are fastened to the optics breadboard encircling the science chamber. This

configuration facilitates the entire structure to be translated in the xy-plane and adjusted in height to be evenly spaced around the science chamber.

Further details of the mount are provided in the subsequent paragraphs.

CHOICE OF MATERIALS It is desirable that the material of the entire construction be non-magnetic and that all parts comprising a full circle be non-conductive in order to avoid the generation of eddy currents. Consequently, PEEK is employed for the supporting plates and brass for the supporting beams.

SUPPORT PLATES The support plates (labelled A in Figure 8.12) have been designed in order to meet the spatial constraints of the setup. It is essential that the plates are of sufficient size to secure the entire construction to the breadboard surrounding the science chamber (as illustrated in Figure 3.1). However, they must also feature cut-outs to accommodate the coil supporting posts. This dual requirement necessitates a meticulous design process, whereby the plates must be crafted with sufficiently large cut-outs to allow for the mount to be inserted and removed without disassembling the coils. Furthermore, the upper support plate is identical in shape to the lower one, ensuring consistent support and balance.

TIP/TILT AND FINE Z-ADJUSTMENTS Each objective is mounted on an additional plate (labelled B in Figure 8.12) that allows for tip/tilt and fine z-adjustments relative to the support plate. This is achieved through three spring-loaded micrometer screws.

XY-PLANE ADJUSTMENTS The objective at the bottom is aligned by moving the entire supporting structure. The upper layer incorporates an additional plate (labelled C in Figure 8.12) situated between the support plate and the plate for tip/tilt adjustment. This enables precise adjustments in the xy-plane, thereby facilitating the alignment of the upper objective with respect to the lower one. The xy-plane adjustments are made by three spring-loaded micrometer screws that push the additional plate while it sits on ceramic balls⁵. This ensures smooth and precise movement.

COARSE Z-TRANSLATION The objective features an outer SM2 thread, which is inadequate for coarse z-translation adjustments due to its insufficient length. To address this issue, an adapter tube with an inner SM2 thread and an outer M60x0.75 thread is employed. The tip/tilt adjustable layer is equipped with an inner M60x0.75 thread,

⁵ 10 mm diameter made of Zirconia and purchased from *Kugel Winnie*

allowing the objective to be mounted onto it via the adapter tube. A retaining ring secures the coarse z-position.



To prevent the retaining ring from being pushed upwards or to the side when the objective is screwed in from below, the spanner has been designed so that it lies firmly against the retaining ring. An additional edge ensures that it cannot be pushed out.

MOUNTING PROCEDURE OBJECTIVE The objective is initially affixed to the adapter tube, which is then inserted into the tip/tilt plate from below. A specialized spanner⁶ is employed to rotate the tube. Given that the spacing between the tip/tilt plate and the coils is narrower than a finger, another specialized spanner (3 mm thick) is utilized to secure the retaining ring in position.

8.6 MOT COMPENSATION OPTICS

In order to image the atoms in the two-dimensional optical trap (described in Section 7) an imaging system in the vertical axis is needed as described in the previous sections. However, the magnetic coils restrict optical access along the vertical axis, thereby making it impossible to guide the MOT beams past the objective at an angle. It is thus necessary to pass the vertical MOT beam through the objective and compensate for it with additional optics.

This section provides an overview of the MOT beam compensation optics. Initially, a brief overview of the entire setup is presented. Following this, detailed descriptions of the optical components are provided, including their precise positioning. The section continues with a discussion on the specialized lens and mirror holder used in the setup. Finally, the pneumatic translation stage is examined, with detailed information on the electrical circuit used to control it.

8.6.1 Brief Overview

The MOT compensation setup includes two lenses which serve to counteract the focusing effect of the imaging objective, as illustrated in Figure 8.13.

The upper MOT beams are combined using a dichroic mirror (green) and then redirected into the vertical plane with another dichroic mirror (purple), which transmits both green (532 nm) and infrared (1064 nm) light. Subsequently, the beams traverse the science chamber. The imaging beam, also originating from the top, is integrated into the beam path through the use of a D-shaped mirror positioned between the two dichroic mirrors. Due to the extended path, the imaging beam exhibits only a slight tilt. Details regarding the imaging setup can be found in Section 8.3.

The MOT beams originating from the bottom have to pass through

⁶ comparable to those used for mounting externally threaded adapters in optical setups

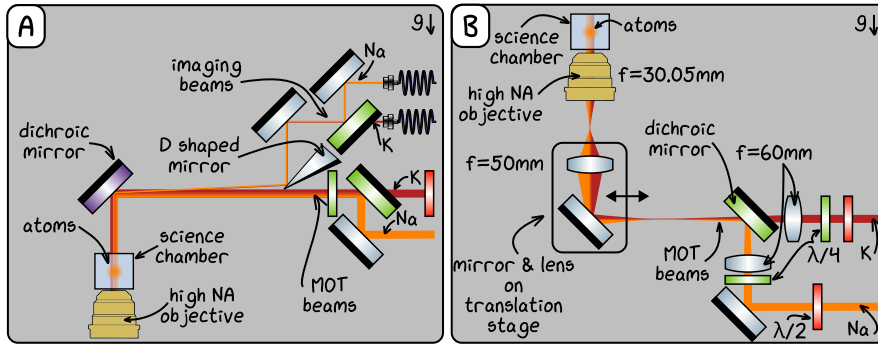


Figure 8.13: Overview of MOT compensation optics. **A:** MOT and imaging beams entering the science chamber from above. The MOT beams are initially overlapped and subsequently reflected into the vertical plane. Similarly, the imaging beams are overlapped and then redirected into the MOT path via the use of a D-shaped mirror. **B:** MOT beams entering the science chamber from below. The objective compensation optics comprises two lenses: one positioned in the MOT beam paths before they are overlapped, and the other situated directly in front of the objective. The mirror and lens positioned before the objective are mounted on a pneumatic translation stage, which enables them to be moved in and out along the beam axis.

the objective. In the absence of compensation, this would result in the beam being focused into the science chamber. To address this issue, two lenses are employed. In the initial stage, the MOT beams are directed through a first lens with a focal length of $f_1 = 60\text{ mm}$, after which they are overlapped. Once the beams have been overlapped, they are reflected into the vertical plane. Subsequently, a second lens with focal length $f_2 = 50\text{ mm}$ collects the diverging beams and before they pass through the objective. The lenses and distances have been selected in order to guarantee that the beams are collimated to their original size of 15 mm diameter following their passage through the objective. The lens and mirror positioned before the objective are mounted on a pneumatic translation stage that can be moved aside during the experimental sequence to allow the imaging and potential future dipole beams to pass.

The MOT beams must be circularly polarized, which is in our current setup achieved using an achromatic quarter-wave plate⁷ to generate the desired circular polarization. Given that the optimal orientation of the waveplate for sodium and potassium light can differ slightly, an additional half-wave plate is used for the potassium beam to allow independent adjustment of the circular polarization's handedness. When the MOT beams enter from the bottom, the wave plates are ideally positioned before the dichroic mirror and the lens, due to spatial constraints and the suboptimal nature of passing uncollimated light through the

⁷ AQWP10M-580 from Thorlabs

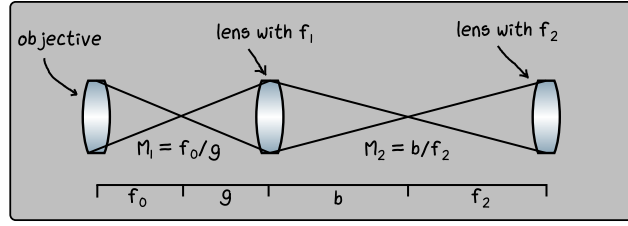


Figure 8.14: General schematic of a three-lens system.

wave plates. Testing of the setup has indicated that an additional half-wave plate in the sodium beam is beneficial in improving the circularity of the polarization.



To compensate the objective for the MOT beam, the easiest solution would be to build a 1:1 telescope. However, this is not feasible in our setup due to spatial constraints.

8.6.2 Optics

This subsection provides detailed information about the lenses selected to compensate for the imaging objective and their precise positioning. To achieve this compensation, a three-lens system is employed, comprising the high NA objective and two additional lenses. A general schematic of such a three-lens system is presented in Figure 8.14.

In our configuration, the first lens is a high numerical aperture (NA) objective with an effective focal length of $f_0 = 30.05$ mm. The remaining two lenses must be selected based on two criteria. Primarily, the lens situated at the centre must satisfy the thin lens equation. Secondly, the total magnification must be equal to one, ensuring that the diameter of the outgoing beam is identical to that of the incoming beam. The two criteria are expressed in the following equations:

$$\frac{1}{f_1} = \frac{1}{b} + \frac{1}{g} \quad (8.7)$$

$$M_1 M_2 \stackrel{!}{=} 1 \quad \text{with} \quad M_1 = \frac{f_0}{g}, \quad M_2 = \frac{b}{f_2}. \quad (8.8)$$

The distances g and b may be selected to accommodate the mechanical constraints of the setup. In our particular case, the lower bound of g is constrained to approximately 28 mm due to the objective holder, without accounting for an air gap. The maximum value of g is constrained by the overall distance between the atoms and the optical table of 440 mm, with additional restrictions imposed by other components. The combined dimensions of the science chamber and objective holder necessitate a minimum of approximately 120 mm, while the planned imaging beam height is 100 mm, reducing the maximum value of g to 220 mm. Furthermore, the thickness and diameters of the optical components must be taken into account.

In consideration of the available lenses and our constraints, a first com-

compensation lens⁸ with $f_1 = 50$ mm and a second lens⁹ with $f_2 = 60$ mm were selected. With this lens configuration, the distances are $g = 75$ mm and $b = 150$ mm.

The configuration of all components along the z-axis is illustrated in Figure 8.15. In the planned setup, the initial compensation lens ($f_1 = 50$ mm) and a mirror are moved into the vertical axis with a translation stage. The translation stage is moving in and out along the MOT beam axis, thus avoiding blockage of valuable space. The distance between the first lens ($f_1 = 50$ mm) and the second lens ($f_2 = 60$ mm) is 180 mm. Consequently, the dichroic mirror combining sodium and potassium light, as well as the second lens for potassium, must be mounted above the sledge of the translation stage. This configuration allows for sufficient space for the imaging optics below. The translation stage is planned to be built on a breadboard together with the other optics, with a beam height of 90 mm with respect to the breadboard.

8.6.3 Lens and Mirror Holder

As previously discussed, there is a limited range of motion available for adjusting the position of the mirror. It was thus necessary to develop a stable and compact mount for the lens and mirror, to be mounted on the translation stage. The mount must permit vertical adjustment of the lens in order to align it with the final objective position, which is currently estimated. Given that the mount will be situated in close proximity to the atoms, it was constructed from *PEEK* in order to avoid eddy currents and magnetisation. Figure 8.16 illustrates the mount for the lens and mirror, the technical drawings are provided in Appendix A.4.

The lens is mounted in a circular holder with a rim of a smaller diameter, which serves to support the lens at the edge. This results in a clear aperture of 37.5 mm. The thickness of the holder is set at 12 mm, which is less than the thickness of the lens. This allows the lens to be affixed to the holder via its side surface. The lens holder is secured into a slot in the mirror mount with a precise fit, enabling vertical translation with minimal rotational play. An engraved ring on the lens holder indicates the principal plane of the lens, which is 17.65 mm from the upper lens surface.

The mirror holder features a 45° angled surface with extending edges, designed to provide support for the mirror. The angled surface is of a greater width than the mirror itself, allowing the side of the mirror to be glued to the mount. A vertical slot permits translation of the

⁸ $f = 50$ mm, $d = 40$ mm achromatic lens from *Edmund Optics* 89-683

⁹ 2" lens from *Thorlabs*

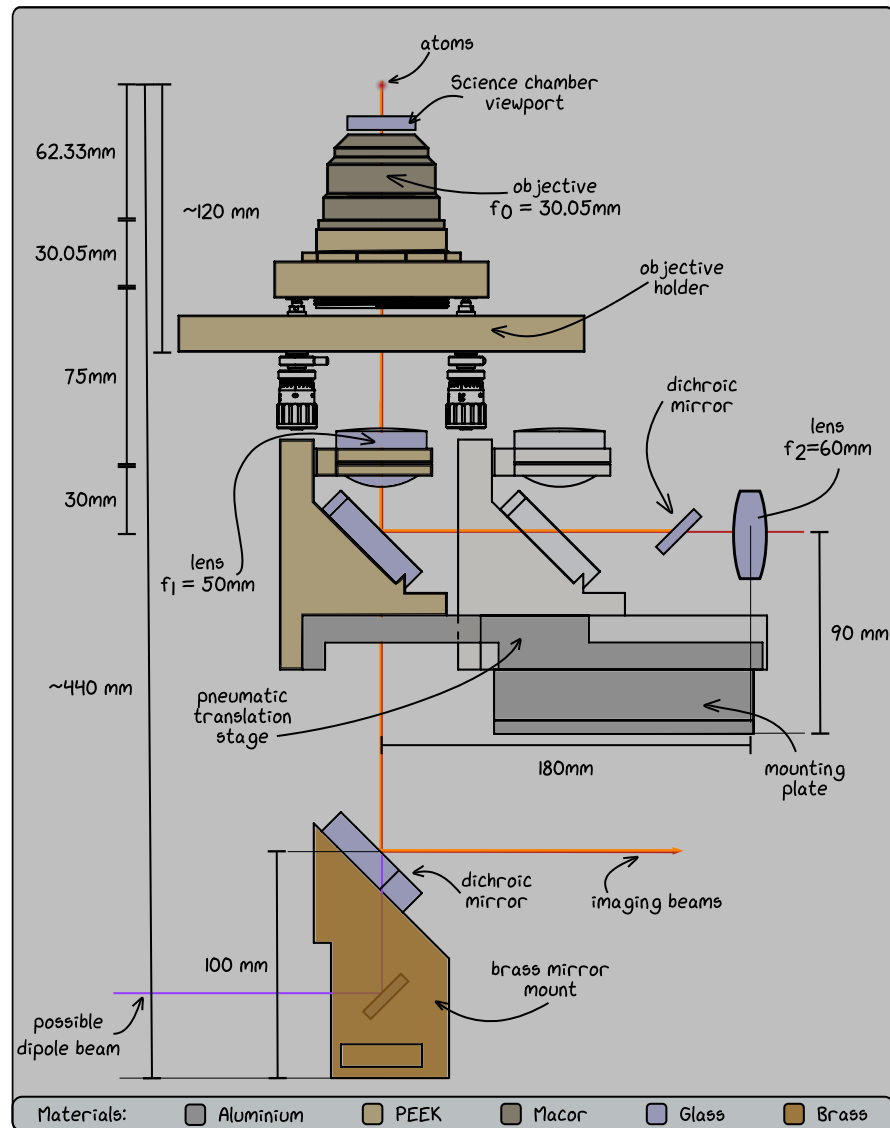


Figure 8.15: Detailed sketch of the MOT compensation optics for the vertical imaging setup. The arrangement of all components along the z -axis is illustrated. Measured distances between the atoms (MOT) and the objective holder is 120 mm, and the distance between the atoms and the optical table is 440 mm. Below the objective holder, the lens $f_1 = 50$ and mirror are mounted on a translation stage, with the moved-in position depicted transparently. A dichroic mirror, which overlaps the sodium and potassium MOT light, and the second lens $f_2 = 60$ mm are mounted above the moving translation stage. During the sequence the MOT optics are moved out of the vertical axis, allowing the imaging beams to travel downward and being reflected into the horizontal plane. A special brass holder allows the potential injection of a dipole beam.

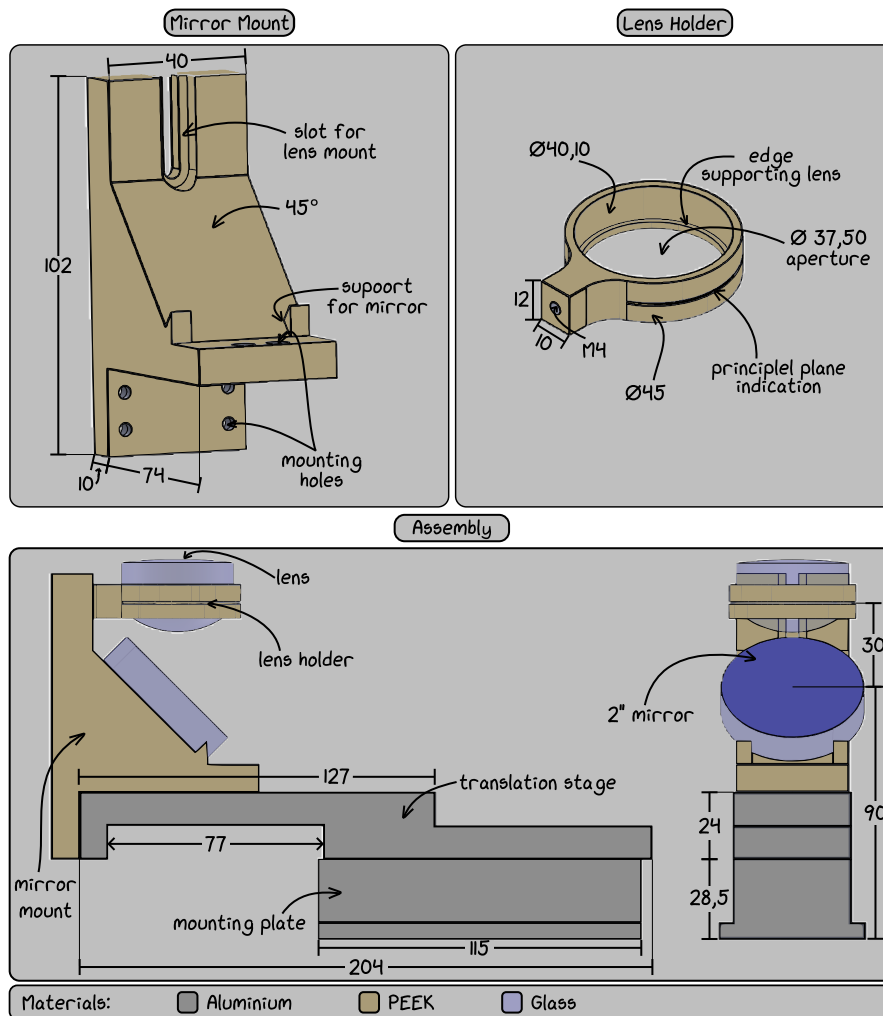


Figure 8.16: The mirror and lens mount **Assembly** includes the lens holder, mirror mount, lens, mirror, translation stage and mounting plate. This configuration has been designed with a total beam height of 90 mm with respect to the mounting breadboard. The pneumatic translation stage has a travel range of 77 mm. Both the mirror mount and lens mount are manufactured from *PEEK*. The **Mirror Mount** features a surface with an angle of 45° for the mirror, which is supported on two edges and glued to the holder. Moreover, a vertical slot is present in the mirror mount, which enables vertical translation of the lens holder. In the **Lens Holder** the lens is supported by the edge of a rim with a thickness of 2 mm, resulting in a clear aperture of 37.5 mm. The lens holder is of a lesser thickness than the lens itself, thus allowing the lens to be glued at the side. A cut-out indicates the principal plane of the lens. The lens holder is mounted to the mirror mount with an M4 screw.

lens. The mirror mount is of a compact design, with the intention of reducing the load on the translation stage.

All components, including the translation stage and additional optics such as secondary lenses and dichroic mirrors, are mounted on a breadboard with a beam height of 90 mm. Consequently, the height of the mounting plates is adjusted to 28.5 mm. The mounting plate has rims on both sides, allowing the translation stage assembly to be securely clamped to the breadboard.

8.6.4 *Pneumatic Translation Stage*

The pneumatic translation stage used for moving the lens and mirror in and out during the experimental sequence must meet several criteria. These include the ability to be externally triggered, reliability over many cycles, precision with minimal deviation, speed, and construction from non-magnetic materials. In order to meet these requirements, a pneumatic translation stage from *Festo*¹⁰ was selected, as this is already used in the BECK experiment for the same purpose [166].

This pneumatic translation stage is designed for industrial environments, ensuring high durability with a large number of duty cycles. The stage features precise end position adjustment via a set screw and a repetition accuracy of less than 0.02 mm. The speed of the stage is 0.8 m/s, which corresponds to a movement time of 100 ms and is thus adequate for our purposes. Furthermore, the stage is made of aluminium, which is suitable for our non-magnetic requirements. However, since the stage incorporates magnets on the guiding rods, which are typically employed for position sensing in industrial applications, we have removed these magnets. This was achieved by disassembling the stage and manually removing the magnets with pliers, as illustrated in Figure 8.17.

It is our aim to control the translation stage from our experimental control system, which uses a TTL signal of 5 V. However, the stage operates on 24 V, which means that it cannot be connected directly to the experimental control system. A *MOSFET* circuit is employed to switch the 24 V supply using the 5 V TTL signal. The operation of the stage is based on the inversion of the compressed air flow, which causes the stage to move in or out depending on the direction of the air flow. The valve has five connections with two states of configuration, generically referred to as "on" and "off", which determine the two positions of the stage. Specifically, the compressed air input is connected to port 1, the stage is connected between ports 2 and 4, and ports 5 and 3 are connected to the laboratory's exhaust system to prevent the accumulation

¹⁰ *Festo* DGST-8-80-Y12A with VUVG-L10-M52-MT-M5-1R8L (solenoid valve) and GRLA-M5-QS-6-D (one-way flow control valve)

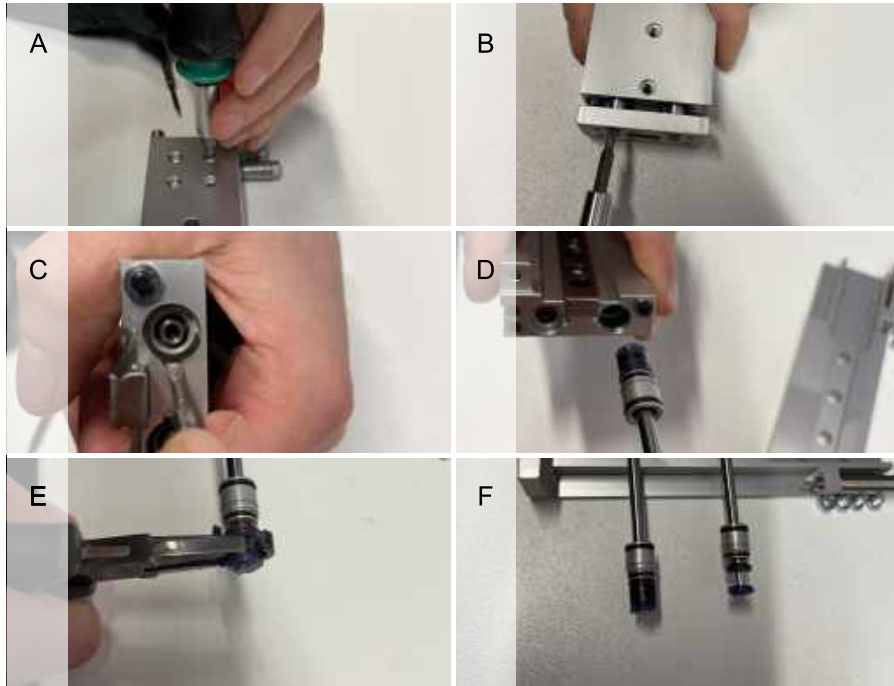


Figure 8.17: Procedure for removing magnets from a pneumatic translation stage. First, unscrew the carriage from the top (**A**) and side (**B**). Next, remove the retaining ring from the guiding rods (**C**) and take out the rods (**D**). The magnet, located between the two silicon rings at the end of the rod, can be removed by firmly squeezing it with pliers (**E**). The magnet typically breaks into two halves, which can then be removed cleanly from the rod (**F**). After removing both magnets, reassemble the translation stage.

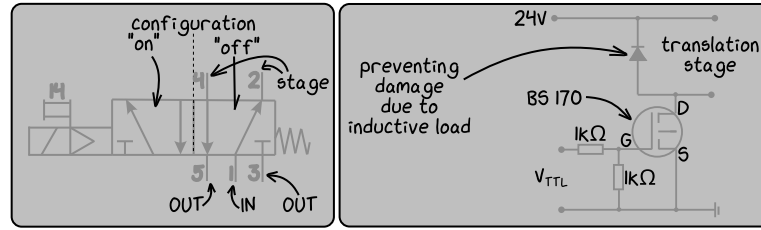


Figure 8.18: **Left:** Schematic of the valve ports and connections. The translation stage is connected between ports 4 and 2. The valve has two configurations, labelled "on" and "off", which control the direction of the airflow between these ports, thereby moving the stage forward or backward. The specific effect of "on" and "off" depends on how the stage is connected to the valve, hence the generic labelling. Pressurized air is supplied to port 1, with exhaust connected to ports 5 and 3. **Right:** Electronic circuit for controlling the valve. The valve requires a 24 V operating voltage, and is controlled via a standard *MOSFET BS170* with a 5 V TTL signal from the experimental control system. To protect the *MOSFET* from potential damage due to the inductive load of the translation stage, a parallel diode is included to redirect any inductive currents.

of dust on the optics. The electronic circuit and valve connections are detailed in Figure 8.18.

8.7 SUMMARY AND DISCUSSION

In this chapter, the planned vertical high-resolution imaging setup was described in detail, including the necessary modifications to the vertical MOT beam.

The objective was tested in a separate setup, where resolutions close to the diffraction limit were observed. Although the true diffraction limit was not achieved, likely due to aberrations in the test setup, the required resolution of $1\ \mu\text{m}$ for resolving typical density changes was attained. A small focus shift between sodium and potassium was observed, attributed to the focal shift of the secondary lens rather than the objective. The field of view provides near-diffraction-limited resolution over several hundred micrometers in the x-direction and at least $80\ \mu\text{m}$ in the vertical direction, making it well-suited for observing the BEC in the two-dimensional optical dipole trap with a typical size of roughly $50\ \mu\text{m}$. During the characterisation of the objective, it was found that the alignment of the secondary lens is critical to the performance of the system, which is also reported in Sergei Piatchenkov's PhD thesis [112]. It should therefore be mounted in a way that allows precise alignment¹¹.

¹¹ For example the precision lens positioner *LP-2A* from *Newport* used in [112]

To implement this imaging setup, two lenses are used to compensate for the objective in the vertical MOT beam. The first lens, used for both species, and a mirror reflecting the MOT beam into the vertical axis, are mounted on a pneumatic translation stage. This configuration allows the optics to move in the beam direction, preserving space for additional optics nearby. Detailed spatial arrangements of all components in the vertical axis, as well as the control mechanism for the pneumatic translation stage, including the electrical circuit and valve connection outline, are provided.

The components are ready for assembly, although a critical evaluation of the setup is not possible at this stage, as it has not yet been built. There is no doubt that the setup will work as desired, as a similar setup has been successfully implemented in our neighbouring experiment, the BECK experiment, without problems [166]. The alignment procedure for the objective to ensure vertical alignment to gravity is described by Maurus Hans in [166]. The imaging beam and the objective have to be aligned with respect to gravity, this was done by using methanol¹² as a liquid mirror.



The exact position of the lens is not critical for achieving an initial MOT - the implementation of the compensation optics in the BECK laboratory has shown that an MOT can be achieved by holding the lens by hand. However, for proper alignment, especially for the D1 grey molasses, precise positioning with a suitable translation stage is essential. It was even thought to not work.

¹² Methanol has the lowest surface tension of standard laboratory liquids.

SUMMARY AND OUTLOOK

SUMMARY

The work presented in this thesis reports progress and challenges towards the creation of a versatile and tunable ultracold atomic mixture experiment using sodium and potassium.

A brief overview of the SoPa experiment is given, outlining the possible building blocks of the experimental sequence. The major changes made during the laboratory rebuild, where the NaLi experiment was dismantled and the SoPa experiment was redesigned, keeping only the previous vacuum system and making full use of the laboratory space, are described. Achieved milestones, such as the sodium Bose-Einstein condensate (detailed in Jan Kilinc's PhD thesis [167]), current setbacks, such as the degradation of the spectroscopy cell, and challenges, such as the poor overlap between the trapping stages (detailed in Anton Eberhardt's master's thesis [90]), are outlined to provide an overview of the experiment.

While all these topics are outlined very briefly, the thesis focuses more on the description of the vacuum setup and the two-dimensional magneto-optical trap (2D MOT) setup.

The SoPa vacuum system consists of a two-chamber solution with a differential pump stage separating the two chambers. This design allows high vapour pressures in the 2D MOT and oven region while maintaining excellent ultra-high vacuum conditions in the science chamber. Decoupling of the atomic species is achieved by providing a 2D MOT chamber for each species. Furthermore, we discuss design considerations for a vacuum system in the field of ultracold atoms, such as the optical access to the chambers, the material of the components used and the different atomic sources available, as well as the damage potential of the atomic beam. In addition, the vacuum chapter covers various vacuum problems encountered in the SoPa and NaLi experiments, providing insights into the assembly of vacuum components, baking, flooding, oven cleaning and filling, and observations such as corrosion of viewports and deposits. While not all of these phenomena can be explained, at least one hypothesis is offered and the implications for experimental performance are discussed.

The second focus of the thesis is the 2D MOT setup, where both the optical layout and the quadrupole magnetic field generated by permanent

magnets are described. The two atomic species are completely separated at this stage, but the setup is largely identical. For the 2D MOT, four independent beams are used, while the quadrupole magnetic field is generated by four stacks of permanent magnets. For the sodium 2D MOT, an additional beam is used which, together with the magnets, acts as a small Zeeman slower for the sodium atoms. In addition, the optimisation routine of the 2D MOT is outlined, where we optimise the 2D MOT to the loading rate of the 3D MOT.

The described experimental setup of the vacuum system and the 2D MOT is critically discussed, as main drawback of the system the compact design of the 2D MOT chamber could be identified. The 2D MOT chamber design causes problems in both the sodium and potassium chambers. While potassium was thought to suffer from "vacuum problems" [76–78]. The leakage current measurements performed indicate that the vacuum problems are caused by leakage current due to potassium deposits on the ion pump. In the sodium 2D MOT chamber, sodium deposits coat and corrode the viewports. For potassium, a cold spot ahead of the ion pump could reduce the amount of potassium reaching the ion pump. For sodium, modifying the 2D MOT chamber to increase the distance between the oven and the viewport or upgrading the magnets ones that can withstand higher operating temperatures could help.

The plan for the near future of the experiment was then discussed. In particular, we focused on the implementation of a two-dimensional optical trap and the associated high-resolution vertical imaging system. To achieve the 2D trap, we are currently implementing an optical dipole trap using a surfboard geometry. We have chosen this approach as a compromise between rapid achievability, ease of construction and experimental constraints. The surfboard geometry uses a single red-detuned laser beam, elliptically shaped to provide high confinement in the z -direction. A knife edge measurement confirmed the theoretically expected beam waist of $21\ \mu\text{m}$. The alignment routine, signal hunting and optimisation approaches are outlined and a first signal from the 2D trap was observed during the writing of this thesis.

The vertical imaging setup has been designed and is described in Chapter 8. In order to characterise the objective, we implemented a test setup to show that resolutions at the diffraction limit can be achieved. The measured resolution is close to the diffraction limit, which we attribute to aberrations caused by slight misalignments in the test setup. Accurate alignment of the secondary lens of the imaging setup was found to be critical and we observed a near diffraction limited resolution of $1\ \mu\text{m}$ over a range of $160 \times 80\ \mu\text{m}^2$, meeting the experimental requirements. Since one of the MOT beams also propagates in the vertical

axis, compensating optics are required. Consequently, the design of the compensating optics is described in detail. Parts of these optics have to be moved in and out of the optical path during each experimental sequence to allow switching between the MOT phase and the imaging phase. The mechanical setup, including the custom optic mounts and control electronics, have been designed. All parts have been manufactured or ordered and are ready for installation.

Overall, this thesis lays the foundation for the development of a robust ultracold atomic mixture platform, while discussing experimental challenges and providing solutions to improve the stability and current performance of the experiment. The future implementations of the vertical imaging setup are described in detail so that they are ready for integration. By providing insight into both the technical challenges and solutions, it is hoped that other experiments will benefit and contribute to progress in the field of ultracold atoms.

OUTLOOK

After achieving the Bose-Einstein condensate, the next goal was and is dual-species degeneracy in two dimensions, including a high-resolution imaging system to observe the atoms. The steps needed to get there can be divided into three categories: technical issues of the experimental setup, the experimental cooling sequence, and future implementations that will extend the experimental setup.

TECHNICAL PROBLEMS OF THE EXPERIMENTAL SET-UP This category is slow to resolve as the problems need to be identified before they can be addressed. For the 2D MOT chambers, we have successfully identified several of these and are considering possible solutions. The problem with potassium is leakage current in the ion getter pump due to potassium deposits in the ion pump. Although in principle the performance of the ion pumps is not affected, it can be helpful for debugging purposes to have an estimate of the pressure, and in the NaLi experiment deposits in the ion pumps led to repeated malfunctions in the later stages of the experiment. A cold spot in front of the ion pump is planned to protect the ion pump from the potassium vapour by ensuring that the potassium atoms stick to the cold wall.

The sodium situation is more critical. The viewports are regularly coated and blocked by sodium, one viewport has recently corroded and developed a leak, and the sodium oven is showing signs of exhaustion. All of these problems lead to poor or no performance of the 2D MOT and therefore to the stoppage of the entire sodium cooling sequence as it is the preparation step for the following cooling steps. There are two ways to proceed from this point. One is to open the vacuum chamber, refill the oven with sodium, replace the leaking viewport and add nip-

ples between the chamber and the viewports to increase the distance to the oven. While this has the potential to solve the problems in the long term, these changes will not only be time consuming to re-establish the UHV vacuum, but the 2D MOT optics will need to be adapted as the viewports are at different heights. On the other hand, we can decide to keep the vacuum chamber sealed and heat the viewports to higher temperatures to effectively keep the centre free of deposits. This would require replacing the permanent magnets with ones that can withstand higher temperatures, as the chamber would also be heated.

While the resolution of technical issues is critical to maintain the stability of the experimental setup and thus the progress of the experiment, these issues must be identified and addressed in parallel with the development of an efficient cooling sequence, which is essential to achieve dual-species degeneracy.

EXPERIMENTAL COOLING SEQUENCE To achieve a dual species condensate, the experimental sequence must be optimised to efficiently cool both species. Identified challenges are significant three-body losses in the highly confined magnetic trap [168] as well as poor overlap between the different trapping stages [90]. Therefore, the current aim is to avoid the magnetic trap altogether and to cool the atoms in an all-optical approach. Therefore, the D1 grey molasses technique is used for both species to cool both species to sub-Doppler temperatures before both are loaded directly into the crossed optical dipole trap. In this scenario, the bias magnetic field can be set directly to 150 G, where the scattering rates are favourable for two species condensation [39].

Although this approach is considered promising, challenges may still arise. It is possible that light assistant collisions in the MOT stage will lead to atom losses and lower atom numbers. To overcome this, a double dark SPOT could be a solution, as reported in a recent experiment with sodium and potassium-40 [36]. Alternatively, sequential loading of the two species to the extent that both species are loaded completely separately, with sodium held in a flat magnetic trap in the $|F = 2, m_F = 2\rangle$ state [43]. The latter two options have been tried and found not to be superior to simultaneous loading.

Multicolour MOTs using D2 and additional D1 light have also been shown to reduce light assistant collisions in MOTs [68] and have recently been implemented for mixing experiments with rubidium and potassium-40 [167].

Due to the D1 grey molasses, the sample volume is quite large compared to the typical trapping volume of an optical dipole trap. Typical approaches are a compressed MOT phase before the molasses to confine the atoms and avoid too large a cloud of atoms after the molasses. The two-colour compressed MOT has been observed to achieve a lower temperature than the D2 compressed MOT [68] and has recently been implemented in a mixture experiment using sodium and potassium-40

[36]. Alternatively, the volume of the crossed optical dipole trap can be effectively increased by modulating the dipole beams [169].

While many cooling techniques are available, the right combination for the SoPa experiment remains to be identified. Achieving the desired two-dimensional experimental geometry requires the precise alignment of the 2D optical dipole trap and the construction of the high-resolution vertical imaging system. Ideally, these hardware components would be aligned and built while both species are available. However, due to the current challenges of working with both species simultaneously, whenever setbacks occur with one species, the focus is shifted to hardware implementation until the dual-species sequence can be optimised.

FUTURE IMPLEMENTATIONS EXTENDING THE EXPERIMENTAL SETUP The next step towards the desired geometry is the correct alignment and reliable loading of the 2D optical dipole trap. The aim is to use the loading of the 2D optical dipole trap as a signal to align the vertical imaging. The objective has to be precisely aligned with respect to gravity, this has already been done in the BECK experiment [166] using the surface of methanol in a container as a water level mirror to align the imaging beam and the objective. In order to install the imaging system, the vertical MOT beams have to be realigned with the planned compensating optics. It is therefore necessary to re-optimize the MOT afterwards.

Looking further into the future, it is advantageous to have not only a harmonic two-dimensional trap but also a box potential, allowing direct comparison with proposed theories and avoiding effects such as the buoyancy effect [60, 62–64], where atoms separate in a miscible region due to the harmonic trapping potential. To achieve a flat trap, the harmonicity of the surfboard trap has to be compensated by additional laser beams.

While the surfboard trap can be flattened relatively easily with two beams, the potential walls are still harmonic. A Digital Micro Mirror Device (DMD) setup, as implemented in the BECK experiment, allows arbitrary potential shapes, but also phase imprints, which are essential for many experimental scenarios.

After the successful loading of the two species into the 2D optical dipole trap and the implementation of the vertical imaging system, the first experiments can be performed. The study of the demixing dynamics is a fundamental physical question, where the miscible mixture is quenched to the immiscible regime leading to domain formation. The time evolution and domain size can be observed for different settings of interaction strengths and population imbalances. Understanding the demixing behaviour for different populations and interaction strengths will not only be an exciting first experiment, but will also enhance our ability to finely control the experiment. This is the gateway to a flexible

and versatile machine that will allow us to pursue the most compelling research directions in the landscape of quantum many-body problems.

In ultracold atom experiments, maintaining progress often means fighting a constant battle against system degradation - a challenge that is magnified in mixture experiments due to their inherent complexity. This makes it particularly difficult to maintain momentum over several generations of students. However, careful planning of the handover process well in advance can help ensure continuity and ultimately be rewarded with a robust and stable mixture machine.

APPENDIX

A

TECHNICAL DRAWINGS AND SPECIFICATION SHEETS

This section presents the technical drawings of the components designed for the experimental setup during this thesis. In addition, for the benefit of future students, specification sheets and technical drawings of components purchased for the experimental setup are also included.

The appendix contains the following technical drawings:

Section A.1: Drawing and specification sheet of the Objective

Section A.2: Drawings for the objective holder

Section A.3: Brass holder for the bottom imaging mirror

Section A.4: Custom mounts for the MOT compensation optics

Subsection A.5.1: Drawings of the main and science chamber

Subsection A.5.2: Drawings of the 2D MOT chamber

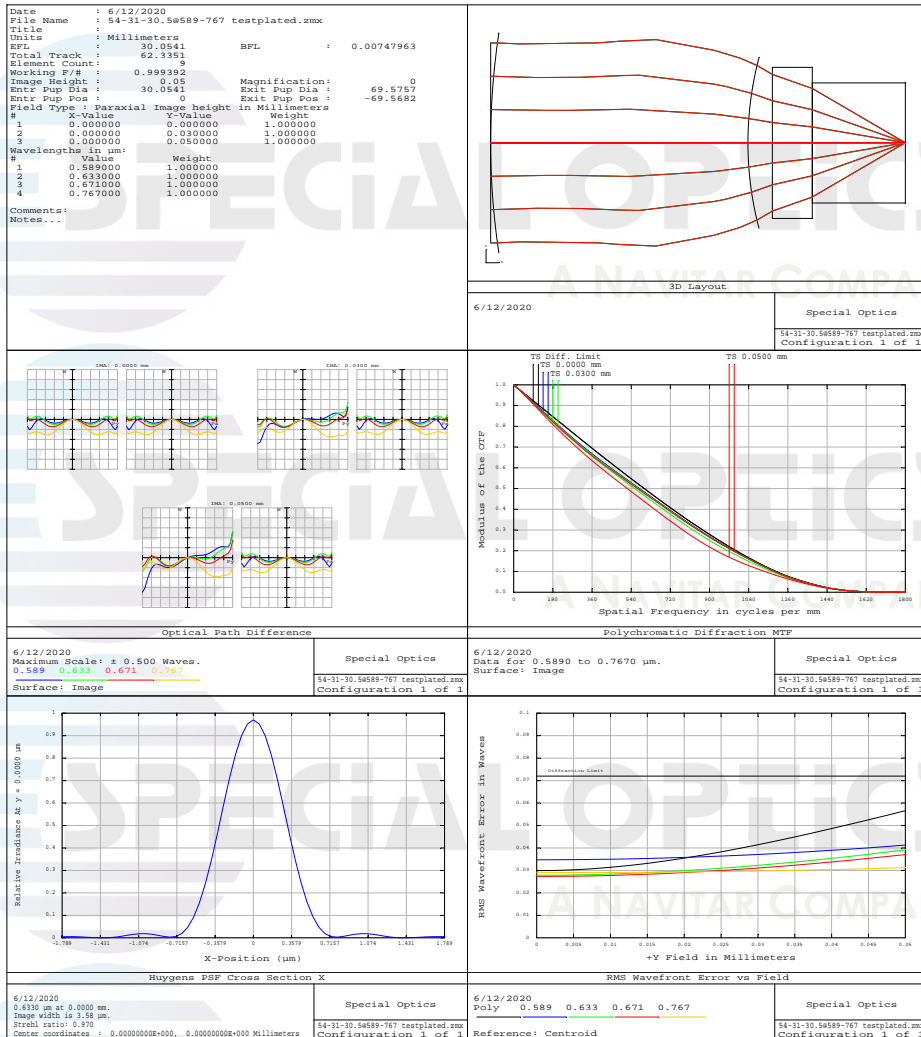
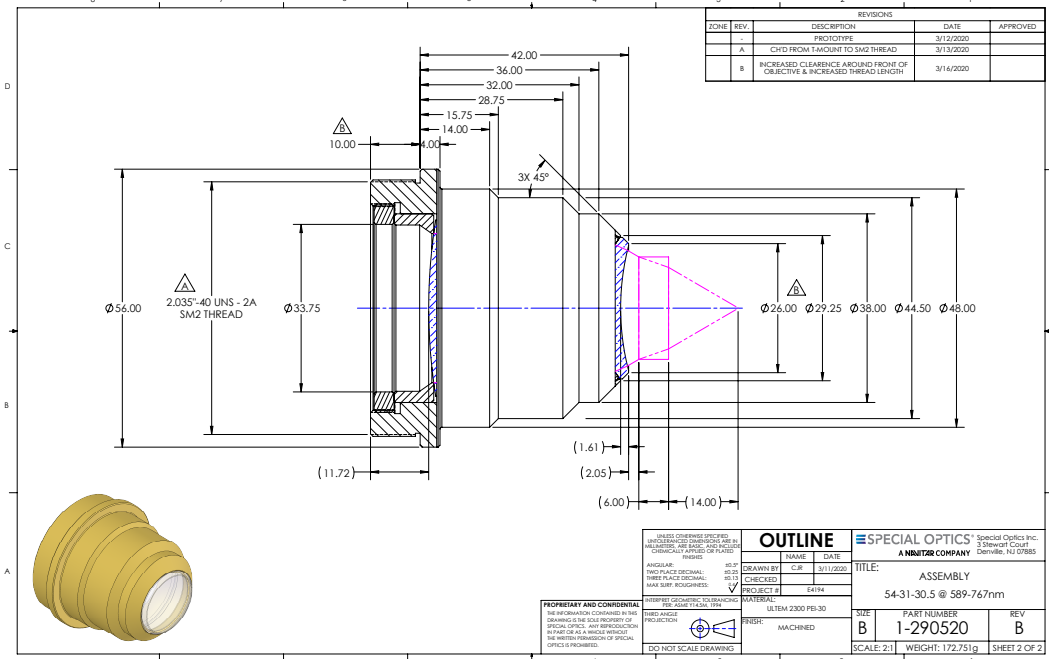
Subsection A.5.3: Drawings of the Science chamber mounting plate and clamps

Section A.6: Drawing of the block for the 2D optical dipole trap

Section A.7: Drawings for the mount of the permanent magnets for the 2D MOT

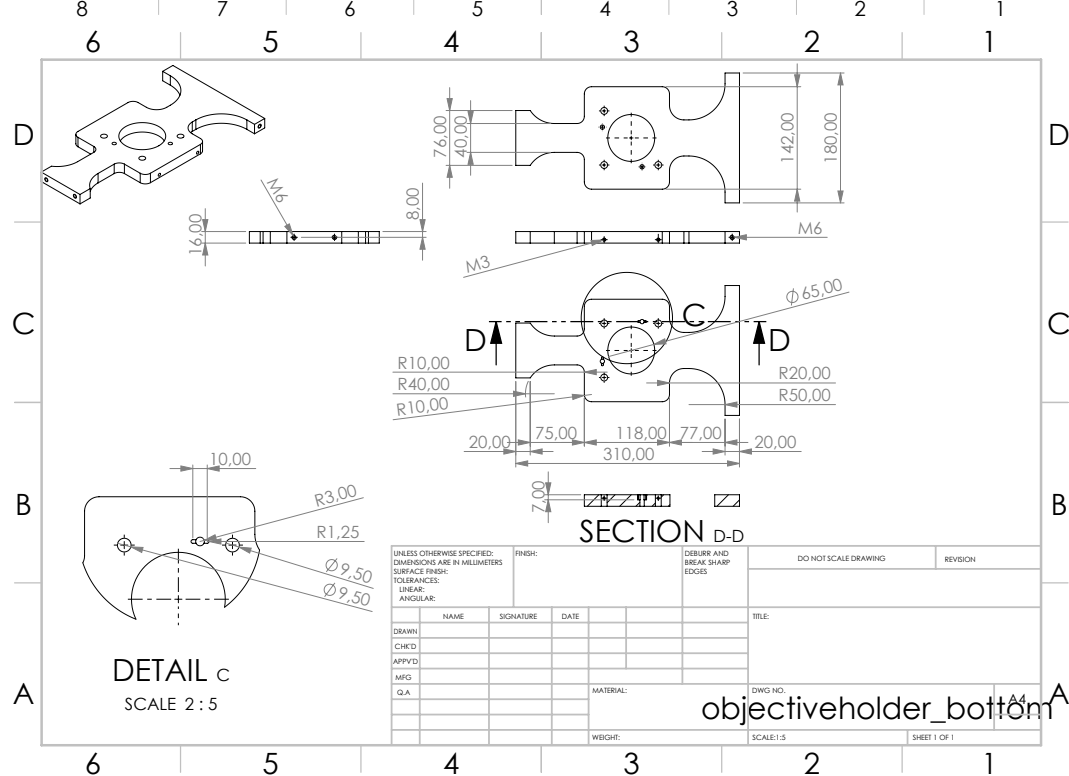
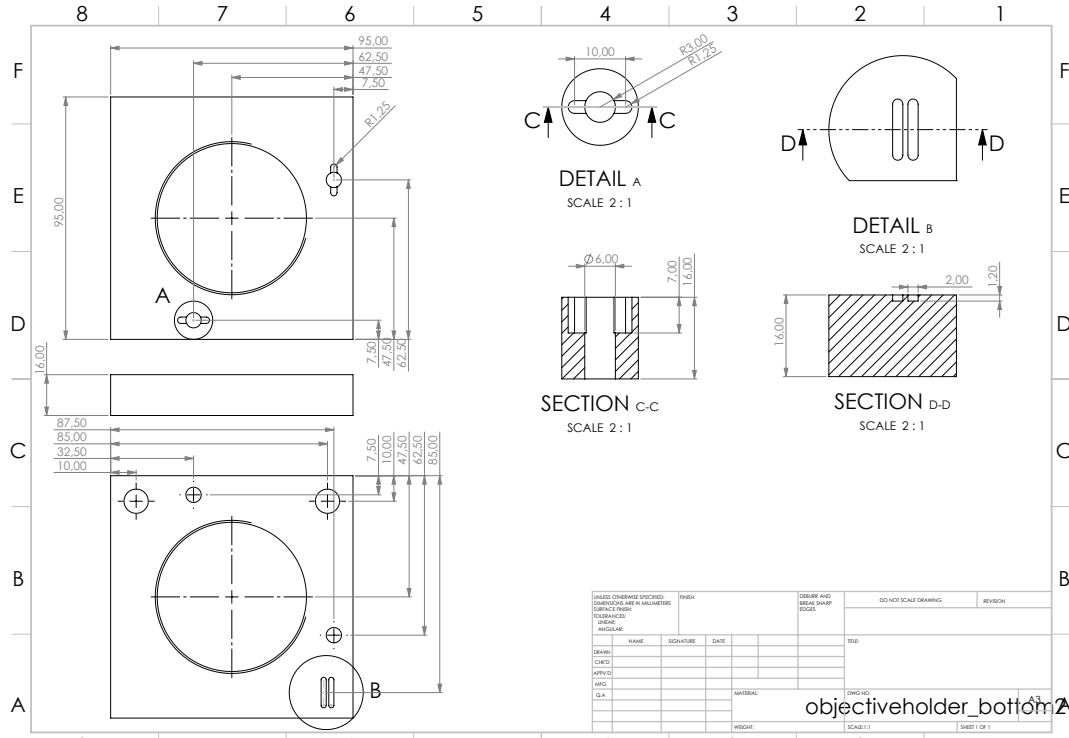
A.1 OBJECTIVE

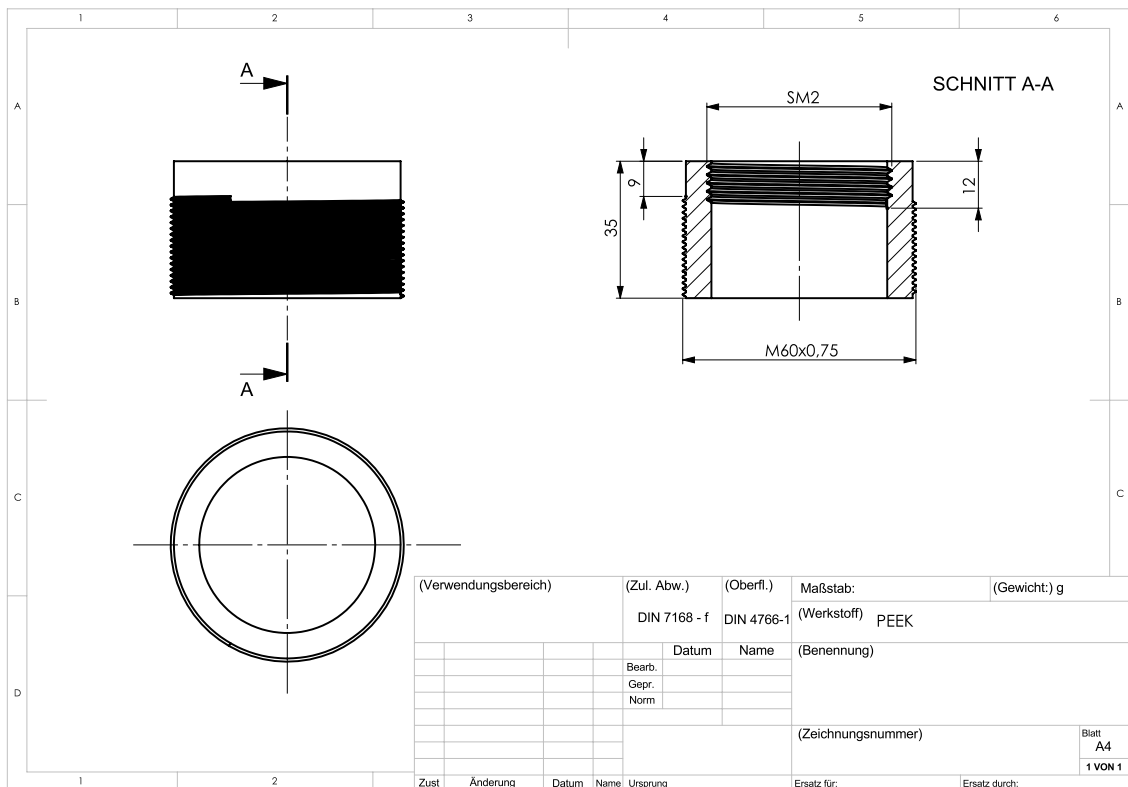
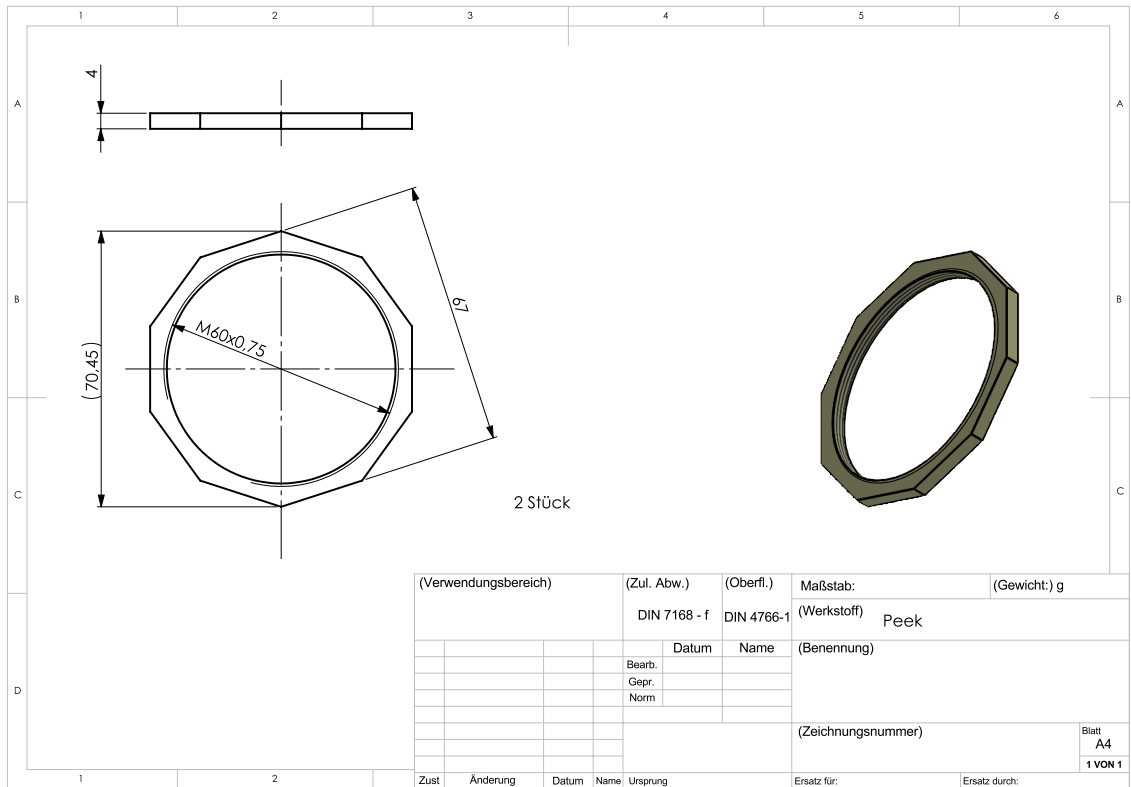
Documents of the objective kindly provided by *Special Optics*.

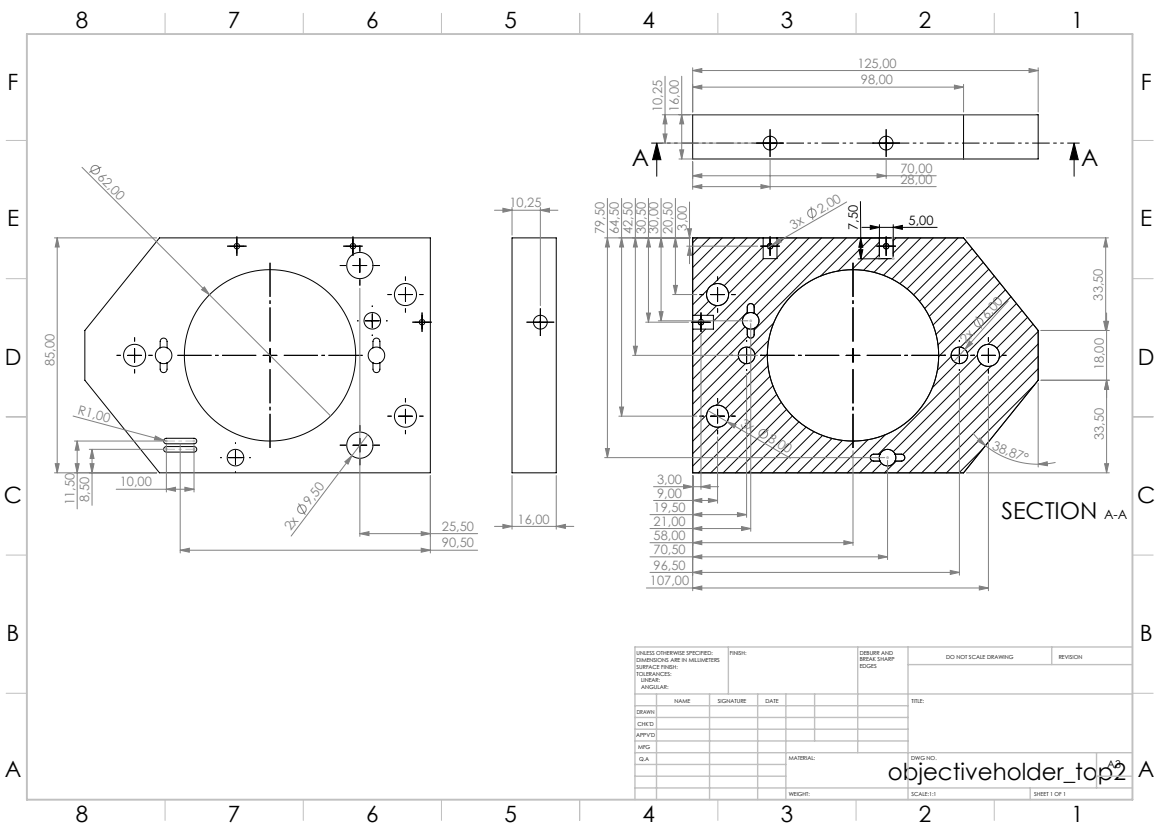
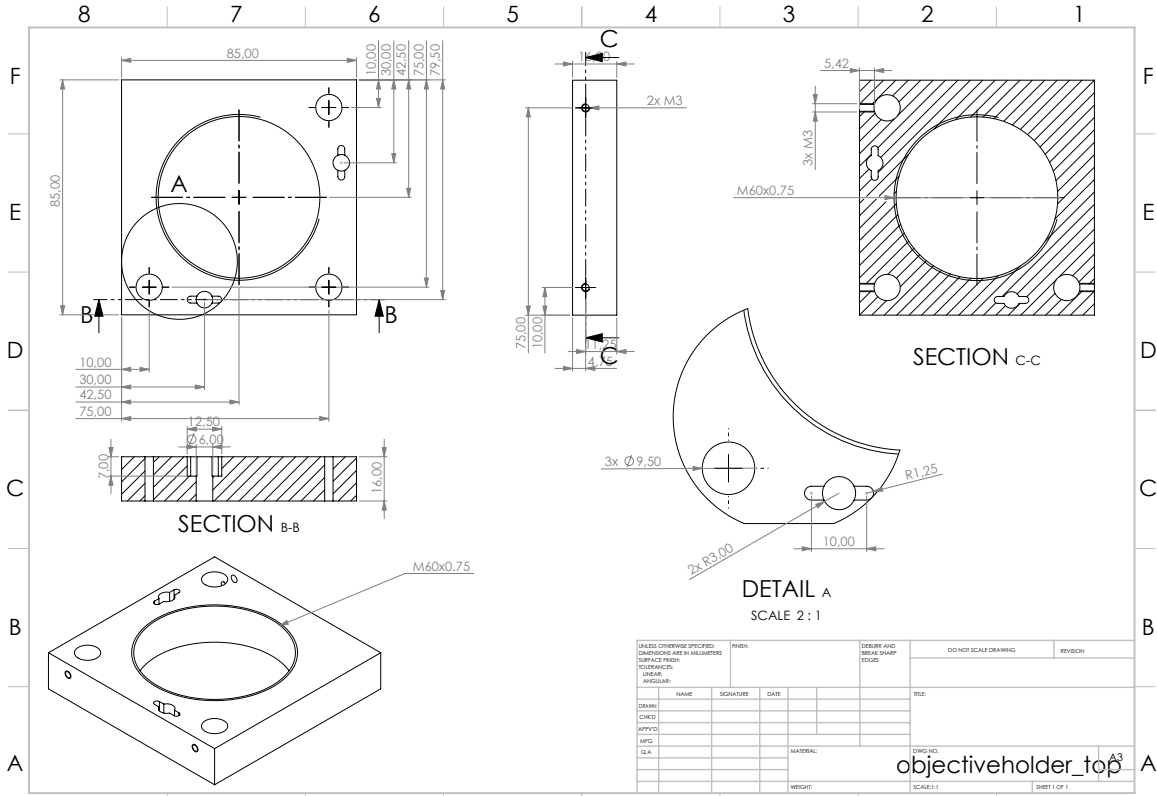


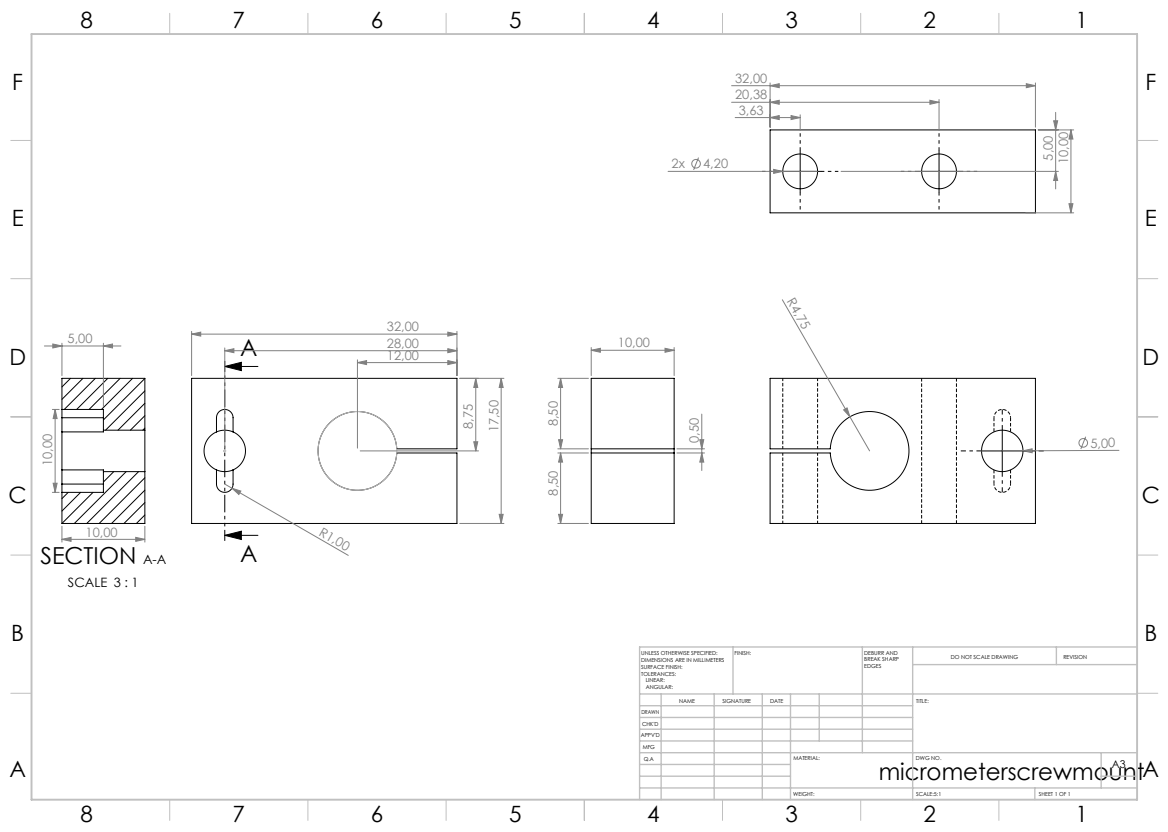
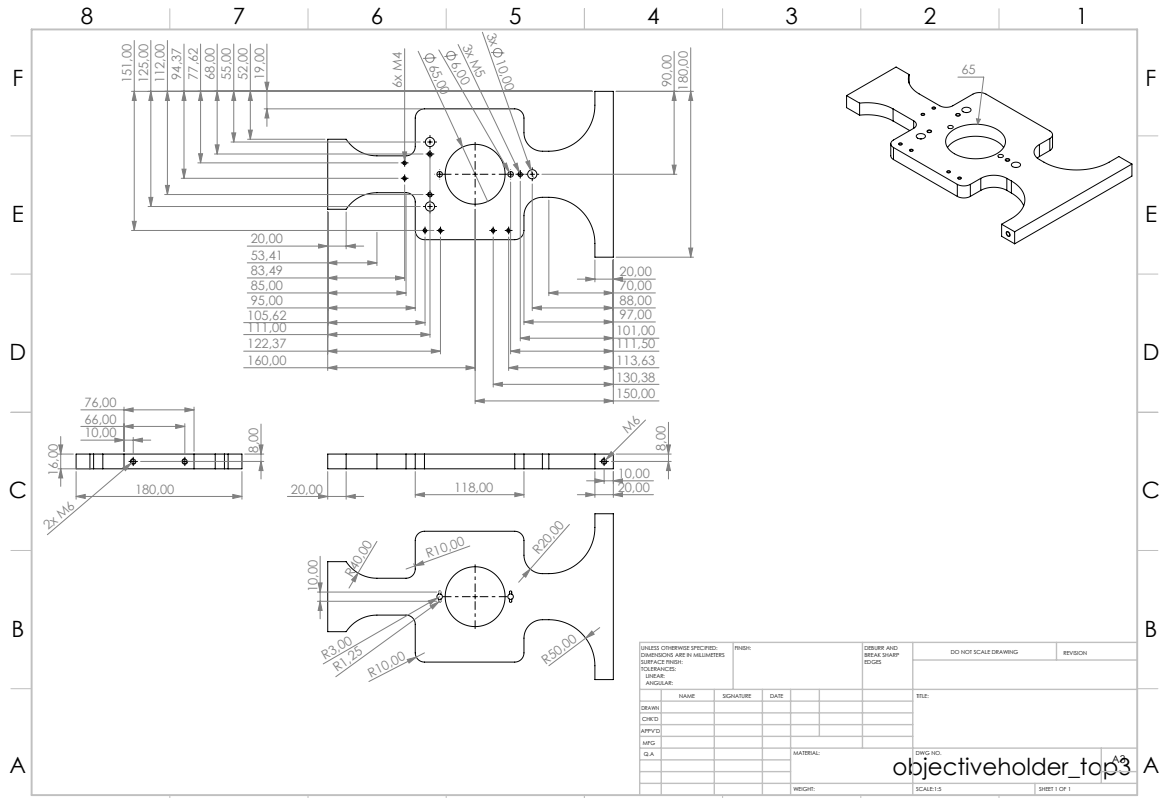
A.2 OBJECTIVE HOLDER

The objective holder is designed to hold two objectives. The design is an adopted design of the objective holder at the BECK experiment which was designed by Maurus Hans [166]. Jan Kilinc has adopted the design for the SoPa experiment.





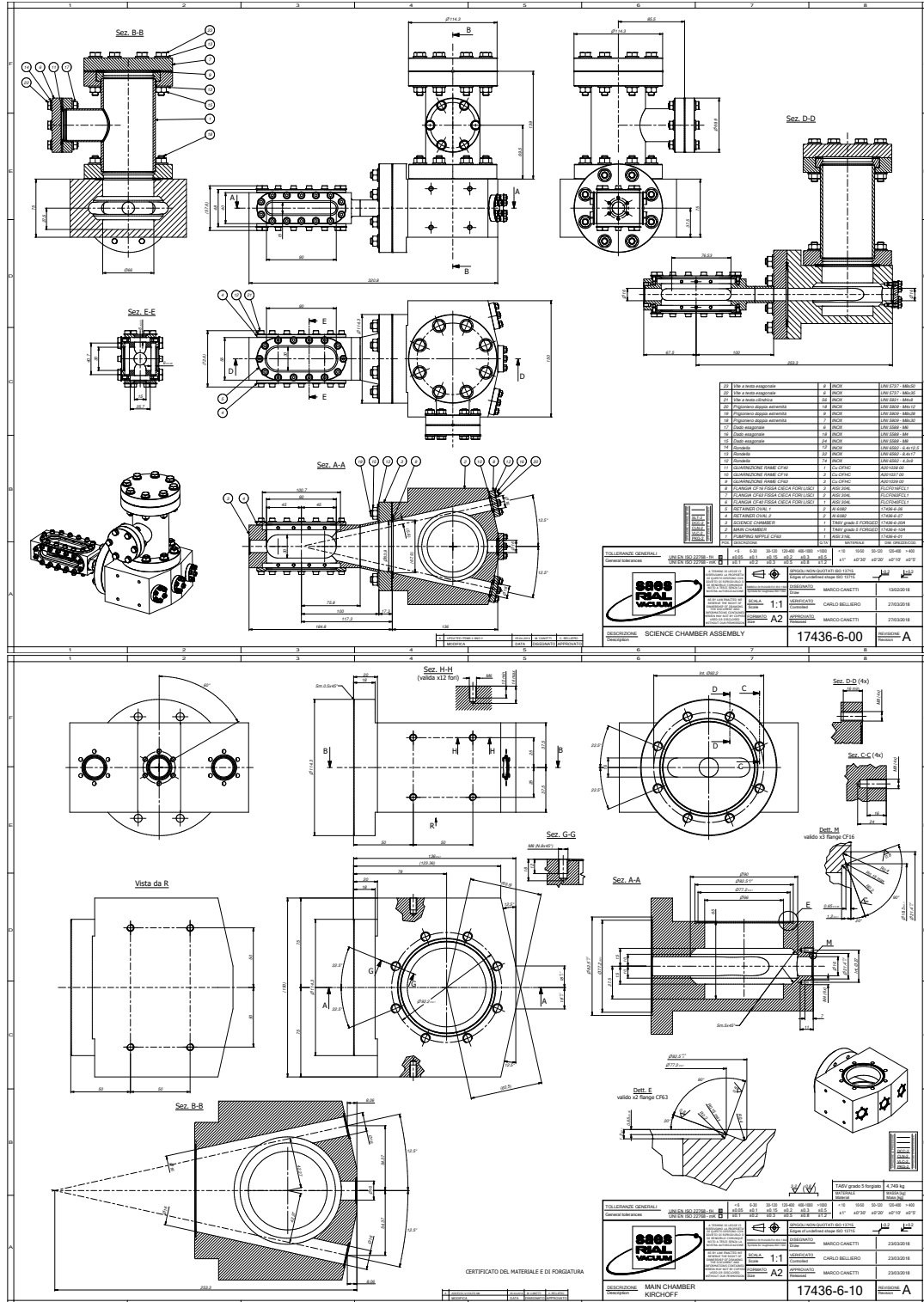


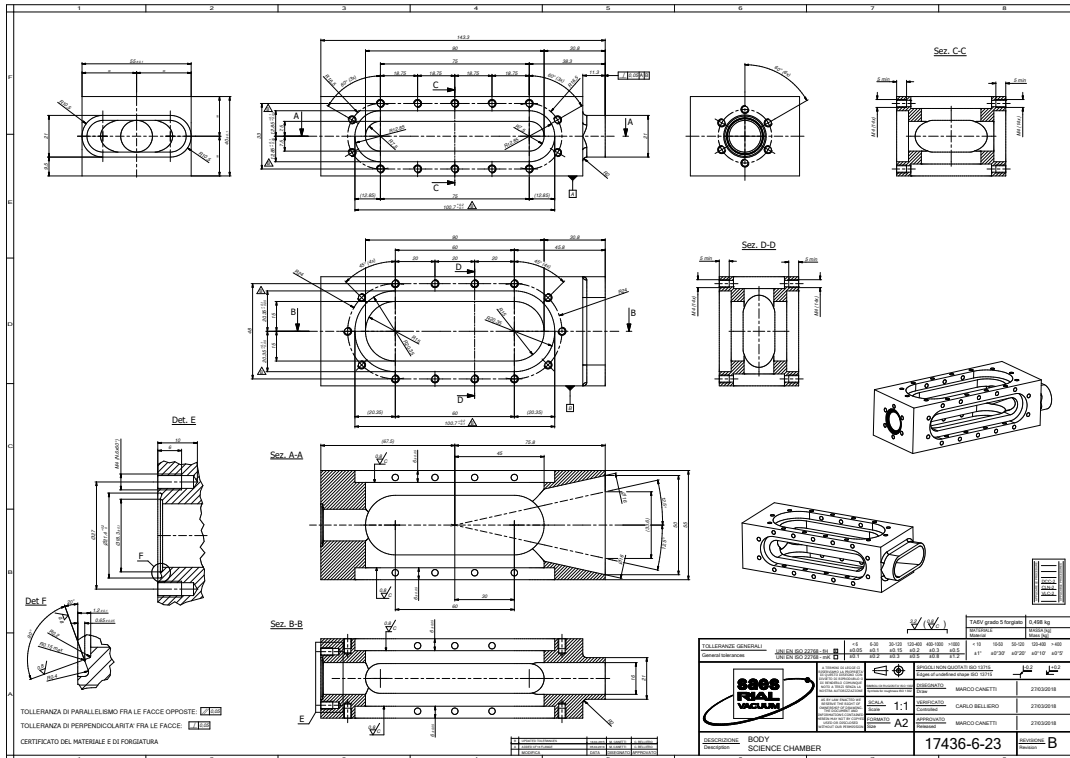


A.5 VACUUM

A.5.1 Main and Science Chamber

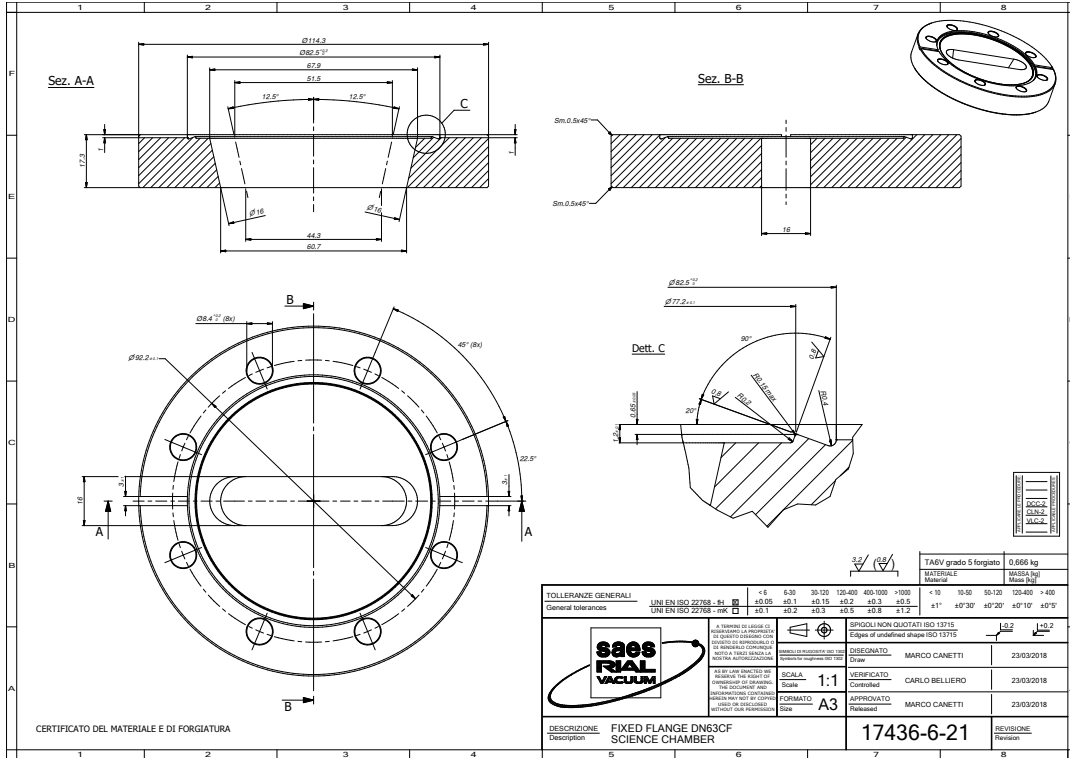
Drawings of the main and Science chamber kindly provided by *SEAS Rials Vacuum* designed by Fred Jendrzejewski.





TOLLERANZA DI PARALLELISMO FRA LE FACCE OPPOSITE ± 0.15
 TOLLERANZA DI PERPENDICOLARITA' FRA LE FACCE ± 0.15
 CERTIFICATO DEL MATERIALE E DI FORGIATURA

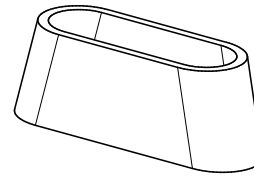
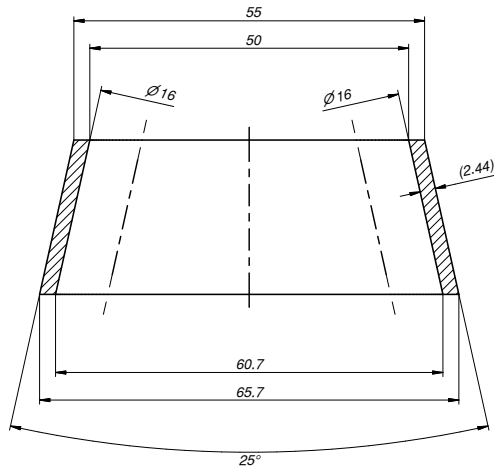
		TAVOLINO 5 forgiato 0.666 kg Materiale Massa netta	
TOLLERANZE GENERALI UNI EN ISO 22768 - h9 UNI EN ISO 22768 - h8		SPINGOLI NON QUOTATI ISO 13715 Edges of unquoted shape ISO 13715	
DESCRIZIONE Description		VERIFICATO / Controlled APPROVATO / Released	
DESIGNAZIONE FIXED FLANGE DN63CF SCIENCE CHAMBER		17436-6-23	
DATA 23/03/2018		DATA 23/03/2018	



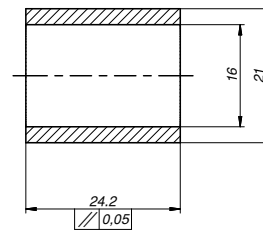
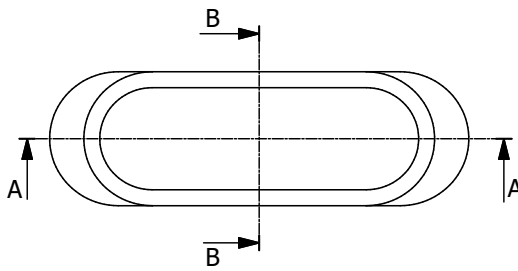
CERTIFICATO DEL MATERIALE E DI FORGIATURA

TOLLERANZE GENERALI General tolerances UNI EN ISO 22768 - h9 UNI EN ISO 22768 - h8		SPINGOLI NON QUOTATI ISO 13715 Edges of unquoted shape ISO 13715	
DESCRIZIONE Description		VERIFICATO / Controlled APPROVATO / Released	
DESIGNAZIONE FIXED FLANGE DN63CF SCIENCE CHAMBER		17436-6-21	
DATA 23/03/2018		DATA 23/03/2018	

Sez. A-A



Sez. B-B



APPLICABILE LE PROCEDURE	
DCC-2	
CLN-2	
VLC-2	



TA6V grado 5	0,037 kg
MATERIALE Material	MASSA [kg] Mass [kg]

TOLLERANZE GENERALI General tolerances	UNI EN ISO 22768 - fh <input checked="" type="checkbox"/>	< 6	6-30	30-120	120-400	400-1000	>1000	< 10	10-50	50-120	120-400	> 400
	UNI EN ISO 22768 - mK <input type="checkbox"/>	±0.05	±0.1	±0.15	±0.2	±0.3	±0.5	±1°	±0°'30'	±0°'20'	±0°'10'	±0°'5'

A TERMINI DI LEGGE CI RISERVIAMO LA PROPRIETA' DI QUESTO DISEGNO CON DIVIETO DI RIPRODURLO O DI RENDERLO COMUNE NOTO A TERZI SENZA LA NOSTRA AUTORIZZAZIONE

AS BY LAW ENACTED WE RESERVE THE RIGHT OF OWNERSHIP OF DRAWING. THE DOCUMENT AND INFORMATION CONTAINED HEREIN MAY NOT BE COPIED OR DISCLOSED WITHOUT OUR PERMISSION

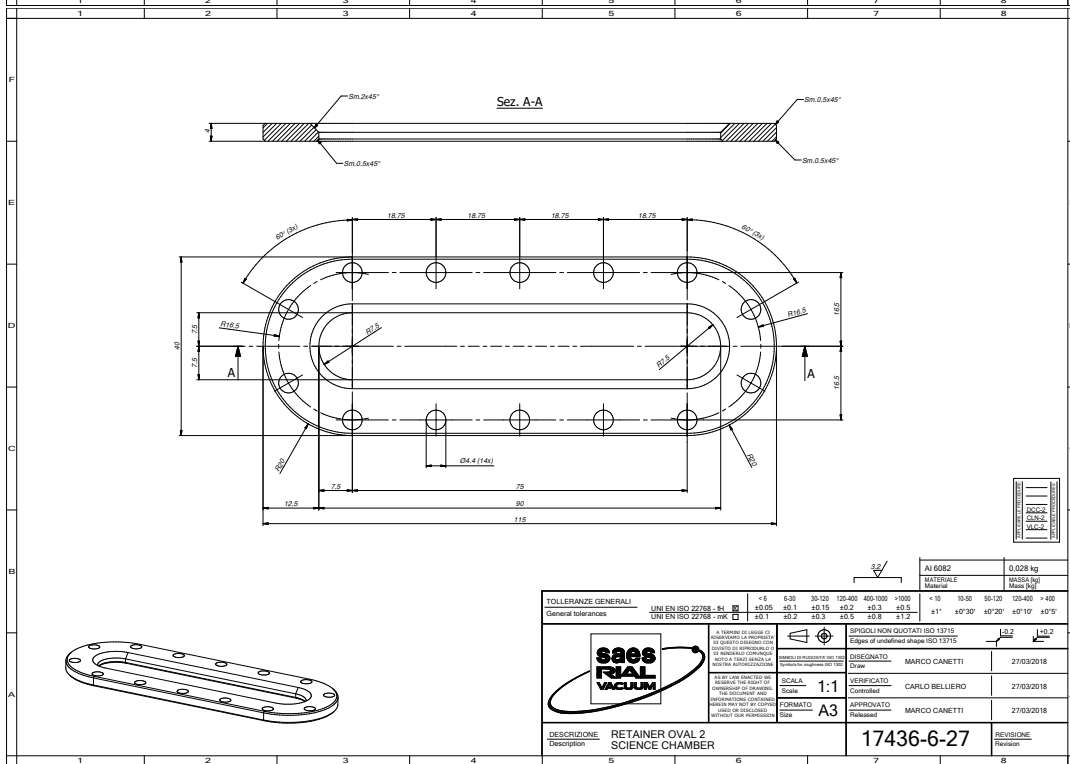
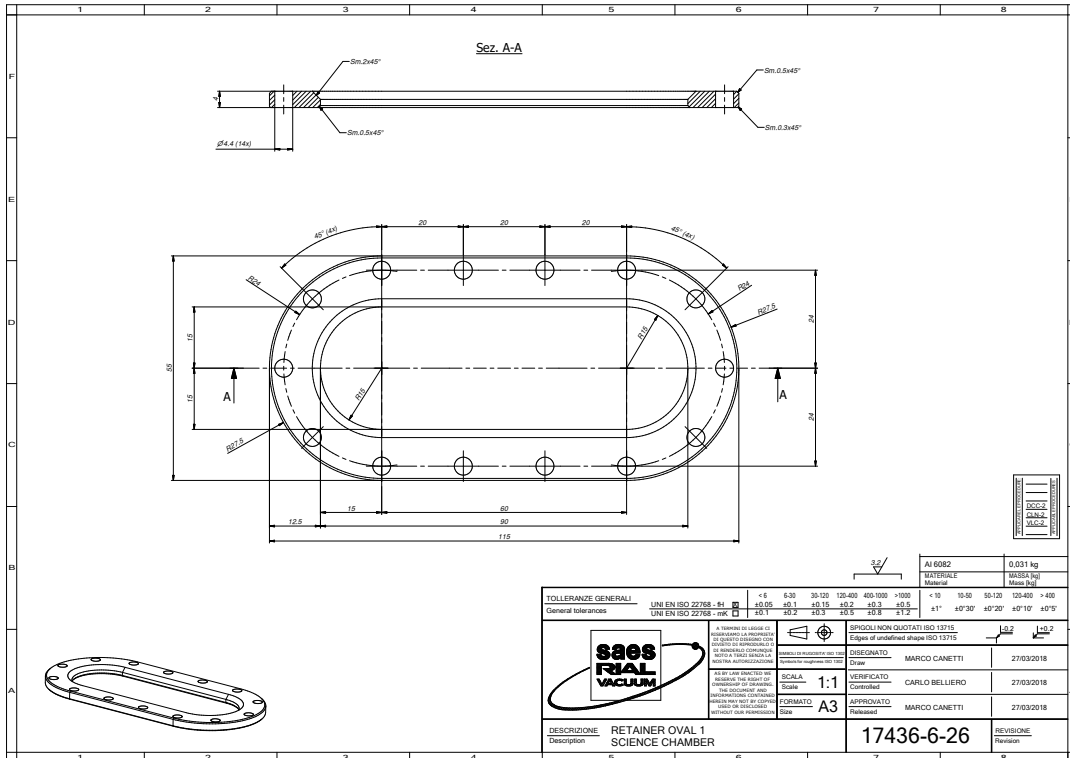
SCALA
Scale 1:1

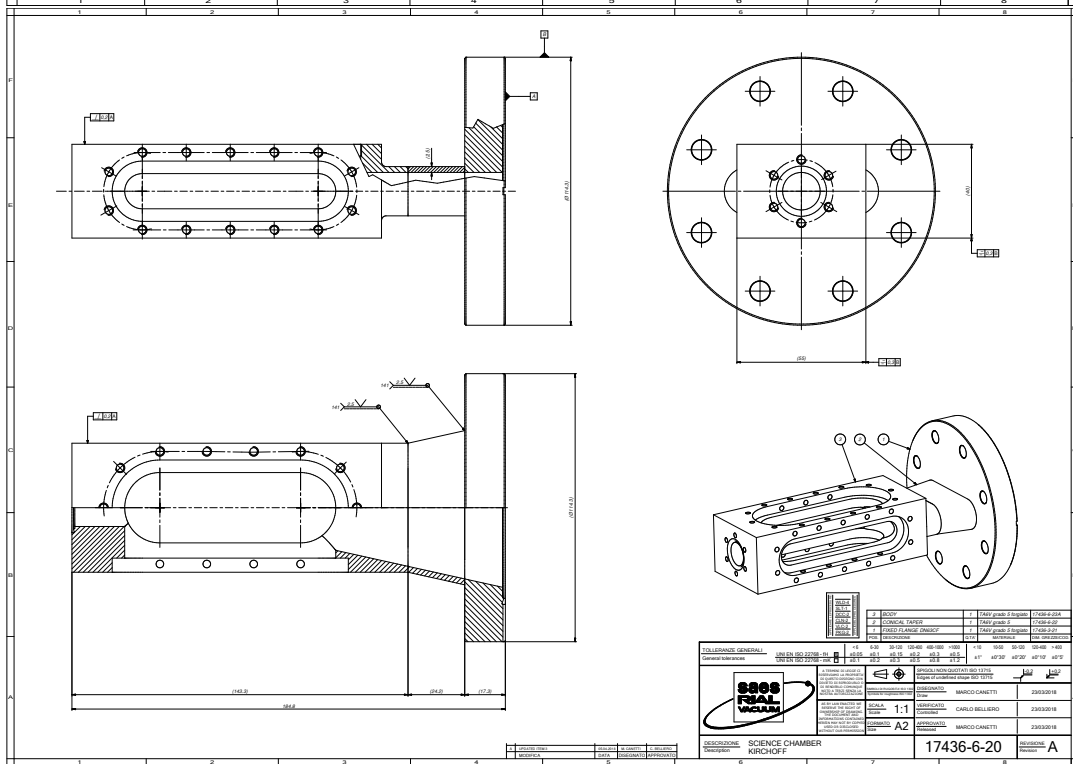
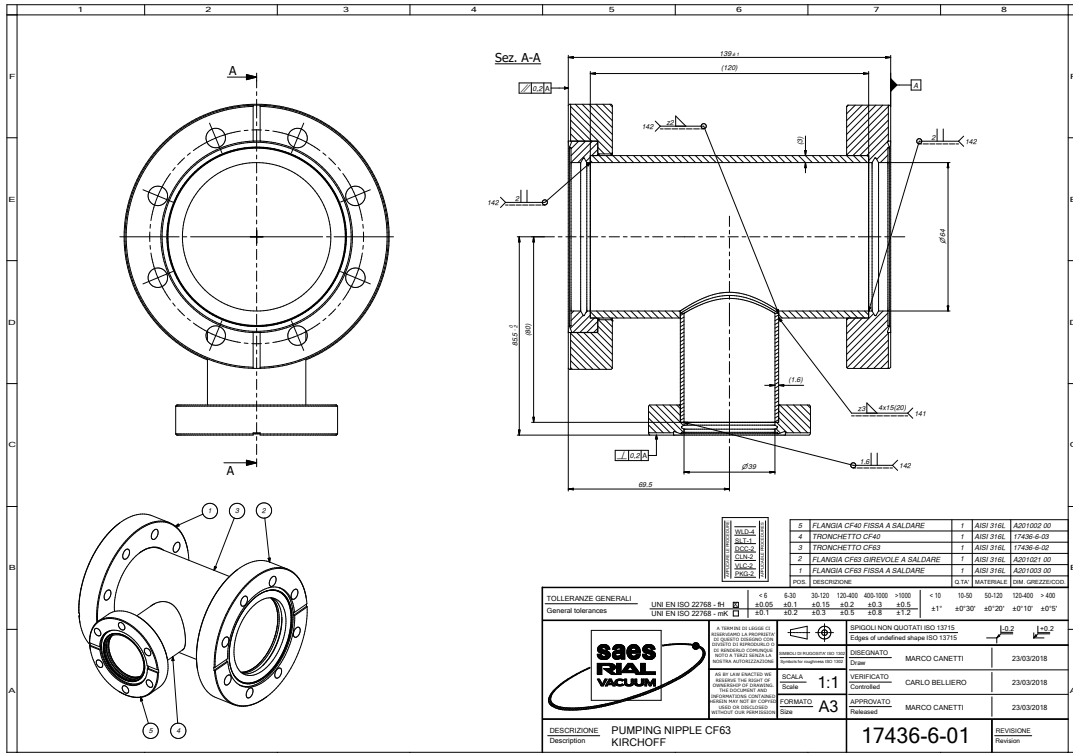
FORMATO
Size A4

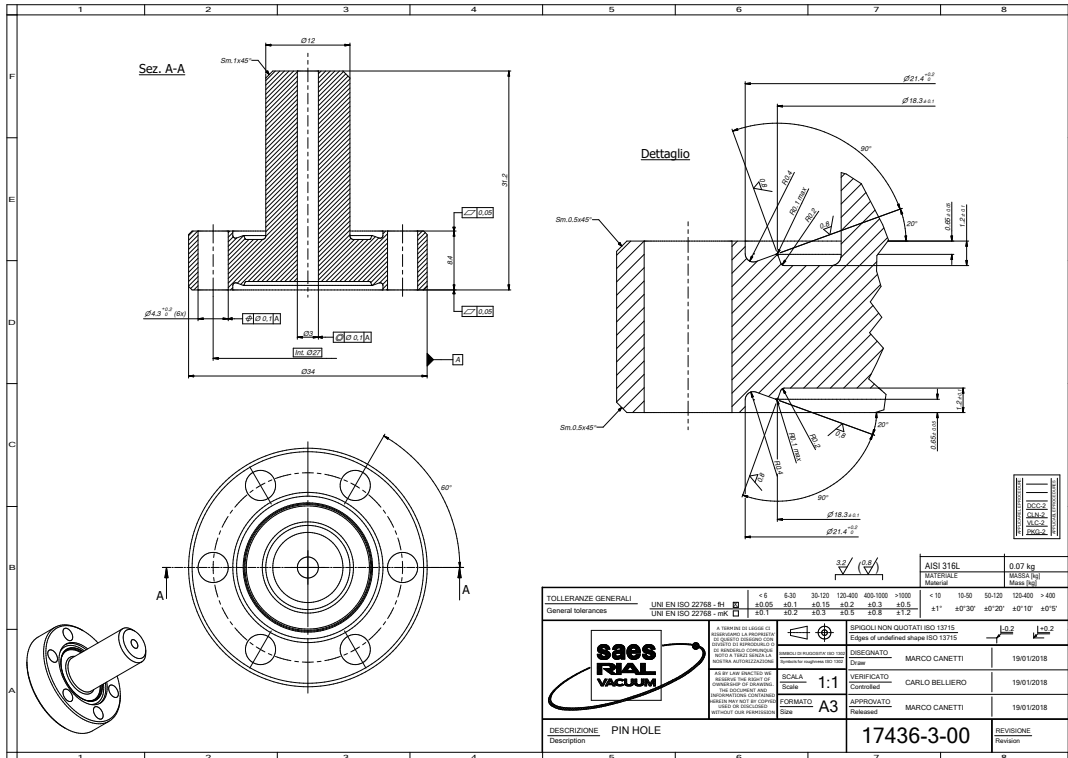
SPIGOLI NON QUOTATI ISO 13715 Edges of undefined shape ISO 13715		±0.2	±0.2
DISEGNATO Draw	MARCO CANETTI	27/03/2018	
VERIFICATO Controlled	CARLO BELLIERO	27/03/2018	
APPROVATO Released	MARCO CANETTI	27/03/2018	

DESCRIZIONE Description	CONICAL TAPER KIRCHOFF
----------------------------	---------------------------

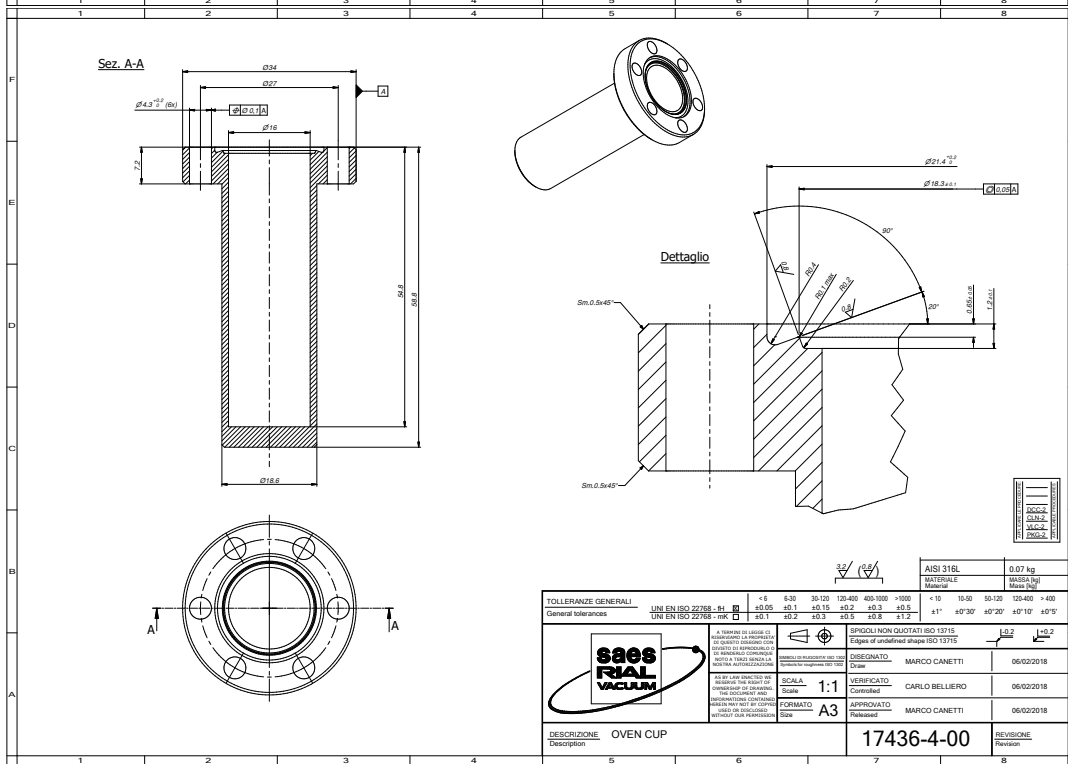
17436-6-22	REVISIONE Revision
------------	-----------------------







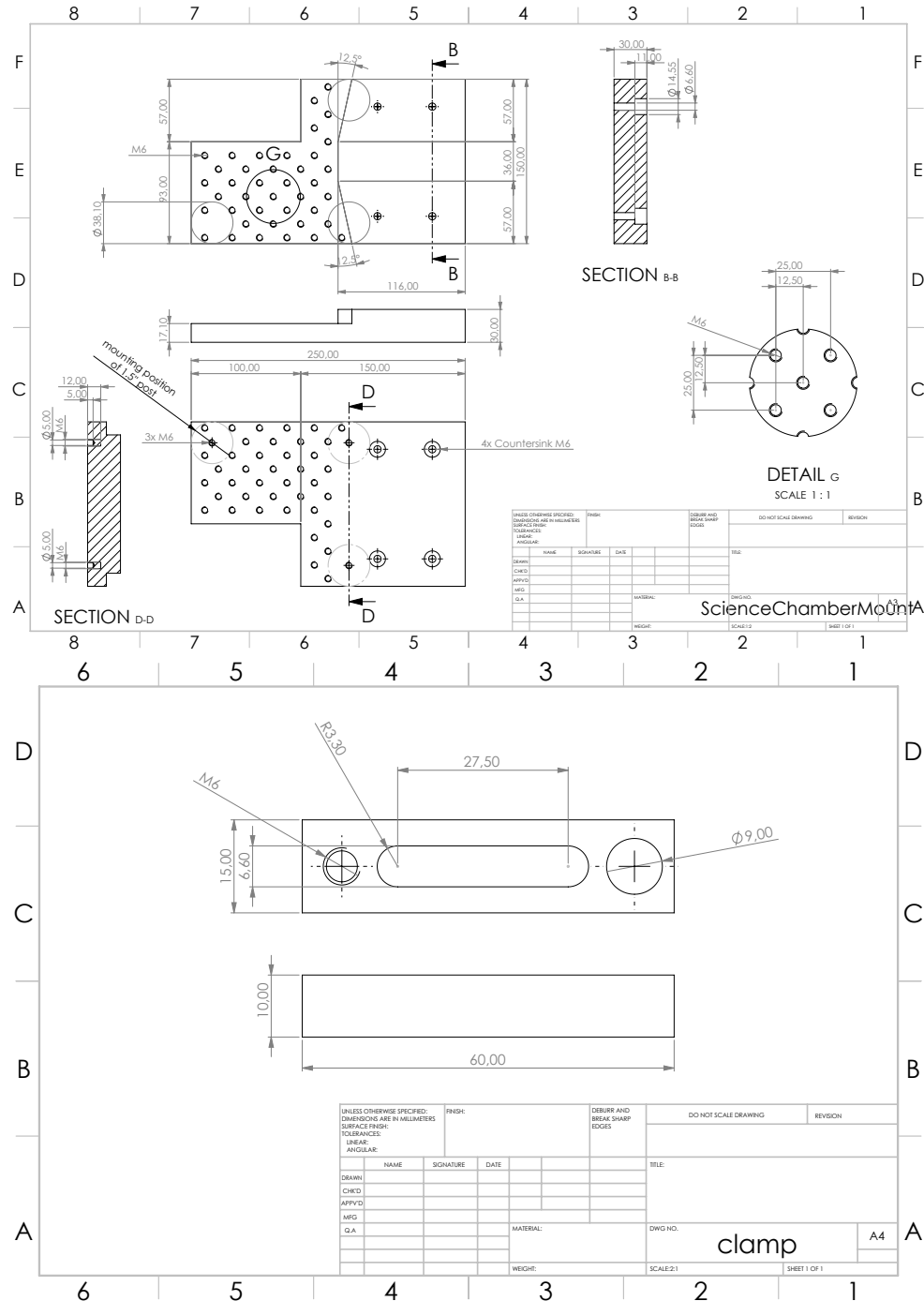
TOLLERANZE GENERALI		UNI EN ISO 22768 - H	< 6	6-30	30-120	120-400	400-1000	> 1000	< 10	10-50	50-120	120-400	> 400
General tolerances		UNI EN ISO 22768 - H	0	±0.05	±0.1	±0.15	±0.2	±0.3	±1*	±0.30*	±0.20*	±0.10*	±0.05*
		UNI EN ISO 22768 - H/K	0	±0.1	±0.2	±0.3	±0.5	±0.8	±1.2				
		* In presenza di tolleranze di riferimento la tolleranza di riferimento deve essere indicata nel disegno.											
		** In presenza di tolleranze di riferimento la tolleranza di riferimento deve essere indicata nel disegno.											
		*** In presenza di tolleranze di riferimento la tolleranza di riferimento deve essere indicata nel disegno.											
DESCRIZIONE		PIN HOLE											
Description		PIN HOLE											
		SPIGOLI NON QUOTATI ISO 13715 Edges of unquoted shape ISO 13715											
		DISEGNATO: MARCO CANETTI Scale: 1:1 VERIFICATO: CARLO BELLIERO Scale: 1:1 APPROVATO: MARCO CANETTI Scale: A3											
		MATERIALI AISI 316L 0.07 kg MASSA [kg] Material Weight [kg]											
		REVISIONE Revision											
		17436-3-00											



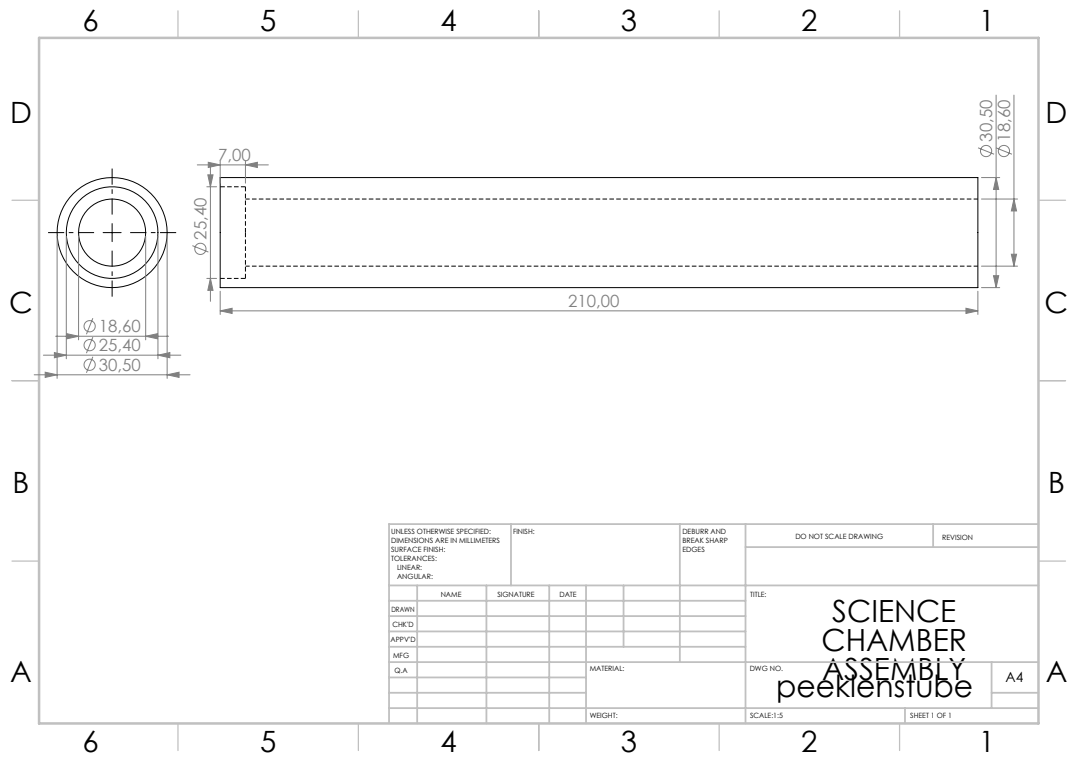
TOLLERANZE GENERALI		UNI EN ISO 22768 - H	< 6	6-30	30-120	120-400	400-1000	> 1000	< 10	10-50	50-120	120-400	> 400
General tolerances		UNI EN ISO 22768 - H	0	±0.05	±0.1	±0.15	±0.2	±0.3	±1*	±0.30*	±0.20*	±0.10*	±0.05*
		UNI EN ISO 22768 - H/K	0	±0.1	±0.2	±0.3	±0.5	±0.8	±1.2				
		* In presenza di tolleranze di riferimento la tolleranza di riferimento deve essere indicata nel disegno.											
		** In presenza di tolleranze di riferimento la tolleranza di riferimento deve essere indicata nel disegno.											
		*** In presenza di tolleranze di riferimento la tolleranza di riferimento deve essere indicata nel disegno.											
DESCRIZIONE		OVEN CUP											
Description		OVEN CUP											
		SPIGOLI NON QUOTATI ISO 13715 Edges of unquoted shape ISO 13715											
		DISEGNATO: MARCO CANETTI Scale: 1:1 VERIFICATO: CARLO BELLIERO Scale: 1:1 APPROVATO: MARCO CANETTI Scale: A3											
		MATERIALI AISI 316L 0.07 kg MASSA [kg] Material Weight [kg]											
		REVISIONE Revision											
		17436-4-00											

A.5.3 Science Chamber Mount

The science chamber is mounted on an aluminium block (ScienceChamberMount) featuring a small double density bread board, designed for a beam height of 50.4 mm¹. The block is mounted on the 1.5" post, which can be adjusted in height due to the levelling knuckle foot they are mounted to, which are clamped to the table by the custom clamps.



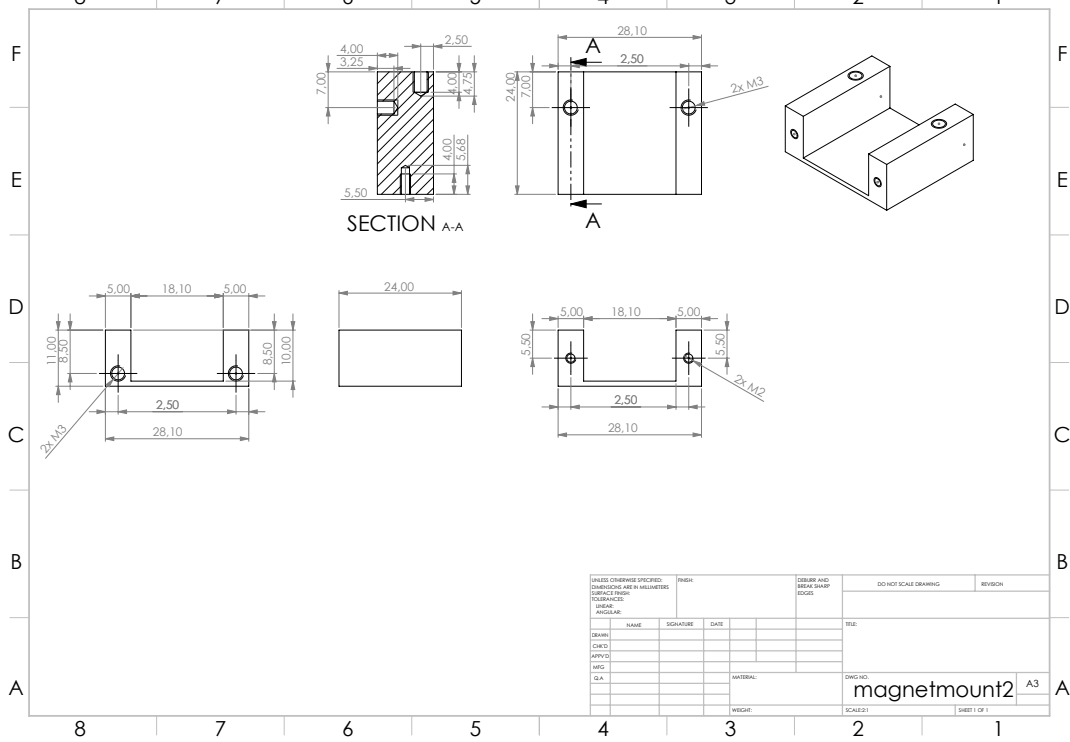
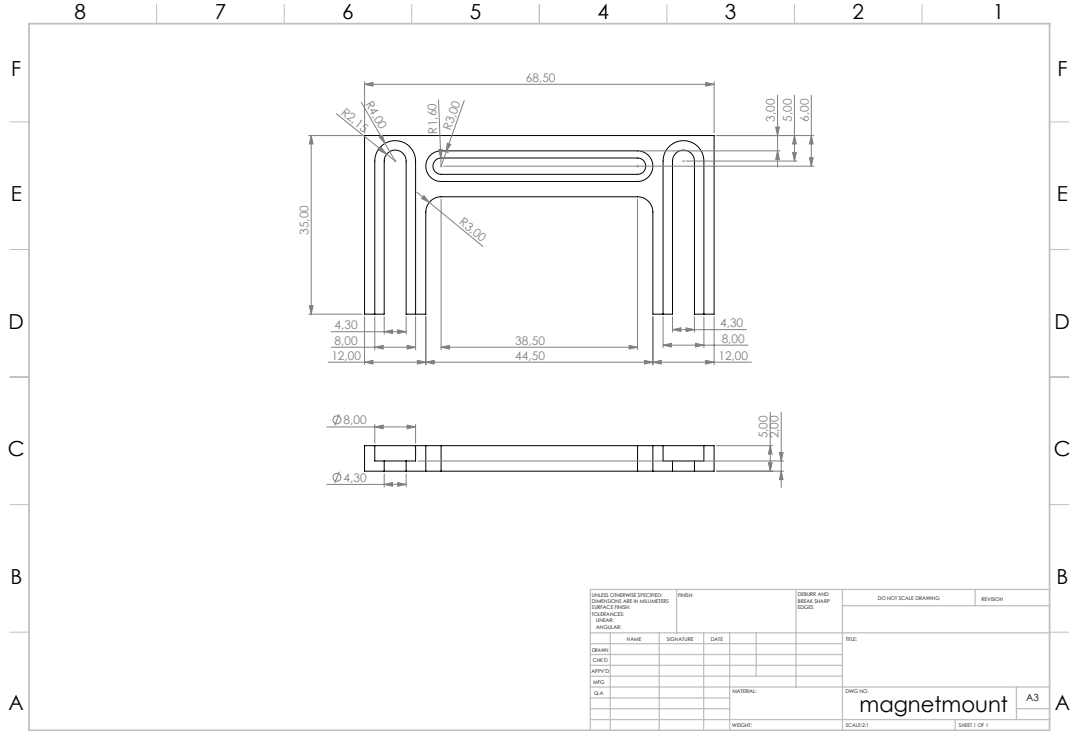
1 25 mm fixed heights posts combined with one-inch *Lioptec* mirror mounts.

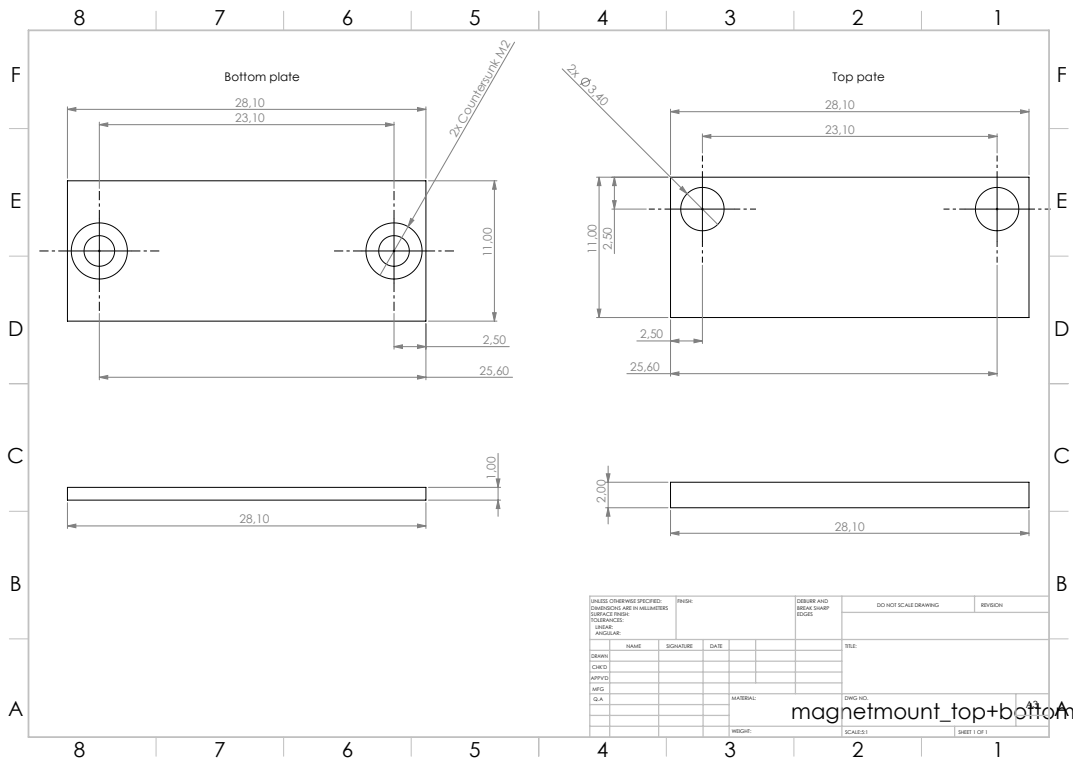


UNLESS OTHERWISE SPECIFIED: DIMENSIONS ARE IN MILLIMETERS				FINISH:	DEBURR AND BREAK SHARP EDGES	DO NOT SCALE DRAWING	REVISION
SURFACE FINISH:							
TOLERANCES:							
LINEAR:							
ANGULAR:							
DRAWN:	NAME	SIGNATURE	DATE			TITLE:	
CHECKED:						SCIENCE CHAMBER ASSEMBLY peeklenstube	
APPROVED:							
MFG:							
Q.A.							
				MATERIAL:		DWG NO.	
				WEIGHT:		SCALE:1:5	SHEET 1 OF 1

A.7 MAGNET MOUNT

The magnets are clamped between two plates in a sleeve, which is mounted to the mounting plate in elongated slots for transversal movement. The mounting plate itself is mounted via elongated slots to the 2D MOT chamber, allowing for translation in the vertical axis.





VACUUM SYSTEM ESTIMATION CALCULATIONS

B.1 ESTIMATING PRESSURE DISCREPANCIES BETWEEN 2D MOT CHAMBER AND ION PUMP

In the SoPa experiment we rely on the ion pump current as a pressure gauge. However, if there is significant outgassing, it is likely that the pressure in the 2D MOT chamber itself could be higher, depending on the conductance of the chamber geometry. To estimate the pressure in the chamber, for this we mainly follow the calculations done by Carl Kindermann for the ATTA experiment [170].

The pressure in the 2D MOT chamber can be estimated by estimating the conductance from the 2D MOT chamber to the pump. To do this, the path from the 2D MOT chamber to the pump is divided into pipes of cross-section A_i with diameter d and length l as shown in Figure B.1. The conductance of an aperture is defined as

$$C_{A_i} = \sqrt{\frac{k_B T}{2\pi m}} A_i \quad (\text{B.1})$$

The conductance of the pipe is

$$C_{T_i} = \alpha C_{A_i}, \quad (\text{B.2})$$

where α is the probability of transmission:

$$\alpha = 1 + y^2 - y\sqrt{y^2 + 1} - \frac{\left((2 - y^2)\sqrt{y^2 + 1} + y^3 - 2\right)^2}{4.5y\sqrt{y^2 + 1} - 4.5\ln(y + \sqrt{y^2 + 1})} \quad (\text{B.3})$$

where $y = l/d$. The aperture A_3 is not circular like the others, but annular. In this case the effective aperture diameter d_h can be estimated by $d_h = d_{out} - d_{in}$ [94]. The total conductance C_{tot} can be calculated with

$$\frac{1}{C_{tot}} = \frac{1}{C_{A_1}} \sum_{i=0}^N \left(\frac{1}{C_{T_i}} - \frac{1}{C_{A_i}} \right) + \sum_{i=0}^{N-1} \left(\frac{1}{C_{A_{i+1}}} - \frac{1}{C_{A_i}} \right) \delta_{i,i+1}, \quad (\text{B.4})$$

where

$$\delta_{i,i+1} = \begin{cases} 1 & \text{for } A_{i+1} < A_i \\ 0 & \text{for } A_{i+1} \geq A_i. \end{cases} \quad (\text{B.5})$$

In the case of the SoPa 2D MOT chamber as shown in Figure B.1, the

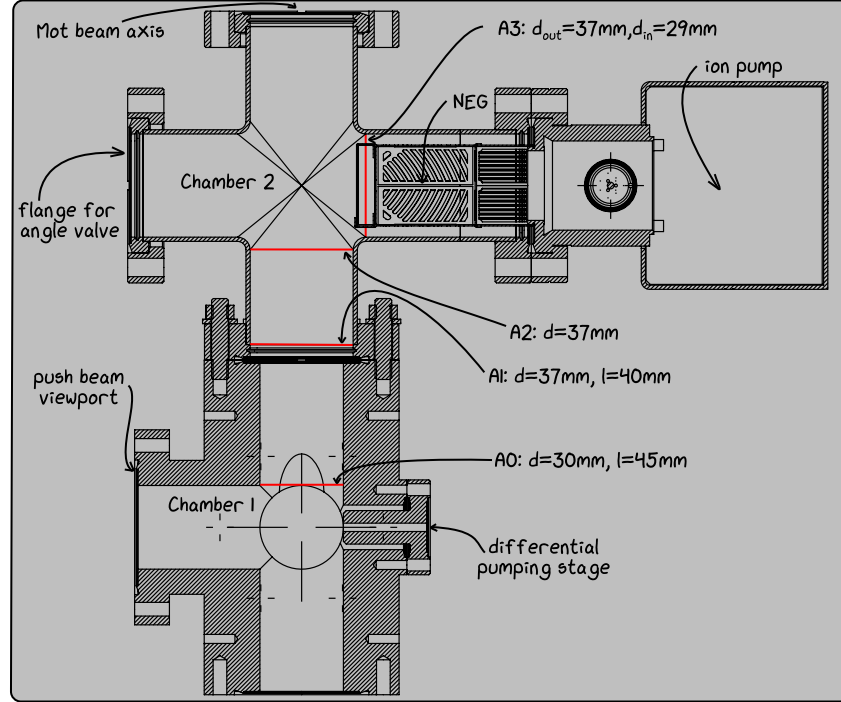


Figure B.1: Estimate the 2D MOT chamber conductance by dividing the path to the pump into pipes with diameter d and aperture A and length l . The pump cross is considered as a second chamber.

Equation B.4 becomes

$$\frac{1}{C_{tot}} = \frac{1}{C_{TC_{T_1}}} - \frac{1}{C_{A_1}} + \frac{1}{C_{A_3}}. \quad (\text{B.6})$$

With the total conductance C_{tot} and the pumping speed S , the effective pumping speed S_{eff} can be calculated with

$$\frac{1}{S_{eff}} = \frac{1}{S} + \frac{1}{C_{tot}}. \quad (\text{B.7})$$

The total gas flow Q is equal to the product of the pump speed and the pressure at the pump, and the product of the effective pump speed and the pressure in the chamber.

$$Q = S \cdot p_{pump} = S_{eff} \cdot p_{chamber}, \quad (\text{B.8})$$

and therefore the pressure in the chamber can be estimated with

$$p_{chamber} = \frac{S p_{pump}}{S_{eff}}. \quad (\text{B.9})$$

To estimate the pressure difference, we assume that the main gas load is water in the first case and hydrogen in the second. The molecular mass of water is 18 u and that of hydrogen is 2 u. The ion pump used in the SoPa 2D MOT chamber has a pumping speed of $S_{H_2O} = 100 \text{ l/s}$ for

water vapour and $S_{H_2} = 1501/\text{s}$ for hydrogen. We assume a pressure of 10^{-11} mbar at the pump. Based on these parameters, we estimate the pressure in the 2D MOT chamber to be $p_{\text{chamber}} = 1.6 \cdot 10^{-7}$ mbar for a water vapor load and $p_{\text{chamber}} = 7.9 \cdot 10^{-8}$ mbar for a hydrogen load.

This indicates that the conductance of the pump path is very low, resulting in a pressure difference of three to four orders of magnitude between the pump and the chamber. Although the calculated pressure in the 2D MOT chamber appears to be quite high, it is likely to be an overestimate. In particular, the outgassing contributions from the tubes and the second chamber have been neglected.

The calculations can also be validated by comparing the theoretical vapour pressure of sodium and potassium with the pressure measured at the ion pump. Since the NEG (Non-Evaporable Getter) element does not pump sodium and potassium, the pumping speed for these gases is only provided by the ion pump and is estimated to be about 5 l/s. Assuming an ion pump pressure reading of the order of 10^{-8} mbar, this corresponds to an estimated pressure in the 2D MOT region of $2.4 \cdot 10^{-6}$ mbar for sodium and $3.5 \cdot 10^{-6}$ mbar for potassium.

The theoretical vapour pressures in the 2D MOT chamber are expected to be $1.4 \cdot 10^{-4}$ mbar for sodium at a oven temperature of 180°C [57] and $3 \cdot 10^{-5}$ mbar for potassium at a oven temperature of 70°C [58]. These theoretical pressures are higher than those estimated from the estimated ion pump reading. However, the ion pump pressure reading was only a rough estimate. Recalculating what the ion pump reading would be based on these theoretical vapour pressures gives pressures on the order of $5.9 \cdot 10^{-7}$ mbar for sodium and $8.7 \cdot 10^{-8}$ mbar for potassium, which is within a plausible range of the observed ion pump readings.

B.2 ESTIMATING GETTER SATURATION TIME

The getter material in the ion getter pump gradually becomes saturated and requires periodic reactivation¹. We estimate the time until the getter is fully saturated, denoted as t , with the following equation:

$$t = \frac{M}{Sp}, \quad (\text{B.10})$$

where M is the sorbed amount, S is the pump speed and p is the pressure in the chamber.

The manual for the NEX Torr Z100 pump² used in our 2D MOT cham-

¹ The NEX Torr Z100 pumps do not have a build in thermocouple, the values we have used to reactivate the getter materials are: 35 W, 4.5 A, 7.7 V

² from *SEAS Rials Manual User's Manual NEX Torr Z 100 Pump*, Doc: M.HIST.0119.23, Rev.2, 24/07/2017

Table B.1: Initial pumping speed and sorbed quantities, M_{low} where the pumping speed starts to drop and M_{up} , where the pumping speed dropped to the minimum. Values taken from manual of the NEX-Torr Z100 pump from *SEAS Rial Vacuum*.

pumed gas	initial pumping speed S [l/s]	sorbed Quantity M_{low} when S starts to drop [Torr l]	sorbed Qunatity M_{up} when S dropped to minimum [Torr l]
N_2	16	0.001	0.7
CO	16.5	0.004	0.7
O_2	17.5	0.02	7
H_2O	100	0.04	10
CH_4	10.5	10	12
H_2	150	>100	-

ber includes a graph showing the pump speed as a function of the amount sorbed. Since the pumping speed decreases non-linearly with the amount of sorbent, we define a lower limit and a upper limit of the operating time. We define the lower bound of the operating time t_{low} as the point where the sorbed amount M_{low} causes the pumping speed to start decreasing. The upper limit t_{up} is defined by the sorbed amount M_{up} at which the pump speed drops to its minimum value. Table B.1 summarises the values of M_{low} and M_{up} for different gases. For gases where the pumping rate varies over a wide range of sorbed qunatities, the two estimates are likely to be far apart, in which case a more appropriate estimate might be to define a value in between where the area under the real curve is similar to the assumed constant pumping rate. However, to illustrate the wide range of pumping speeds, the upper and lower bounds are discussed here.

In discussions with the *SEAS Rials vacuum*, we learned that when a gas saturates the surface of the getter, reducing the pumping rate, there is no room for other gases. However, since hydrogen penetrates the getter, there is still a reduced pumping effect for hydrogen. Our vaporised atoms, sodium and potassium, are not pumped by the NEG element because they do not undergo chemisorbtion onto the getter material, but they can cover the NEG surface, likely reducing the pumping speed.

Considering a chamber pressure of 10^{-6} mbar and the maximum specified pumping speed, the operating time of the getter is $t_{low} = 5$ s and $t_{up} = 1$ h for nitrogen and $t_{low} = 31$ s and $t_{up} = 2$ h for water.

Taking the conductance of the 2D MOT setup into account, as discussed in Section B.1, the effective pumping speed at room temperature is only $S_{eff} = 6$ ml/s for water and $S_{eff} = 5$ ml/s for nitrogen. This shows that the setup significantly limits the pumping speed, making it relatively independent of the initial pumping speed. Therefore we approximate

the effective pumping speed with 5 l/s for water with a partial pressure of 10^{-6} mbar the saturation time is $t_{low} = 1$ week and $t_{up} = 8.5$ months.

The high pressure in the chamber is mainly due to the vapour pressure of sodium and potassium, which are not pumped by the NEG element. Consequently, our estimates represent a lower bound. Assuming a constant outgassing rate for water in a well-baked 2D titanium MOT chamber of 10^{-10} mbar l/s cm^{-2} [106], and a chamber surface area of 265.43 cm^2 , we estimate the partial pressure due to water in the chamber to be $3 \cdot 10^{-8}$ mbar. Under these conditions, the operating time would be $t_{low} = 11.3$ months and $t_{up} = 235$ years.

ACKNOWLEDGEMENTS

I would certainly not have reached this point without the help of many others. This journey faced several significant challenges, including the COVID-19 lockdowns, contact restrictions, and disruptive changes in the lab.

First of all, I would like to thank Markus for taking over the SoPa experiment, including me. Thank you for your boundless optimism, for always having faith in me and for supporting so many creative projects.

Special thanks to Thomas Pfeifer for reviewing this thesis and to my other referees Thomas Gasenzer and Prof. Aeschbach for being part of my committee.

Thank you Jan, without you SoPa would certainly not exist anymore and I would not have been able to finish this thesis. Thank you for all the wonderful Turkish family food you have generously offered me over the past few years. Now I have to learn how to make all those delicious things myself!

Thank you, Helmut, for your valuable input and for always having time to discuss.

With all the massive changes in the lab, the old days seem far away. However, I would be remiss if I didn't acknowledge the good times we shared. Thanks to all the previous members of the SoPa+NaLi+NaKa team: Apoorva, Andy, Rohit, Yannick, Ingrid, Gopal, Hannes, Fred, and everyone else. Special thanks to Andy, Apoorva, Rohit and Jan for introducing me to new foods and beverages.

Thanks to the bachelor students Lorenz and Joris for bringing new motivation and joy to the experimental construction.

The whole effort would be pointless without the next generation of students continuing the project - thank you Toni, Malaika and Brian for keeping SoPa alive and pushing it towards an ongoing experiment.

Thanks so much, David and Julia, for all your support. Your quick turnaround on our workshop orders was crucial for making the lab changes happen on time. It's always been great working with you, whether it was dealing with those last-minute tasks, brainstorming on design ideas, or just having a chat.

I also have to thank Mr. Lamade for always being very helpful in discussing all the designs. And the whole Workshop team for manufacturing our parts.

Creative processes are often spontaneous and certainly more enjoyable when other people are around. Sometimes that creativity starts with people you have just met. Thank you, Louis, for your commitment to brainstorming this figure. The first figure in this thesis is the result of a spontaneous brainstorming session with Louis and Niklas at the graduate days - thanks to both of you, although I was not able to implement all the ideas.

I'd like to thank the whole Matterwave group for generously sharing their knowledge and equipment. A special thank you to Carl for our great vacuum discussions, Alexandra for organising the Artsy Monday session and the Bias workshop, Ido for the fantastic group retreat in Arezzo with those fun pen & paper sessions, and Celia for our invaluable conversations about the future and for motivating me to pursue my post-PhD dreams. I'm also really grateful to everyone who helped me with the PhD hats; your support made all the difference in bringing these creative projects to life. And to anyone I may have missed - thank you too!

The matterwave group is lucky to have such nice group secretaries, thank you Dagmar, Christiane, and Petra. Thank you for all your reminders to fill in forms. And for dealing with our chaotic travel arrangements.

Many thanks to Mr. Azeroth, who helped us with a lot of electronic stuff.

Mr Martin-Almendral and Mrs Müller: Setting up an experiment always involves ordering a lot of things. I don't know how many orders I've placed in the last five years and how many I've had to correct. Thank you, Mr Martin-Almendral and Mrs Müller, for dealing with this flood of orders.

Thank you to my family and friends Alexandra, Arne, Clemens, Flavi, Hanna, Irmi, Leo, Martina, Maurus, and Valerie for your unforgettable support.

When writing a thesis, it is crucial to get valuable comments from proofreaders. Thank you Alexandra, Arne, Helmut, Jan for your comments.

I received valuable technical and emotional support from the caving

group and the UWR team. Special thanks to Ansgar, Bernhard and Tim for all the insightful discussions.

Thank you, Alexandra, Evelyn, Irmis and Malaika, for motivating me to stay active, and Tiergartenbad for providing a great place to do so.

Thanks to Ines and Daniel for bringing back those good vibes from our old study sessions. I'm really grateful to both of you for keeping up the weekend working sessions.

During my PhD, I had a second home: Lyon. Where, in retrospect, I spent incredibly nice weekends enjoying French food and friendly French flatmates and friends: Fanny, Gustav, Simon and Mahiedienne. Thank you Arne for making Lyon my second home.

I would like to acknowledge the use of the xkcd-font created by ipython in the figures of this thesis.³ The font is licensed under the Creative Commons Attribution-NonCommercial 3.0 License. Further details can be found at: <https://creativecommons.org/licenses/by-nc/3.0/>.

I acknowledge the use of the Inkscape *ComponentLibrary* created by Alexander Franzen in the optical layout figures of this thesis. This library has been invaluable not only in the optical layouts for this thesis, but also in many graphics throughout my studies, including previous projects⁴. It is licensed under the Creative Commons Attribution-NonCommercial 3.0 License. Further details can be found at: <https://creativecommons.org/licenses/by-nc/3.0/>.

I would like to thank André Miede and Vel for the Classicthesis Typographic Thesis LaTeX template, version 1.4 (1/1/16), which made formatting this thesis much easier⁵. It is licensed under the GNU General Public License (v2). Further details can be found at: <https://www.gnu.org/licenses/gpl-2.0.html>.

Please note that this acknowledgement applies only to the use of the template; the content of this thesis is not subject to the GNU General Public License (v2).

The *Labsnack Goldfish* illustrations in the margins are hand-drawn adaptations inspired by various publicly available graphics. I thank the original artists, unknown to me, for their inspiring work. Thank you all, and everyone I may have forgotten, for your contributions and support.

³ The font was obtained from the GitHub repository maintained by ipython at the following URL: <https://github.com/ipython/xkcd-font>

⁴ The Inkscape ComponentLibrary was obtained from <http://www.gwoptics.org/ComponentLibrary/>.

⁵ This template was downloaded from <http://www.LaTeXTemplates.com>

BIBLIOGRAPHY

- [1] Jan Kilinc. “A new setup for experiments with an ultracold ^{23}Na - ^{39}K mixture”. PhD Thesis. University of Heidelberg, 2024. DOI: 10.11588/heidok.00034438. URL: [Link](#).
- [2] I. M. Georgescu, S. Ashhab, and Franco Nori. “Quantum simulation”. In: *Reviews of Modern Physics* 86.1 (Mar. 2014). arXiv: 1308.6253 Publisher: American Physical Society. ISSN: 15390756. DOI: 10.1103/RevModPhys.86.153.
- [3] Gordon E. Moore. “Gramming more components onto integrated circuits”. In: *Electronics* 38.8 (Apr. 1965).
- [4] Thomas N. Theis and H.-S. Philip Wong. “The End of Moore’s Law: A New Beginning for Information Technology”. In: *Computing in Science & Engineering* 19.2 (Mar. 2017), pp. 41–50. ISSN: 1558-366X. DOI: 10.1109/MCSE.2017.29. URL: [Link](#).
- [5] Richard P Feynman. “Simulating Physics with Computers”. In: *International Journal of Theoretical Physics* 21.6 (1982).
- [6] Rajeev Acharya et al. “Suppressing quantum errors by scaling a surface code logical qubit”. In: *Nature* 614.7949 (Feb. 2023). Publisher: Nature Publishing Group, pp. 676–681. ISSN: 1476-4687. DOI: 10.1038/s41586-022-05434-1. URL: [Link](#).
- [7] Sebastian Krinner et al. “Realizing repeated quantum error correction in a distance-three surface code”. In: *Nature* 605.7911 (May 2022). Publisher: Nature Publishing Group, pp. 669–674. ISSN: 1476-4687. DOI: 10.1038/s41586-022-04566-8. URL: [Link](#).
- [8] Youwei Zhao et al. “Realization of an Error-Correcting Surface Code with Superconducting Qubits”. In: *Physical Review Letters* 129.3 (July 2022), p. 030501. ISSN: 0031-9007, 1079-7114. DOI: 10.1103/PhysRevLett.129.030501. URL: [Link](#).
- [9] C. Ryan-Anderson et al. “Realization of Real-Time Fault-Tolerant Quantum Error Correction”. In: *Physical Review X* 11.4 (Dec. 2021). Publisher: American Physical Society, p. 041058. DOI: 10.1103/PhysRevX.11.041058. URL: [Link](#).
- [10] Simon J. Devitt, William J. Munro, and Kae Nemoto. “Quantum error correction for beginners”. In: *Reports on Progress in Physics* 76.7 (June 2013). Publisher: IOP Publishing, p. 076001. ISSN: 0034-4885. DOI: 10.1088/0034-4885/76/7/076001. URL: [Link](#).

- [11] John Preskill. “Quantum Computing in the NISQ era and beyond”. In: *Quantum* 2 (Aug. 2018), p. 79. DOI: 10.22331/q-2018-08-06-79. URL: Link.
- [12] Ehud Altman et al. “Quantum Simulators: Architectures and Opportunities”. In: *PRX Quantum* 2.1 (Feb. 2021), p. 017003. ISSN: 2691-3399. DOI: 10.1103/PRXQuantum.2.017003. URL: Link.
- [13] Immanuel Bloch, Jean Dalibard, and Sylvain Nascimbène. “Quantum simulations with ultracold quantum gases”. In: *Nature Physics* 8.4 (Apr. 2012), pp. 267–276. ISSN: 17452473. DOI: 10.1038/nphys2259.
- [14] Christian Gross and Immanuel Bloch. “Quantum simulations with ultracold atoms in optical lattices”. In: *Science* 357.6355 (Sept. 2017). Publisher: American Association for the Advancement of Science, pp. 995–1001. DOI: 10.1126/science.aal3837. URL: Link.
- [15] Jae-yoon Choi. “Quantum simulations with ultracold atoms in optical lattices: past, present and future”. In: *Journal of the Korean Physical Society* 82.9 (May 2023), pp. 875–881. ISSN: 1976-8524. DOI: 10.1007/s40042-023-00777-y. URL: Link.
- [16] M H Anderson, J R Ensher, M R Matthews, C E Wieman, and E A Cornell. *Observation of Bose-Einstein Condensation in a Dilute Atomic Vapor*. Tech. rep. DOI: 10.1126/science.269.5221.198.
- [17] K B Davis, M.-O Mewes, M R Andrews, N J Van Druten, D S Durfee, D M Kurn, and Ketterle. “Bose-Einstein Condensation in a Gas of Sodium Atoms”. In: *Phys. Rev. Lett.* 75.22 (1995). publisher: American Physical Society, pp. 3969–3973. DOI: <https://doi.org/10.1103/PhysRevLett.75.3969>. URL: Link.
- [18] Hans-Joachim Miesner and Wolfgang Ketterle. “Bose-Einstein condensation in dilute atomic gases”. In: *Solid State Communications* 107.11 (1998), pp. 629–637. ISSN: 0038-1098. DOI: [https://doi.org/10.1016/S0038-1098\(98\)00217-8](https://doi.org/10.1016/S0038-1098(98)00217-8). URL: Link.
- [19] S. Inouye, M. R. Andrews, J. Stenger, H.-J. Miesner, D. M. Stamper-Kurn, and W. Ketterle. “Observation of Feshbach resonances in a Bose-Einstein condensate”. In: *Nature* 392.6672 (Mar. 1998). Publisher: Nature Publishing Group, pp. 151–154. ISSN: 1476-4687. DOI: 10.1038/32354. URL: Link.
- [20] D M Stamper-Kurn, M R Andrews, A P Chikkatur, S Inouye, H.-J Miesner, J Stenger, and W Ketterle. “Optical Confinement of a Bose-Einstein Condensate”. In: *Phys. Rev. Lett.* 80.10 (1998), pp. 2027–2030. DOI: <https://doi.org/10.1103/PhysRevLett.80.2027>. URL: Link.

- [21] Maximilian Prüfer, Philipp Kunkel, Helmut Strobel, Stefan Lannig, Daniel Linnemann, Christian Marcel Schmied, Jürgen Berges, Thomas Gasenzer, and Markus K. Oberthaler. “Observation of universal dynamics in a spinor Bose gas far from equilibrium”. In: *Nature* 563.7730 (Nov. 2018). arXiv: 1805.11881 Publisher: Nature Publishing Group, pp. 217–220. ISSN: 14764687. DOI: 10.1038/s41586-018-0659-0.
- [22] Sebastian Erne, Robert Bücker, Thomas Gasenzer, Jürgen Berges, and Jörg Schmiedmayer. “Universal dynamics in an isolated one-dimensional Bose gas far from equilibrium”. In: *Nature* 563.7730 (Nov. 2018). Publisher: Nature Publishing Group, pp. 225–229. ISSN: 14764687. DOI: 10.1038/s41586-018-0667-0.
- [23] Mireia Tolosa-Simeón et al. “Curved and expanding spacetime geometries in Bose-Einstein condensates”. In: *Physical Review A* 106.3 (Sept. 2022). arXiv: 2202.10441 Publisher: American Physical Society. ISSN: 24699934. DOI: 10.1103/PhysRevA.106.033313.
- [24] Celia Viermann et al. “Quantum field simulator for dynamics in curved spacetime”. In: *Nature* 611.7935 (Nov. 2022). arXiv: 2202.10399 Publisher: Nature Research, pp. 260–264. ISSN: 14764687. DOI: 10.1038/s41586-022-05313-9.
- [25] C. J. Myatt, E. A. Burt, R. W. Ghrist, E. A. Cornell, and C. E. Wieman. “Production of Two Overlapping Bose-Einstein Condensates by Sympathetic Cooling”. In: *Physical Review Letters* 78.4 (Jan. 1997). Publisher: American Physical Society, pp. 586–589. DOI: 10.1103/PhysRevLett.78.586. URL: [Link](#).
- [26] G. Modugno, G. Ferrari, G. Roati, R. J. Brecha, A. Simoni, and M. Inguscio. “Bose-Einstein Condensation of Potassium Atoms by Sympathetic Cooling”. In: *Science* 294.5545 (Nov. 2001). Publisher: American Association for the Advancement of Science, pp. 1320–1322. DOI: 10.1126/science.1066687. URL: [Link](#).
- [27] Cosetta Baroni, Giacomo Lamporesi, and Matteo Zaccanti. *Quantum Mixtures of Ultracold Atomic Gases*. arXiv:2405.14562. May 2024. URL: [Link](#).
- [28] Alexander Mil, Torsten V. Zache, Apoorva Hegde, Andy Xia, Rohit P. Bhatt, Markus K. Oberthaler, Philipp Hauke, Jürgen Berges, and Fred Jendrzejewski. “A scalable realization of local U(1) gauge invariance in cold atomic mixtures”. In: *Science* 367.6482 (Mar. 2020). Publisher: American Association for the Advancement of Science, pp. 1128–1130. DOI: 10.1126/science.aaz5312. URL: [Link](#).
- [29] Francesco Scazza, Matteo Zaccanti, Pietro Massignan, Meera M. Parish, and Jesper Levinsen. “Repulsive Fermi and Bose Polarons in Quantum Gases”. In: *Atoms* 10.2 (June 2022). Pub-

- lisher: Multidisciplinary Digital Publishing Institute, p. 55. ISSN: 2218-2004. DOI: 10.3390/atoms10020055. URL: [Link](#).
- [30] Magnus G. Skou, Thomas G. Skov, Nils B. Jørgensen, Kristian K. Nielsen, Arturo Camacho-Guardian, Thomas Pohl, Georg M. Bruun, and Jan J. Arlt. “Non-equilibrium quantum dynamics and formation of the Bose polaron”. In: *Nature Physics* 17.6 (June 2021). Publisher: Nature Publishing Group, pp. 731–735. ISSN: 1745-2481. DOI: 10.1038/s41567-021-01184-5. URL: [Link](#).
- [31] Zoe Z. Yan, Yiqi Ni, Carsten Robens, and Martin W. Zwierlein. “Bose polarons near quantum criticality”. In: *Science* 368.6487 (Apr. 2020). Publisher: American Association for the Advancement of Science, pp. 190–194. DOI: 10.1126/science.aax5850. URL: [Link](#).
- [32] Xing-Can Yao, Hao-Ze Chen, Yu-Ping Wu, Xiang-Pei Liu, Xiao-Qiong Wang, Xiao Jiang, Youjin Deng, Yu-Ao Chen, and Jian-Wei Pan. “Observation of Coupled Vortex Lattices in a Mass-Imbalance Bose and Fermi Superfluid Mixture”. In: *Physical Review Letters* 117.14 (Sept. 2016), p. 145301. ISSN: 0031-9007, 1079-7114. DOI: 10.1103/PhysRevLett.117.145301. URL: [Link](#).
- [33] Andrea Richaud, Vittorio Penna, Ricardo Mayol, and Montserrat Guilleumas. “Vortices with massive cores in a binary mixture of Bose-Einstein condensates”. In: *Physical Review A* 101.1 (Jan. 2020), p. 013630. ISSN: 2469-9926, 2469-9934. DOI: 10.1103/PhysRevA.101.013630. URL: [Link](#).
- [34] Alessia Burchianti, Chiara D’Errico, Marco Prevedelli, Luca Salasnich, Francesco Ancilotto, Michele Modugno, Francesco Minardi, and Chiara Fort. “A Dual-Species Bose-Einstein Condensate with Attractive Interspecies Interactions”. In: *Condensed Matter* 5.1 (Mar. 2020). Publisher: Multidisciplinary Digital Publishing Institute, p. 21. ISSN: 2410-3896. DOI: 10.3390/condmat5010021. URL: [Link](#).
- [35] Sagar Sutradhar, Anirban Misra, Gourab Pal, Sayari Majumder, Sanjukta Roy, and Saptarishi Chaudhuri. “Fast loaded dual species magneto optical trap of cold sodium and potassium atoms with light-assisted inter-species interaction”. In: *AIP Advances* 13.6 (June 2023), p. 065317. ISSN: 2158-3226. DOI: 10.1063/5.0154985. URL: [Link](#).
- [36] Ziliang Li, Zhengyu Gu, Zhenlian Shi, Pengjun Wang, and Jing Zhang. “Quantum degenerate Bose-Fermi atomic gas mixture of ^{23}Na and ^{40}K ”. In: *Chinese Physics B* 32.2 (Feb. 2023), p. 023701. ISSN: 1674-1056. DOI: 10.1088/1674-1056/aca14f. URL: [Link](#).

- [37] Cheng Chin, Rudolf Grimm, Paul Julienne, and Eite Tiesinga. “Feshbach resonances in ultracold gases”. In: *Reviews of Modern Physics* 82.2 (Apr. 2010). Publisher: American Physical Society, pp. 1225–1286. DOI: 10.1103/RevModPhys.82.1225. URL: Link.
- [38] Rudolf Grimm, Matthias Weidemüller, and Yurii B. Ovchinnikov. *Optical dipole traps for neutral atoms*. arXiv:physics/9902072. Feb. 1999. URL: Link.
- [39] Torben A. Schulze, Torsten Hartmann, Kai K. Voges, Matthias W. Gempel, Eberhard Tiemann, Alessandro Zenesini, and Silke Ospelkaus. “Feshbach spectroscopy and dual-species Bose-Einstein condensation of ^{23}Na - ^{39}K mixtures”. In: *Physical Review A* 97.2 (Feb. 2018). Publisher: American Physical Society. ISSN: 24699934. DOI: 10.1103/PhysRevA.97.023623.
- [40] M. Landini, S. Roy, G. Roati, A. Simoni, M. Inguscio, G. Modugno, and M. Fattori. “Direct evaporative cooling of ^{39}K atoms to Bose-Einstein condensation”. In: *Physical Review A* 86.3 (Sept. 2012). Publisher: American Physical Society, p. 033421. DOI: 10.1103/PhysRevA.86.033421. URL: Link.
- [41] P. C. M. Castilho, E. Pedrozo-Peñafiel, E. M. Gutierrez, P. L. Mazo, G. Roati, K. M. Farias, and V. S. Bagnato. “A compact experimental machine for studying tunable Bose-Bose superfluid mixtures”. In: *Laser Physics Letters* 16.3 (Mar. 2019). arXiv:1901.01089, p. 035501. ISSN: 1612-2011, 1612-202X. DOI: 10.1088/1612-202X/ab00fb. URL: Link.
- [42] G. Lamporesi, S. Donadello, S. Serafini, and G. Ferrari. “Compact high-flux source of cold sodium atoms”. In: *Review of Scientific Instruments* 84.6 (June 2013). arXiv: 1301.6566. ISSN: 00346748. DOI: 10.1063/1.4808375.
- [43] Jee Woo Park, Cheng-Hsun Wu, Ibon Santiago, Tobias G. Tiecke, Sebastian Will, Peyman Ahmadi, and Martin W. Zwierlein. “Quantum degenerate Bose-Fermi mixture of chemically different atomic species with widely tunable interactions”. In: *Physical Review A* 85.5 (May 2012). Publisher: American Physical Society, p. 051602. DOI: 10.1103/PhysRevA.85.051602. URL: Link.
- [44] Jaeryeong Chang, Sungjun Lee, Yoonsoo Kim, Younghoon Lim, and Jee Woo Park. “Dual-species Bose-Einstein condensates of ^{23}Na and ^{41}K with tunable interactions”. In: *Physical Review Research* 6.1 (Feb. 2024). Publisher: American Physical Society, p. 013183. DOI: 10.1103/PhysRevResearch.6.013183. URL: Link.
- [45] Édouard Le Cerf. “Demixing phenomena in 2D Bose gases”. PhD thesis. 2020. URL: Link.

- [46] C. J. Foot. *Atomic physics*. en. Oxford master series in physics 7. Atomic, Optical, and laser physics. OCLC: ocm57478010. Oxford ; New York: Oxford University Press, 2005. ISBN: 978-0-19-850695-9 978-0-19-850696-6.
- [47] J. Pérez-Ríos and A. S. Sanz. “How does a magnetic trap work?” en. In: *American Journal of Physics* 81.11 (Nov. 2013), pp. 836–843. ISSN: 0002-9505, 1943-2909. DOI: 10.1119/1.4819167.
- [48] Hannes Kiehn, Vijay Pal Singh, and Ludwig Mathey. “Superfluidity of a laser-stirred Bose-Einstein condensate”. In: *Physical Review A* 105.4 (Apr. 2022). Publisher: American Physical Society, p. 043317. DOI: 10.1103/PhysRevA.105.043317. URL: [Link](#).
- [49] A. Görlitz et al. “Realization of Bose-Einstein condensates in lower dimensions”. In: *Physical Review Letters* 87.13 (Sept. 2001). arXiv: cond-mat/0104549, pp. 130402/1–130402/4. ISSN: 00319007. DOI: 10.1103/PhysRevLett.87.130402.
- [50] Jae Yoon Choi, Sang Won Seo, and Yong Il Shin. “Observation of thermally activated vortex pairs in a quasi-2D bose gas”. In: *Physical Review Letters* 110.17 (Apr. 2013). arXiv: 1211.5649. ISSN: 00319007. DOI: 10.1103/PhysRevLett.110.175302.
- [51] K Henderson, C Ryu, C MacCormick, and M G Boshier. “Experimental demonstration of painting arbitrary and dynamic potentials for Bose–Einstein condensates”. In: *New Journal of Physics* 11.4 (Apr. 2009), p. 043030. ISSN: 1367-2630. DOI: 10.1088/1367-2630/11/4/043030. URL: [Link](#).
- [52] Mathieu De Goër De Herve, Yanliang Guo, Camilla De Rossi, Avinash Kumar, Thomas Badr, Romain Dubessy, Laurent Longchambon, Hélène Perrin, and Héi Ene Perrin. “A versatile ring trap for quantum gases”. In: *Journal of Physics B: Atomic, Molecular and Optical Physics* (2021). URL: [Link](#).
- [53] N. L. Smith, W. H. Heathcote, G. Hechenblaikner, E. Nugent, and C. J. Foot. “Quasi-2D confinement of a BEC in a combined optical and magnetic potential”. In: *Journal of Physics B: Atomic, Molecular and Optical Physics* 38.3 (Jan. 2005), p. 223. ISSN: 0953-4075. DOI: 10.1088/0953-4075/38/3/007. URL: [Link](#).
- [54] P. Cladé, C. Ryu, A. Ramanathan, K. Helmerson, and W. D. Phillips. “Observation of a 2D bose gas: From thermal to quasicondensate to superfluid”. In: *Physical Review Letters* 102.17 (Apr. 2009). ISSN: 00319007. DOI: 10.1103/PhysRevLett.102.170401.
- [55] Celia Viermann. “Cosmological particle production and curved spaces in an ultracold quantum gas”. PhD Thesis. University of Heidelberg, 2022.

- [56] J. L. Ville et al. “Loading and compression of a single two-dimensional Bose gas in an optical accordion”. In: *Physical Review A* 95.1 (Jan. 2017), p. 013632. ISSN: 2469-9926, 2469-9934. DOI: 10.1103/PhysRevA.95.013632. URL: [Link](#).
- [57] Daniel A. Steck. *Sodium D Line Data*. revision 2.3.3. May 2024. URL: [Link](#).
- [58] T. G. Tiecke. *Properties of Potassium*. version 1.03. 2019. URL: [Link](#).
- [59] Lev Pitaevskii and Sandro Stringari. *Bose-Einstein Condensation and Superfluidity*. First Edition. Oxford University Press, 2016. ISBN: 978-0-19-875888-4.
- [60] E. Timmermans. “Phase Separation of Bose-Einstein Condensates”. In: *Physical Review Letters* 81.26 (Dec. 1998), pp. 5718–5721. ISSN: 0031-9007, 1079-7114. DOI: 10.1103/PhysRevLett.81.5718. URL: [Link](#).
- [61] Giacomo Lamporesi. *Two-component spin mixtures*. arXiv:2304.03711. May 2023. URL: [Link](#).
- [62] Eike Nicklas. “A new tool for miscibility control: Linear coupling”. PhD Thesis. Heidelberg University, 2013. URL: [Link](#).
- [63] H. Pu and N. P. Bigelow. “Properties of Two-Species Bose Condensates”. In: *Physical Review Letters* 80.6 (Feb. 1998). Publisher: American Physical Society, pp. 1130–1133. DOI: 10.1103/PhysRevLett.80.1130. URL: [Link](#).
- [64] Tin-Lun Ho and V. B. Shenoy. “Binary Mixtures of Bose Condensates of Alkali Atoms”. In: *Physical Review Letters* 77.16 (Oct. 1996). Publisher: American Physical Society, pp. 3276–3279. DOI: 10.1103/PhysRevLett.77.3276. URL: [Link](#).
- [65] Emmanuel Mercado Gutierrez, Gustavo Alves de Oliveira, Kilvia Mayre Farias, Vanderlei Salvador Bagnato, and Patricia Christina Marques Castilho. “Miscibility regimes in a ^{23}Na - ^{39}K quantum mixture”. In: *Applied Sciences (Switzerland)* 11.19 (Oct. 2021). arXiv: 2108.06440 Publisher: MDPI. ISSN: 20763417. DOI: 10.3390/app11199099.
- [66] Wolfgang Ketterle, Kendall B. Davis, Michael A. Joffe, Alex Martin, and David E. Pritchard. “High densities of cold atoms in a dark spontaneous-force optical trap”. In: *Physical Review Letters* 70.15 (Apr. 1993). Publisher: American Physical Society, pp. 2253–2256. DOI: 10.1103/PhysRevLett.70.2253. URL: [Link](#).
- [67] Alexandra Alice Beikert. “Controlled Frequency Generation for Grey Molasses Cooling”. BA Thesis. University of Heidelberg, 2021.

- [68] G. Salomon, L. Fouché, P. Wang, A. Aspect, P. Bouyer, and T. Bourdel. “Gray-molasses cooling of ^{39}K to a high phase-space density”. In: *Europhysics Letters* 104.6 (Jan. 2014). Publisher: EDP Sciences, IOP Publishing and Società Italiana di Fisica, p. 63002. ISSN: 0295-5075. DOI: 10.1209/0295-5075/104/63002. URL: [Link](#).
- [69] Dipankar Nath, R Kollengode Easwaran, G. Rajalakshmi, and C. S. Unnikrishnan. “Quantum-interference-enhanced deep sub-Doppler cooling of ^{39}K atoms in gray molasses”. In: *Physical Review A* 88.5 (Nov. 2013). Publisher: American Physical Society, p. 053407. DOI: 10.1103/PhysRevA.88.053407. URL: [Link](#).
- [70] Giacomo Colzi, Gianmaria Durastante, Eleonora Fava, Simone Serafini, Giacomo Lamporesi, and Gabriele Ferrari. “Sub-Doppler cooling of sodium atoms in gray molasses”. In: *Physical Review A* 93.2 (Feb. 2016), p. 023421. ISSN: 2469-9926, 2469-9934. DOI: 10.1103/PhysRevA.93.023421. URL: [Link](#).
- [71] Malaika Göritz. “tba”. PhD thesis. University of Heidelberg, 2024.
- [72] Xiyuan Xia. “Towards a more reliable ultracold mixture platform”. PhD Thesis. University of Heidelberg, 2022. DOI: 10.11588/heidok.00032040. URL: [Link](#).
- [73] Apoorva Hegde. “Noisy Dynamics of U(1) Lattice Gauge Theory in Ultracold Atomic Mixtures”. PhD thesis. PhD Thesis, University of Heidelberg, 2022. DOI: 10.11588/heidok.00031631. URL: [Link](#).
- [74] Alexander Mil. “Experimental realization of U(1) gauge invariance in ultracold atomic mixtures”. PhD Thesis. University of Heidelberg, 2020. DOI: 10.11588/heidok.00028454. URL: [Link](#).
- [75] T. Schuster, R. Scelle, A. Trautmann, S. Knoop, M. K. Oberthaler, M. M. Haverhals, M. R. Goosen, S. J. J. M. F. Kokkelmans, and E. Tiemann. “Feshbach spectroscopy and scattering properties of ultracold Li + Na mixtures”. In: *Physical Review A* 85.4 (Apr. 2012). Publisher: American Physical Society, p. 042721. DOI: 10.1103/PhysRevA.85.042721. URL: [Link](#).
- [76] Jan Kilinc. “Starting a Na-K experiment for simulating quantum many-body phenomena”. MA thesis. University of Heidelberg, 2019. URL: [Link](#).
- [77] Lilo Höcker. “Building up a modular Na-K quantum gas experiment”. MA thesis. University of Heidelberg, 2019. URL: [Link](#).
- [78] Rohit Prasad Bhatt. “Developing tools for cold atom research : an ultracold Na-K experiment, proposals for unitary k-designs, and a web interface”. PhD Thesis. University of Heidelberg, 2022.

- [79] Torsten Hartmann, Torben A. Schulze, Kai K. Voges, Philipp Gersema, Matthias W. Gempel, Eberhard Tiemann, Alessandro Zenesini, and Silke Ospelkaus. “Feshbach resonances in $^{23}\text{Na}+^{39}\text{K}$ mixtures and refined molecular potentials for the NaK molecule”. In: *Physical Review A* 99.3 (Mar. 2019). Publisher: American Physical Society. ISSN: 24699934. DOI: 10.1103/PhysRevA.99.032711.
- [80] Maurus Hans. “An experimental setup for a potassium Bose-Einstein condensate with tunable interactions”. MA thesis. University of Heidelberg, 2017. URL: [Link](#).
- [81] Marius Sparn. “Magnetic Fields for Cooling and Trapping of Potassium Atoms”. BA Thesis. University of Heidelberg, 2017. URL: [Link](#).
- [82] Alexander Mil. “Design and Implementation of a Versatile Imaging Objective for Imaging of Ultracold Mixtures of Sodium and Lithium”. MA thesis. University of Heidelberg, 2016. URL: [Link](#).
- [83] Fabián A. Olivares L. “Towards Lattice Gauge Theories in Ultracold Mixtures of Sodium and Lithium”. PhD Thesis. University of Heidelberg, 2018.
- [84] Nikolaus Walter Buchheim. “Dual-species apparatus for creating a dipolar quantum gas of ^{23}Na ^{40}K molecules”. PhD Thesis. University of Munich, 2015. DOI: 10.5282/edoc.18978. URL: [Link](#).
- [85] Torben A. Schulze. “Quantum degenerate mixtures of ^{23}Na - ^{39}K and coherent transfer paths in NaK molecules”. PhD Thesis. Leibniz University Hannover, 2018. DOI: <https://doi.org/10.15488/3429>. URL: [Link](#).
- [86] Hartmann Torsten. “An experiment apparatus for the production of ultracold bosonic dipolar ground state $^{23}\text{Na}^{39}\text{K}$ molecules and Feshbach spectroscopy in a cold mixture of ^{23}Na and ^{39}K ”. PhD Thesis. Leibniz University Hannover, 2018. DOI: <https://doi.org/10.15488/4699>. URL: [Link](#).
- [87] Jiří Etrych, Gevorg Martirosyan, Alec Cao, Jake A. P. Glidden, Lena H. Dogra, Jeremy M. Hutson, Zoran Hadzibabic, and Christoph Eigen. “Pinpointing Feshbach resonances and testing Efimov universalities in ^{39}K ”. In: *Physical Review Research* 5.1 (Mar. 2023). Publisher: American Physical Society, p. 013174. DOI: 10.1103/PhysRevResearch.5.013174. URL: [Link](#).
- [88] Chiara D’Errico, Matteo Zaccanti, Marco Fattori, Giacomo Roati, Massimo Inguscio, Giovanni Modugno, and Andrea Simoni. “Feshbach resonances in ultracold ^{39}K ”. In: *New Journal of Physics* 9.7 (July 2007), p. 223. ISSN: 1367-2630. DOI: 10.1088/1367-2630/9/7/223. URL: [Link](#).

- [89] Helmut Strobel. “Fisher information and entanglement of non-Gaussian spin states”. PhD Thesis. Heidelberg University, 2016. URL: [Link](#).
- [90] Anton Eberhardt. “Advances in construction of a ^{23}Na - ^{39}K Ultracold Bosonic Mixture Experiment for Analog Quantum Simulations”. MA thesis. Heidelberg University, 2024.
- [91] Pfeiffer Vacuum GmbH. *The Vacuum Technology Book*. Vol. Volume II. Pfeiffer, 2013.
- [92] Rebecca Grinham and Andrew Chew. “A Review of Outgassing and Methods for its Reduction”. In: *Applied Science and Convergence Technology* 26.5 (Sept. 2017). Publisher: The Korean Vacuum Society, pp. 95–109. DOI: 10.5757/asct.2017.26.5.95.
- [93] Manoj Kumar Gupta, Abhinav Priyadarshi, and Ziauddin Khan. “Hydrogen in Stainless Steel as Killing Agent for UHV: A Review”. In: *Materials Today: Proceedings* 2.4-5 (2015). Publisher: Elsevier Ltd, pp. 1074–1081. ISSN: 22147853. DOI: 10.1016/j.matpr.2015.07.011.
- [94] Karl Jousten, ed. *Handbuch Vakuumtechnik*. Berlin, Germany: Springer Vieweg Wiesbaden, Mar. 2018.
- [95] Pramod K. Naik. *Vacuum Science, Technology and Applications*. CRC Press, 2018.
- [96] “Accelerator School Vacuum in accelerators”. In: ed. by Daniel Brandt. Geneva, 2007. DOI: 10.5170/CERN-2007-003.
- [97] Niels Marquardt. “Introduction to the principles of vacuum physics”. In: *CAS - CERN Accelerator School : Vacuum Technology* (1999). DOI: 10.5170/CERN-1999-005.1.
- [98] Matthias Weidemüller and Claus Zimmermann, eds. *Cold Atoms and Molecules*. Weinheim: WILEY-VCH Verlag GmbH & Co. KGaA, 2009. ISBN: 978-3-527-40750-7.
- [99] Umakant D. Rapol, Ajay Wasan, and Vasant Natarajan. “Loading of a Rb magneto-optic trap from a getter source”. In: *Physical Review A - Atomic, Molecular, and Optical Physics* 64.2 (2001), p. 5. ISSN: 10941622. DOI: 10.1103/PhysRevA.64.023402.
- [100] P. F. Griffin, K. J. Weatherill, and C. S. Adams. “Fast switching of alkali atom dispensers using laser-induced heating”. In: *Review of Scientific Instruments* 76.9 (Sept. 2005). ISSN: 00346748. DOI: 10.1063/1.2038167.
- [101] H J Lewandowski, D M Harber, D L Whitaker, and E A Cornell. “Simplified System for Creating a Bose-Einstein Condensate”. In: *Journal of Low Temperature Physics* 132.6 (2003).

- [102] David R Scherer, David B Fenner, and Joel M Hensley. “Characterization of alkali metal dispensers and non-evaporable getter pumps in ultrahigh vacuum systems for cold atomic sensors”. In: *Journal of Vacuum Science & Technology A* 30.6 (Oct. 2012), p. 061602. ISSN: 0734-2101. DOI: 10.1116/1.4757950. URL: [Link](#).
- [103] P. della Porta, C. Emili, and S.J. Hellier. “Alkali Metal Generation and Gas Evolution from Alkali Metal Dispensers”. In: (1968).
- [104] Tobias Hammel. “Design and Construction of a New Experiment for Programmable Quantum Simulation using Ultracold ^6Li Fermions”. MA thesis. Heidelberg University, 2021. URL: [Link](#).
- [105] H Kurisu, K Ishizawa, S Yamamoto, M Hesaka, and Y Saito. “Application of titanium materials to vacuum chambers and components”. en. In: *Journal of Physics: Conference Series* 100.9 (Mar. 2008), p. 092002. ISSN: 1742-6596. DOI: 10.1088/1742-6596/100/9/092002. URL: [Link](#).
- [106] James A. Fedchak, Julia K. Scherschligt, Sefer Avdiaj, Daniel S. Barker, Stephen P. Eckel, Ben Bowers, Scott O’Connell, and Perry Henderson. “Outgassing rate comparison of seven geometrically similar vacuum chambers of different materials and heat treatments”. In: *Journal of Vacuum Science & Technology B, Nanotechnology and Microelectronics: Materials, Processing, Measurement, and Phenomena* 39.2 (Mar. 2021), p. 024201. ISSN: 2166-2746, 2166-2754. DOI: 10.1116/6.0000657. URL: [Link](#).
- [107] R J Reid. “Cleaning for Vacuum Service”. In: *CERN European Organization for Nuclear Research Reports* (1999), pp. 139–154. URL: [Link](#).
- [108] Oliver Posth, Heiko Wunderlich, Michael Flämmich, and Ute Bergner. “Cleaning of vacuum components for UHV and UCV applications”. In: *Vakuum in Forschung und Praxis* 24.6 (Dec. 2012). Publisher: Wiley-VCH Verlag, pp. 18–25. ISSN: 15222454. DOI: 10.1002/vipr.201200511.
- [109] C Benvenuti. “Extreme Vacua: Achievements and Expectations”. In: *Physica Scripta* 22 (1988), pp. 48–54. DOI: 10.1088/0031-8949/1988/T22/006.
- [110] Tobias Rentrop. “Observation of the Phononic Lamb Shift in a Synthetic Vacuum”. PhD Thesis. Heidelberg University, 2016. DOI: 10.11588/heidok.00021572. URL: [Link](#).
- [111] R Calder and G Lewin. “Reduction of stainless-steel outgassing in ultra-high vacuum”. In: *British Journal of Applied Physics BRIT. J. APPL. PHYS* 18 (1967). DOI: 10.1088/0508-3443/18/10/313. URL: [Link](#).

- [112] Sergei Piatchenkov. “A versatile ultracold strontium apparatus: from construction to new tools for quantum simulation”. PhD Thesis. University of Amsterdam, 2019. URL: [Link](#).
- [113] Nikolas Liebster, Elinor Kath, Marius Sparn, and Helmut Strobel. *Personal Discussions*.
- [114] C. D. Park, S. M. Chung, and Paolo Manini. “Combination of compact nonevaporable getter and small ion pumps for ultrahigh vacuum systems”. In: *Journal of Vacuum Science & Technology A: Vacuum, Surfaces, and Films* 29.1 (Jan. 2011), p. 011012. ISSN: 0734-2101, 1520-8559. DOI: 10.1116/1.3529379. URL: [Link](#).
- [115] E Maccallini, P Manini, A Conte, F Siviero, and A Bonucci. “New Approach to meet vacuum requirements in UHV/XHV systems by Non Evaporable Getter Technology”. In: *Journal of Physics: Conference Series* 390 (Nov. 2012), p. 012006. ISSN: 1742-6588, 1742-6596. DOI: 10.1088/1742-6596/390/1/012006. URL: [Link](#).
- [116] H. W. Roesky. “A facile and environmentally friendly disposal of sodium and potassium with water”. In: *Inorganic Chemistry* 40.26 (Dec. 2001), pp. 6855–6856. ISSN: 00201669. DOI: 10.1021/ic010594m.
- [117] Darrell Ebbing and Steven Gammon. *General Chemistry*. 9th Edition. Boston: Houghton Mifflin Company, 2009. ISBN: 0-618-93469-3. URL: [Link](#).
- [118] Hermann Sicius. *Wasserstoff und Alkalimetalle: Elemente der ersten Hauptgruppe*. essentials. Wiesbaden: Springer Fachmedien, 2016. ISBN: 978-3-658-12267-6 978-3-658-12268-3. DOI: 10.1007/978-3-658-12268-3. URL: [Link](#).
- [119] Uwe Böhme. *Inertgastechnik: Arbeiten unter Schutzgas in der Chemie*. Berlin, Boston: De Gruyter Oldenbourg, 2020.
- [120] *Prudent Practices in the Laboratory: Handling and Disposal of Chemicals*. Washington, D.C.: National Academies Press, Aug. 1995. ISBN: 978-0-309-05229-0. DOI: 10.17226/4911. URL: [Link](#).
- [121] Jim Clark. *The Reaction Between Alcohols and Sodium*. Oct. 2013. URL: [Link](#) (visited on 08/03/2024).
- [122] William D Callister and David G Rethwisch. *Materials science and engineering : an introduction*. 10th Edition. Hoboken NJ: John Wiley & Son, 2018. ISBN: 978-1-119-40543-6. URL: [Link](#).
- [123] F Schreck. *Personal Discussion*. 2024.
- [124] Brian Bostwick. *Personal Discussion*. 2024.

- [125] Mario Castro, Rodolfo Cuerno, Matteo Nicoli, Luis Vázquez, and Josephus G. Buijnsters. “Universality of cauliflower-like fronts: From nanoscale thin films to macroscopic plants”. In: *New Journal of Physics* 14 (Oct. 2012). ISSN: 13672630. DOI: 10.1088/1367-2630/14/10/103039.
- [126] Timo Bihr, Fabrizio Zagros Sadafi, Udo Seifert, Robin Klupp Taylor, and Ana Sunčana Smith. “Radial Growth in 2D Revisited: The Effect of Finite Density, Binding Affinity, Reaction Rates, and Diffusion”. In: *Advanced Materials Interfaces* 4.1 (Jan. 2017). Publisher: Wiley-VCH Verlag. ISSN: 21967350. DOI: 10.1002/admi.201600310.
- [127] Nayiri Khatcheressian, Christian Latgé, Xavier Joulia, Thierry Gilardi, and Xuan Meyer. “Development of a transfer model for the design and the operation of sodium purification systems for fast breeder reactors”. In: *Canadian Journal of Chemical Engineering* 93.2 (Feb. 2015). Publisher: Wiley-Liss Inc., pp. 213–224. ISSN: 1939019X. DOI: 10.1002/cjce.22127.
- [128] R. Meppelink. “Hydrodynamic excitations in a Bose-Einstein condensate”. PhD Thesis. Utrecht University, Oct. 2009. URL: [Link](#).
- [129] N. SivaiBharasi, Nanda Gopala Krishna, A. Ravi Shankar, S. Krishnakumar, S. Chandramouli, Vijay Karki, S. Kannan, and John Philip. “Influence of long term Sodium Exposure on the Corrosion and Tensile Properties of AISI Type 316LN stainless steel and modified 9Cr-1Mo steel”. In: *Journal of Nuclear Materials* 567 (Aug. 2022), p. 153830. ISSN: 0022-3115. DOI: 10.1016/j.jnucmat.2022.153830. URL: [Link](#).
- [130] Matthieu Rivollier, Jean Louis Courouau, Michel Tabarant, Cécile Blanc, and Marie Laurence Giorgi. “Oxidation of 316L(N) stainless steel in liquid sodium at 650°C”. In: *Journal of Nuclear Materials* 500 (Mar. 2018). Publisher: North-Holland, pp. 337–348. ISSN: 0022-3115. DOI: 10.1016/J.JNUCMAT.2017.12.037.
- [131] N. P. Bhatt and H. U. Borgstedt. “Corrosion behaviour of structural materials in sodium influenced by formation of ternary oxides”. In: *Materials and Corrosion* 39.3 (1988), pp. 115–123. ISSN: 15214176. DOI: 10.1002/maco.19880390302.
- [132] Vaidehi Ganesan and Vedaraman Ganesan. “Corrosion of annealed AISI 316 stainless steel in sodium environment”. In: *Journal of Nuclear Materials* 256.1 (July 1998). Publisher: North-Holland, pp. 69–77. ISSN: 0022-3115. DOI: 10.1016/S0022-3115(98)00041-5.

- [133] M. G. Barker and D. J. Wood. “The corrosion of chromium, iron, and stainless steel in liquid sodium”. In: *Journal of the Less Common Metals* 35.2 (Apr. 1974), pp. 315–323. ISSN: 0022-5088. DOI: 10.1016/0022-5088(74)90243-4. URL: Link.
- [134] Sylvie Chatain, Nicolas David, David Bonina, Jean Louis Flèche, Christophe Bonnet, Jean Louis Courouau, and Marion Rouhard. “Thermodynamic study of the sodium chromite NaCrO_2 ”. In: *Journal of Alloys and Compounds* 882 (Nov. 2021). Publisher: Elsevier Ltd. ISSN: 09258388. DOI: 10.1016/j.jallcom.2021.160784.
- [135] J. Schoser, A. Batär, R. Löw, V. Schweikhard, A. Grabowski, Yu. B. Ovchinnikov, and T. Pfau. “Intense source of cold Rb atoms from a pure two-dimensional magneto-optical trap”. In: *Physical Review A* 66.2 (Aug. 2002), p. 023410. ISSN: 1050-2947, 1094-1622. DOI: 10.1103/PhysRevA.66.023410. URL: Link.
- [136] T. G. Tiecke, S. D. Gensemer, A. Ludewig, and J. T.M. Walraven. “High-flux two-dimensional magneto-optical-trap source for cold lithium atoms”. In: *Physical Review A - Atomic, Molecular, and Optical Physics* 80.1 (Aug. 2009). ISSN: 10502947. DOI: 10.1103/PhysRevA.80.013409.
- [137] Jianshun Gao. “A First Two-Dimensional Magneto-Optical Trap for Dysprosium”. Ph.D. admission thesis. University of Heidelberg, 2022. URL: Link.
- [138] Shuwei Jin, Jianshun Gao, Karthik Chandrashekhara, Christian Götzhäuser, Joschka Schöner, and Lauriane Chomaz. “Two-dimensional magneto-optical trap of dysprosium atoms as a compact source for efficient loading of a narrow-line three-dimensional magneto-optical trap”. In: *Physical Review A* 108.2 (Aug. 2023). Publisher: American Physical Society. ISSN: 24699934. DOI: 10.1103/PhysRevA.108.023719.
- [139] Simone Donadello. “A compact high-flux source of cold sodium atoms”. MA thesis. University of Trento, 2012.
- [140] *Preparatory Material Magneto-optical Trap*. University of Heidelberg, Physikalische Institut. Mar. 2023. URL: Link.
- [141] E Pedrozo-Peñafiel, F Vivanco, P Castilho, R R Paiva, K M Farias, and V S Bagnato. “Direct comparison between a two-dimensional magneto-optical trap and a Zeeman slower as sources of cold sodium atoms”. In: *Laser Physics Letters* 13.6 (2016). DOI: 10.1088/1612-2011/13/6/065501. URL: Link.
- [142] Jens Appmeier. “Immersed Quantum Systems: A Sodium Bose-Einstein Condensate for Polaron Studies”. PhD thesis. University of Heidelberg, 2010. DOI: 10.11588/heidok.00010949. URL: Link.

- [143] Patricia Christina Marques Castilho. “New experimental system to study coupled vortices in a two-species Bose-Einstein condensate ^{23}Na - ^{41}K with tunable interactions”. PhD Thesis. Universidade de São Paulo, 2017. DOI: 10.11606/T.76.2017.tde-11092017-082144. URL: [Link](#).
- [144] Ivaylo Sashkov Madjarov. “Entangling, controlling, and detecting individual strontium atoms in optical tweezer arrays”. en. PhD Thesis. California Institute of Technology, 2021. DOI: 10.7907/d1em-dt34. URL: [Link](#).
- [145] Jae Yoon Choi, Woo Jin Kwon, and Yong Il Shin. “Observation of topologically stable 2D skyrmions in an antiferromagnetic spinor bose-einstein condensate”. In: *Physical Review Letters* 108.3 (Jan. 2012). ISSN: 00319007. DOI: 10.1103/PhysRevLett.108.035301.
- [146] Matthias Wenzel. “Macroscopic States of Dipolar Quantum Gases”. PhD Thesis. University of Stuttgart, 2018. URL: [Link](#).
- [147] Steven Chu, J. E. Bjorkholm, A. Ashkin, and A. Cable. “Experimental Observation of Optically Trapped Atoms”. In: *Physical Review Letters* 57.3 (July 1986), pp. 314–317. ISSN: 0031-9007. DOI: 10.1103/PhysRevLett.57.314. URL: [Link](#).
- [148] Johanna Elise Bohn. “Towards an ultracold three-component Fermi Gas in a two-dimensional optical lattice”. Diploma Thesis. University of Heidelberg, 2012. URL: [Link](#).
- [149] Mathias Neidig. “A realization of a two-dimensional Fermi gas in a standing wave trap”. MA thesis. University of Heidelberg, 2013. URL: [Link](#).
- [150] Todd Philip Meyrath. “Experiments with Bose-Einstein Condensation in an Optical Box”. PhD Thesis. The University of Texas at Austin, 2005. URL: [Link](#).
- [151] T. P. Meyrath, F. Schreck, J. L. Hanssen, C. S. Chuu, and M. G. Raizen. “A high frequency optical trap for atoms using Hermite-Gaussian beams”. In: *Optics Express* 13.8 (2005), p. 2843. ISSN: 1094-4087. DOI: 10.1364/OPEX.13.002843. URL: [Link](#).
- [152] Nathan Llewellyn Smith. “The Tilting Mode and Two Dimensional Confinement of a Bose-Einstein Condensed Gas”. PhD Thesis. University of Oxford, 2005.
- [153] Sebastian J Krinner. “Quantum Transport of Ultracold Atoms”. PhD Thesis. ETH Zürich, 2015. DOI: 10.3929/ethz-a-010556528. URL: [Link](#).
- [154] Kristian Fenech. “Kinematics and Thermodynamics of a Two-Dimensional Fermi Gas”. PhD Thesis. Swinburne University of technology, 2016. URL: [Link](#).

- [155] T. C. Li, H. Kelkar, D. Medellin, and M. G. Raizen. “Real-time control of the periodicity of a standing wave: an optical accordion”. In: *Optics Express* 16.8 (Apr. 2008), p. 5465. ISSN: 1094-4087. DOI: 10.1364/OE.16.005465. URL: [Link](#).
- [156] Eleonora Lippi. “Realization of a large-spacing optical lattice for trapping fermionic lithium gases in two dimensions”. MA thesis. University of Florence, 2017. URL: [Link](#).
- [157] James P Landry. “Appendix F: Waist Radius Measurement of Gaussian Beams”. in PhD Thesis. University of California, 2008. URL: [Link](#) (visited on 08/04/2024).
- [158] W. Ketterle, D. S. Durfee, and D. M. Stamper-Kurn. *Making, probing and understanding Bose-Einstein condensates*. Apr. 1999. DOI: 10.48550/arXiv.cond-mat/9904034. URL: [Link](#).
- [159] G. Reinaudi, T. Lahaye, Z. Wang, and D. Guery-Odelin. “Strong saturation absorption imaging of dense clouds of ultracold atoms”. In: (July 2007). arXiv: 0707.2930. DOI: 10.1364/OL.32.003143. URL: [Link](#).
- [160] Klaus Hueck, Niclas Luick, Lennart Sobirey, Jonas Siegl, Thomas Lompe, Henning Moritz, Logan W. Clark, and Cheng Chin. “Calibrating high intensity absorption imaging of ultracold atoms”. In: *Optics Express* 25.8 (Apr. 2017). arXiv: 1702.01943 Publisher: The Optical Society, p. 8670. ISSN: 10944087. DOI: 10.1364/oe.25.008670.
- [161] Marius Sparn. “A Setup for Creating Arbitrary Potentials in a Two-dimensional ^{39}K BEC with a Digital Micromirror Device”. MA thesis. Heidelberg University, 2020. URL: [Link](#).
- [162] Maurice Rieger. “Magnetic field characterisation and spin manipulation in ultracold dysprosium using radio-frequency driving and AC Stark shifts”. BA Thesis. Heidelberg University, 2023. URL: [Link](#).
- [163] Sarah Philips. “Characterizing a High-Resolution Imaging System for the Dysprosium Experiment”. MA thesis. Heidelberg University, 2023. URL: [Link](#).
- [164] Timo Ottenstein. “A New Objective for High Resolution Imaging of Bose-Einstein Condensates”. Diploma Thesis. Heidelberg University, 2006. URL: [Link](#).
- [165] Robert M Bunch. *Optical Systems Design Detection Essentials*. Bristol, UK: IOP Publishing, 2021. ISBN: 978-0-7503-2252-2.
- [166] Maurus Hans. “Physical Computing on a Versatile Setup for Ultra-cold Potassium”. PhD Thesis. University of Heidelberg, 2022. DOI: 10.11588/heidok.00032365. URL: [Link](#).

- [167] Yann Kiefer, Max Hachmann, and Andreas Hemmerich. “Two-color laser cooling for ^{40}K - ^{87}Rb quantum gas mixtures”. In: *Physical Review A* 109.2 (Feb. 2024), p. 023320. ISSN: 2469-9926, 2469-9934. DOI: 10.1103/PhysRevA.109.023320. URL: [Link](#).
- [168] Marcel Kern. “Enhanced Local Control of Two-Dimensional Ultracold Atomic Clouds”. MA thesis. Heidelberg University, 2024. URL: [Link](#).
- [169] Péter Juhász. “Optical trapping and transport of ultracold erbium atoms”. PhD Thesis. University of Oxford, 2019. URL: [Link](#).
- [170] Carl Kindermann. “Optimization of ArTTA: New Statistical Analysis and Investigation of the High Vacuum System”. MA thesis. Heidelberg University, 2024.

ERKLÄRUNG

Ich versichere, dass ich diese Arbeit selbstständig verfasst und keine anderen als die angegebenen Quellen und Hilfsmittel benutzt habe.

Heidelberg, den 4. August, 2024

Lilo Höcker